STUDIES OF GRAVITY WAVE AND THERMAL TIDE AND THEIR INTERACTIONS IN THE MIDDLE ATMOSPHERE

BY

XIAN LU

DISSERTATION

Submitted in partial fulfillment of the requirements
for the degree of Doctor of Philosophy in Atmospheric Sciences
in the Graduate College of the
University of Illinois at Urbana-Champaign, 2011

Urbana, Illinois

Doctoral Committee:

Associate Professor Alan Z. Liu, Chair
Professor Gary R. Swenson
Professor Steven J. Franke
Professor Robert M. Rauber

ABSTRACT

Gravity waves (GWs) and tides are two strongest and most persistent waves in the middle atmosphere of the Earth. They are usually generated in the lower atmosphere and propagate upward to the middle and upper atmosphere, where they play important roles in the atmospheric composition, chemistry, dynamics and energetics. This dissertation focuses on a case-study of the propagation and dissipation characteristics of an inertial GW, the seasonal variation of the diurnal tide based on both the observations and models, and also the interactions between GWs and tides.

One-night (October 28, 2003) temperature and horizontal wind measurements by a resonance sodium (Na) wind/temperature lidar in Maui (20.7°N, 156.3°W) and temperature measurement by a Rayleigh lidar at Mauna Loa Observatory (MLO, 19.5°N, 155.6°W), HI, are used as a case study of the GW propagation from the lower stratosphere to the lower thermosphere (35-103 km). A dominant wave mode is identified from the simultaneous temperature observations by both lidars. The wave is partially dissipated and propagates upward with an e-fold height of temperature amplitude at ∼14 km. A damping layer is present around the stratopause where the wave amplitude is relatively smaller, corresponding to a low static stability layer. The vertical wavelengths are larger in the mesosphere (12-13 km) than in the stratosphere (6-7 km), consistent with the decreasing static stability with altitude. The wave is propagating northward and the horizontal wavelength is ∼2140 km and intrinsic period is 15 hrs in the region of 84-103 km. The apparent period is ∼ 6 hrs and consistent with Doppler shift of the background wind. It is suggested that the convective zone over the equator to the south of Hawaii provides a constant GW source that

is responsible for the observed GW throughout the night.

The seasonal variability of the diurnal tide in the mesosphere and lower thermosphere (MLT) over Maui, HI is investigated using the meteor radar horizontal wind measurement from years 2002 to 2007. The semiannual oscillation (SAO) of tidal amplitudes is dominant above ∼88 km, with amplitudes at the equinoxes 2-3 times larger than at the solstices. Below 88 km, the annual oscillation (AO) dominates and its magnitude is smaller than the SAO. The AO dominates in the phase variation of the diurnal tide, which advances in winter and lags in summer as compared with the equinoxes. The vertical wavelength also has a noticeable seasonal variation with shorter vertical wavelengths found at the equinoxes. The reconstruction of the diurnal tide by superposing the migrating and nonmigrating tides derived from Thermosphere Ionosphere Mesosphere Energetics and Dynamics/Doppler Interferometer (TIMED/TIDI) and TIMED/Sounding of the Atmosphere using Broadband Emission Radiometry (SABER) temperature is compared with the meteor radar observation, and a consistency is found in the seasonal variation of the tidal amplitude. Based on the TIDI and SABER measurements, the migrating diurnal tide (DW1) is the dominant tidal component while three other nonmigrating tides, DW2, DS0 and DE3, are non-negligible. The seasonal variation of the diurnal tide is well captured by the Global Scale Wave Model (GSWM) and the Whole Atmosphere Community Climate Model (WACCM) while discrepancies are also presented and discussed.

Since the WACCM is capable of reproducing the tidal seasonality, it is used to examine the physical mechanisms. First, the effects of GW forcing and advection on the momentum balance of DW1 are investigated, because they are the two most dominant terms in the momentum equation that account for the discrepancies between classical tidal theory and the calculations based on the full primitive equations. In the WACCM, GW forcing in the wave breaking region always damps DW1 and advances its phase, thus shortening the vertical wavelength of the tide locally. The linear advection largely determined by the latitudinal shear of the zonal mean wind mostly contributes to the phase change in the zonal wind. For

the meridional wind, however, nonlinear advection is more important than GW drag and linear advection for the amplitude and phase changes. The DW1 amplitudes are smaller than TIMED observations, suggesting that the GW forcing is overestimated in the WACCM and result in an unrealistic large damping on DW1.

Second, the seasonal variations of GW forcing, tidal heating and mean wind effects are examined using the WACCM. Similar to the tidal amplitude, stronger GW forcing is also found at the equinox, which can not account for the tidal seasonality because GW forcing always damps DW1. Instead, the radiative tidal heating due to the water vapor absorption of infrared solar radiation largely determines the SAO of DW1. The effect of mean winds leads to a 1-month time shift of the maximum amplitude. The AO in the tidal phase is due to the seasonal change of mean winds. At the solstice, a stronger antisymmetric (1,2) Hough mode is generated which significantly distorts the tidal structure. Because the phase of the (1,2) mode changes by 12-hrs every half a year, it causes a phase advance in winter and a lag in summer, thus leading to an AO of the phase.

As GWs and tides reach the MLT region, they can maintain large amplitudes thus strong interactions between them are expected. High-frequency GW variances are calculated as the residual horizontal wind variances based on the meteor radar measurements in Maui, HI and Urbana, IL (40°N, 88°W). Monte-Carlo simulations are performed in order to evaluate the sensitivity of the GW variance calculation on the meteor rate. It is indicated that the residual horizontal wind variance can be used as a good proxy of GW activities. The diurnal and semidiurnal variations of the GW variances are most dominant, while periods of 2-day, 5-day and 10-day are also observed. The vertical phase structures of the GW variances and tidal winds are consistent with each other, implying the GW variances are modulated by tides. In most cases, the GW variances increase with altitude and the growth rates are slower than freely propagating waves. A further study on the physical mechanisms resulting in the tidal modulations is needed in the future.

To my parents, for their love and support.

ACKNOWLEDGMENTS

Firstly, I want to thank my advisor Dr. Alan Liu for his continuous support and guidance on my PhD research. He led me a way to this research area and encouraged me to explore and develop my own interests. During my 5-year PhD study, Alan has always been patient, inspiring and supportive. He can always explain a complex scientific question in a simple and illuminative way. Meanwhile, he captures and points out my mistakes and weaknesses in understanding my research topics all the time. He took every opportunity to support me to attend academic conferences, from where I obtained broader and more comprehensive views on our own research. I also wish to thank my group mate Zhenhua Li, who is smart and very good at finding new things, such as new softwares in our research areas. Zhenhua helped me on solving not only scientific questions, but also technique problems. I wish to thank Dr. Gary Swenson. I can always learn something from Gary by the helpful scientific discussion with him. Gary has been generously supporting me and providing me the office resources. I have been working closely with Alan, Zhenhua and Gary, who unselfishly shared their scientific insights and working experiences with me, which are of great values for my future career.

In addition, I am very grateful to the scientists I worked with when I was visiting HAO, NCAR. They are Dr. Hanli Liu, Dr. Qian Wu, Chihoko Yamashita, Dr. Jia Yue, Dr. Joe McInerney, Dr. Art Richmond and many others who I didn't directly work with but helped me on all kinds of problems. Especially, I want to thank Hanli for making this visit possible, valuable and memorable. His broad knowledge and profound understanding on the atmospheric dynamics and modeling impressed me and made me believe they are intriguing

and important. I also thank Dr. David Ortland (NWRA), Dr. Anne Smith (ACD/NCAR), Dr. Jia Yue and Dr. Loren Chang for their expertise and patient help on my tidal research. I appreciate Dr. Xinzhao Chu and Dr. Xiaoli Zhang's (The University of Colorado at Boulder) encouragement and help during my NCAR visit in Boulder. Dr. Steven Franke provided me the meteor radar data and Dr. Maura Hagan provided the access to the GSWM model results. Dr. Qian Wu and Dr. Jens Oberheide (Clemson University) provided me the TIMED satellite data, who also gave me good suggestion on my latest paper. I am grateful to them for making this study possible.

Last but not the least, I would like to thank my parents for their tolerance, support and understanding without any conditions. Everything I have would become worthless without their love.

TABLE OF CONTENTS

LIST OF TABLES

LIST OF FIGURES

CHAPTER 1

INTRODUCTION

This dissertation focuses on the gravity waves (GWs) and diurnal tides in the stratosphere, mesosphere and lower thermosphere (MLT) region. Atmospheric waves, such as GWs and tides are usually generated in the lower atmosphere, propagate upward and reach the MLT region with large amplitudes and significant influences. The generation of the tides is predictable and persistent, while the excitation of GWs is more random but it occurs all over the planet. So both wave activities are ubiquitous in the Earth's atmosphere. As their amplitudes grow large enough and induce instabilities, GWs and tides break in the MLT region and deposit momentum to the mean flow [*Lindzen*, 1981]. The acceleration due to the wave momentum deposition is balanced by the meridional residual circulation. It is also accompanied by the vertical motion due to the mass continuity. Due to the filtering effects of the stratospheric jets, the momentum deposition is preferentially eastward (westward) in the summer (winter) hemisphere in terms of the Northern Hemisphere (NH). The zonal acceleration is balanced by a summer-to-winter-hemisphere meridional residual circulation due to the Coriolis effect. The corresponding vertical motion is upward (downward) in the summer (winter) hemisphere. Associated with the vertical adiabatic motion, a cooling (warming) effect is found in the summer (winter) hemisphere and this is the reason why the minimum temperature of the Earth is located at the summer mesopause. Therefore, GWs and tides are important for the mean circulation and thermal balance through wave momentum transport and body forces arising from wave dissipation and momentum divergence [*Holton*, 1982; *Fritts*, 1984; *Garcia and Solomon*, 1985; *Fritts and Alexander*, 2003].

Although the stratosphere and MLT are not directly related to either the meteorological

weather or space weather, they consist of an important coupling region in between which can bring the impacts of the lower atmosphere to the upper, and vice versa. It has been recognized that the state of the ionosphere is also affected by processes in the lower atmosphere, such as fronts, convection systems, sudden stratospheric warmings (SSW), etc., through the upward-propagating tides, planetary waves (PWs) and GWs [*Forbes et al.*, 2000]. *Immel et al.* [2006] found that the ionospheric densities varying with the strength of nonmigrating diurnal atmospheric tides are mainly driven by weather in the tropics. They also suggested that although the upward-propagating tidal momentum is heavily damped at upper E-region altitudes, the polarization electric fields the tides produce are transmitted upward into the F-region with significant tidal signals. Tides and GWs play an important role in the coupling process from the lower to the upper atmosphere.

Due to their significant impacts, tides and GWs have been studied extensively in the past few decades in that many observations and models are dedicated to investigating their dynamics, climatology and influences. Nevertheless, some of their characteristics in the middle and upper atmosphere are still the least known and understood areas. It is not surprising because every observational technique and model has limitations. For instance, radiosonde, radar, lidar and rocket observations are more sensitive to inertial GWs and airglow imager can only observe GWs with relatively larger vertical wavelengths and shorter horizontal scales. The complete GW spectrum at the source level and its evolution with altitude are difficult to be retrieved. Because the constraints from GW observations are quite limited, the GW parameterizations used in global models still have a large degree of uncertainty. In addition, the interaction between GWs and tides is a controversial question since different GW parameterizations give rise to the opposite conclusions [*McLandress*, 1998]. Overall, a whole complete picture of the dynamics and energetics associated with GWs and tides is still missing and needs further investigations.

The focus of this chapter is on the basic theories and concepts involving GWs and tides, which are related to the studies in this dissertation.

1.1 Gravity Waves

1.1.1 Introduction

As it is named as "Gravity Wave" (GW), the gravity is the restoring force of GW. As an air parcel is displaced vertically, the gravity force will bring it back to the initial location if the atmosphere is stably stratified, thus generating an oscillation about the equilibrium level. This oscillation propagates away by making the surrounding air parcels oscillate at a same frequency and a GW is generated. The atmosphere stratification is important because the density difference between the air parcel and the environment is required to generate GWs. They can be traced as the occurrence of mountain lee waves and the formation of clear air turbulence (CAT).

The most significant triggering forces for GWs in the lower atmosphere include topography, convection and geostrophic adjustment, etc. Mountain waves are generated when the winds blow over a mountain or a mountain range and the forced vertical motion leads to the periodic changes of the atmospheric density, temperature, pressure and winds. Mountain waves have dominant scales of ∼10-100 km and phase speeds near zero [*Bacmeister et al.*, 1990]. Thus they always tend to decelerate the mean flow. The released latent heat in the convection zone generates a time and space varying thermal forcing that can interact with the stable atmospheric layer and shear in a complex way and excite GWs. Unlike mountain waves which have horizontal scales comparable to the associated topography, the waves generated by convection are characterized by a full range of wave frequencies and horizontal and vertical scales [*Fritts and Alexander*, 2003]. The GW excitation by the geostrophic adjustment involves the restoration of a balanced flow, when an initial unbalanced flow relaxes to a new balanced state and radiates the excess energy away as inertia-GWs. *Guest et al.* [2000] found that the generation of the inertial GWs was highly correlated with a synoptic pattern with a jet stream. The geostrophic adjustment associated with frontogenesis and baroclinic instability are also capable of exciting inertia-GWs with the adjusted mean and wave scales

largely determined by the unbalanced flow [*O'Sullivan and Dunkerton*, 1995; *Griffiths and Reeder*, 1996; *Reeder and Griffiths*, 1996]. Typical vertical scales of these inertial-GWs are a few to tens of kilometers, with horizontal scales about 10-100 times larger [*Fritts and Alexander*, 2003]. Wave periods are from hours to the inertial period, which is latitude dependent. Dissipation of GWs mainly results from wave breaking and instabilities [*Lindzen*, 1981; *Fritts and Rastogi*, 1985; *Fritts and Yuan*, 1989; *Lombard and Riley*, 1996; *Gardner et al.*, 2002; *Liu and Gardner*, 2004; *Li et al.*, 2005a,b], wave-wave and wave-mean flow interactions [*Yeh and Liu*, 1981; *Fritts and Rastogi*, 1985], and radiative damping [*Buhler and McIntyre*, 1999].

The observations of GW characteristics, such as wave spectra, intrinsic properties and magnitudes, are essential to understanding GW momentum fluxes, instability dynamics and vertical constituents transport [*Swenson et al.*, 2003; *Liu and Gardner*, 2004, 2005]. Inertia GWs in the troposphere and lower stratosphere (<35 km) can be observed by radiosondes which measure the *in situ* temperature and wind profiles [*Sato and Yamada*, 1994; *Yoshiki and Sato*, 2000; *Wang and Geller*, 2003; *Tsuda et al.*, 2004; *Gong et al.*, 2008]. Observations in the stratosphere and lower mesosphere are often made using Rayleigh lidar technique [*Chanin and Hauchecorne*, 1981; *Gardner et al.*, 1989; *Whiteway and Carswell*, 1995; *Murayama et al.*, 1994; *Sivakumar et al.*, 2006]. GWs in the upper mesosphere have been frequently observed by sodium (Na) resonance lidars [*Lintelman and Gardner*, 1994; *Hu et al.*, 2002; *Li et al.*, 2007a], potassium resonance lidars [*Fricke-Begemann et al.*, 2002; *Friedman*, 2003], radars [*Manson and Meek*, 1988; *Gavrilov et al.*, 1996; *Serafimovich et al.*, 2005] and airglow imagers [*Taylor et al.*, 1995; *Smith et al.*, 2000; *Tang et al.*, 2002; *Li et al.*, 2005b]. In addition to the ground-based measurement, global structure and distribution of GWs are provided by space-borne instruments, such as the Limb Infrared Monitor of the Stratosphere (LIMS) which retrieves temperature profiles from 15 to 60 km [*Fetzer and Gille*, 1994], Cryogenic Infrared Spectrometers and Telescopes for the Atmosphere (CRISTA) with temperature measurement extending from ∼20 to 80 km [*Preusse et al.*, 2000] and High Res-

olution Dynamics Limb Sounder (HIRDLS) [*Alexander et al.*, 2008]. A global map of GW potential energy was also derived based on the GPS occultation temperature data [*Tsuda et al.*, 2000].

Observations of GWs are important for global models to simulate the realistic dynamics, energetics and composition of the atmosphere. GW effects on the mean circulation, thermal balance and constituent transport are paratermized in global models due to their sub-grid scales. Ideally, observations can provide constraints on the GW parameters which are incorporated into the models and play key roles, especially in the stratosphere and mesosphere. Many GW parameterization schemes have been proposed and currently used in global models [*Lindzen*, 1981; *Holton*, 1982; *McFarlane*, 1987; *Fritts and Lu*, 1993; *Hines*, 1997a,b; *Alexander and Dunkerton*, 1999; *Warner and McIntyre*, 2001]. Among these complicated GW schemes, three basic components can be identified, 1) wave spectrum in the source level, 2) wave propagation and/or spectral evolution as altitude increases, 3) wave dissipation and effects on the background atmosphere [*Fritts and Alexander*, 2003]. Unfortunately, the observational constraints on GW parameterization such as the wave spectrum in the source level are still lacking details and arbitrary to some extent. For global models, the GW parameters are usually chosen to reproduce the realistic background temperature, wind and trace gas distribution, rather than determined by the direct GW observations. From this point of view, more extensive and detailed observational studies on GW sources and the generated wave characteristics, wave propagation and dissipation through the atmosphere and GW climatologies, etc., are needed in the future.

1.1.2 Linear Theory

In linear theory, GW perturbations are treated as small departures from a stably stratified background state varying only in the vertical. The dispersion and polarization relations are derived based on the linear theory and will be used for the GW study in Chapter 3. We

start from the fundamental momentum, mass and energy conservation equations in Cartesian coordinates:

$$\frac{Du}{Dt} - fv + \frac{1}{\rho}\frac{\partial p}{\partial x} = X \tag{1.1}$$

$$\frac{Dv}{Dt} + fu + \frac{1}{\rho}\frac{\partial p}{\partial y} = Y \tag{1.2}$$

$$\frac{Dw}{Dt} + \frac{1}{\rho}\frac{\partial p}{\partial z} + g = 0 \tag{1.3}$$

$$\frac{1}{\rho}\frac{D\rho}{Dt} + \frac{\partial u}{\partial x} + \frac{\partial v}{\partial y} + \frac{\partial w}{\partial z} = 0 \tag{1.4}$$

$$\frac{D\theta}{Dt} = Q \tag{1.5}$$

$$\theta = \frac{p}{\rho R}\left(\frac{p_s}{p}\right)^{\kappa} = Q \tag{1.6}$$

where X, Y represent non-conservative mechanical forces such as wave-driven forces and diffusion. Q represents the heating term and $Q = 0$ is for an adiabatic process. The potential temperature θ is defined as in equation (1.6). It is assumed in the linear theory that the total field is a superposition of a mean state flow and perturbation (e.g., $u = \bar{u} + u'$) and the perturbed fields in pressure and density are much smaller than the mean states (e.g., $p' << p_0$, $\rho' << \rho_0$). The linearization process ignores all the quadratic terms of the wave perturbations (e.g., $u'u', u'v'$ and $u'w'$) which are considered to be of second-order smaller. We assume there are no external forcing and heating $(X, Y, Q) = 0$ and background potential temperature, pressure and density only vary vertically. Then the conservative forms of equations (1.1) to (1.6) based on a horizontally uniform hydrostatic basic state ($d\bar{w}/dt = 0$) with background winds $(\bar{u}, \bar{v}, 0)$ are [*Fritts and Alexander*, 2003]:

$$\frac{Du'}{Dt} + w'\frac{\partial \bar{u}}{\partial z} - fv' + \frac{\partial}{\partial x}\left(\frac{p'}{\bar{\rho}}\right) = 0 \tag{1.7}$$

$$\frac{Dv'}{Dt} + w'\frac{\partial \bar{v}}{\partial z} + fu' + \frac{\partial}{\partial y}\left(\frac{p'}{\bar{\rho}}\right) = 0 \tag{1.8}$$

$$\frac{Dw'}{Dt} + \frac{\partial}{\partial z}\left(\frac{p'}{\bar{\rho}}\right) - \frac{1}{H}\left(\frac{p'}{\bar{\rho}}\right) + g\frac{\rho'}{\bar{\rho}} = 0 \tag{1.9}$$

$$\frac{D}{Dt}\left(\frac{\theta'}{\bar{\theta}}\right) + w'\frac{N^2}{g} = 0 \tag{1.10}$$

$$\frac{D}{Dt}\left(\frac{\rho'}{\bar{\rho}}\right) + \frac{\partial u'}{\partial x} + \frac{\partial v'}{\partial y} + \frac{\partial w'}{\partial z} - \frac{w'}{H} = 0 \tag{1.11}$$

$$\frac{\theta'}{\bar{\theta}} = \frac{1}{c_s^2}\left(\frac{p'}{\bar{\rho}}\right) - \frac{\rho'}{\bar{\rho}} \tag{1.12}$$

where $D/Dt = \partial/\partial t + \bar{u}\cdot\partial/\partial x + \bar{v}\cdot\partial/\partial y$ involves the local time derivative plus advection by the mean horizontal winds. By neglecting the background shear (e.g., $\partial\bar{u}/\partial z = 0$) and assuming the GWs solutions take a form of a monochromatic wave perturbation:

$$\left(u', v', w', \frac{\theta'}{\bar{\theta}}, \frac{p'}{\bar{\rho}}, \frac{\rho'}{\bar{\rho}}\right) = (\hat{u}, \hat{v}, \hat{w}, \hat{\theta}, \hat{p}, \hat{\rho}) \cdot \exp\left[i(kx + ly + mz - \omega t) + \frac{z}{2H}\right] \tag{1.13}$$

where (k, l, m) are wavenumber components and ω is the ground-based frequency, equations (1.7) to (1.12) can be written as:

$$-i\hat{\omega}\hat{u} - f\hat{v} + ik\hat{p} = 0 \tag{1.14}$$

$$-i\hat{\omega}\hat{v} + f\hat{u} + il\hat{p} = 0 \tag{1.15}$$

$$-i\hat{\omega}\hat{w} + \left(im - \frac{1}{2H}\right)\hat{p} = -g\hat{\rho} \tag{1.16}$$

$$-i\hat{\omega}\hat{\theta} + (N^2/g)\hat{w} = 0 \tag{1.17}$$

$$-i\hat{\omega}\hat{\rho} + ik\hat{u} + il\hat{v} + \left(im - \frac{1}{2H}\right)\hat{w} = 0 \tag{1.18}$$

$$\hat{\theta} = \hat{p}/c_s^2 - \hat{\rho} \tag{1.19}$$

where $\hat{\omega} = \omega - k\bar{u} - l\bar{v}$ is the intrinsic frequency. The above equations can be combined to form a single equation for the vertical velocity perturbation. Demanding the coefficients of this equation go to zero gives the GW dispersion relation:

$$\hat{\omega}^2 = \frac{N^2(k^2+l^2) + f^2(m^2 + \frac{1}{4H^2})}{k^2 + l^2 + m^2 + \frac{1}{4H^2}} \tag{1.20}$$

or alternatively in terms of the vertical wavenumber as:

$$m^2 = \frac{(N^2 - \hat{\omega}^2)(k^2+l^2)}{\hat{\omega}^2 - f^2} - \frac{1}{4H^2} \tag{1.21}$$

The GW dispersion relation relates the wave intrinsic frequency $\hat{\omega}$ with its horizontal and vertical scales (k, l, m) and the mean background state (N^2, H). N is the Brunt-Väisälä frequency associated with the static stability. When the instability occurs ($N^2 < 0$), GWs will break and deposit momentum to the mean flow. For the propagating waves with real (k, l, m), the intrinsic frequency is within a range of $f < \hat{\omega} < N$. The polarization relation can also be derived based on equations (1.14) to (1.19) and the one relating the zonal and meridional wave amplitudes is:

$$\hat{u} = \left(\frac{i\hat{\omega}k - fl}{i\hat{\omega}l + fk}\right)\hat{v} \tag{1.22}$$

For high frequency waves, air parcels oscillate more vertically. The horizontal wavenumber is comparable to the vertical wavenumber, thus:

$$\hat{\omega}^2 = \frac{N^2(k^2+l^2)}{(k^2 + l^2 + m^2 + 1/4H^2)} \tag{1.23}$$

For inertial GWs, the rotation of the Earth is important and the wave frequency is comparable with the Coriolis parameter ($\hat{\omega} \sim f$) while being much smaller than the buoyancy frequency N. The horizontal scales are larger than the vertical scales and the horizontal wavenumbers are much smaller ($k^2 + l^2 << m^2$). In this case, the dispersion relation can be

approximately written as:

$$\hat{\omega}^2 = N^2 \frac{(k^2 + l^2)}{m^2} + f^2 \tag{1.24}$$

The reader is referred to *Fritts and Alexander* [2003] for more details.

1.1.3 Static Stability and Buoyancy Frequency

Two important concepts associated with GWs are static stability and buoyancy frequency. GWs can only propagate in a statically stable atmosphere while the convective instability induces wave breaking. Buoyancy frequency is an important factor determining the intrinsic characteristics of GWs. The mean background temperature and wind shear can alter GW vertical wavelengths with the change of the buoyancy frequency.

When an air parcel is displaced from its original place and undergoes an adiabatic process, the rate of the temperature decrease with altitude is called the lapse rate. No heat is transferred between the air parcel and the surrounding environment for an adiabatic process. So the first law of thermodynamics can be written in a differential form with respect to altitude as:

$$\frac{d(c_p \ln T - R \ln p)}{dz} = 0 \tag{1.25}$$

With the assumptions of the hydrostatic balance $\frac{dp}{dz} = -\rho g$ and the ideal gas law, we have:

$$\frac{dp}{dz} = -\rho g = -\frac{p}{RT} g \tag{1.26}$$

By combining these two equations, the dry adiabatic lapse rate can be calculated as:

$$-\frac{dT}{dz} = \frac{g}{c_p} = \Gamma_d \approx 9.8^{\circ}\mathrm{C/km} \tag{1.27}$$

The temperature of an upward-displaced air parcel decreases with altitude at a dry adiabatic lapse rate due to the air expansion. If the environment temperature is warmer

than the air parcel, then the negative buoyancy will drag the air parcel downward to the equilibrium level. In this case, the oscillations with respect to the equilibrium level will occur and wave motions can propagate. The atmosphere in this situation is said to be statically stable or stably stratified. The competing factors determining the stability of the atmosphere are the dry adiabatic lapse rate and the lapse rate of the environment atmosphere. If the atmosphere lapse rate, $\Gamma = -\dfrac{\partial T}{\partial z}$ is less than the adiabatic lapse rate, the atmosphere is stable because any displaced air parcel will return to the equilibrium level. Otherwise, the atmosphere is unstable. So the condition for the static instability is: $\Gamma > \Gamma_d$.

In a stably stratified atmosphere, when an air parcel oscillates about its equilibrium level, the characteristic frequency is referred to as the buoyancy frequency or Brunt-Väisälä frequency. If we specify the densities of the air parcel and the environment atmosphere to be ρ and ρ_0, respectively, the vertical acceleration is determined by the gravity and buoyancy force as:

$$\frac{dw}{dt} = \frac{d^2\delta z}{dt^2} = g\left(\frac{\rho_0 - \rho}{\rho}\right) = g\frac{\theta_0 - \theta}{\theta_0} \tag{1.28}$$

For a small vertical displacement δz, the change of the potential temperature can be calculated as:

$$\theta_0 - \theta = -\frac{d\theta_0}{dz}\delta z \tag{1.29}$$

Then the equation (1.28) becomes:

$$\frac{d^2\delta z}{dt^2} = -g\frac{d\ln\theta_0}{dz}\delta z = -N^2\delta z \tag{1.30}$$

So if $N^2 > 0$, the air parcel will oscillate about its equilibrium level with a period of $\tau = 2\pi/N$ and if $N^2 < 0$, the displacement will increase exponentially with time which corresponds to an unstable condition. The more detailed introduction of the static stability and buoyancy frequency can be found in *Holton* [2004].

1.2 Atmospheric Thermal Tides

1.2.1 Introduction

People are familiar with the word "tide" from the experiences of the rise and fall of sea levels with periods of the subharmonics of a solar day, which are so-called the ocean tides. They are generated by the periodic changes of the gravitational forces of the Moon and the Sun exerting on the rotating Earth. Tides also exist in the atmosphere characterized by the similar periodic oscillations in the atmospheric pressure, density, temperature and wind [*Hagan et al.*, 2001], while the generating mechanisms are different from the ocean tides.

Atmospheric thermal tides are mainly excited by the thermal forcing such as the solar radiative heating and latent heat release. The thermal tides maintain large amplitudes and significant influences in the MLT region as they propagate upward from the troposphere and lower stratosphere. Tides are important not only because their amplitudes are comparable to or even larger than the magnitude of the mean winds, but also because their interactions with PWs and GWs play influential roles in atmospheric dynamics [*Fritts and Vincent*, 1987; *Norton and Thuburn*, 1999; *Liu et al.*, 2007]. Tides can affect the propagation of GWs as a part of the background flow [*Lu et al.*, 2009] and modulate GW momentum fluxes [*Espy et al.*, 2004] while tidal structures can be significantly adjusted by GW forcing at the same time [*Fritts and Vincent*, 1987; *Ortland and Alexander*, 2006]. Additionally, migrating tides can interact with PWs and generate non-migrating tides [*Hagan and Roble*, 2001; *Forbes et al.*, 2003; *Mayr and Mengel*, 2005; *Mayr et al.*, 2005; *Liu et al.*, 2007]. Tides can also affect the thermal and dynamical structures of the atmosphere, which may result in the increase of the temperature gradient and/or wind shear and lead to instabilities [*Hecht et al.*, 1997; *Liu et al.*, 2004; *Li et al.*, 2009; *Yue et al.*, 2010]. The atmospheric tides are also responsible for ionospheric variabilities [*Forbes et al.*, 2000; *Rishbeth and Mendillo*, 2001; *Liu et al.*, 2010a]. In the upper part of the middle atmosphere, the vertical tidal transport influences the chemical composition and thus the total heating by solar energy [*Smith et al.*, 2003].

Atmospheric thermal tides are global-scale waves and can be represented by the sinusoidal functions with respect to the universal time t and longitude λ as:

$$f(t,\lambda) = A(t,\lambda)\cos(\omega t + s\lambda - \phi(t,\lambda)) = A(t,\lambda)\cos(\sigma\Omega t + s\lambda - \phi(t,\lambda)) \tag{1.31}$$

where $(A(t,\lambda), \phi(t,\lambda))$ are tidal amplitude and phase, Ω is the rotation rate of the Earth and s is the wavenumber. Since the tidal periods are harmonics of a solar day, ω can be represented as an integer multiple of the rotation rate of the Earth (i.e., $\omega = \sigma\Omega$). The relation between the local time and the universal time is $t_{LT} = t + \lambda/\Omega$, so the equation (1.31) can be rewritten as:

$$f(t,\lambda) = A(t,\lambda)\cos(\sigma\Omega t_{LT} + (s-\sigma)\lambda - \phi(t,\lambda)) \tag{1.32}$$

where $\sigma(= 1, 2, 3)$ corresponds to the periods of the diurnal (24 hrs), semidiurnal (12 hrs) and terdiurnal (8 hrs) tides and $s(= ..., -3, -2, -1, 0, 1, 2, 3, ...)$ represents the zonal wavenumber. Each pair of (σ, s) is referred to as a tidal component. $s = \sigma$ for the migrating tide, which means the tidal phase defined as the local time corresponding to maximum amplitude is independent of longitude. If the frequency ω is always positive, then positive s is chosen for the westward propagating tide and negative is for the eastward propagating tide. So the migrating tides can only propagate westward, following the motion of the Sun. Traditionally, the notion "D" is utilized to represent the diurnal tide and "W", "E" and "S" are used to denote the westward, eastward propagating and stationary tides, respectively. The numbers following them correspond to the zonal wavenumbers. Therefore, DW1 means the diurnal westward propagating tide with zonal wavenumber 1. Since its zonal wavenumber $s = \sigma$, DW1 is the migrating diurnal tide. By the same token, DW2 and DE3 represent the westward propagating diurnal tide with wavenumber 2 and eastward propagating diurnal tide with wavenumber 3, respectively. Since for DW2 and DE3, $s \neq \sigma$, they are nonmigrating tides.

Migrating tides are mainly excited by the absorption of near-infrared (IR) solar radiation by water vapor in the troposphere and ultraviolet solar radiation by ozone in the stratosphere [*Forbes*, 1995]. Migrating tides in the MLT can also be excited locally through the absorption of ultraviolet radiation by oxygen atoms in the thermosphere. DW1 is most dominant at low latitudes and the (1,1) Hough mode is the gravest mode of DW1 in the MLT region [*Forbes*, 1995]. DW1 reaches the maximum temperature amplitude around the equator and reaches the maximum horizontal wind amplitude around 20° latitude [*McLandress et al.*, 1996; *Wu et al.*, 2008]. Non-migrating tides are mainly excited by latent heat release in the tropical region [*Hagan and Forbes*, 2002] and nonlinear interactions between the migrating tides and quasi-stationary PWs [*Hagan and Roble*, 2001; *Lieberman et al.*, 2004].

1.2.2 Classical Tidal Theory

The classical tidal theory [*Chapman and Lindzen*, 1970] provides a first-order prediction of the tidal structures in terms of modal latitudinal structure (Hough modes) and vertical wavelengths. It involves a set of linearized and simplified primitive equations governing the global-scale tidal oscillations. It is assumed that the atmosphere is isothermal and motionless, leading to a separation of *Laplace's tidal equation* determining the latitudinal structure of tides and *vertical structure equation*, connected by equivalent depths (eigenvalues) [*Forbes*, 1995]. Associated with a particular equivalent depth, a certain solution (Hough mode) is prescribed for the *Laplace's tidal equation*. So each Hough mode has a unique equivalent depth which is related to its vertical structure and a unique latitudinal distribution. The different superposition of the Hough modes in different season is considered to be a potential mechanism for the seasonal variation of tides [*Forbes and Hagan*, 1988; *Oberheide and Forbes*, 2008; *Zhang et al.*, 2011].

The equations used by classical tidal theory are similar to equations (1.7)-(1.12) except spherical coordinates are used here due to the global-scale of tidal oscillations. Since it is

assumed that mean winds equal to zero, advection and curvature terms are not present in classical tidal equations. The conservation equations of momentum, mass and energy are:

$$\frac{\partial u'}{\partial t} - fv' + \frac{1}{a\cos\phi}\frac{\partial \Phi'}{\lambda} = 0 \tag{1.33}$$

$$\frac{\partial v'}{\partial t} + fu' + \frac{1}{a}\frac{\partial \Phi'}{\partial \phi} = 0 \tag{1.34}$$

$$\frac{1}{a\cos\phi}\left[\frac{\partial u'}{\partial \lambda} + \frac{\partial}{\partial \phi}(v'\cos\phi)\right] + \frac{1}{\rho_0}\frac{\partial}{\partial z}(\rho_0 w') = 0 \tag{1.35}$$

$$\frac{\partial}{\partial t}\Phi'_z + N^2 w' = \frac{\kappa Q'}{H} \tag{1.36}$$

Where Q' is the heating per unit mass. The time derivatives of the zonal and meridional tidal winds are only determined by the Coriolis force and pressure gradient force, which are called classical terms in [*McLandress*, 2002a]. The time derivative of the vertical geopotential gradient is changed by either vertical motion or external heating. We further assume the tidal perturbation is a periodic oscillation with respect to time and longitude, so it takes a following form:

$$\{u', v', w', \Phi'\} = \{\hat{u}, \hat{v}, \hat{w}, \hat{\Phi}\}\exp[i(s\lambda + \omega t)] \tag{1.37}$$

Substituting equation (1.37) into the tidal equations eliminates the derivatives with respect to time and longitude. After $(\hat{u}, \hat{v}, \hat{w})$ are replaced by $\hat{\Phi}$, equations (1.33)-(1.36) are consolidated into a single second-order partial differential equation in terms of $\hat{\Phi}$ in z and ϕ. The assumption of zero mean winds and isothermal atmosphere leads to the separation of z and ϕ, and $\hat{\Phi}$ can be denoted as:

$$\hat{\Phi} = \sum_n \Theta_n(\phi) G_n(z) \tag{1.38}$$

where Θ_n is a function of latitude and G_n is a function of altitude. n is the meridional index, with each n corresponding to a latitudinal structure. The second-order partial differential

equation in terms of $\hat{\Phi}$ is divided into two separate equations while they are connected by a set of eigenvalues, which is referred to as the "equivalent depth" h_n. The equation associated with the latitudinal structure (Hough mode) of the tide is known as the *Laplace's tidal equation* [*Laplace*, 1825]:

$$\frac{d}{d\mu}\left[\frac{(1-\mu^2)}{(f^2-\mu^2)}\frac{d\Theta_n}{d\mu}\right] - \frac{1}{f^2-\mu^2}\left[-\frac{s}{f}\frac{(f^2+\mu^2)}{(f^2-\mu^2)} + \frac{s^2}{1-\mu^2}\right]\Theta_n + \epsilon_n\Theta_n = 0 \tag{1.39}$$

where $\mu = \sin\theta$ and $\epsilon_n = (2\Omega a)^2/gh_n$. The other equation is associated with the vertical structure of the tide:

$$i\omega H\left[\frac{1}{\rho_0}\frac{\partial}{\partial z}\rho_0\frac{\partial}{\partial z}G_n\right] + \frac{1}{\rho_0}\frac{\partial}{\partial z}(\rho_0\kappa Q_n) = -\frac{i\omega\kappa}{h_n}G_n \tag{1.40}$$

It is an eigenfunction-eigenvalue problem to find solutions to equations (1.39) and (1.40). For each choice of wave frequency and zonal wavenumber (ω and s), there are sets of ϵ_n and Θ_n satisfying the *Laplace's tidal equation* under certain boundary conditions. Each set (s, ω, n) corresponds a "mode" and it is linked with a eigenfunction/eigenvalue pair determined by equations (1.39) and (1.40). The solution to the *Laplace's tidal equation*, Θ_n is called "Hough function" and all Θ_n are orthogonal to each other. A common nomenclature in identifying modes is to explicitly express the zonal wavenumber s and meridional index n as the (s, n) mode. The period is mentioned in order to fully specify a certain tidal mode, e.g., the (1,1) mode of the diurnal tide.

Similar to the geopotential Φ (equation (1.38)), the zonal and meridional winds are separated as:

$$\hat{u} = \frac{\omega}{4\Omega^2 a}\sum_n U_n(\phi)G_n(z) \tag{1.41}$$

$$\hat{v} = -\frac{i\omega}{4\Omega^2 a}\sum_n V_n(\phi)G_n(z) \tag{1.42}$$

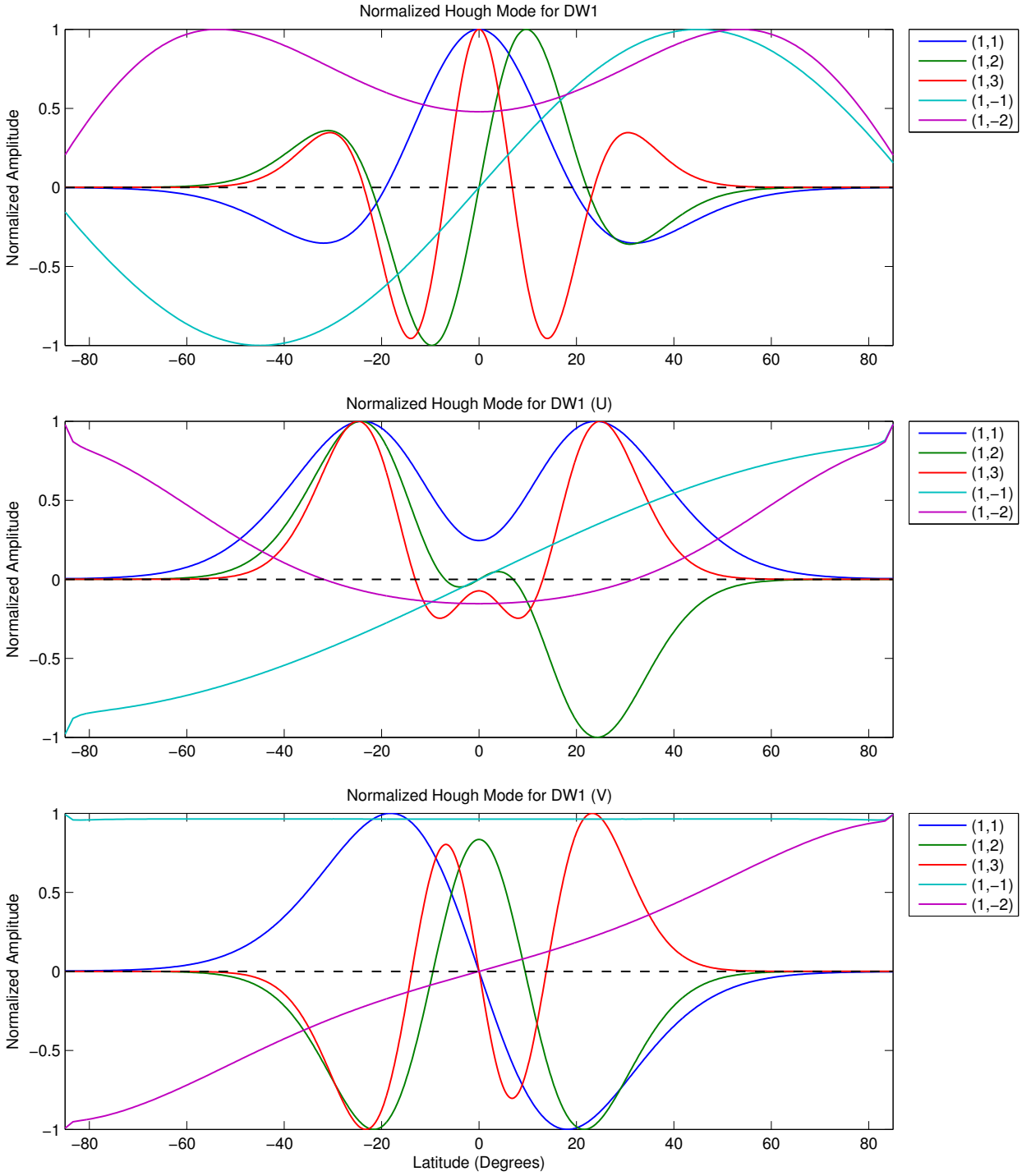

Figure 1.1: Hough functions for the geopotential (upper panel), zonal wind (middle panel) and meridional wind (lower panel), respectively. Five dominant Hough modes (1,1), (1,2) (1,3) (1,-1) and (1,-2) are represented by different colors.

where $U_n(\phi)$ and $V_n(\phi)$ are Hough functions for the zonal and meridional winds, respectively. Note that the vertical structure functions are the same for the three quantities. From equations (1.33) to (1.36), the relations between $U_n(\phi)$, $V_n(\phi)$ and $\Theta_n(\phi)$ can be derived as:

$$U_n = \frac{1}{(f^2 - \sin^2\phi)} \left[\frac{s}{\cos\phi} + \frac{\sin\phi}{f} \frac{d}{d\phi} \right] \Theta_n \tag{1.43}$$

$$V_n = \frac{1}{(f^2 - \sin^2\phi)} \left[\frac{s\tan\phi}{f} + \frac{d}{d\phi} \right] \Theta_n \tag{1.44}$$

Figure 1.1 shows five most dominant Hough functions for DW1. The gravest Hough mode in the MLT region is the (1,1) Hough mode, which is referred to as the first symmetric propagating mode. The latitudinal structure of the (1,1) mode is symmetric to the equator in terms of the geopotential and zonal wind, while antisymmetric for the meridional wind. The (1,2) mode is the first antisymmetric propagating diurnal tide, while the (1,-1) and (1,-2) modes are trapped modes.

The propagating characteristic (i.e., whether it is a propagating mode or a trapped mode) is determined by its *vertical structure equation* (1.40). By defining $G'_n = G_n \rho_0^{1/2} N^{-1}$, taking $N^2 = \kappa g/H$ for an isothermal atmosphere where $H = 7.5$ km, and replacing z by $x = z/H$, we can rewritten the *vertical structure equation* for an isothermal atmosphere as:

$$\frac{d^2 G'_n}{dx^2} + \left[\frac{\kappa H}{h_n} - \frac{1}{4} \right] G'_n = -\frac{\rho^{-1/2}}{i\omega N} \frac{d}{dx}(\rho_0 Q_n) \tag{1.45}$$

If $\alpha_n^2 = \dfrac{\kappa H}{h_n} - \dfrac{1}{4} < 0$, then $G'_n \sim e^{(-|\alpha_n|x)}$, which means wave oscillations are "trapped" or "evanescent" because their amplitudes dissipate exponentially with the distance away from the source region. Trapped modes correspond to the conditions $h_n < 0$ or $h_n > 4\kappa H$. Thus when the equivalent depth h_n is negative or positive with a large value, the tidal oscillation is more likely to be trapped. Table 1.1 gives the corresponding equivalent depths and vertical wavelengths from the (1,-2) to (1,3) modes for the diurnal tide. The characteristic of each mode is also provided by *Forbes* [1995].

Wave	(s,n)	h_n (km)	$\lambda_z(km)$	Characteristics
Diurnal tide	(1,1)	0.6909	27.9	first symmetric propagating
Diurnal tide	(1,2)	0.2385	15.9	first antisymmetric propagating
Diurnal tide	(1,3)	0.1203	11.2	second symmetric propagating
Diurnal tide	(1,-1)	803.356		first antisymmetric trapped
Diurnal tide	(1,-2)	-12.2703		first symmetric trapped
Diurnal tide	(1,-4)	-1.7581		second symmetric trapped

Table 1.1: Equivalent depths and vertical wavelengths of the Hough Modes of the diurnal tide.

1.2.3 Tidal Heating

Atmospheric thermal tides are forced by thermal excitation. During the day time, the Sun heats the atmosphere, while it cools down at night without the direct solar radiation absorption. The day-night periodic solar heating gives rises to tidal waves with periods of integral subharmonics of a solar day. Figure 1.2 shows the time variation of the ultraviolet (UV) radiative heating by ozone absorption in the stratosphere (∼50 km) at four different UT times. Since the self-rotation of the Earth is eastward with respect to the Sun, the maximum heating following the Sun propagates westward with time. For the migrating tides, their motions follow the motion of the Sun so they can only propagate westward. Nonmigrating tides, however, can propagate in both directions.

Similar to the gepotential, the heating term can also be decomposed as a superposition of all the Hough modes. For instance, in equation (1.46), $Q_n(z)$ is a projection of the heating term Q' onto the (s,n) mode, and Q' can be decomposed as:

$$Q' = \sum_s \sum_\omega \sum_n \Theta_n(\phi) Q_n(z) \exp[i(s\lambda + \omega t)] \tag{1.46}$$

Notice that the Hough function Θ_n is the same for geopotential and heating. So in order to generate a strong response in the mode (s,n), the latitudinal structure of the tidal heating needs to match that of the geopotential (or temperature), by which the tidal heating can be projected on this mode most efficiently.

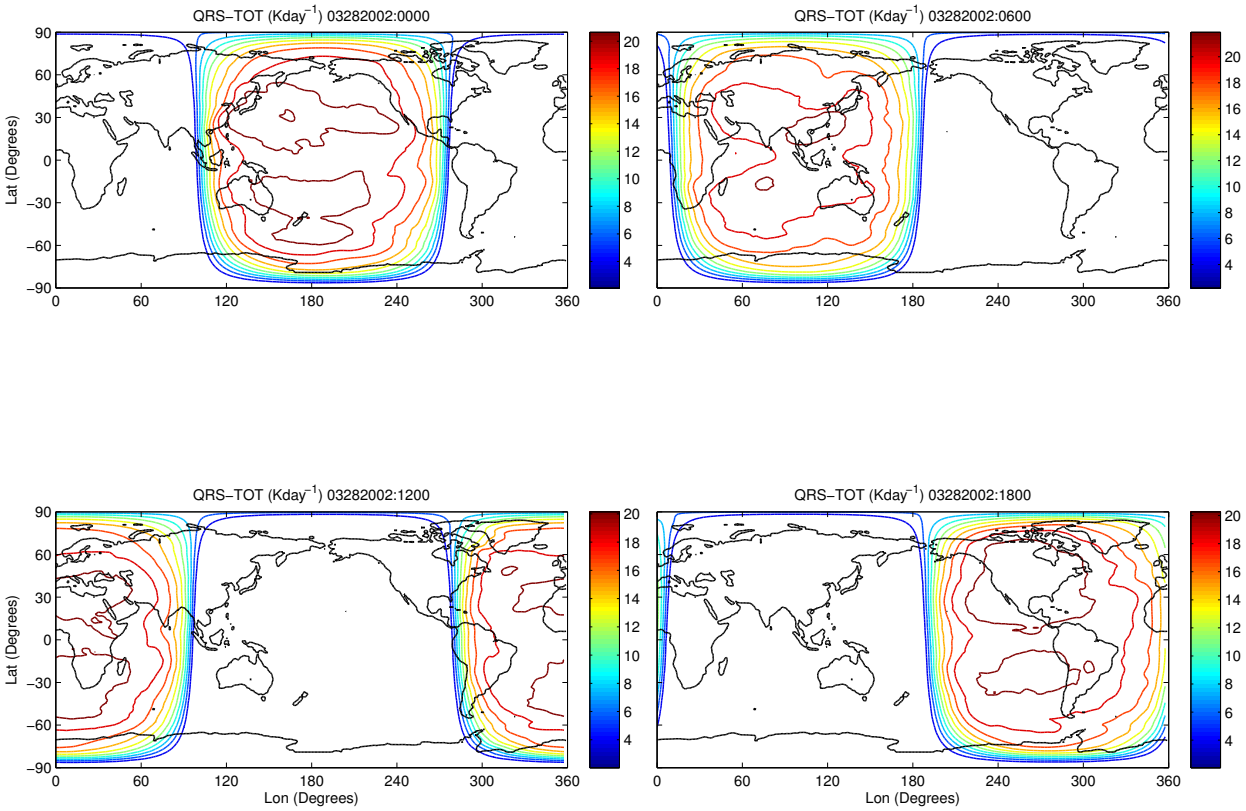

Figure 1.2: Horizontal structure of total short-wave radiative heating by ozone and its variation with time in the WACCM4. Four panels correspond to 0000UT, 0600UT, 1200UT and 1800 UT, respectively.

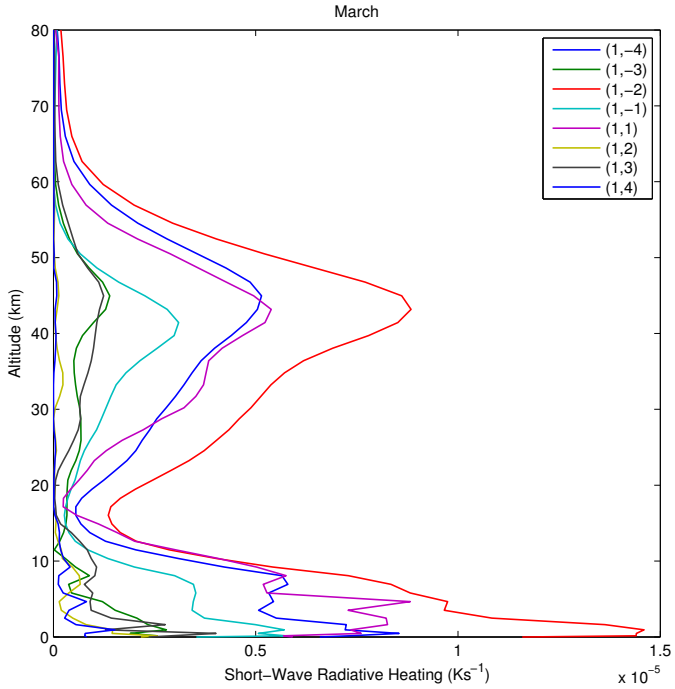

Figure 1.3: Vertical structure of short-wave radiative heating projected on Hough modes from (1,-4) to (1,4) for DW1. The heating is normalized by a density factor $e^{-z/2H}$, where $H = 7.5$ km.

Figure 1.3 shows the vertical structure of the short-wave radiative heating by water vapor in the troposphere and ozone in the stratosphere, for Hough modes from (1,-4) to (1,4). The short-wave radiative heating rates are based on the Whole Atmosphere Community Climate Model (WACCM) results. The Hough mode decomposition method used here will be described in section 2.5.3. Since there is no significant heating source near the MLT region, the diurnal tide observed by the meteor radar and satellite between 80 and 100 km is generated in the lower atmosphere. It propagates upward and reaches the MLT region before it dissipates. As shown by Figure 1.3, the majority of tidal heating goes to the three modes: (1,-2), (1,1) and (1,-4). The (1,-2) mode is generated with a largest amplitude in the source region. The reason why the (1,1) mode dominates in the MLT region is the (1,-2) and (1,-4) modes are largely trapped in the source regions, so they are not able to reach higher altitudes. A tutorial review of classical tidal theory and tidal heating can be found in *Forbes* [1995].

1.2.4 Seasonal Variation of the Diurnal Tide

There are plenty of observations on the semiannual oscillation (SAO) of the amplitude of the diurnal tide based on both single-station and satellite measurements. The SAO contributes to the largest variability at low latitudes for the diurnal tide and has been extensively reported from equatorial to polar regions using radars [*Tsuda et al.*, 1988; *Franke and Thorsen*, 1993; *Chang and Avery*, 1997; *Hocking et al.*, 1997; *Vincent et al.*, 1998; *Deepa et al.*, 2008], lidars [*States and Gardner*, 2000a; *She et al.*, 2004; *Yuan et al.*, 2006] and satellite observations [*Burrage et al.*, 1995; *McLandress et al.*, 1996; *Huang and Reber*, 2003; *Wu et al.*, 2008; *Xu et al.*, 2009]. Among all these observational analyses, the diurnal tide has a significant seasonal variability with larger amplitudes at equinoxes and weaker amplitudes at solstices.

Based on the seasonal variations of nonmigrating tides studied by *Forbes et al.* [2003], the maximum amplitudes for DW2 meridional wind occur during October-November and January-February; the maximum amplitudes for DE3 in the zonal wind occur during June-October; DS0 exists for every month but it is stronger in the southern hemisphere. The similar seasonal variations of the three most dominant nonmigrating diurnal tides DW2, DE3 and DS0 were also shown by the Thermosphere Ionosphere Mesosphere Energetics and Dynamics/Doppler Interferometer (TIMED/TIDI) wind measurements [*Oberheide et al.*, 2006]. Note that from a single-station measurement, the combined effects of both migrating and non-migrating tides are observed, which contribute to both seasonal and longitudinal variations of the diurnal tide [*Forbes et al.*, 2003].

The SAO in the amplitude of the diurnal tide has been extensively reported using observations and simulated by both general circulation models and mechanistic models. The underlying mechanisms associated with the seasonal variability of the diurnal tide involve the interference of different tidal components or different tidal modes. The mechanisms can also be tidal heating source, mean wind-wave and wave-wave interactions. It is found

that the tidal heating is most symmetric at equinoxes and project most efficiently onto the first symmetric propagating mode (1,1) of DW1, which is partly responsible for the stronger diurnal tides at equinoxes at latitude 20°[*Forbes et al.*, 2001]. However, the heating source alone cannot fully explain the amplitude and phase variations of the diurnal tide and mean wind plays a role as well [*McLandress*, 2002b]. The mean wind is also found to be the only cause for the phase variation [*McLandress*, 2002b]. The importance of mean winds on the seasonal variation of the diurnal tide was also addressed by *Achatz et al.* [2008]. Meanwhile, they noticed that PWs take an active role in interfering with the diurnal tide.

Norton and Thuburn [1999] proposed that the nonlinear interaction between the tide and quasi-two day PW (QTDW) is a potential cause for the tidal variability as an anti-correlation of their amplitudes was observed. The anti-correlation between QTDW and diurnal tide was also reported by *Lima et al.* [2004] based on the meteor radar observation. *Palo et al.* [1999] simulated a QTDW event using the Thermosphere Ionosphere Mesosphere Electrodynamics General Circulation Model (TIME-GCM) and found that a significant amplitude decrease of 40-50% occurs for DW1 when the QTDW is present.

Another potential mechanism is attributed to the GW/tidal interaction. GWs can break and deposit momentum to mean flows as their amplitudes grow large enough to induce instability [*Lindzen*, 1981]. This momentum deposition will modulate the amplitude and phase of the diurnal tide and may result in seasonal variabilities due to the inherent variations in GW sources and/or filtering effects from mean winds and tides. Unfortunately, it is still not clear whether the interactions would increase or decrease the diurnal tide since different parameterizations for capturing small scale GWs lead to different conclusions. One conclusion that GWs suppress the diurnal tide in the MLT region was drawn by *Miyahara and Forbes* [1991] and *Forbes et al.* [1991] based on the Lindzen's GW parameterization scheme [*Lindzen*, 1981]. Conversely, the conclusion using Hines′ Doppler-Spread Parameterization (DSP) [*Hines*, 1997a,b; *Mayr et al.*, 1998] is that GWs enhance the diurnal tide. The role of the GW forcing on the diurnal tide is still an open question.

It should be noted that all the current explanations for the seasonal variability of the diurnal tide are mostly based on models, which highly dependent on GW and other physical parameterization schemes. Until now, observations of GWs are still insufficient to provide a complete constraint on modeling and allow the development of a more realistic GW scheme. So some explanations can be valid only for a specific self-consistent model with its own GW scheme. Observations on those resolved waves such as tides and PWs can be used as a verification to models and more observations on the heating rates, mean winds and GW characteristics are also required to improve models and lead to better explanations of the tidal variations.

1.3 GW/Tidal Interactions

Superimposed on the mean winds, the diurnal tidal winds become a part of the background environment that affects the propagation and dissipation of high-frequency GWs. Since the amplitudes of the diurnal tide are very large, saturation and momentum deposition of GWs are modulated by the tidal winds, thus characterized by the oscillations same as the tidal periods. A GW/tidal interaction model proposed by *Fritts and Vincent* [1987] is elucidated here since it can explain the concept of GW/tidal interaction in a simple and illuminative way. Based on the linear, monochromatic saturation hypothesis of *Lindzen* [1981] and the assumption that a zonally propagating, high-frequency GW with phase speed $c < \bar{u}$ is saturated below 80 km, the amplitude of the wave motion is limited to:

$$u' = \bar{u} - c \tag{1.47}$$

and an induced zonal acceleration back to the mean flow is given by:

$$\bar{u}_t = -\frac{k(\bar{u}-c)^2}{2N}\left[\frac{(\bar{u}-c)}{H} - 3\bar{u}_z\right] \tag{1.48}$$

where $\bar{u}_t = \partial\bar{u}/\partial t$ and $\bar{u}_z$ represents the vertical shear of the zonal mean wind. The momentum flux is calculated as:

$$\overline{u'w'} = -\frac{k}{2N}(\bar{u} - c)^3 \tag{1.49}$$

For an easterly propagating GW ($c - \bar{u} < 0$), if the mean winds plus tidal winds have a easterly shear ($\bar{u}$ becomes more westward as altitude increases), the wave amplitude determined by an envelop of $|c - \bar{u}|$ also decreases with altitude and same for the negative momentum flux (Figure 1.4a). Oppositely, if the mean winds and tidal winds have westerly shear with altitude, the wave amplitude and negative momentum flux increase, as shown in Figure 1.4b. The mean wind settings in Figure 1.4a and 1.4b are called condition (a) and (b). It is expected that if the GW propagates eastward with respect to the mean flow ($c - \bar{u} > 0$), which means the phase speed line c locates to the right of mean wind curve $\bar{u}$, then wave amplitude and momentum flux increase in the (a) condition and decrease in the (b) condition, which is in contrast to the case with westward propagating GW. Note that GW-induced variances $\overline{u'u'}$ can also be modulated by the tidal winds in a similar manner.

If the increase of the momentum flux ceases above 90 km in Figure 1.4b, a large westward momentum deposition and deceleration to the mean flow will occur due to the negative momentum that GW carries. And this situation is very likely to occur in the background where the large tidal winds are present. Since the tidal winds basically determine the vertical profile of $\bar{u}$, they modulate the momentum deposition and mean flow acceleration induced by GWs. In return, the mean flow acceleration has a feedback on the tidal structure, changing the tidal amplitude and phase. A case study was performed by *Fritts and Vincent* [1987] using a dual-beam Doppler radar which calculated the tidal winds and the momentum flux due to GWs. Figure 1.5 is a schematic showing the GW effects on the diurnal tide based on this case study. As the GW-induced acceleration has a diurnal variation and is anti-correlated with the tidal variation (Figure 1.5b), it will change the diurnal tide by decreasing its amplitude and advancing its phase. In Figure 1.5c, the dashed line is the

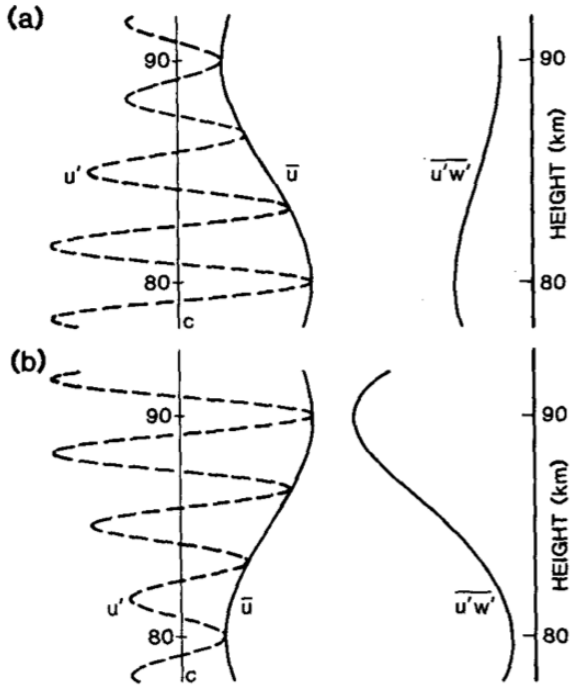

Figure 1.4: Schematic of wave amplitude and momentum flux for a saturated westward propagating GW in an environment that the mean background wind has (a) an easterly vertical shear and (b) a westerly vertical shear, [*Fritts and Vincent*, 1987].

initial tidal variation and the solid line shows the diurnal tide after considering the time tendency caused by the GW momentum deposition ($\bar{u}_{t,GW}$). It should be recognized that in reality, the GW/tidal interaction can be more complicated. Nonlinear interaction not only involves GWs and tides, but also PWs and mean winds. Also multiple quasi-monochromatic high-frequency GWs are often observed, which further complicate the interacting processes.

GW/tidal interaction is ubiquitous and found by many observations. For instance, the evidence of GW/tidal interaction was observed by using a MST radar at Poker Flat in July of 1986 [*Wang and Fritts*, 1991], wherein the tidal winds and momentum flux were characterized by an out-of-phase correlation over a number of heights. GW/tidal interaction was also found affecting the local time variability of the airglow emissions [*England et al.*, 2006]. Based on radar observations, spectra of GW variances for two years of data displayed peaks at tidal and PW periods, mainly near 12-hr, 24-hr, 2-day, and 16-day periods [*Isler and Fritts*, 1996].

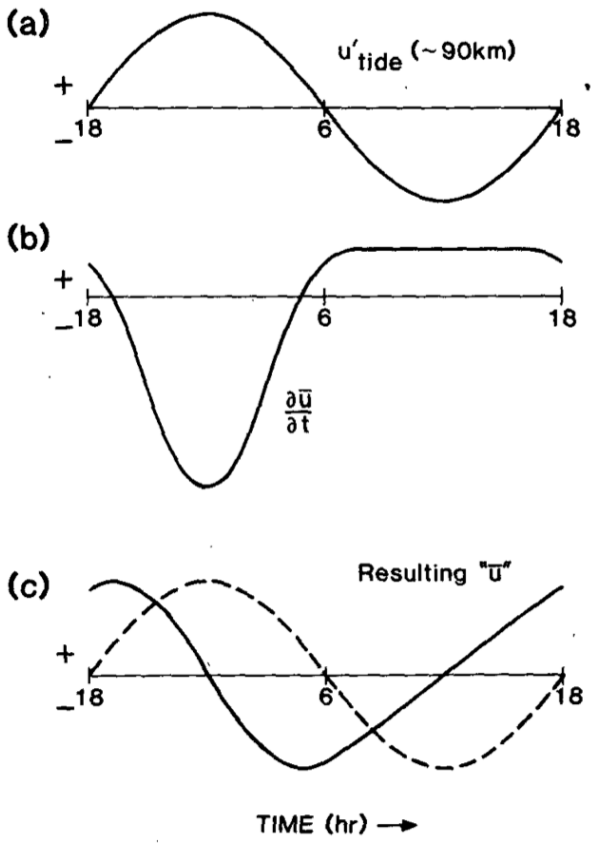

Figure 1.5: Schematic showing the effects of a diurnally varying zonal drag induced by GW on the diurnal tide. (a) is the initial time variation of the diurnal tide and (b) is the time variation of the GW acceleration; (c) are the initial diurnal tide (dashed line) and altered diurnal tide (solid line) after the feedback of GW acceleration is considered, [*Fritts and Vincent*, 1987].

Walterscheid [1981] attributed the day-to-day variability in amplitude and phase of the semidiurnal tide to the acceleration induced by inertia-GWs. He also reported this variability was large but local and random. In terms of the global-scale influences, the contribution of GW acceleration to the day-to-day variability is relatively small. So GW effect is likely to be responsible for the short-term variability of the diurnal tide, but not for the seasonal change.

GW effects on the tides are not only investigated by observational studies, but also by modeling work. It is well known that GW forcing is an important parameterization in the general circulation model (GCMs) such as WACCM, Canadian Middle Atmosphere Model (CMAM) and Hamburg Model of the Neutral and Ionized Atmosphere (HAMMONIA). Since DW1 is a salient feature in the MLT region, a realistic simulation of tide is also important for GCMs and undoubtedly, a correct simulation of GW/tidal interaction is a key to improve model performance. However, based on the models, it is still not clear whether the GW/tidal interactions would increase or decrease the diurnal tide because the GW/tidal interaction is sensitive to which GW scheme and parameterization are utilized by the model [*McLandress*, 1998]. By using Lindzen's GW scheme, GW forcing damps DW1 [*Miyahara and Forbes*, 1991] while Hines' Doppler-Spread Parameterization (DSP) [*Hines*, 1997a,b] leads to an opposite conclusion that GW forcing amplifies the tide [*McLandress*, 1998; *Mayr et al.*, 1998]. *Watanabe and Miyahara* [2009] quantified the GW forcing on DW1 in the GW-resolved Japanese Atmosphere General Circulation Model for Upper Atmosphere Research (JAGUAR) and concluded that the GW forcing amplified the tide at the equinox and suppressed it at the solstice in the upper mesosphere. A shortage in their model is that small-scale GWs with horizontal wavelength between 30 and 180 km are still not resolved. These small-scale and high-frequency GWs are frequently observed in the upper mesosphere by airglow imagers [*Tang et al.*, 2005] and they make a large contribution to the GW momentum deposition [*Fritts and Vincent*, 1987]. Therefore, more observational studies on GW/tidal interaction are valuable and required in the future.

1.4 Objectives

There are four topics included in this dissertation and they are inherently related to each other. The first topic involves a case-study of an inertial GW. Inertial GWs are capable of modulating the structure of DW1 [*Ortland, AGU Chapman Conference*, 2011], besides internal GWs [*Ortland and Alexander*, 2006]. The second and third topics focus on the studies of the diurnal tide from two different perspectives, observations and model simulations. The models are compared with the observations and meanwhile, they are used to identify and explain the physical mechanisms. The GW/tidal interaction is a two-way process and the third topic covers one of them, the GW effects on DW1 based on the WACCM simulation. The last topic focuses on the other-way process, the tidal modulations of the GW variances. The goal of this dissertation is trying to provide a better understanding of the characteristics of GWs, tides and their interactions.

For the first topic, an inertial GW is identified propagating from the stratosphere to the MLT region using the temperature measurement from Rayleigh and Na lidars. The uniqueness of this study is that the simultaneous observations of temperature, which facilitate the study of wave propagation and dissipation, have been rare. The questions need to be answered are as the following:

1. What are the characteristics of the inertial GW identified simultaneously by the lidars, including its horizontal and vertical wavelengths, phase speed and period? Are they consistent with the Dopper-shifting effect of the background wind?

2. What are the effects of the background, specifically the static stability on changing the propagation, dissipation and vertical wavelength of the GW?

The second topic involves the observational studies of the seasonal variation of the diurnal tide, based on the meteor radar and satellite measurements. Meanwhile, the model simulations are presented and compared with observations. The uniqueness of this study is

the seasonal variation of the diurnal tide can be studied in detail based on the long term (5 years) and high temporal resolution data retrieved from the meteor radar. During the same observational period, TIMED satellite measured the temperature and horizontal winds, which are used to separate migrating and nonmigrating diurnal tides. The objectives for this topic are:

1. Identify the dominant seasonal variations of the amplitudes, phases, vertical wavelengths of the diurnal tide and the magnitudes of the seasonal variations.

2. Identify the dominant tidal component contributing to the seasonal variation and examine the consistency between the ground-based meteor radar and satellite observations in terms of the monthly mean tidal amplitudes.

3. Evaluate the seasonal variations of the diurnal tide predicted by models and investigate the similarities and discrepancies between observations and models.

As it will be shown, the WACCM is capable of reproducing the tidal seasonality. A merit of WACCM is GW sources (convection and frontogenesis) are newly modified by incorporating physically parameterized schemes representing convective and frontal systems. So for the third topic, it is used to systematically investigate the physical mechanisms of the tidal seasonality. The questions for this part are:

1. To what extent does classical tidal theory predict the structure of DW1 and what are the dominant terms accounting for the differences from classical tidal theory? What are the impacts of these terms on the tidal amplitudes and phases?

2. For these terms, are their seasonal variations determining the tidal seasonality? If not, what are the other potential mechanisms leading to the SAO of the tidal amplitudes and the annual oscillation (AO) of the phases?

For the last topic, one of the objectives is to evaluate the accuracy and efficiency of the method used to calculate the GW variances based on the meteor radar horizontal wind

measurement. The evidences of the tidal modulations are illustrated with some preliminary results and a further investigation will be performed in the follow-up work.

CHAPTER 2

DATA SOURCE AND ANALYSIS METHOD

This chapter focuses on the data sources and analysis methods included in this dissertation. The data are retrieved from Rayleigh and Sodium (Na) lidars, the meteor radar and the TIMED/TIDI and TIMED/Sounding of the Atmosphere using Broadband Emission Radiometry (TIMED/SABER) instruments. The modeling results are obtained from the Global Scale Wave Model (GSWM) and WACCM. The analysis methods are introduced in this chapter, including how to extract GW perturbations from Rayleigh and Na lidars and how to extract the diurnal tide from the meteor radar, TIMED satellite and WACCM. Particularly, the hodograph method is introduced to extract GW characteristics and the Hough Mode Extension (HME) method is used to obtain DW1 in the horizontal winds based on TIMED/SABER temperature measurement.

2.1 Rayleigh and Sodium Lidars

The JPL Rayleigh/Raman lidar at Mauna Loa Observatory (MLO, 19.5°N, 155.6°W) has been making regular measurements of ozone, temperature and aerosol profiles for the Network for Detection of Stratospheric Change (NDSC) program since July 1993 [*Mcdermid et al.*, 1995]. The current system of JPL Rayleigh/Raman lidar system at MLO employs a Nd:YAG laser emitting at 355 nm, a 1-m Cassegrain telescope collecting the laser light backscattered by the atmospheric molecules, and a set of beam-splitters dividing the collected signals into three temperature-dedicated channels. Two of these channels receive elastic Rayleigh/Mie-backscattered light at 355 nm for the retrieval of temperature between ∼30

and 90 km, and one receives Raman-shifted light backscattered by atmospheric nitrogen at 387 nm, which allows temperature retrieval from 40 km down to about 15 km even in the presence of thin volcanic aerosols and clouds. A detailed description can be found in [*Leblanc et al.*, 1999a,b]. The raw signals were initially collected in 300-m vertical bins and saved every 4-10 minutes. Depending on the signal-to-noise ratio of the data and the nature of application, the analysis programs further average the raw photon profiles over a longer time interval and over a larger vertical range. In the raw data analysis, the raw photon profiles were smoothed with a hamming window function (2 km is the full width half maximum).

Laser radiation transmitted into the atmosphere is backscattered by the molecules in the atmosphere. The number of the received photons is proportional to the number of photons emitted in the laser pulse and also the air density. The relative air density can be deduced based on the Rayleigh lidar equation and temperature is then derived from the relative air density, according to the hydrostatic balance and ideal gas law assumption [*Leblanc et al.*, 1999a]. The selected reference point is dependent on the signal-to-noise ratio and usually between 80 and 90 km. The reference temperature comes from MSIS-90 model. The 15 K difference between the reference atmosphere and the real temperature is common at the top of the profile. The uncertainty due to this temperature difference decreases when integrating the profile downward, reaching about only 3 K at 80 km and less than 1K near 75 km [*Leblanc et al.*, 1998]. Therefore, the temperature uncertainty we derived below 80 km is mainly due to the photon noise. The relative uncertainty of temperature is inversely proportional to the square root of received photon counts. As the altitude increases, received photons decrease exponentially with the altitude, and temperature errors increase rapidly. The JPL system at MLO was upgraded in early 2001, leading to more output power at 355 nm ($\sim$10 W), and higher signal-to-noise ratio of return signals in the stratosphere and mesosphere [*Li et al.*, 2008].

The University of Illinois at Urbana-Champaign (UIUC) Na wind/temperature lidar system [*Gardner and Papen*, 1995] measured winds and temperature from $\sim$80 to 105 km.

The Na lidar emits a laser pulse to the atmosphere and collects the scattered photons by co-located telescopes. When the laser frequency is tuned to a resonant line of Na, a Na atom will absorb a photon and re-emits a photon to the atmosphere with the same energy as it absorbs. This is the so-called resonance fluorescence scattering process. The shape of the absorption cross-section is sensitive to the temperature as Figure 2.1a shows [*Chu and Papen*, 2005]. So the temperature can be inferred from the broadening of the absorption spectrum. The wind information is derived from the Doppler frequency shift of the central frequency as Figure 2.1b shows [*Chu and Papen*, 2005]. A three-frequency technique was used to determine the shape of the absorption spectrum for the Maui Na lidar [*She and Yu*, 1994; *States and Gardner*, 2000b].

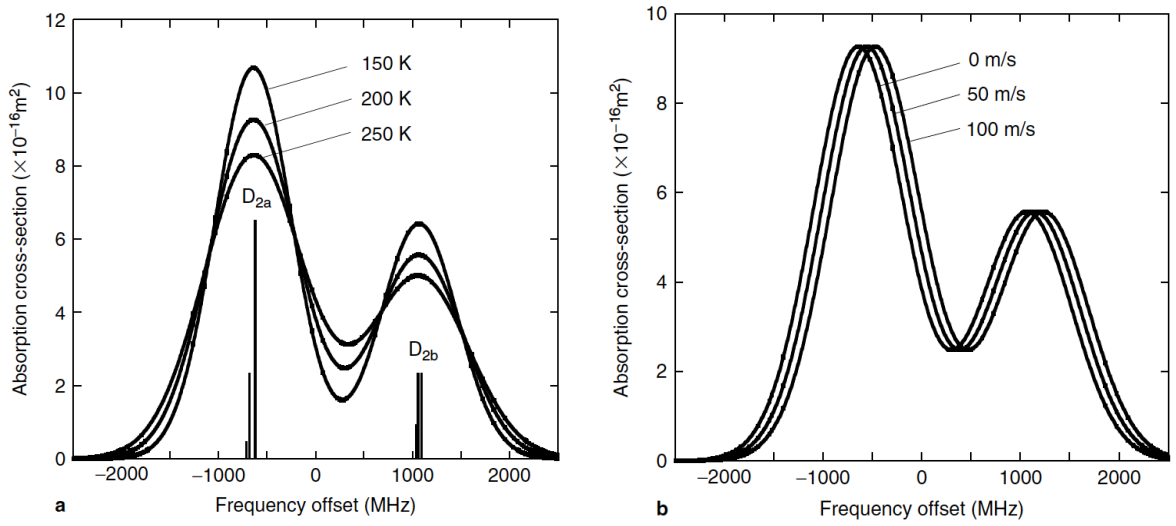

Figure 2.1: (a) Na absorption cross section for three temperatures, the radial velocity equals to zero. (b) Na absorption cross section for three different radial velocities: 0, 50 and 100 $\mathrm{m\,s^{-1}}$ at $T = 200$ K, [*Chu and Papen*, 2005].

The UIUC Na wind/temperature lidar system was located on Mt. Haleakala in Maui, HI (20.7°N, 156.3°W), which is $\sim$ 150 km away from MLO. The lidar system was coupled with a steerable 3.67 m diameter astronomical telescope at the Air Force Maui Optical Station. It has made high-resolution measurements of Na density, temperature, and winds in 35 nights during the period from Jan 2002 to Mar 2005. The temporal resolution of the temperature

measurement is ∼2 min and vertical resolution is 480 m. The lidar was directed to the zenith (Z), 30° off zenith toward north (N), east (E), south (S) and west (W) in the sequence of ZNEZSW. The relations between the horizontal winds and the off-zenith line-of-sight (LOS) winds are [*Liu et al.*, 2002; *Li et al.*, 2005a]:

$$V_E = u_E \sin\theta + w\cos\theta \tag{2.1}$$

$$V_W = -u_W \sin\theta + w\cos\theta \tag{2.2}$$

$$V_N = v_N \sin\theta + w\cos\theta \tag{2.3}$$

$$V_S = -v_S \sin\theta + w\cos\theta \tag{2.4}$$

where V is the LOS wind and θ is the zenith angle. The subscripts denote the lidar beam positions. The vertical wind is much smaller than the horizontal winds and can be ignored. Then, the zonal and meridional winds are derived as:

$$u'_E = V_E / \sin\theta \tag{2.5}$$

$$u'_W = -V_W / \sin\theta \tag{2.6}$$

$$v'_N = V_N / \sin\theta \tag{2.7}$$

$$v'_S = -V_S / \sin\theta \tag{2.8}$$

On the night of October 28, 2003, the Rayleigh lidar observation started from 5:01 to 15:13 UT and Na lidar started from 5:19 to 15:55 UT. The overlapping observation period between 5:19 and 15:13 UT was selected for the GW study in Chapter 3. The Na lidar data were smoothed temporally by using a 12-min Hanning window to obtain the same temporal resolution as the Rayleigh lidar data. At this resolution, the minimum nightly averaged uncertainty of temperature from Na lidar is ∼0.5 K at 92.3 km and increases to ∼1.5 K

below 84 km and ∼3.5 K above 103 km. So only the observations between 84 and 103 km were used.

2.2 Meteor Radar

Meteor radar uses an active radar technique to measure the atmospheric winds between 80 and 100 km. Basically, it measures the neutral winds by transmitting radio waves into the atmosphere and detecting the backscattered signals by meteor trails. The meteors enter the Earth at high speed and ionize atoms and molecules of the atmosphere, thus leaving behind a trail of ionized air. Most meteoroid crumble and disintegrate completely above 80 km. By observing how the meteor trail drifts with time, the neutral winds are deduced according to the Doppler-shift effect by the mean winds.

Currently, there are almost 30 meteor radars distributed world-wide and more are under development [*Hocking*, 2005]. The University of Illinois at Urbana-Champaign (UIUC) Maui meteor radar system used a SKiYMET radar [*Hocking et al.*, 2001] operating at 40.92 MHz. The meteor trails were illuminated by one three-element Yagi antenna directed toward the zenith with an average transmitted power of approximately 170 W from a 13.3 μs pulse length, 6 kW peak envelope power and 466 μs interpulse period. The backscattered signals were received by five two-element Yagi antennas oriented along two orthogonal baselines and they were sampled every 13.3 μs, resulting in a range resolution of 2 km. The receiving antenna in the center was at the cross of the two orthogonal baselines, with the outer antennas being separated from the center antenna by 1.5 and 2.0 wavelengths [*Franke et al.*, 2005].

When a meteor echo is detected, phase shifts between the five antennas are used to determine an unambiguous angle-of-arrival and trail positions. The rates of phase changes are converted to radial drift velocities [*Hocking et al.*, 2001]. Wind velocities were determined from the trail positions and Doppler shifts [*Hocking et al.*, 2001] with an assumption that

the horizontal wind field is uniform within a time-height interval and the vertical wind is neglected. A weighted least square fit was used to minimize the weighted residual and determine the values for horizontal winds [*Franke et al.*, 2005]:

$$\chi^2 = \sum_i \left(\frac{v_r^i - u \sin\theta^i \cos\varphi^i - v \sin\theta^i \sin\varphi^i}{\sigma^i}\right)^2 \tag{2.9}$$

where v_r^i is the measured radial velocity, θ^i and φ^i are the zenith and azimuth angles of the ith meteor trail. The inverse of the weighting function σ^i was related to zenith angle θ^i and distance r^i of the ith meteor echo. When the RMS uncertainty of the radial velocity exceeded $7\,\mathrm{m\,s^{-1}}$, the echo was discarded. In fact, the value of the weighted residual term χ^2 is a measure of fluctuations about the uniform wind fields. It serves as a crude indicator of GW activity and turbulence strength [*Liu et al.*, 2002].

The least square fit was based on echoes collected within 1 hr time bin. The height resolution was determined by RMS uncertainties in distance and zenith angle. The meteor data were binned into a height interval of 4 km. Consequently, the data had 1 hr time and 4 km height resolution. The vertical profiles were then oversampled at a 1 km height interval. In Maui, most echoes were detected around 90 km and within the zenith angle 40-60° (Figure 2.2). The meteor radar can cover a distance of 500 km from the center where the radar locates, while most of the meteors are detected in a circular area with a radius of 400 km. For meteors at 90 km and with zenith angle 50°, the height uncertainty was ∼2.2-3.9 km [*Franke et al.*, 2005].

The detection rate of the meteor radar strongly depends on altitude and season. Generally, the highest detection rate is detected at solstices and lowest at equinoxes. The average detection rate can reach 7000/night in summer and winter, which is as twice large as that in spring and fall. The meteor detection rate is also a function of Universal Time (UT). In Maui, the largest detection rate occurs around 1600 UT (Figure 2.3). The maximum daily meteor rates averaged between 80 and 100 km occurring in June and July can reach about

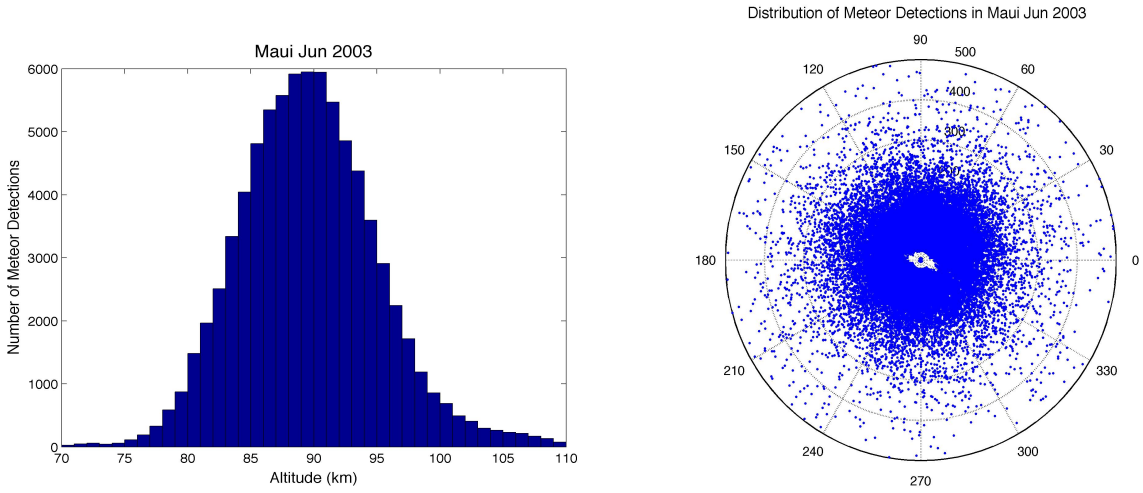

(a) (b)

Figure 2.2: Distribution of the meteor radar detection rate as a function of (a) altitude and (b) azimuth angle in June, 2003. The outermost circle in (b) corresponds to a distance of 500 km from the center point where the radar locates.

25 hr^{-1}. The bottom figure in Figure 2.3 shows yearly averaged meteor rates as functions of UT and altitude. The maximum value during a day is centered around 90 km and occurs around 16 UT for the yearly mean. The meteor detection rate is dependent primarily on the speed when it enters the atmosphere, which is in turn determined by the speeds of the meteoroid in its elongated orbit and the Earth in its path around the Sun. Before midnight, the Earth is on the trailing edge as it moves around the Sun, so the meteors have to catch up to the Earth in order to enter the atmosphere. After midnight, the Earth is on the leading edge and meteors enter the atmosphere at much higher speeds than before midnight. This explains why the detection rate is generally highest during the pre-dawn period.

Although there have been numerous observations on the seasonal variability of the diurnal tide, most studies were focused on middle and high latitudes or near equatorial regions and the study of the diurnal tide at low latitudes based on a high-resolution and long-term observation has been rare. During the Maui mesosphere and lower thermosphere (Maui MALT) campaign, a multi-year observation of horizontal winds was obtained with a meteor radar from May 2002 to Jun 2007 in Maui, HI (20.7°N, 156.3°W) [*Franke et al.*,

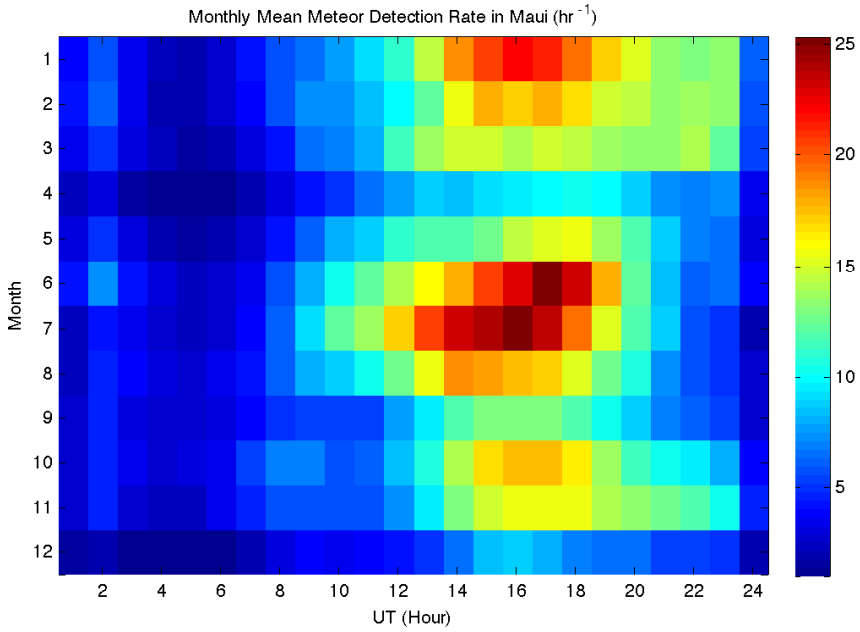

(a)

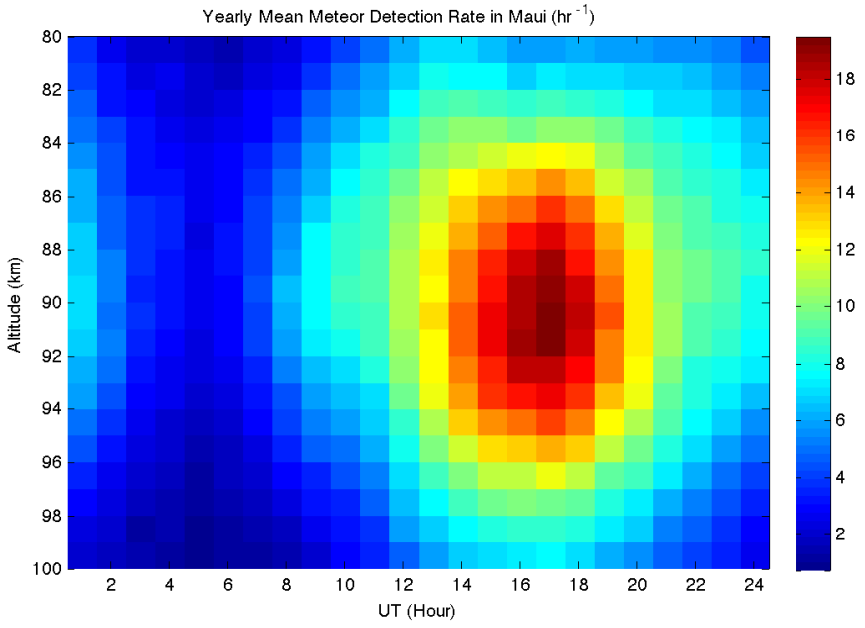

(b)

Figure 2.3: (a) Monthly mean daily meteor detection rate in Maui as functions of the universal time and month. The meteor rate is averaged between 80 and 100 km. (b) Yearly averaged meteor rate as functions of universal time and altitude in the year 2003.

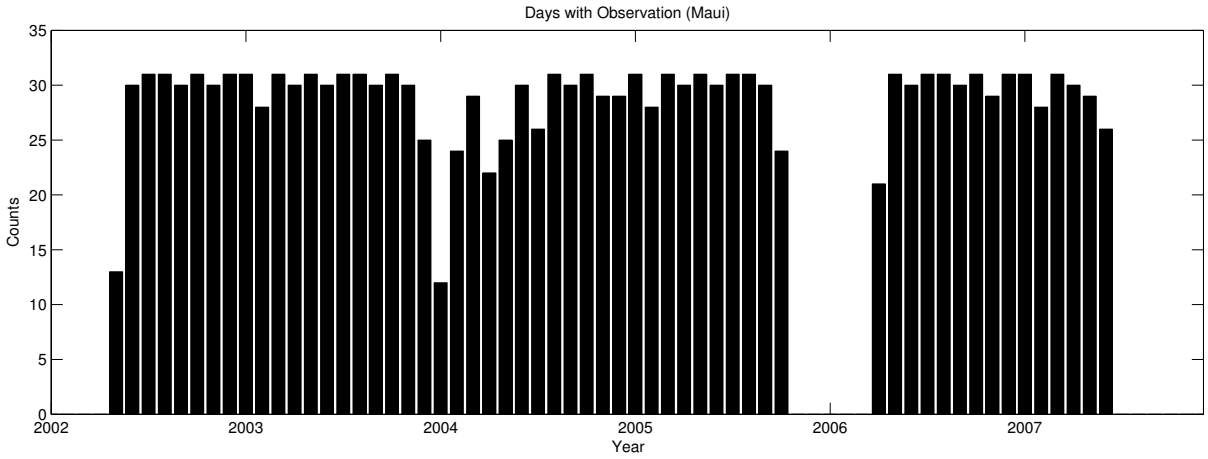

Figure 2.4: The number of days with observations for each month as observed by the UIUC meteor radar in Maui.

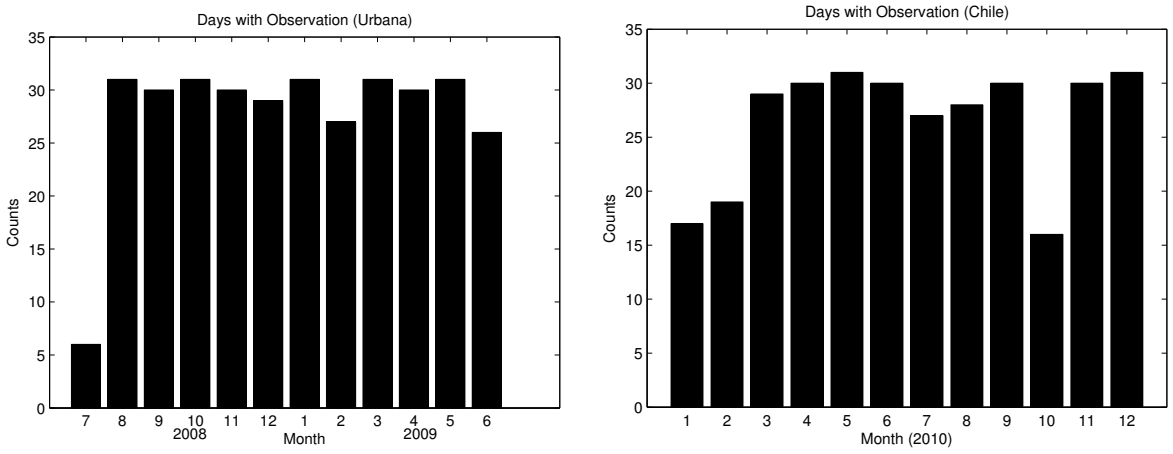

(a) (b)

Figure 2.5: Same as Figure 2.4 except for (a) Urbana and (b) Chile.

2005]. Figure 2.4 shows the statistics of the meteor radar measurement in terms of days with observations for each month in Maui. It was taking data from July, 2008 to June, 2009 in Urbana, IL (40°N, 88°W) and moved to Cerro Pachón, Chile (30°S, 70°W), taking data from September, 2009 up to now. Figure 2.5 shows the statistics of the meteor radar measurements in Urbana and Cerro Pachón in the year 2010, respectively.

For the observational study of the seasonal variation of the diurnal tide in Chapter 4, only the Maui data are used because firstly, Maui is at the latitude where DW1 attains its maximum amplitude in the horizontal winds and secondly, it has the longest data set. In order to provide a reference, we also include the figures showing the seasonal variations of the diurnal tides in Urbana and Chile and the seasonal variations of the semidiurnal diurnal tides in the three sites in Appendix B. For the GW/tidal interaction study in Chapter 6, the meteor radar data from Maui and Urbana are utilized since the diurnal tide is dominant in Maui while the semidiurnal tide is dominant in Urbana. Thus the different tidal modulations are anticipated and compared between these two different sites.

2.3 TIMED Satellite

As an initial mission in the NASA's Solar Terrestrial Probes Program, the TIMED spacecraft was launched on December 7, 2001 and science operations began on January 22, 2002. The TIMED mission focuses on the Mesosphere and Lower Thermosphere/Ionosphere (MLTI) region (∼60-180 km), with a scientific objective of studying the influence of the Sun and humans. It also aims at understanding the MLTI region's basic pressure, temperature and wind structure and the spatial and temporal variations that result from the transfer of energy into and out of this region [http://www.timed.jhuapl.edu].

The TIMED satellite is quasi-sun-synchronous and its orbit is at ∼625±25 km and 74.1°±0.1° inclined with respect to the equator. It precesses slowly in local time (3 deg/day) or 12 hrs in 60 days. The satellite has ascending and descending nodes, which are separated

by close to 10 hrs. So the satellite can cover 24 hrs for every 60 days if ascending and descending nodes are combined [*Oberheide et al.*, 2006; *Wu et al.*, 2008]. Thus the tidal amplitude represents a mean value averaged in a 60-day window. The satellite orbits the Earth 15 times per day and the local time of the sampling points barely changes during a day (Figure 2.6). In Figure 2.6, red dots correspond to ascending nodes and blue dots correspond to descending nodes.

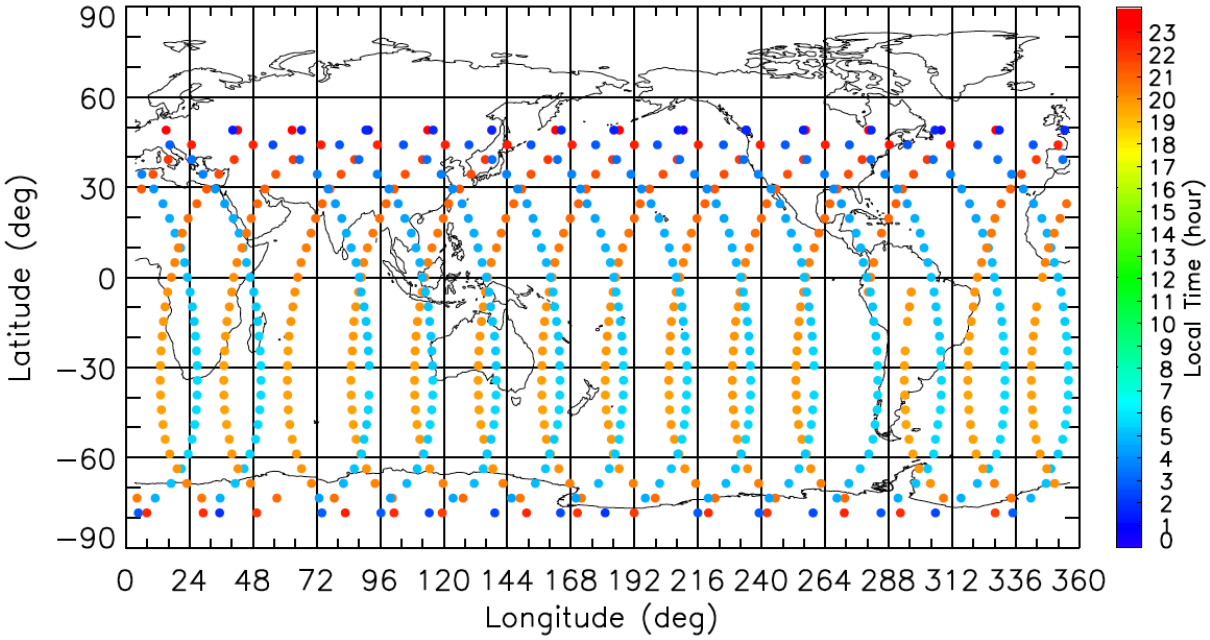

Figure 2.6: An illustration of the quasi-sun-synchronous orbits for the TIMED satellite during day 349, 2003. Each color dot in the latitude-longitude coordinate represents the location where the temperature was measured. The color code represents the local time at that location, [*Zhang et al.*, 2006].

The four instruments on board the TIMED satellite are: GUVI (Global Ultraviolet Imager), SABER, SEE (Solar Extreme Ultraviolet Experiment) and TIDI, respectively. The TIMED/SABER and TIMED/TIDI observations are used for this study. SABER limb scans vertically by a 10-channel broadband radiometer in the near to mid-infrared from 1.27 μm to 17 μm, measuring the vertical radiance profile and emission of the atmosphere. The kinetic temperature can be inferred from the radiance profile in a spectral band of CO_2, for which the mixing ratio is already known [*Russell et al.*, 1999]. TIDI is used to measure

the neutral winds via limb scanning the upper atmosphere airglow layers and monitoring the Doppler shift by winds [*Killeen et al.*, 2006]. It has four identical telescopes, two on the warm side and the other two on the cold side of the satellite. For each side, the two telescopes will sample the same location 9 min apart as the satellite moves along its orbit at 625 km. The two telescopes view the same region from nearly orthogonal directions, which allow measurements from two viewing directions to be decomposed into meridional and zonal wind components [*Killeen et al.*, 2006]. An assumption is made that the wind fields are the same during a period of 9 min.

It is not hard to find that ground-based and space-borne observations have their own advantages and disadvantages. Ground-based observations such as lidar and radar have a merit of high temporal resolution, while they can not provide a global coverage. Lidar measurement is also limited to the local weather condition, so it can not be regularly operated. Instead, space-borne satellite measurement is capable of providing a global picture of tides and it is operating continuously. However, it needs a long accumulating period to cover enough local time in a 24 hrs period in order to retrieve tides. In terms of the tidal study, the migrating and nonmigrating diurnal tides cannot be separated by ground-based observations because there is no information about the tidal structure along the longitude, while satellite can separate them. But the tides from satellite observations are obtained in a climatology sense (e.g., 2-month average for TIMED satellite) and they also suffer an aliasing problem. Because the temporal variations introduced by the mean state and/or PWs versus tides can be indistinguishable, mean state and/or PW-induced variations are possibly aliased to the tidal variations due to the sparse sampling of the satellite measurement in local time. Ground-based observations with higher temporal resolution, however, can resolve the temporal variations without ambiguity but there is no information about their spatial characteristics.

2.4 WACCM and GSWM

The WACCM is a GCM extending from the Earth's surface through the lower thermosphere, based on the Community Atmosphere Model (CAM). The WACCM4 has been released recently as the atmospheric component of the Community Earth System Model (CESM), which is extended to the thermosphere by incorporating most of the important physical and chemical mechanisms [*Garcia et al.*, 2007]. The other components of the CESM are land, glacier, ocean and ice. All the components are connected by a coupling module in the CESM. Unlike the Thermosphere Ionosphere Mesosphere Electrodynamic-General Circulation Model (TIME-GCM) in which the most important tidal components are retrieved from the GSWM and launched at the lower boundary (∼30 km), tides and PWs are generated self-consistently in the WACCM and free to interact both linearly and nonlinearly [*Chang et al.*, 2008]. The horizontal resolution used for the WACCM is $2.5^\circ \times 1.9^\circ$ (longitude×latitude). It has 66 vertical levels from the ground to ∼145 km. The vertical resolution is 1.1 km in the troposphere, 1.1-1.4 km in the lower stratosphere, 1.75 km at the stratopause and 3.5 km above 65 km. The seasonal variation of the diurnal tide is well simulated in the WACCM [*Liu et al.*, 2010b].

The GW drag and vertical diffusion parameterizations were newly modified for WACCM3.5 and are also used in WACCM4. The frontal system and convective GW source parameterizations are used for nonorographic wave sources, instead of an arbitrarily specified GW source spectrum [*Richter et al.*, 2010]. For the convective source parameterization, the Beres parameterization scheme is used in which the convective heating depth is an important factor to determine the dominant GW horizontal phase speed and the basic shape of the momentum flux spectrum in phase speed [*Beres et al.*, 2005]. Deep heating ($\geq$ 10 km) tends to generate GWs with long vertical wavelengths and large horizontal phase speeds while shallow heating ($\leq$ 5 km) generates GWs with short vertical wavelengths and small horizontal phase speeds [*Beres et al.*, 2005; *Richter et al.*, 2010]. For the frontal GW source parameterization, GWs

are launched from a source level of 600 hPa only if a frontogenesis threshold is reached, which typically occurs in regions of strong wind shear and temperature gradients. The intermittency in the wave source now depends on the simulated atmosphere, rather than an artificial intermittency parameter [*Richter et al.*, 2010]. The GWs are generated by three sources: orography, convection and frontal system. By using the source-oriented GW parameterization in the WACCM, an attempt is made to be more realistic and self-consistent.

The GSWM is a 2-dimensional, linearized, steady-state numerical tidal and PW model which extends from the ground to the thermosphere [*Hagan et al.*, 1995, 1999]. It solves the linearized perturbation equations in the presence of a prescribed background atmosphere, IR and UV solar forcing and dissipation profiles (GSWM00). The nonmigrating atmospheric tide was simulated by GSWM02 including latent heat release associated with deep tropical convection [*Hagan and Forbes*, 2002]. The GSWM is widely used for comparing the tidal amplitude and phase with observations at different locations [*Vincent et al.*, 1998; *Leblanc et al.*, 1999a; *Kishore et al.*, 2002; *She et al.*, 2002; *Deepa et al.*, 2006; *Yuan et al.*, 2006]. Some features including the seasonal variabilities of tides are well captured by the GSWM.

We use both models to obtain monthly mean amplitudes, phases and vertical wavelengths of the diurnal tide at the location corresponding to Maui and compare them with observations. Monthly mean wave amplitudes and phases are provided by the GSWM00/02. A 1-year run of the WACCM4 with 3-hourly output of horizontal wind fields enables us to derive the monthly mean amplitudes and phases of the diurnal tide by fitting a sinusoidal function with a period of 24 hrs.

2.5 Analysis Method

2.5.1 Extraction of GWs from Lidars

In chapter 3, relative temperature perturbations derived from Rayleigh and Na lidars are used to study wave propagation and dissipation by investigating their spectral behaviors and vertical variations. Wind perturbations from Na lidar are also used to derive wave properties, such as horizontal wavelength, propagation direction as well as intrinsic period. Both temperature and wind perturbations are derived by subtracting the nightly mean series. Relative temperature perturbations are calculated by dividing the temperature perturbations by the nightly mean. Since the influences of diurnal and semidiurnal tides are not negligible at low latitudes like Mauna Loa and Maui, the perturbation at each altitude is detrended by fitting and subtracting a second order polynomial as a function of time in order to minimize the tidal effects. By subtracting this background, contributions from low frequency waves are effectively reduced if not removed. A linear trend of each vertical profile is also removed to reduce the effects of long vertical wavelength waves.

Both Rayleigh and Na temperature perturbations are interpolated to the same vertical interval of 0.5 km. Since the raw data of Rayleigh temperature are smoothed with full-width-half maximum (FWHM) of 2 km, waves with vertical wavelengths less than 2 km are removed. So the data used in this study include GWs with vertical wavelengths longer than 2 km and wave periods longer than 24 minutes.

Hodograph method is used to derive GW intrinsic properties from Na lidar temperature and wind similar to *Hu et al.* [2002]. After wind and temperature perturbations are derived, we use Welch's averaged periodogram spectral estimation method [*Welch*, 1967] to obtain the mean dominant vertical wavenumber. For every vertical profile, a dominant wavenumber is identified when there are peaks at common wavenumber on both temperature and wind spectra that exceed a confidence level. The average wavenumber (m_0) is then used in a GW model to fit the wind and temperature perturbations. The model consists of wave amplitudes

(u_0, v_0, T_0), an exponential term, and a sinusoidal component. The GW model is described as:

$$\begin{aligned} u'(z) &= u_0 \exp(\beta z) \cos(m_0 z + \theta_u) \\ v'(z) &= v_0 \exp(\beta z) \cos(m_0 z + \theta_u) \\ T'(z) &= T_0 \exp(\beta z) \cos(m_0 z + \theta_T) \end{aligned} \tag{2.10}$$

where u_0 is the in-phase wind perturbation along the wave propagation direction, v_0 is the wind perturbation perpendicular to the wave propagation direction and T_0 is the temperature perturbation. According to equation (1.22), along the wave propagating direction, the intrinsic frequency ω is then determined from the polarization relation:

$$|u'|/|v'| = \omega/f \tag{2.11}$$

where f is the inertial frequency. The corresponding inertial period at the latitude of 20° is 35.1 h. The horizontal wavenumber k is determined from the dispersion relation [*Fritts and Alexander*, 2003],

$$k^2 = \frac{\omega^2 - f^2}{N_0^2} m_0^2 \tag{2.12}$$

where N_0 is the vertically averaged Brunt-Väisälä frequency. In the hodograph of zonal and meridional winds, the major axis determines the horizontal direction of wave propagation and the length ratio of the major to minor axes equals to the ratio of intrinsic to inertial frequencies. More details of the hodograph method is given by *Hu et al.* [2002].

In order to investigate the variation of the dominate vertical wavelength with altitude, a sliding vertical window with a width of 20 km is used to calculate the power spectrum by using Welch's averaged periodogram [*Welch*, 1967]. The window is shifted every 1 km. The power spectra from all profiles of the night are then averaged. This power spectrum represents the temperature variance versus vertical wavenumber. To represent the true wave energy variation with altitude, we need to scale the power spectra to be proportional to the

wave potential energy, which is defined as:

$$E_{pv}^2 = \frac{\rho_0(z)}{2} \frac{g^2}{N^2(z)} \overline{\left(\frac{T'(z)}{T_0(z)} \right)^2} \tag{2.13}$$

where E_{pv}^2 denotes the potential energy per unit volume and $N(z)$ denotes the time averaged Brunt-Väisälä frequency.

The wave potential energy is thus proportional to the variance of relative temperature perturbations, the density profile $\rho_0(z)$ and the inverse of $N^2(z)$. Therefore we scale the power spectra according to equation (2.13). Here $N^2(z)$ is calculated as:

$$N^2 = \frac{g}{T} \left(\frac{\partial T}{\partial z} + \frac{g}{c_p} \right) \tag{2.14}$$

where g is the gravity acceleration, c_p is the specific heat at constant pressure. N^2 is calculated for each temperature profile and then averaged over the night. A fourth-order polynomial is fitted to the nightly mean profile to obtain a smoothed N^2. The effect of $\rho_0(z)$ is also considered by multiplying the spectra with an exponential term $\exp(-z/H_0)$, where $H_0 = 7$ km. This scaled power spectra should be approximately constant with altitude for nondissipating waves and decrease with altitude when there is an energy loss. Details about the scaled power spectra will be further discussed in section 3.2.

2.5.2 Diurnal Tide from Meteor Radar and TIMED Satellite

As mentioned in section 2.2, the horizontal winds are measured hourly by the meteor radar. Figure 2.7 is an example of 10-day observations of the zonal and meridional winds in Maui. The diurnal tide is a very persistent feature, with strong winds changing from -100 $\mathrm{m\,s^{-1}}$ to 100 $\mathrm{m\,s^{-1}}$ day after day. After the horizontal winds are obtained, a nonlinear least-square curve fit in a form of sinusoidal function is used to derive wind amplitudes and phases of the diurnal tide. The period of the sinusoidal function is 24 hrs. It is applied in a window of

5 days. Horizontal winds are linearly detrended in order to remove mean background winds before fitting. The amplitude derived by using a narrower window is slightly larger but the phase is more likely contaminated and wrongly shifted by coexisting semi-diurnal tides or inertial GWs. A wider window in the time domain introduces contributions from PWs. The window width of 5 days is chosen to obtain more stable and accurate phase information while minimizing the PW contamination at the same time. In order to be consistent with the phase provided by the GSWM, we define it as the local time (LT) corresponding to the first maximum amplitude. The amplitudes and phases are recorded and used as valid data points where 80 % of the total points fall within the fitting window. The window is stepped forward in time by every 5 days to obtain the variations of amplitudes and phases. No overlapping is present and derived values are independent. This procedure is performed from 80 to 100 km with an interval of 1 km.

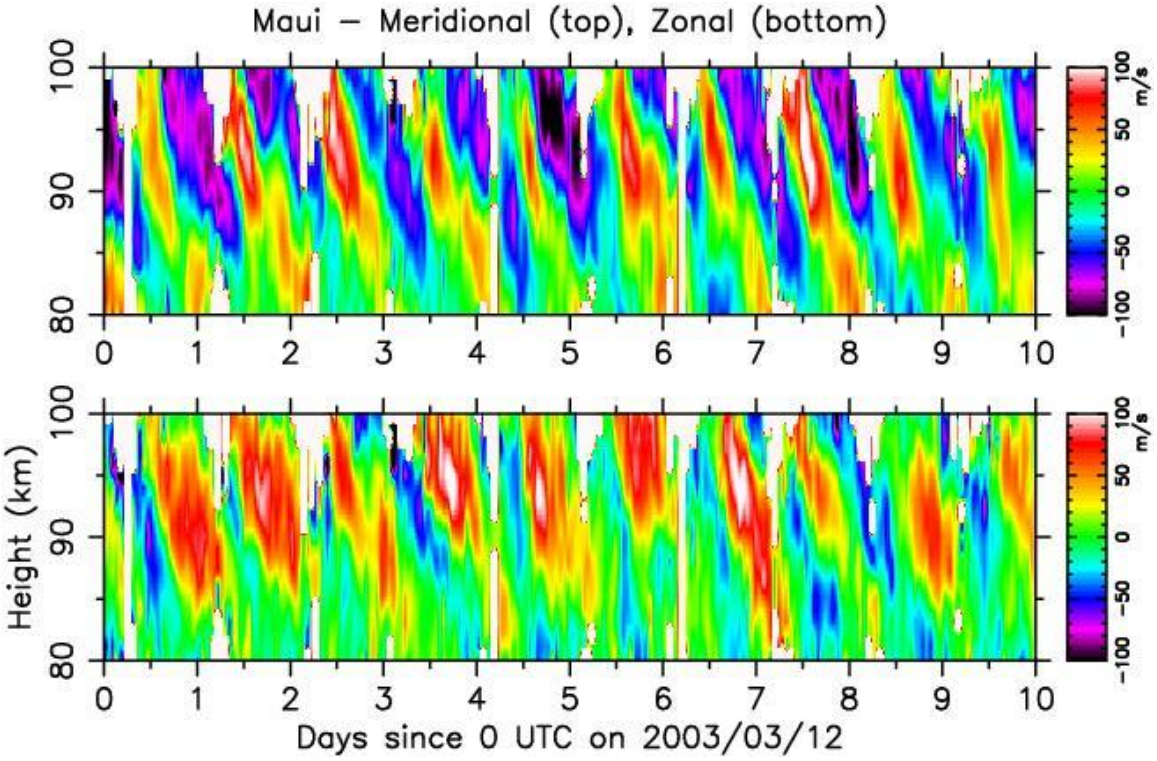

Figure 2.7: 10-day horizontal wind measurement since March 12, 2003. Courtesy of Dr. Steven Franke.

Nonmigrating diurnal tides DW5 to DE3 are derived from TIDI wind observations using

the NCAR data version V0307a [*Wu et al.*, 2008] and the two-dimensional Fourier analysis described by *Oberheide et al.* [2006] who also provide details of amplitude and phase errors (Table 2.1). As a rule of thumb, amplitude accuracy (precision) is about 10% (1 $\mathrm{m\,s^{-1}}$) and phase precision is between 1-2 hrs.

Component	Amplitude Accuracy (u, %)	Amplitude Accuracy (v, %)	Amplitude Precision (u, ms^{-2})	Amplitude Precision (v, ms^{-1})	Phase Precision (u, hrs)	Phase Precision (v, hrs)
DW4	9	9	0.7	0.9	2.1	2.1
DW3	7	14	0.8	1.0	2.0	2.0
DW2	13	11	1.1	1.3	1.5	1.4
DS0	16	13	1.4	1.1	1.6	1.4
DE1	15	16	0.8	1.1	1.8	1.7
DE2	16	14	0.8	0.9	1.4	1.8
DE3	12	11	0.9	1.0	1.1	1.5

Table 2.1: Zonal (u) and meridional (v) wind errors of the monthly mean amplitudes of nonmigrating diurnal tides. Taken from *Oberheide et al.* [2006].

Classical Hough modes are the solutions to the linearized primitive equations of the atmosphere assuming temperature is isothermal, mean winds and dissipation are zero. The concept of Hough Mode Extensions (HMEs) was developed by *Lindzen et al.* [1977] and *Forbes and Hagan* [1982] in order to deal with the changes in shape of Hough modes by dissipation. A HME represents the solution to the same set of equations except that the dissipation above the source region is taken into account. For a given wavenumber and frequency, a HME can be thought as a latitude vs. height table of amplitudes and phases for the velocity, temperature and density perturbations. These perturbation fields maintain internally self-consistent relative amplitude and phase relations for any given HME [*Svoboda et al.*, 2005]. Thus, if the amplitude and phase of the temperature field are known, all the other fields can be derived based on HMEs.

HME modeling is an approach to convert observed temperature tides in a self-consistent manner into tidal winds. It has been discussed in detail by *Oberheide and Forbes* [2008] and follows the procedure of *Svoboda et al.* [2005]. *Forbes and Wu* [2006] successfully established

the consistency between temperature tides from MLS on UARS and tidal winds from HRDI and WINDII at 95 km. *Oberheide and Forbes* [2008] also showed the quantitative consistency of the DE3 tides from SABER temperature and TIDI winds in the MLT region. Systematic comparisons with ground-based observations made during the CAWSES tidal campaigns show that DW1 winds derived from temperatures are a realistic representation of the true DW1 winds [*Ward et al.*, 2010]. The migrating tide DW1 from TIDI is of limited quality due to instrumental and sampling issues. Therefore, in our study, DW1 in the horizontal wind is derived from SABER migrating tidal temperature using the HME modeling [*Forbes et al.*, 2008].

2.5.3 Hough Mode Decomposition

In the modeling study of the diurnal tide (chapter 5), Hough mode decomposition is used to investigate the seasonal variation of each mode and the effects of their superposition. As discussed in section 1.2.2, the solutions to the *Laplace's tidal equation* are a set of orthogonal Hough functions in the geopotential field. Related to each Hough function (Θ_n) which depicts the latitudinal structure of the geopotential tide (or temperature), the latitude structures of horizontal winds are correspondingly specified by the associated Hough functions, U_n and V_n. The relation between them is shown in equation (1.43).

A least-square fit in a form of $\left[\hat{\Theta}, \hat{U}, \hat{V}\right] = \sum_n [a_n\Theta_n, b_nU_n, c_nV_n]$ is used to obtain the amplitude for each mode. Here $(\hat{\Theta}, \hat{U}, \hat{V})$ are the complex amplitudes of the tidal fields in geopotential, zonal and meridioanl winds. (a_n, b_n, c_n) are the corresponding amplitudes for the n_{th} Hough mode. $\hat{\Theta}$ and Θ_n are both functions of latitude. The least-square fit is performed at each altitude so the vertical structure of each mode can be obtained.

2.5.4 GW Variances from Meteor Radar

In section 2.2, it is mentioned that the value of the weighted residual term is a measure of fluctuations about the uniform wind fields. The reason why it can serve as a crude indicator of GW activity and turbulence strength [*Liu et al.*, 2002] is elucidated here. Meteor radar can detect the position and radial drift of each meteor. The horizontal wind of a particular meteor is derived based on its radial velocity and the zenith angle. When a meteor is detected, its horizontal wind is determined by the superposition of mean winds, PWs, tides and GWs at this particular position and time. Then in order to calculate the GW variance, the contributions from mean winds and other waves such as PWs and tides need to be removed. The residual term in equation (2.9) corresponds to what is left after removing the background wind effect, which is represented by $(u \sin\theta^i \cos\varphi^i - v \sin\theta^i \sin\varphi^i)$. Thus, it can be used as a proxy of the variances induced by GWs.

We follow the method used by *Mitchell and Beldon* [2009] for the meteor radar technique of deriving GW variances and we call it "MR technique" hereinafter. In this study, the horizontal winds are calculated in a 4 km $\times$ 4 hrs domain using the same least-square fit described in section 2.2. And they are viewed as the background winds. Here, the background winds include the contributions from mean winds, PWs, tides and long period GWs. After projecting the background horizontal wind onto each meteor, the difference between the projection and the original horizontal wind of each meteor is accounted as the wind velocity induced by short period GW. This difference is caused by GW activities with periods less than 4 hrs and horizontal wavelengths less than 400-500 km which corresponds to the collecting volume of the radar (Figure 2.2). It is noted that the MR technique can not resolve individual GW within the collecting volume. Rather, it provides a measure of the total level of small-scale wave activity in a certain altitude range and a period of time [*Mitchell and Beldon*, 2009].

In order to optimize the data quality, the meteor echoes with low signal-to-noise ratio

(<2) and high radial velocity uncertainties (>5 $\mathrm{m\,s^{-1}}$) are discarded. Also, the horizontal wind variances due to GWs are calculated only if the meteor number is larger than 30. Figure 2.8 shows an example of the horizontal winds with and without background winds

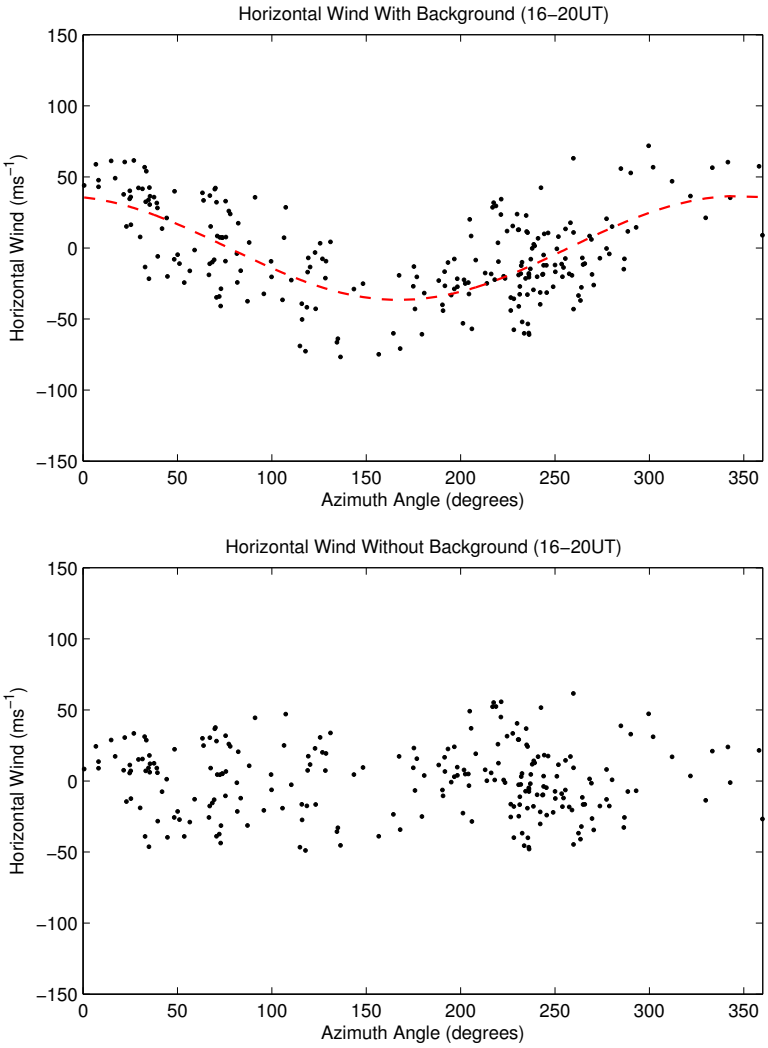

Figure 2.8: Horizontal wind with (upper panel) and without (bottom panel) background as a function of azimuth angle. The red dashed line represents the mean wind variation.

during 16-20 UT on June 14, 2003. The red dashed line in the upper figure is the background horizontal wind as a function of azimuth. Since it is a constant vector within 4 hrs, it is a sinusoidal function of azimuth. After the background winds are subtracted, it is apparent that the sinusoidal trend disappears which means the background wind effects are sufficiently reduced, if not totally removed. In the bottom figure, the bond of the horizontal winds

becomes narrower and thus, the variance of the horizontal winds becomes smaller than that with background winds present. The smaller variance is thought to be induced by only small-scale GWs and used for the following GW variance study. Figure 2.9 is the same except for the entire night. It is clearly seen that this technique can efficiently remove the long-term varying winds and retrieve the variances mainly from GWs. The GW variance is calculated for a period of 4 hrs and the calculation is shifted by every 1 hour.

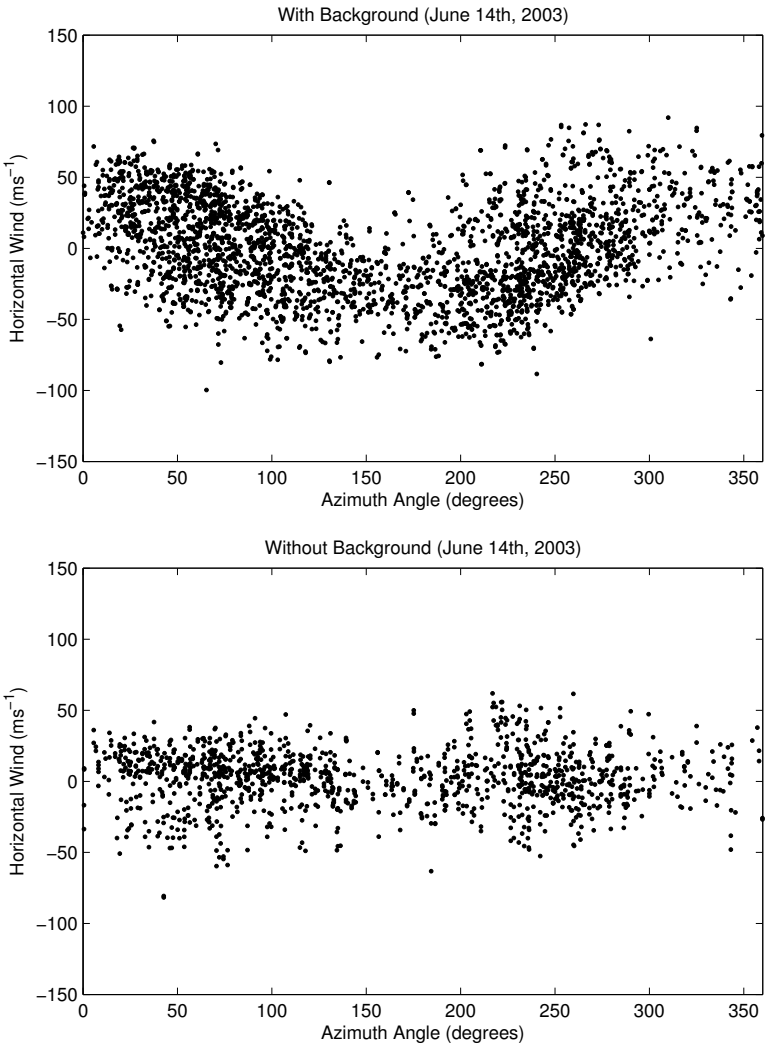

Figure 2.9: Same as Figure 2.8 except for the entire night of June 14, 2003.

CHAPTER 3

LIDAR STUDIES ON THE PROPAGATION AND DISSIPATION OF AN INERTIAL GW

Rayleigh and Na lidars are frequently used to observe GWs. However, the simultaneous observations of GW activities using both lidars are not common [*Beatty et al.*, 1992; *Alpers et al.*, 2004; *Rauthe et al.*, 2006] and rarely reported at low latitudes. In this chapter, we focus on a case study of an inertial GW using the temperature measurement from the Rayleigh lidar and the temperature/wind measurements from the Na lidar over the Hawaii islands (∼20°N). Both lidars made temperature measurements and had a decent overlapping observation period on the night of October 28, 2003. The temperature/wind measurements from Na lidar on this night were also used to study the dynamical instabilities by *Li et al.* [2005b]. This study is focused on the GW propagating and dissipation from the stratosphere to the lower thermosphere, while the wave characteristics such as amplitudes, horizontal and vertical wavelengths and intrinsic period are also described. A published paper about this study is *Lu et al.* [2009].

3.1 Background and Perturbations

Temperature measurements by Na lidar and Rayleigh lidar are shown in Figure 3.1. The highest temperature of ∼270 K is observed in the stratopause region. A prominent inversion layer associated with the diurnal tide is present between ∼90 and ∼100 km. The center of the inversion layer descends from ∼96 km at 0800 UT to ∼91 km at 1300 UT. The phase speed of downward progression of the inversion layer is about 0.28 $\mathrm{m\,s^{-1}}$. The downward phase progression is much more noticeable at higher altitudes. The phase speed of

the downward progression was consistent with that of an upward propagating diurnal tides [*Li et al.*, 2005b]. At higher altitudes, tidal oscillations are much stronger. In the following analysis, tidal oscillations are removed to obtain GW perturbations.

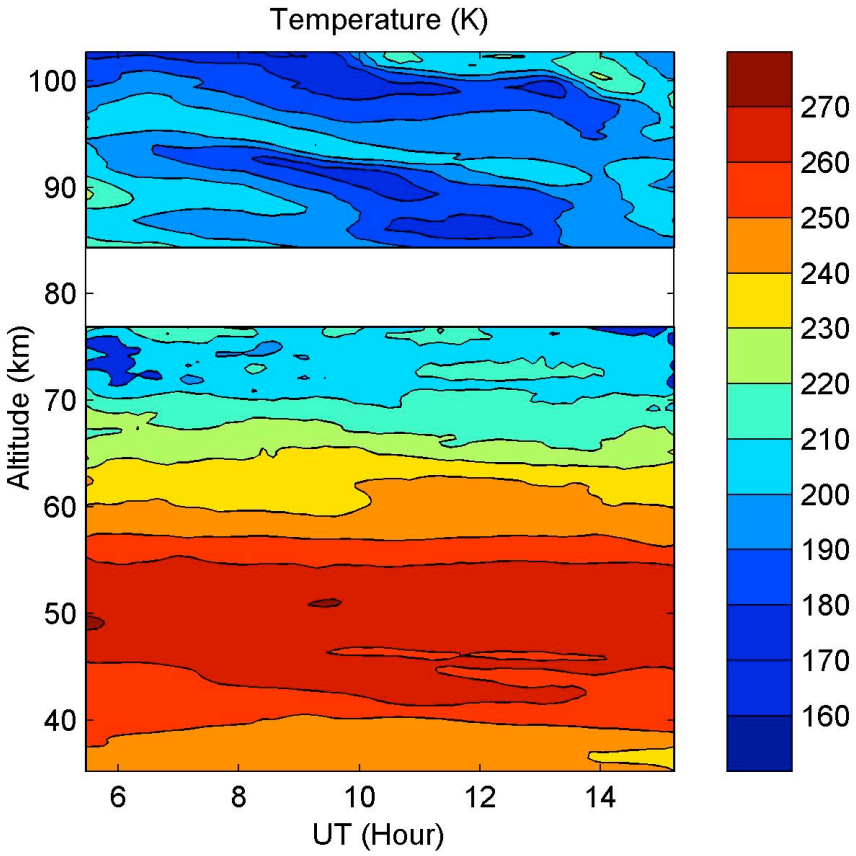

Figure 3.1: Temperature on the night of October 28, 2003. Data below 80 km is from Rayleigh lidar and above 80 km is from Na lidar. The gap around 80 km is where both Na and Rayleigh lidars have low signals and no reliable data can be obtained.

Figure 3.2 shows the nightly mean temperature profiles from the lidar measurements and two reference atmospheres, CIRA86 [*Chandra et al.*, 1990] and MSIS00 models [*Picone et al.*, 2002]. The nightly mean temperature observed by the Rayleigh lidar shows that the stratopause is located at ∼51 km, with a maximum temperature of ∼266.4 K. The structure of the upper mesosphere and lower thermosphere observed by Na lidar is more complicated. Two prominent temperature minima were present at ∼86 and 100 km, respectively. This "double mesopause" while not in the reference atmospheres, was also observed over Tenerife

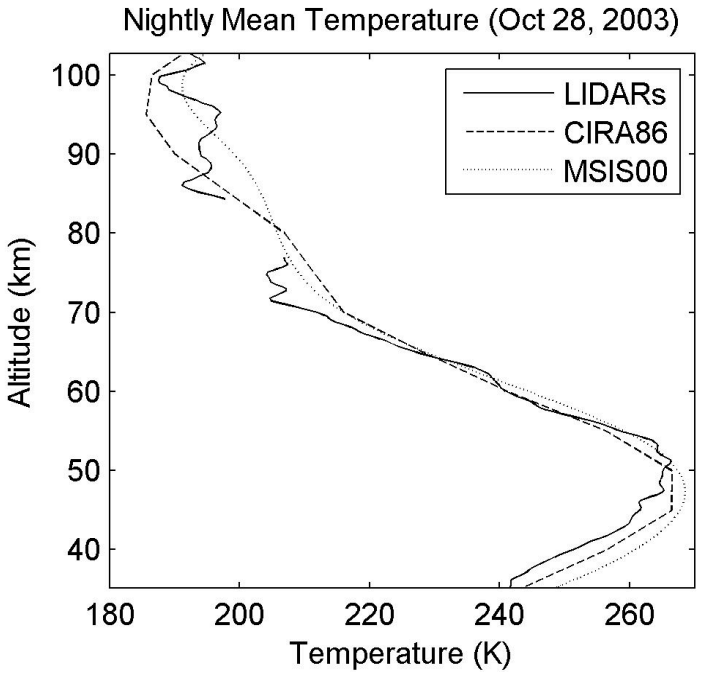

Figure 3.2: Mean temperature profile averaged from 5:19 to 15:13 UT, October 28, 2003. The black lines show the lidar observations over Maui and Mauna Loa; the dashed and the dotted lines represent the CIRA86 and MSIS00 reference atmospheres, respectively.

(28°N) [*Fricke-Begemann et al.*, 2002], Starfire Optical Range (35°N) [*Chu et al.*, 2005] and Fort Collins (41°N) [*Yu and She*, 1995]. The best match between measurements and reference atmospheres is between ∼50 and ∼66 km. Above ∼66 km, their differences increase significantly and vary with altitude; below ∼50 km, observed temperatures are lower than both reference atmospheres. *Sharma et al.* [2006] compared the monthly mean temperature profiles with CIRA86 and MSIS00 models over tropic and subtropic stations and had similar findings. The higher temperatures of CIRA86 model below the stratopause were also reported by *McDonald et al.* [1998] with Rayleigh and MST lidar measurements at Aberystwyth (52.4°N, 4.1°W) in Wales.

Na lidar also provides nighttime horizontal wind measurements, as shown by Figure 3.3. The downward phase progression is more obvious in the meridional wind than in the zonal wind. There was a strong vertical shear of zonal wind between 87 and 90 km before 1200 UT, which gave rise to the dynamic instability and ripple structures [*Li et al.*, 2005b].

Around 95 km, strong northward winds persisted for almost the entire night, which can result in a prominent Doppler shift for northward propagating waves. The nightly-mean zonal and meridional winds are also shown in Figures 3.3c and 3.3d. The large wind shear is also present in the nightly-mean zonal wind, with wind velocity changing from ∼80 $\mathrm{m\,s^{-1}}$ to ∼-50 $\mathrm{m\,s^{-1}}$ in a layer of ∼ 5 km.

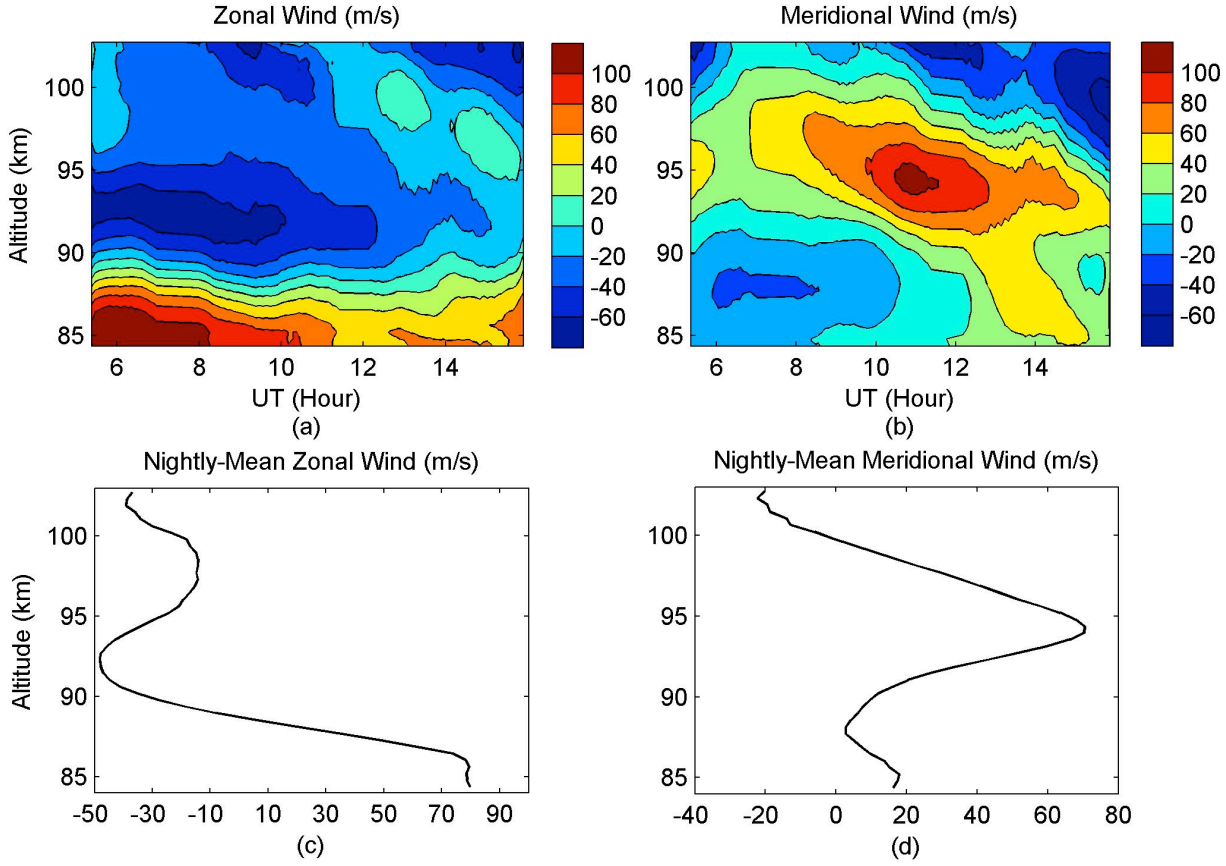

Figure 3.3: (a) Zonal and (b) meridional winds on the night of October 28, 2003. Lower panels denote the nightly mean (c) zonal and (d) meridional winds.

As mentioned in section 2.5.1, the relative temperature perturbations derived from Rayleigh and Na lidars are used to investigate the GW propagation and dissipation characteristics. Figure 3.4a shows the relative temperature perturbations from 35 to 103 km, with a gap between 76 and 84 km. Figure 3.4b shows their standard deviations and measurement uncertainties. The data were smoothed using running average with 1-h and 2.5-km win-

dows in time and altitude, respectively. In Figure 3.4a, the most significant feature is that a coherent wave structure was observed in both Rayleigh lidar and Na lidar temperatures. The phase fronts of the wave are highlighted by black dotted lines along negative phases of perturbations. The downward phase progression indicates the presence of an upward propagating wave. This dominant wave mode lasted for the entire night.

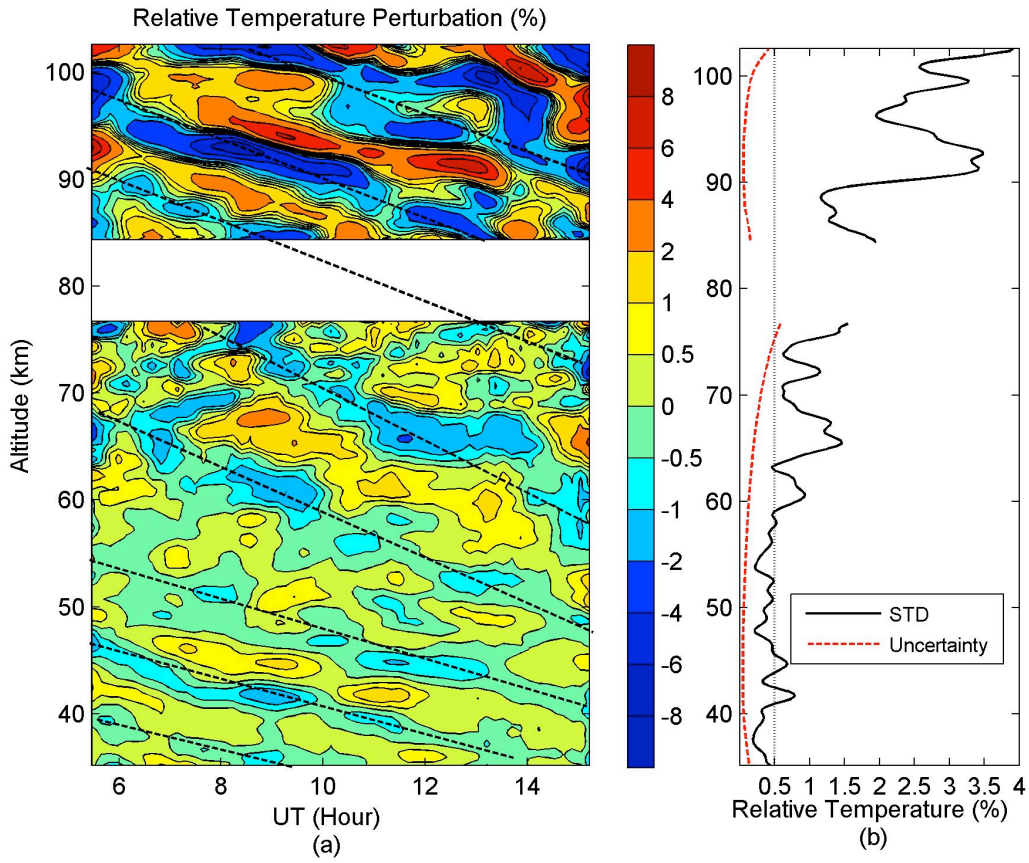

Figure 3.4: (a) Smoothed relative temperature perturbations after removing tides and high-frequency perturbations. Black dashed lines indicate the downward phase progression. (b) The standard deviation of relative temperature perturbations over the night (solid black line) and its statistical uncertainty (dashed red line).

The vertical wavelength of the dominant wave is about 10 km. This result is comparable to the observations of *Rauthe et al.* [2006] and *Sica and Russell* [1999], who found that only a few dominant wave components exist in such observations. Since the wave perturbations have similar structures throughout the altitude and the phase progression lines can be connected

through the gap region, it suggests that they were originated from a same wave packet and representing a same wave mode. The following discussions are based on our premises that perturbations observed at all levels are from the same wave packet throughout the night and the waves horizontal scale is large compared to the distance between the two observation sites so the difference from the two sites due to horizontal variation of the wavefield can be ignored. These premises will be further affirmed in section 3.3.

A distinct dominant GW mode with long period (several hours) and large vertical wavelength (tens of kilometers) that was similar to our findings was also found in the stratosphere and lower mesosphere (∼35-60 km), as studied by *Wilson et al.* [1991]. Besides, according to lidar observation over a low-latitude site (Gadanki, 13.5°N), it was found that the dominant perturbations seen at lower heights (<50 km) with low rates of downward phase progression were due to large vertical wavelength and long-period GWs [*Sivakumar et al.*, 2006]. By analyzing the meteor radar winds at MLT region and Rayleigh composite night temperatures (not shown), we believe that the observed dominate mode of vertical wavelength is likely due to a GW because the vertical wavelength of the diurnal tide is much longer (about 25 $\sim$ 40 km), as will be shown in the study of the diurnal tide by the meteor radar (Chapter 4). The semidiurnal tide has even longer wavelength.

Figure 3.4b shows the standard deviations of the relative temperature perturbations generally increase with altitude, indicating an amplitude growth. It is also shown that the standard deviations are much larger than the measurement uncertainties. Thus the dominant wave structures are due to a real geophysical variability and the dominant GW mode observed simultaneously by both lidars is a robust feature.

The same smoothing was applied to the horizontal wind perturbations observed by the Na lidar, which are shown in Figure 3.5. Wind uncertainties vary with the altitude but all are less than 0.8 $\mathrm{m\,s^{-1}}$, much smaller than the perturbation magnitude with a largest value reaching ∼20 $\mathrm{m\,s^{-1}}$. Similar to the relative temperature perturbations, wind perturbations also show an upward propagating GW structure with vertical wavelength of ∼10 km. The

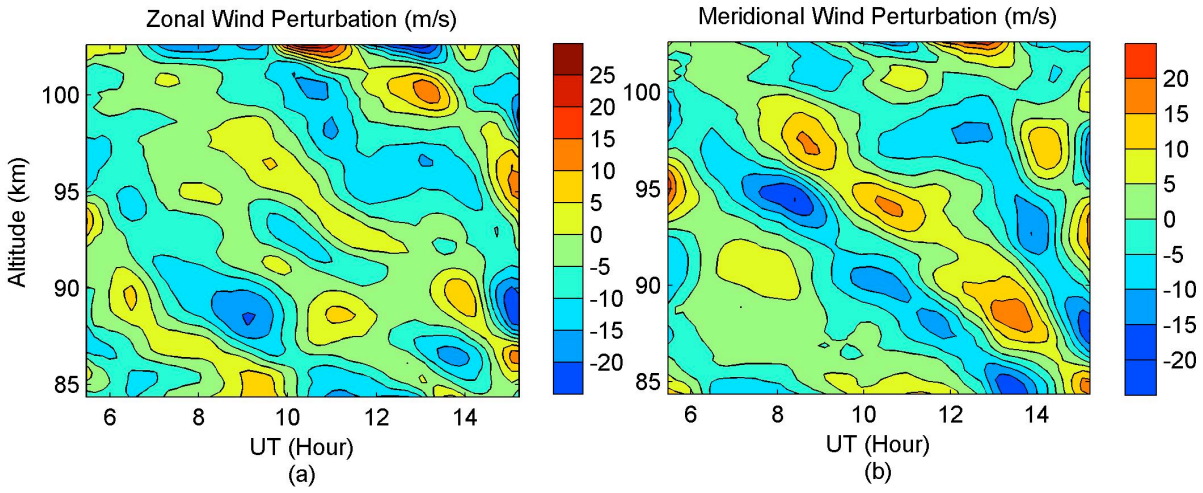

Figure 3.5: (a) Smoothed zonal and (b) meridional wind perturbations from Na lidar after removing tides and high-frequency perturbations.

zonal and meridional wind perturbations are used to derive the intrinsic wave properties by the hodograph method discussed in section 2.5.1 and will be shown in section 3.3.

3.2 Wave Propagation and Dissipation

As shown in Figure 3.4a, the amplitude of relative temperature perturbations increases almost all the way up from the stratosphere to the lower thermosphere, except for the region around stratopause where the wave structure seems to be partly disrupted. Figure 3.6 shows all temperature perturbation profiles together with the standard deviation (yellow) and measurement uncertainties (white). The standard deviation profile is also fitted with an exponential function defined as:

$$f(\frac{\Delta T}{\bar{T}}) = a \exp \frac{z - z_0}{2H} \tag{3.1}$$

where a denotes the amplitude roughly at the height $z_0(z_0 = 35.2$ km) and H denotes the scale height. The fitting results are:

$$a = 0.26 \pm 0.04\% \tag{3.2}$$

$$H = 14 \pm 1\text{km} \tag{3.3}$$

This is shown as the red line in Figure 3.6. A green line with a scale height of 7 km is also shown, which indicates the amplitude growth of a freely propagating GW. They have the same amplitudes at the starting point $z_0 = 35.2$ km. The substantial discrepancy between the red and green lines indicates that the waves were not freely propagating and the observed GWs were partially dissipated.

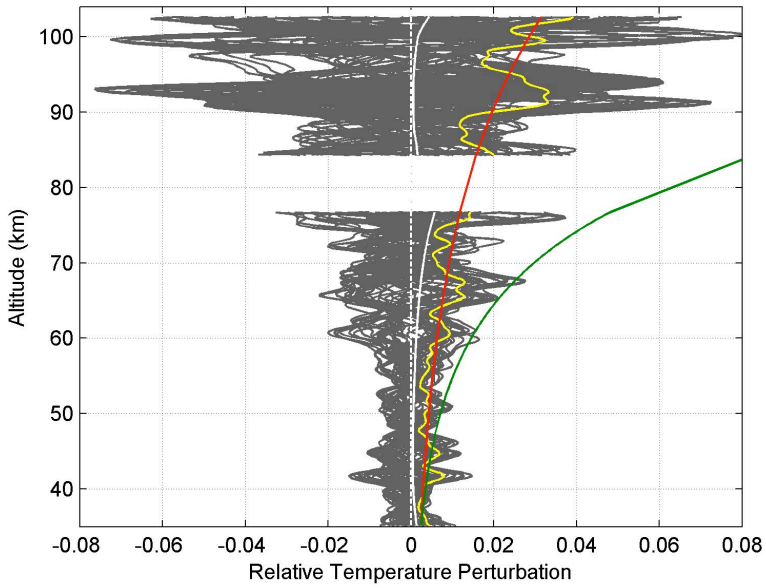

Figure 3.6: Individual relative temperature perturbations profiles (grey), standard deviation (yellow) and measurement uncertainty (white). The red line is an exponential fit to the standard deviation, and the green line indicates the exponential increase of a freely propagating GW with a scale height of 7 km.

It is noticed that the vertical fluctuation profile has a wavy structure, which means that fluctuations do not always increase with the altitude. Instead, at some altitudes, minima and

maxima fluctuations are frequently observed. For instance, as shown in Figure 3.6, there are several minimum values located at ∼43, 48, 54, 63 and 70 km in the lower layer, and at ∼89 and 96 km in the upper layer. The altitudes with minimal fluctuations were also observed and referred to as "nodes" by *Rauthe et al.* [2006]. Between 46 and 58 km, the fluctuations are smallest, all less than 0.5%. This suggests that the GW experiences severe dissipation in this region. In addition, Figure 3.4a also shows that the "disrupted layer" starts at ∼58 km early in the night and then descends to ∼46 km toward the end of the night. We will refer to this layer as the "damping layer" hereinafter. It appears that the wave experienced strong dissipation as it propagated through the damping layer but then reappeared above it. Generally, the center of the damping layer descends with time and its thickness has a scale of about one vertical wavelength.

It is particularly named not only because within the damping layer, wave fluctuations are small (less than 0.5%) and not increasing with the altitude, but also because it is linked with a change of the vertical wavelength, as the scaled power spectra of vertical wave number shows in Figure 3.7a. As discussed in section 2.5.1, the scaled power spectra for all profiles of the night were calculated and then averaged for the entire night. Figure 3.7a shows the mean scaled power spectra of relative temperature perturbations from 45 to 66 km. It represents the GW energy variation as a function of vertical wave number and altitude. The white cross in Figure 3.7a indicates the wave number where the PSD is maximum at each altitude. Figure 3.7b shows the nightly mean N_2 as a function of altitude. Its fourth-order polynomial fitting is represented by the dark solid line.

A prominent feature of the spectra is that the wave energy decreases above 45 km and reaches minimum values between 49 and 55 km. Above 55 km, the wave energy increases again. The significant damping occurs around the stratopause, where a gradual increase of the dominant vertical wavelength is also observed. The dominant vertical wavelength increases from ∼6-7 km at 45 km to ∼12-13 km at 66 km.

Recalling the dispersion relation discussed in section 1.1.2, the wave dispersion relation

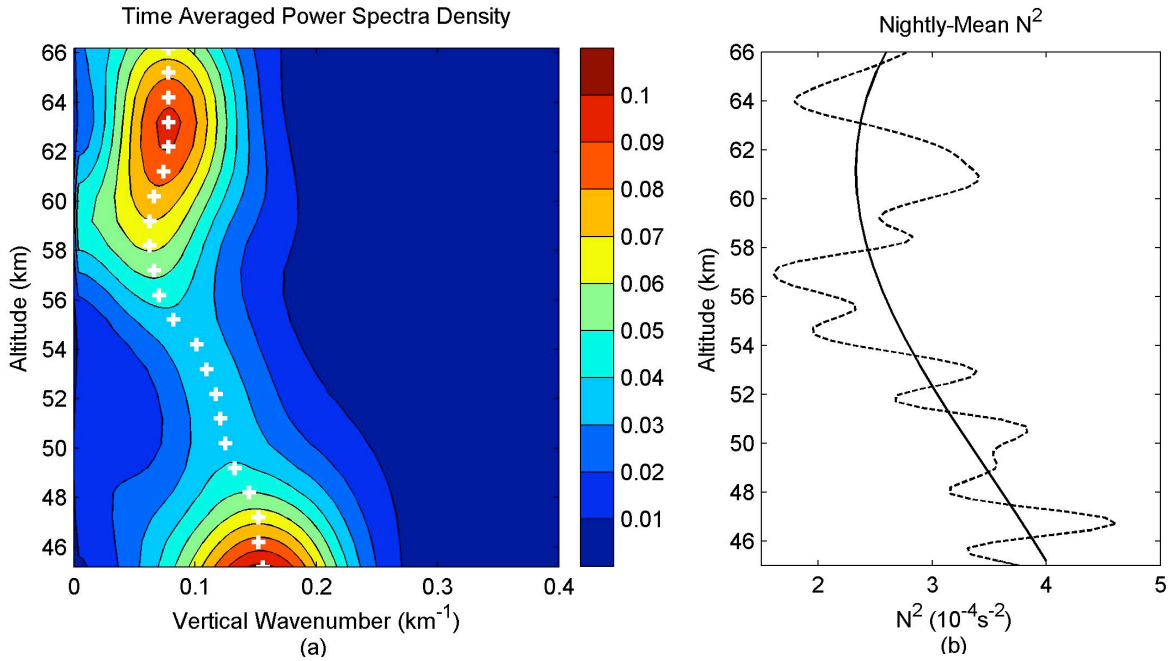

Figure 3.7: (a) Power spectral density proportional to GW potential energy. Unit is arbitrary. The white crosses indicate wavenumbers corresponding to maximum power densities. (b) Nightly mean N^2 (dashed line) and its four-order polynomial fit (solid line).

can be rewritten as:

$$m^2 = \frac{k^2 N^2}{\omega^2 - f^2} = \frac{N^2}{\omega^2/k^2 - f^2/k^2} = \frac{N^2}{|c-U|^2 - f^2/k^2} \tag{3.4}$$

where ω is the intrinsic wave frequency, c is the ground-based horizontal phase speed and U is the background wind speed in the direction of wave propagation. It shows that the vertical wavelength can vary with N_2 and the background horizontal wind U. The vertical wavenumber is proportional to N and inversely proportional to the vertical wavelength. Thus the increase of the dominant vertical wavelength with altitude is consistent with the decrease of N shown in Figure 3.7b. We note that the vertical wavelength is also sensitive to the background winds. However, we cannot examine the wind effect directly for this case due to the lack of the wind data below 80 km. On the basis of the Horizontal Wind Model (HWM) [*Hedin et al.*, 1996] at the same time and location as our observations, we found

that the zonal wind has the order of 10 $\mathrm{m\,s^{-1}}$ and meridional wind starts with 10 $\mathrm{m\,s^{-1}}$ at 35 km and can reach roughly 45 $\mathrm{m\,s^{-1}}$ near 60 km on this night over Hawaii. This wind background can lead to the change of vertical wavelength of the order of 10 km. It implies that the background wind may also be important to the variation of the vertical wavelength, as found in other studies [*Sato and Yamada*, 1994; *Li et al.*, 2007b]. But since HWM cannot represent the real wind fields on this night, the conclusion is not made.

In summary, a dominant GW mode is observed propagating from the stratosphere to the lower thermosphere based on the quasi-colocated Rayleigh and Na lidar observations. A significant damping layer is found around the stratopause region. In the damping layer, the dominant vertical wavelength generally increases with altitude below 60 km, which is consistent with the decrease of static stability. In the following section, we will derive wave properties on the basis of a monochromatic GW assumption.

3.3 Wave Properties

Because of the noticeable wavelength change above and below the damping layer, we derive wave properties separately in the stratosphere and mesosphere from Rayleigh lidar data. We define the "lower layer" from 35 to 55 km and the "middle layer" from 55 to 76 km. The layer observed by Na lidar from 84 to 103 km is referred to as the "upper layer". The spectral analyses were carried out for the three layers by applying the same Welchs periodogram method, with a vertical window of 20 km and shifted every 12 min in time. Figure 3.8 shows the spectra of relative temperature perturbations in three layers, the spectra of two horizontal wind components, and a normalized total power spectral density for all five quantities. The power spectral density is derived in terms of the square of wave amplitude. Dominant vertical wave numbers are marked by white crosses.

According to Figures 3.8a-3.8e, wave intensities show large temporal variations, and they reach maximum at slightly different times for different quantities. On the basis of the

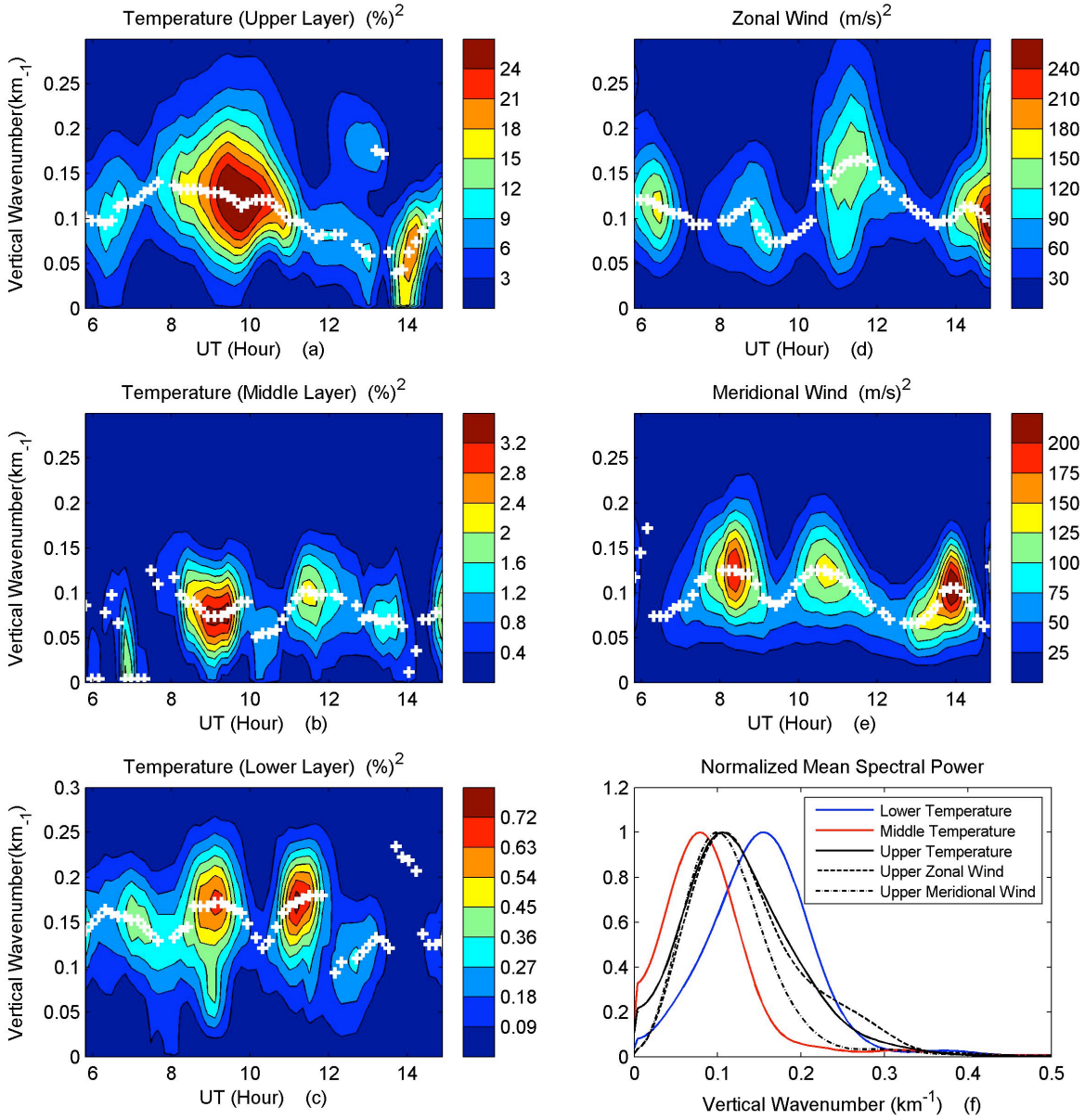

Figure 3.8: PSDs for relative temperature perturbations in the (a) upper, (b) middle and (c) lower layers, PSDs for the (d) zonal and (e) meridional perturbations, and (f) the normalized PSDs averaged over the night.

PSD of temperature perturbations in the lower layer (Figure 3.8c), a strong wave occurred between ∼0800 and 1000 UT and another one occurred between ∼1030 and 1130 UT. The first maximum can be also found in middle and upper layers while the second one become relatively weaker at higher altitudes. The strongest signal in zonal wind is found at the end of the observation period. Three maximum signals are present in the meridional wind, which are centered at ∼0830 UT, 1100 UT and 1400 UT. The dominant wavelengths also vary with time in the range of about 6-12 km.

Figure 3.8f shows the normalized mean PSDs. Red, blue and black solid lines denote the lower, middle and upper layer temperatures while black dashed line represents the zonal wind and dash-dotted line represents the meridional wind in the upper layer. It shows that the mean dominant vertical wavelengths are ∼6.4 km and 12.8 km in the lower and middle layers. The dominant vertical wavelengths in the upper layer are ∼9.5 km, 9.1 km and 10.2 km in temperature, zonal and meridional winds, respectively. Waves with similar vertical wavelengths have also been identified in previous studies [*Chanin and Hauchecorne*, 1981; *Shibata et al.*, 1986; *Hu et al.*, 2002].

Wave amplitudes are derived from their corresponding PSDs and the mean and maximum values are listed in Table 3.1. If the wave is freely propagating which means the amplitude will increase with the scale height $2H_s$ as the density decrease exponentially with H_s ($H_s \approx 7$ km), the maximum amplitudes in the middle layer would be 3.6% and the upper layer would be 30.9% corresponding to the initial value 0.9% in the lower layer, which are much larger than the maximum amplitudes observed. The observed maximum amplitudes in the middle and upper layers are 2.2% and 5.4%, respectively (Table 3.1). It means that the wave was not freely propagating and dissipated as it propagated upward. The maximum amplitudes of the zonal and meridional winds were 16 and 15 $\mathrm{m\,s^{-1}}$, respectively.

Since both temperature and wind data were available in the upper layer from the Na lidar measurement, the wave parameters can be derived from hodograph analysis described in section 2.5.1. Figure 3.9 is the hodograph of zonal and meridional winds from all the

Amplitude	Lower Layer Temperature (%)	Middle Layer Temperature (%)	Upper Layer Temperature (%)	Upper Layer Zonal Wind (ms^{-1})	Upper Layer Meridional Wind (ms^{-1})
Maximum	0.9 (2.2 K)	2.0 (4.6 K)	5.4 (10.4 K)	16	15
Mean	0.6 (1.5K)	1.2 (2.6 K)	3.8 (7.4 K)	10	10

Table 3.1: Maximum and Mean Amplitudes of GWs.
(Precentage represents amplitudes of the relative temperature perturbations; the corresponding temperature perturbations are given in parentheses.)

profiles with significant wave amplitudes and common dominant vertical wavelengths in both temperature and winds. The wave propagated along the major axis of the hodograph and according to the rotation direction of temperature and in-phase wind perturbations with the altitude, it propagated northward [*Hu et al.*, 2002]. The average intrinsic period is 15 h and the average horizontal wavelength is 2140 km, which is significantly larger than the distance between two lidar observation sites (∼150 km). For the two sites, the properties of the dominant mode are similar, which reaffirms our assumption that the wavefield was nearly homogeneous between the two stations for the dominant wave mode.

The ground-based phase speed can also be estimated from the measured ground-based wave period. After both the intrinsic and ground-based wave periods or phase speeds are obtained, the mean background winds can be derived. As shown by the temporal spectrum in Figure 3.10, the wave period varies between 5 and 7 h from the lower to the upper layers with a mean value around 6 h. The relation between observed and intrinsic periods can be written as:

$$\lambda_h = |c - U|\tau_1 = c\tau_0 \tag{3.5}$$

where τ_1 and τ_0 are the intrinsic and observed (ground-based) periods, respectively and λ_h is the horizontal wavelength. Here we use the following values:

$$\lambda_h = 2140\text{km}, \tau_1 = 15\text{h}, \tau_0 = 6\text{h} \tag{3.6}$$

and it can be estimated that $c = 99\ \text{m}\,\text{s}^{-1}$ and $|c-U| = 40\ \text{m}\,\text{s}^{-1}$. This gives $U = 59\ \text{m}\,\text{s}^{-1}$ if

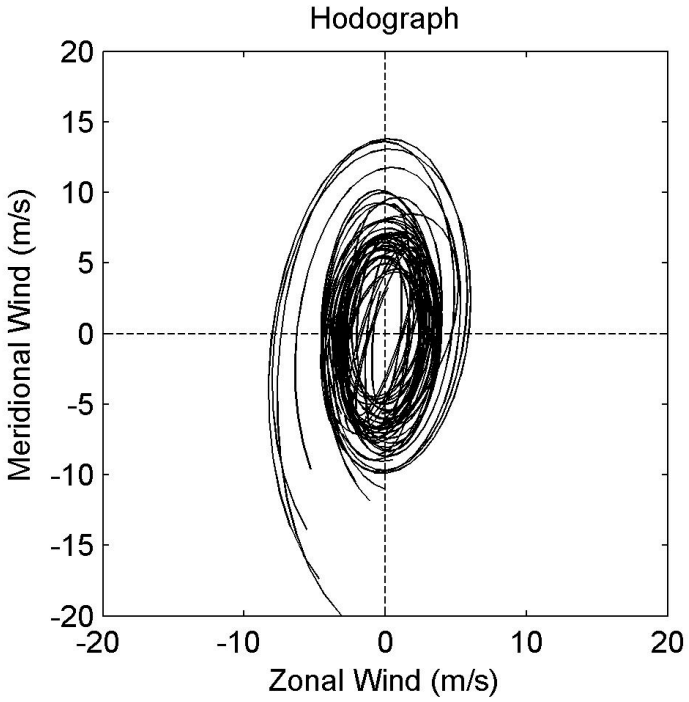

Figure 3.9: Hodograph of zonal and meridional wind perturbations.

the background wind is in the same direction as the wave propagation and $U = 139\ \mathrm{m\,s^{-1}}$ if they are opposite. At the altitude where this quasi-6-h wave was the strongest (∼93 km), we can find that the background meridional wind (Figure 3.3d) is about $60\ \mathrm{m\,s^{-1}}$, in agreement with the first solution of U. It further indicates that the wave was propagating northward in this altitude region, which is consistent with the hodograph analysis.

The vertical phase speeds were also calculated from observed vertical wavelengths and periods. The mean vertical phase speed increases from $0.3\ \mathrm{m\,s^{-1}}$ in the lower layer to $0.6\ \mathrm{m\,s^{-1}}$ in the middle layer and is $0.44\ \mathrm{m\,s^{-1}}$ in the upper layer. Same as the vertical wavelength, the vertical phase speed is also larger in the mesosphere compared to the stratosphere owing to the change of the static stability. *Rauthe et al.* [2006] also pointed out that vertical phase velocity was larger in the mesosphere than in the stratosphere because of the decreasing static stability. In the stratosphere, N is larger compared to the mesosphere which results in smaller vertical wavelengths and smaller vertical phase speeds which is also

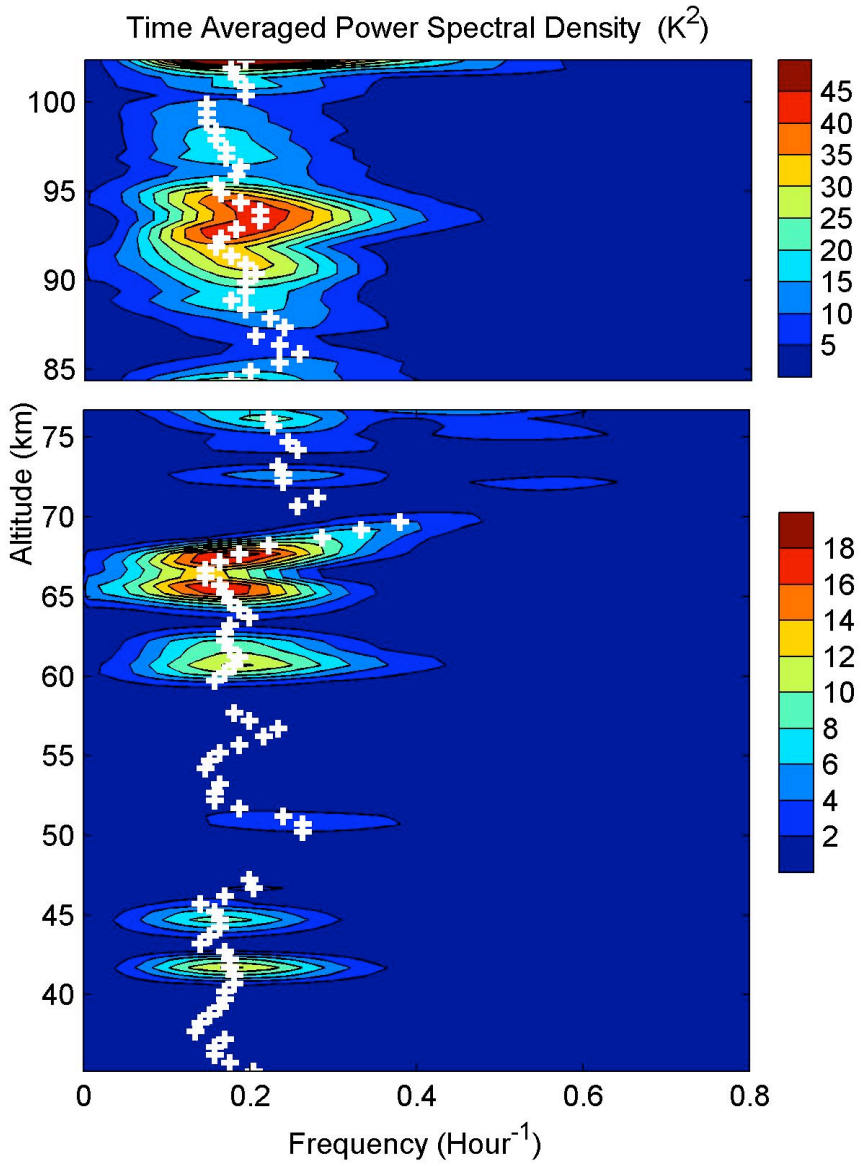

Figure 3.10: Nightly mean frequency PSDs of GW perturbations as a function of altitude. White crosses indicate dominant frequencies at each altitude.

observed in our analysis.

The values of vertical phase speeds are quite typical compared with previous radar and lidar observations. For instance, *Gardner et al.* [1989] obtained values of the vertical phase speeds ranging from 0.11 to 0.85 $\mathrm{m\,s^{-1}}$ with a mean value of 0.39 $\mathrm{m\,s^{-1}}$ in the stratosphere using Rayleigh lidar observations. *Sivakumar et al.* [2006] estimated the rate of downward progression of GWs at around 0.15-0.3 $\mathrm{m\,s^{-1}}$ for lower heights (<50 km) on the basis of four nights of Rayleigh lidar observations over Gadanki (13.5°N). For the higher altitude, the vertical phase speed measured in the Na layer (85-105 km) ranged from 0.36 to 1.75 $\mathrm{m\,s^{-1}}$ [*Gardner and Voelz*, 1987]. And the combined lidar temperature measurements of GWs from 1 to 105 km indicated the vertical phase speed ranged from 0.25 to 0.75 $\mathrm{m\,s^{-1}}$ in November 2003 [*Rauthe et al.*, 2006]. The variation of the vertical phase speed with altitude was also reported by *Chanin and Hauchecorne* [1981], who showed that the vertical phase velocity was near 1 $\mathrm{m\,s^{-1}}$ at 50-70 km and less than 0.2 $\mathrm{m\,s^{-1}}$ below 50 km. It is believed that GWs with similar phase speeds were frequently observed in different seasons and at different locations. Weather events, like convective systems and jet streams can excite GWs for the most part of the world, which may be a source for the universally observed GWs [*Fritts and Alexander*, 2003]. It should be noticed that they are different from globally migrating tides, considering the distinctive wave sources.

3.4 Static Stability

When the propagation characteristics of the GWs is examined earlier in this Chapter, a "disrupted layer" is found near the stratopause associated with the small and non-increasing GW amplitudes. In this section, we investigate the static stability, which may be one possible mechanism to explain the presence of the "disrupted layer". Figure 3.11a shows N^2 as a function of time and altitude, and Figure 3.11b shows its nightly mean. In Figure 3.11a, red color represents unstable regions with N^2 less than zero. Pink areas are so-called marginally

stable areas with $0 \leq N^2 \leq 2 \times 10^{-4}$ s^{-2} and blue color corresponds to stable areas with positive and larger static stability.

It is found that there is a persistent low-stability layer between 54 and 58 km for the entire night, which is right above the stratopause (near 50 km) where the temperature starts to decrease with altitude. Some unstable regions are located mainly above 60 km in the middle layer and some are found in the upper layer. Notice that because of lower signal-to-noise ratio, some of the unstable regions above 60 km are likely due to measurement uncertainties [*Zhao et al.*, 2003]. The persistent low-stability layer between 54 and 58 km, however, is a robust feature and contributes to the observed damping layer. When GWs propagate through this layer, they are more vulnerable to saturate and the wave energy dissipates. As mentioned in section 2.1, the temporal resolution for Rayleigh and Na lidar observations is ∼12 min, which is long enough to possibly smooth out a larger vertical temperature gradient which may occur in a shorter period of time (<12 min). Thus, the unstable conditions are like to occur in this low-stability layer even if the static stability is still positive after being averaged for 12 min.

In the upper layer, the stable and unstable regions have a downward phase progression, which is caused by the temperature changes associated with the diurnal tide and/or the inertial GW. The nightly-mean N^2 shows that the smallest static stability occurs near the "disrupted layer" ($\sim$ 55 km), implying that the atmospheric stability causes the dissipation of GWs when they propagate through it. Although the nightly-mean stability in the upper mesosphere and lower thermosphere is larger than that in the stratosphere and and lower mesosphere, it does not mean waves are more stable in the upper mesosphere and lower thermosphere. The reason is the tidal oscillations are smoothed out by nightly averaging, which may result in the increase of the temperature gradient and/or wind shear and lead to instabilities [*Hecht et al.*, 1997; *Liu et al.*, 2004; *Li et al.*, 2009; *Yue et al.*, 2010].

Also shown in Figure 3.11c is the GWs potential energy as defined in equation (2.13). It is calculated based on the standard deviation of the relative temperature perturbation

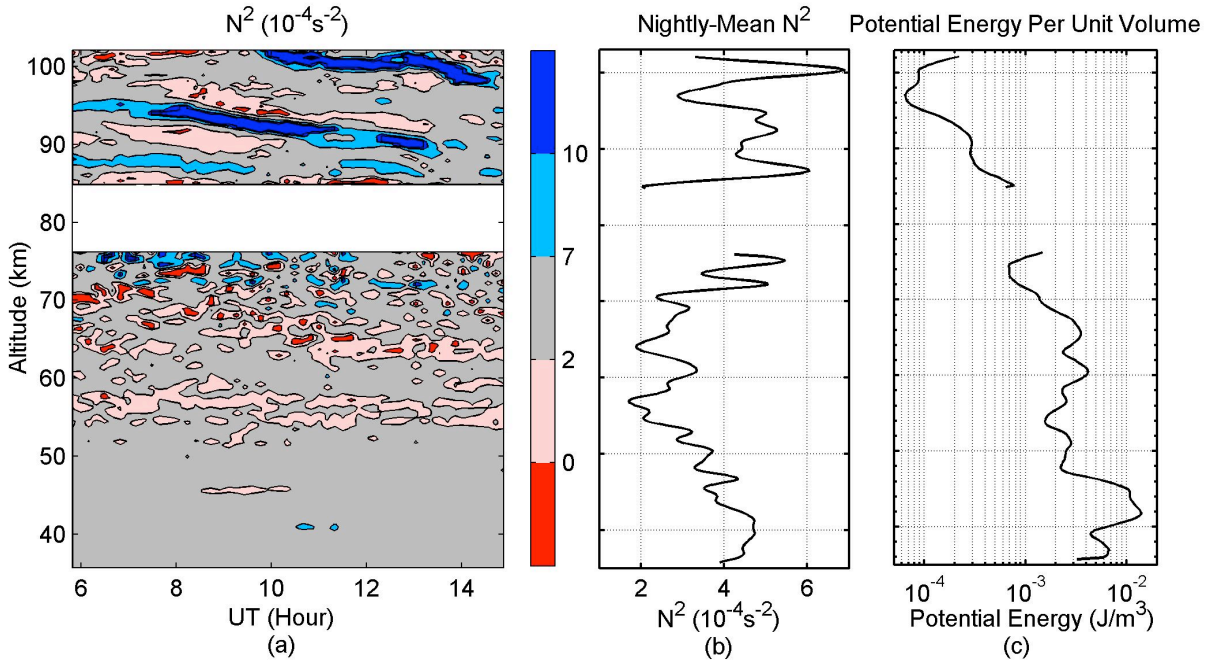

Figure 3.11: (a) Time-altitude variation of N^2, (b) nightly mean N^2 and (c) potential energy per unit volume. In (a), red color denotes convectively unstable areas and pink denotes marginally stable areas where $0 \leq N^2 \leq 2 \times 10^{-4}$ s^{-2}.

shown in Figure 3.4b and the nightly mean N^2 in Figure 3.11b. The atmospheric density is obtained from the MSIS00 model. It is interesting to note that several local minima of the nightly mean N^2 in Figure 3.11b all correspond to local minima of the potential energy in Figure 3.11c. For instance, the common local minima are found at ∼54, 63, 89 and 96 km. It suggests that the static stability imposes a significant influence on the wave propagation and wave energy is more likely to dissipate where the static stability becomes small.

3.5 Summary

A low-frequency inertial GW packet was observed to propagate upward from the stratosphere to the mesosphere (35-103 km) based on the simultaneous measurements of Rayleigh and Na lidars over Hawaii islands on the night of October 28, 2003. On the basis of the relative temperature perturbations, a persistent wave mode was found. We define the lower

layer to be in a range of 35-55km, the middle layer in a range of 55-76 km and the upper layer in 84-103 km. Maximum wave amplitudes were 2.2, 4.6 and 10.4 K in the lower, middle and upper layers, respectively. The e-fold height of the relative temperature fluctuation with altitude was ∼14 km, implying that GW was not freely propagating but instead dissipated. A significant damping layer with the wave structure being clearly disrupted was observed above the stratopause, where the static stability was small. The mean dominant vertical wavelength was ∼6.4 km in the lower layer and ∼12.8 km in the middle layer. In the upper layer, the mean dominant vertical wavelength was found to be around 9.6 km for the GW in both temperature and horizontal winds. The vertical variation of the dominant vertical wavelength was consistent with the variation of background static stability, i.e., larger static stability corresponding to a shorter vertical wavelength.

Na lidar temperature and horizontal winds were used in hodograph analysis to further determine the wave parameters. Both hodograph analysis and polarization relation of GW show that the GW was propagating northward, with an apparent horizontal phase speed of 99 $\mathrm{m\,s^{-1}}$. It had an intrinsic horizontal phase speed of 40 $\mathrm{m\,s^{-1}}$, intrinsic period of 15 h, and horizontal wavelength of 2140 km. The background wind inferred from the difference between ground-based and intrinsic phase speeds of the GW was around 60 $\mathrm{m\,s^{-1}}$ northward, consistent with what we observed based on the Na lidar.

This analysis showed that the combined measurements from lower stratosphere to the mesopause region are of great values for the study of GW propagation. The wind data in the MLT region in addition to temperature allowed us to derive wave intrinsic parameters, and revealed that the wave was Doppler shifted by the meridional wind. Wind measurement in the stratosphere and lower mesosphere could further quantify such analysis.

The presence of a low-frequency inertial GW throughout the night is perhaps not uncommon, as it has also been observed in other studies. However, the measurement at single location also proposed some limitations in the interpretation of the observed wave characteristics. In our analysis, the implicit assumption is that the wavefield is horizontally uniform

and temporally invariant. This is of course not always true. A varying wave source may contribute to a periodic structure observed at a single location that can be erroneously identified as a wave. If a wave packet is not horizontally homogeneous, it can also produce a vertical wave-like structure as it moves across a single station. While these possibilities cannot be ruled out, the assumptions may be often applicable for our nighttime measurements during clear weather conditions at Hawaii. Since the wave was propagating northward, it is likely that the GW we observed on this night was from a nearly constant wave source south of Hawaii near the equator, where tropical convections are present. In the tropics, where it is less likely to have GW generation from topography and baroclinic instability, the source of inertial GWs in the troposphere or the lower stratosphere is most likely tropical convection as has been found in many studies [*Pfister et al.*, 1993; *Tsuda et al.*, 1994; *Karoly et al.*, 1996; *Vincent and Alexander*, 2000].

Tropical convection provides an important mechanism to excite the inertial GWs as we observed here. The low-frequency waves were usually generated in the lower atmosphere near the convective source and can be observed in the middle atmosphere at large horizontal distance from it [*Fritts and Alexander*, 2003]. For us to observe the inertial GWs over the Hawaii islands, the upward and northward propagation should be present to observe GWs originated from the tropical convection region. The fact that the GW we identified was propagating northward supports this notion.

CHAPTER 4

OBSERVATIONS OF THE SEASONAL VARIATION OF THE DIURNAL TIDE

The seasonal variation of the diurnal tide is studied using 5-year meteor radar observations in Maui, HI (21°N). The diurnal tide in the horizontal wind reaches the maximum amplitude at latitude around 20°, which makes Maui be an optimal site for this study. One of the goals is to identify the most important tidal components that dominate the amplitude variation. The seasonal variabilities of the diurnal tide in light of the phase, vertical wavelength, propagation and dissipation characteristics are also investigated, which were less frequently addressed in the previous literature. The observations are also compared with the GSWM and WACCM, from which the capabilities of the models to capture the tidal seasonality are evaluated and differences are identified at the same time. A paper involving this study is in press [*Lu et al.*, 2011].

4.1 5-Year Climatology of Monthly Mean Amplitudes and Phases

In order to focus on the seasonal variability of the diurnal tide and suppress the effects from synoptic and intraseasonal oscillations, the amplitudes and phases for radar observation are averaged monthly and shown in Figure 4.1 and 4.2, respectively. This averaging eliminates the oscillations with periods less than one month. Notice that the color scales for zonal and meridional components are different and the meridional amplitudes are generally larger than the zonal counterparts by up to a factor of 1.5. The maximum monthly mean amplitude of the diurnal tide in zonal wind is $\sim$44 m s^{-1} and in meridional wind is $\sim$56 m s^{-1}. The minimum monthly mean amplitudes are at the beginning of 2005, when the amplitudes

for the zonal and meridional winds are below ∼10 $\mathrm{m\,s^{-1}}$ and ∼15 $\mathrm{m\,s^{-1}}$, respectively. The amplitude uncertainties from the nonlinear curve fitting are on the order of 1-2 $\mathrm{m\,s^{-1}}$, much smaller than the minimum amplitudes.

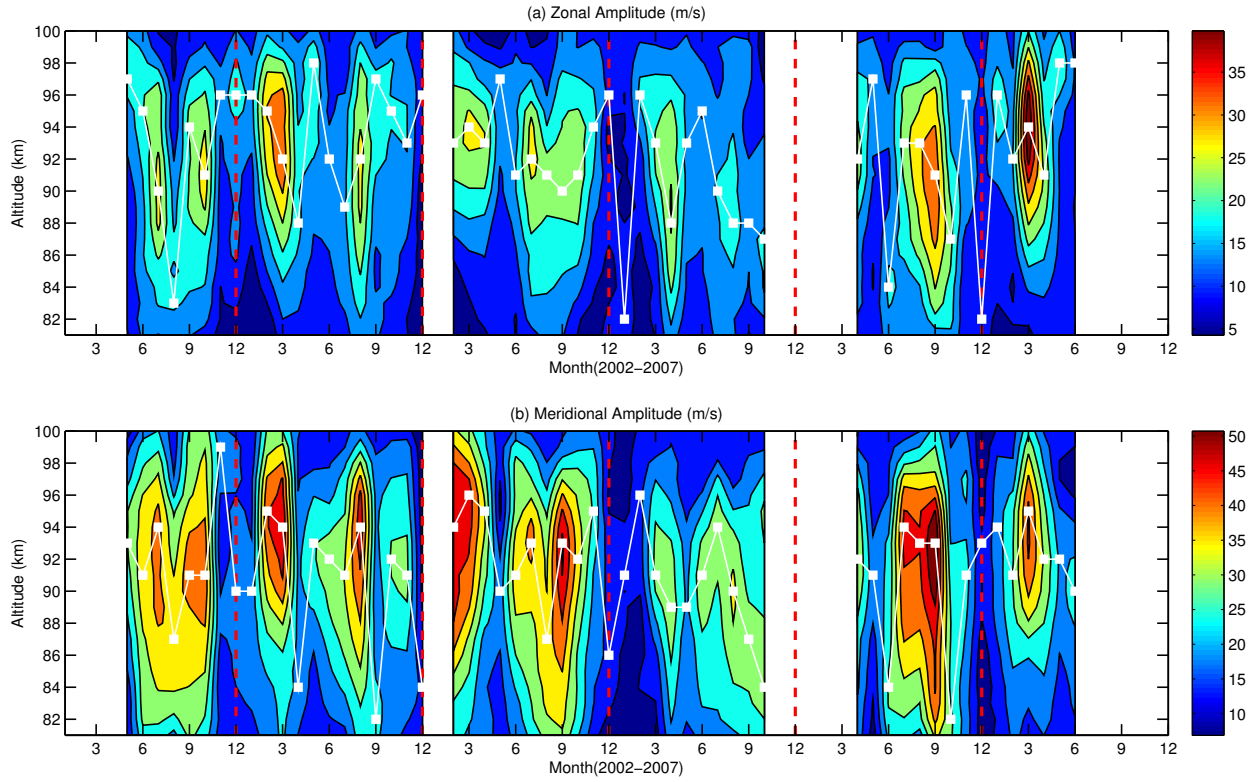

Figure 4.1: Monthly mean amplitudes of the diurnal tide from years 2002 to 2007 based on the meteor radar observation. Red dotted line indicates the beginning of each year and gaps are periods with no data. White squares represent the altitudes corresponding to the maximum amplitudes.

Figure 4.2 shows the monthly mean phases from the meteor radar observation as a function of local time, which corresponds to the time of maximum tidal amplitude. The decrease of phase with altitude implies that wave energy propagates upward and the wave source is below 80 km. The tidal phase of meridional wind is leading the zonal component by ∼6 hrs below 96 km and ∼8-10 hrs above, which may imply the superposition of the migrating and nonmigrating diurnal tides. The phase uncertainties are less than 1 hr at all altitudes. The smallest uncertainties are ∼0.4 hr for the zonal wind and ∼0.25 hr for the meridional wind at 90 km where the number of meteor echos is largest.

Figure 4.1 and Figure 4.2 show significant seasonal and interannual variations of the amplitudes and phases of the diurnal tide. We will discuss the seasonal variation in detail

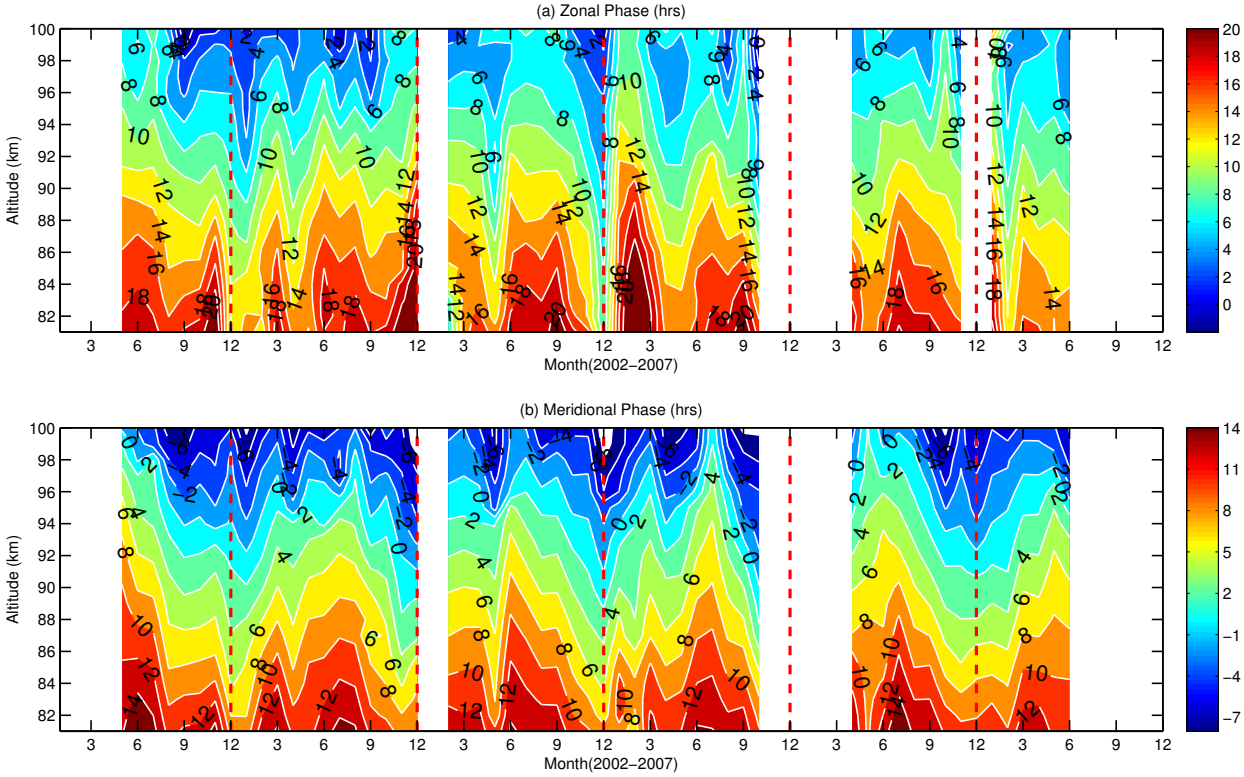

Figure 4.2: Same as Figure 4.1 but for tidal phases. The phase is defined as the local time corresponding to the maximum tidal amplitude.

in the next section. The year-to-year variation of the amplitude shows the diurnal tide is the weakest in year 2005 and it is stronger in 2004 and 2006, for both zonal and meridional winds. In order to identify the dominant oscillation at each altitude, the Lomb-Scargle (LS) periodogram [*Scargle*, 1982] is applied to derive the spectral power densities of the amplitudes shown in Figure 4.1. The LS periodogram is a powerful tool to treat unevenly sampled data and locate peak frequencies precisely providing an optimal method to analyze the dataset with gaps.

Figure 4.3 shows the spectral density of tidal amplitude fluctuation (unit of $m^2\,s^{-2}$) with upper panel for the zonal wind and lower panel for the meridional wind. The peak frequencies are identified and marked by white squares. It illustrates that the strongest

oscillation in amplitudes is the SAO and AO is also dominant. A period of ∼24 months is found for the tide in meridional wind but this oscillation is not significant in zonal wind. *Xu et al.* [2009] found that the period of a Quasi-Biennial Oscillation (QBO) for DW1 was 24-25 months in the mesosphere and it was variable in the stratosphere. Besides the SAO and AO, other oscillations with periods around 8 months and 4 months are also noticeable, which are possibly caused by the interference between AO and QBO and between AO and SAO, respectively. The same method is applied for the phase and the dominant oscillation is found to be the AO (not shown).

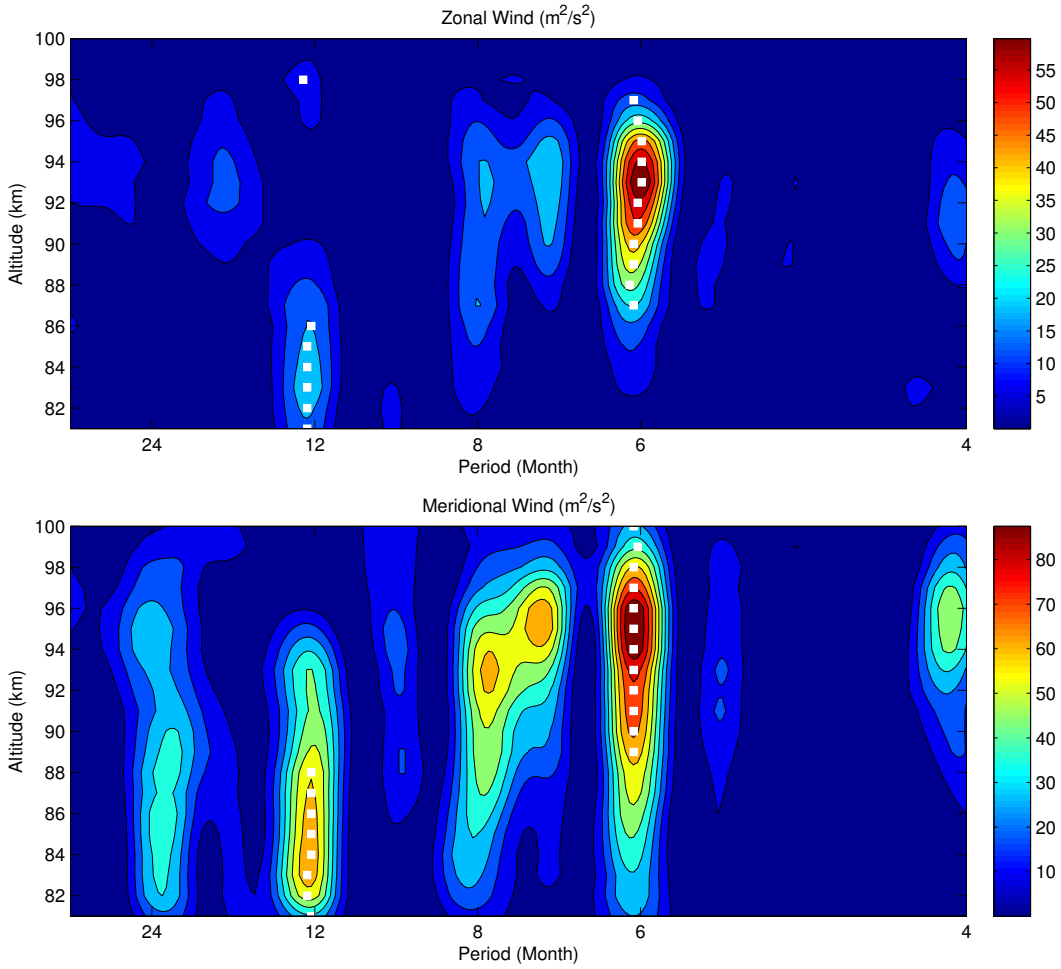

Figure 4.3: Lomb-Scargle periodogram of the amplitudes of diurnal tides. White squares correspond to the peak frequencies.

Figure 4.3 also shows that the dominant oscillation changes with altitude. For the

diurnal tide in zonal wind, the SAO dominates above 87 km and becomes the strongest at 93 km. Below that, the AO dominates but the intensity is much weaker. A similar dominance transition for the meridional wind occurs at 88 km. The strongest SAO for the tide in meridional wind is located at 95 km. The dominant oscillation of amplitudes could be affected by the variability in the mean background winds and/or other waves that would interact with tides and modulate their amplitudes.

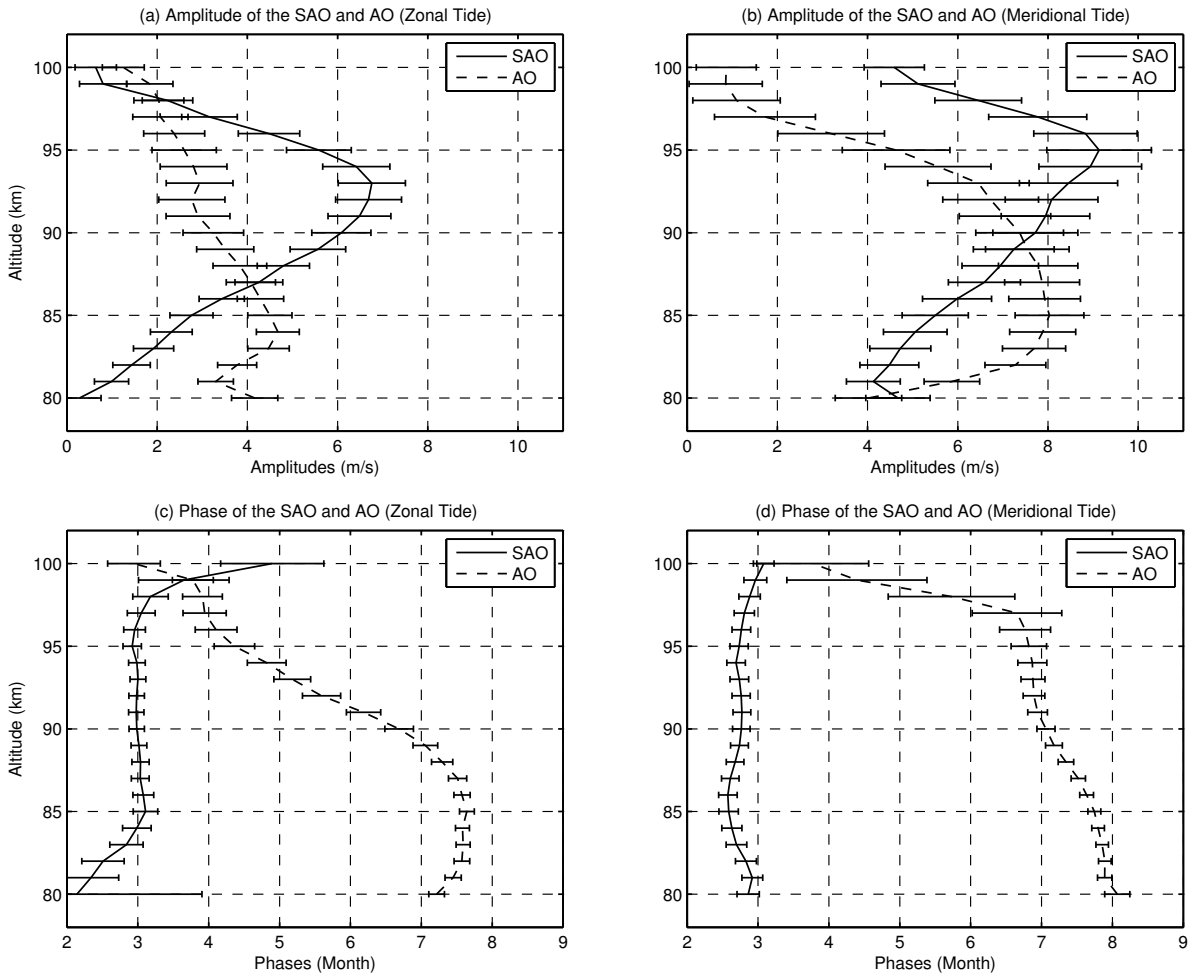

Figure 4.4: Amplitudes of the SAO (solid lines) and AO (dashed lines) of tidal amplitudes in (a) zonal and (b) meridional winds, respectively. (c) and (d) are the same except for phases. Error bars indicate the standard deviations.

Figure 4.4a and 4.4b show the amplitudes of the SAO (solid lines) and AO (dashed lines) for the zonal and meridional diurnal tides, respectively. Figure 4.4c and 4.4d are

the same as Figure 4.4a and 4.4b except for phases. They are derived by fitting sinusoidal functions to monthly mean amplitudes (Figure 4.1) and phases (Figure 4.2). The periods of the sinusoidal functions for SAO and AO are 6 month and 12 month, respectively. The phases of SAO and AO are the months corresponding to the maximum amplitudes.

The amplitudes of the AO and SAO of the tidal amplitudes are larger in the meridional wind than those in the zonal wind. For the diurnal tide in the zonal wind, the maximum amplitude of the AO is $\sim$4.5 $\mathrm{m\,s^{-1}}$ at 84 km and the SAO is $\sim$7 $\mathrm{m\,s^{-1}}$ at 93 km. For the diurnal tide in the meridional wind, the maximum amplitude of the AO is 8 $\mathrm{m\,s^{-1}}$ at 85 km and the SAO is $\sim$9 $\mathrm{m\,s^{-1}}$ at 95 km. Above 87-88 km, the amplitudes of the SAO exceed those of the AO and dominate the amplitude oscillation, which is consistent with the LS periodogram spectra. The phases of the SAO (around March/September) are similar for tides in zonal and meridional winds with relatively small variations with altitude. Unlike the SAO, the phases of the AO vary gradually with altitude, starting from July-August at 80 km and receding to March-April at 100 km for the diurnal tides in both zonal and meridional winds.

4.2 Seasonal Variabilities

According to Figure 4.1 and LS spectral analysis, the SAO of the diurnal tide is most significant as it shows a larger amplitude at equinox and smaller at solstice by a factor of 2-3. In order to display the seasonal variability more clearly and remove the interannual effects, we averaged the monthly mean tidal amplitudes (Figure 4.1) for 5 years from May 2002 to June 2007. The averaged amplitudes for the zonal and meridional winds are shown in Figure 4.5a and 4.5b, respectively. The diurnal tide in zonal wind is strongest at spring equinox (March-April) and less strong at fall equinox (September-October) while the strength of the tide in meridional wind is more comparable at spring and fall equinoxes. This can be seen in Figure 4.1 also for years 2003, 2004 and 2005, when observations during both spring

and fall equinoxes are available. The white squares denote the altitudes corresponding to the maximum amplitudes, which indicates that the diurnal tide starts to dissipate above 95 km. Based on the TIDI wind measurement at 21°N, *Wu et al.* [2008] showed that the DW1 component also reached its maximum amplitude around 95 km.

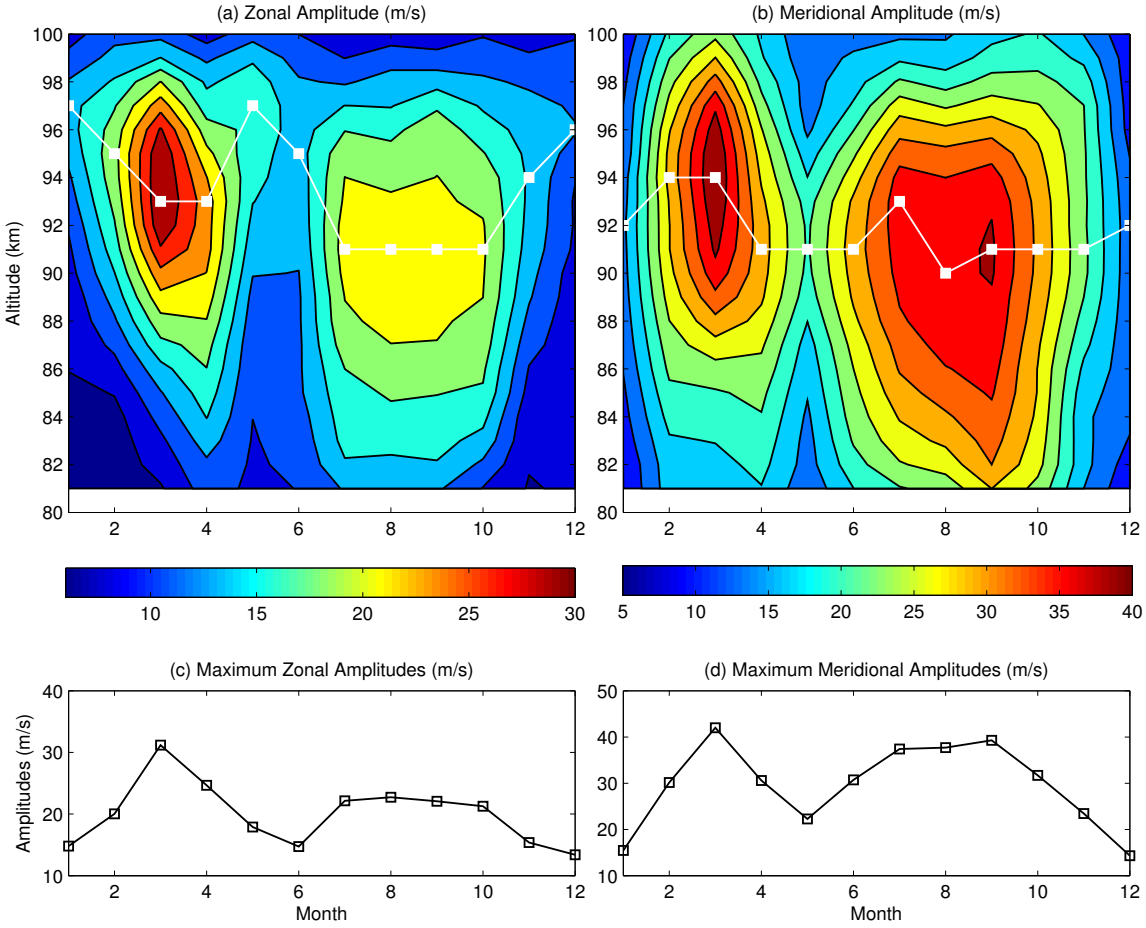

Figure 4.5: Monthly mean amplitudes of the diurnal tide averaged for years 2002-2007 based on Figure 4.1 for (a) zonal and (b) meridional winds, respectively. (c) and (d) are maximum amplitudes for each month at altitudes marked by white squares in (a) and (b).

Figure 4.5c and 4.5d show the maximum amplitude between 80 and 100 km for each month in one year, corresponding to the values highlighted by white squares in Figure 4.5a and 4.5b. After being averaged for 5 years, the largest maximum monthly mean amplitude of the diurnal tide is ~32 $\mathrm{m\,s^{-1}}$ in the zonal wind, occurring in March at 93 km. It is approximately twice as large as the smallest maximum amplitude in December at 96 km

with a value of ∼15 m s^{-1}. In January and June, the diurnal tides in zonal winds are also quite weak. Unlike the zonal winds, two peaks in maximum tidal amplitudes are observed in March and September for meridional winds, respectively. They are of the order ∼40 m s^{-1} and about 3 times larger than the smallest maximum amplitudes at winter solstice (December-January). The diurnal tide in the meridional wind is also weak in May with an amplitude of ∼20 m s^{-1}.

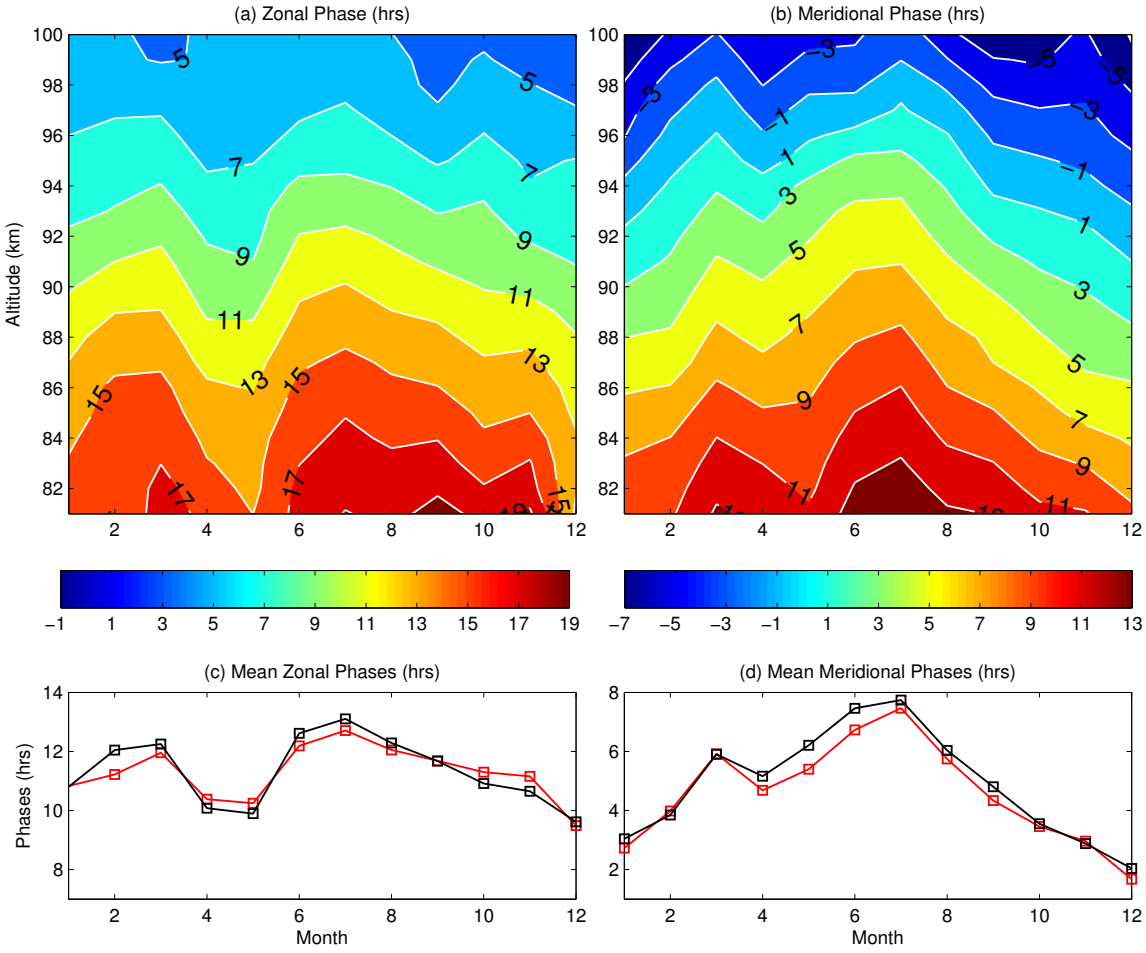

Figure 4.6: Monthly mean phases of the diurnal tide averaged for years 2002-2007 based on Figure 4.2 for (a) zonal and (b) meridional winds. Monthly mean phases at 90 km (black square lines) and averaged mean phases of all altitudes (red square lines) for (c) zonal and (d) meridional winds, respectively.

The seasonal variability of the amplitude of the diurnal tide has been reported in scientific literature as we referred in the introduction part of this dissertation. However, the

phase variation is less frequently addressed. It should be noted that a close examination of the phase variation is crucial for quantifying the effect of the mean wind [*McLandress*, 2002b] and GW/tidal interaction [*Ortland and Alexander*, 2006]. For a purpose of providing a detailed local phase variation of the diurnal tide, the monthly mean phases (Figure 4.2) are also averaged for 5 years and shown in Figure 4.6a and 4.6b.

It is most significant that the observed phases vary with season, advancing to earlier local times in winter and delaying to later times in summer as compared with equinoxes, illuminating a dominant AO. The phase transition at fall equinox is much smoother than spring equinox, especially for the zonal wind. Approximately 2-hr phase differences are observed for March/April and May/June in the zonal wind due to the advance of phase in April and May. A smaller phase advance is also found in April in the meridional wind with a value of $\sim$1 hr.

Quantitative evaluations on the phase variations at 90 km are shown by the black square lines in Figure 4.6c and 4.6d for the diurnal tides in zonal and meridional winds, respectively. This is the altitude where the strongest signals are detected by the Maui meteor radar and the phase errors are the smallest. At 90 km, the phase error is $\sim$0.9 hr for the zonal wind and $\sim$0.6 hr for the meridional wind, respectively. The monthly mean phases averaged within all the altitudes based on Figure 4.6a and 4.6b are also given and represented by red square lines in Figure 4.6c and 4.6d. It is expected that they are close to the phases at 90 km, the center of the radar altitude range. As mentioned earlier, it shows that the diurnal tide in the meridional wind leads the zonal wind approximately for 6 hrs but the exact phase differences vary with both altitude and season. For instance, the phase difference between zonal and meridional winds in winter time tends to be larger than that in summer time. At 90 km, the largest phase difference of 8 hrs occurs in December and the smallest one is 5 hrs in July.

Meanwhile, it is not hard to notice that the magnitude of tidal phase change within a year is larger in the meridional wind as shown in Figure 4.6c and 4.6d. The earliest and latest

local times for the diurnal tide in the zonal wind to reach maximum amplitudes are ∼9.5 LT in December and ∼13 LT in July, respectively. For the meridional wind, the corresponding values are ∼2 LT and ∼8 LT. So the phase change of the diurnal tide in the meridional wind is ∼6 hrs between winter and summer and it is approximately twice as large as that in the zonal wind. The seasonal variation of the tidal phase becomes weaker as altitude increases. At 96 km, the phase differences between winter and summer decrease to half of those at 90 km.

The monthly mean vertical wavelengths are calculated based on the vertical profiles of monthly mean phases. Figure 4.7 shows the monthly mean vertical wavelengths with different markers representing different years. 5-year mean vertical wavelengths are denoted by the two solid lines. Black color is for the diurnal tide in the zonal wind and red for the

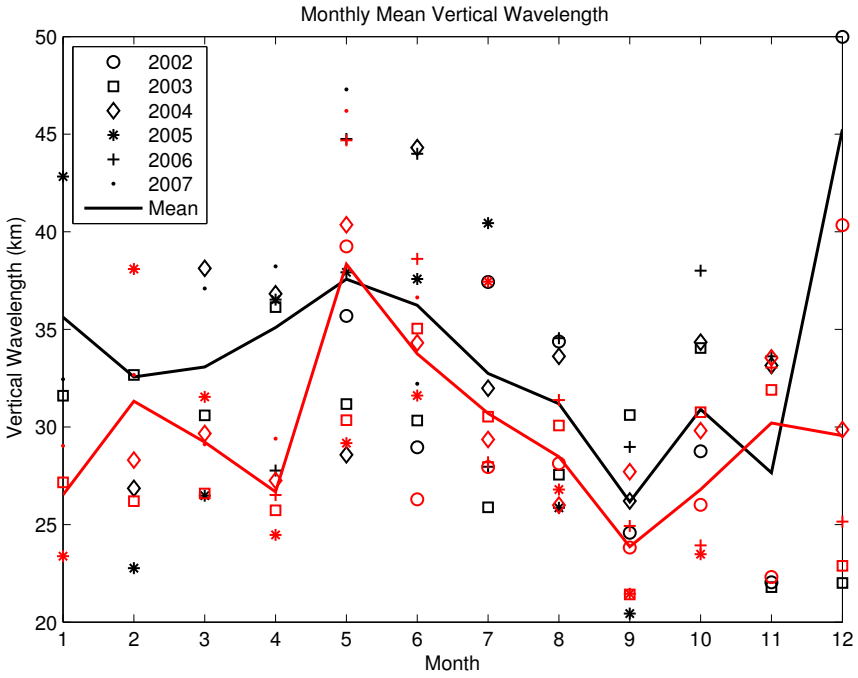

Figure 4.7: Monthly mean vertical wavelengths. Black and red markers represent the vertical wavelengths of tides in zonal and meridional winds for each year, respectively. Black and red solid lines are the mean vertical wavelengths averaged for 5 years.

meridional wind. The vertical wavelengths are mainly between 20 and 45 km. In most cases, the vertical wavelengths of the zonal wind (black solid line) are 2-3 km longer than those of

the meridional wind (red solid line). As we discussed in the seasonal variability of the tidal phase, above 96 km where DW1 starts to dissipate, the interference of nonmigrating tide is more important and some nonmigrating tides can have longer vertical wavelengths such as DE3 ($\sim$ 56 km). According to the TIDI wind observation on the seasonal variations of nonmigrating diurnal tides, DE3 has a larger amplitude in the zonal wind than the meridional component [*Oberheide et al.*, 2006] and it reaches the maximum amplitude at a much higher altitude ($\sim$ 110 km) [*Zhang et al.*, 2010]. The strength of DE3 is close to DW1 in the lower thermosphere [*Liu et al.*, 2010b]. It should be noted that by a single-site meteor radar measurement, the vertical wavelength of the diurnal tide is determined by a superposition of the migrating and nonmigrating diurnal tides, especially at altitudes where their magnitudes are comparable. The superposition of migrating and nonmigrating diurnal tides can change the phase, thus changing the vertical wavelength of the diurnal tide.

Although the month-to-month and year-to-year variations of the vertical wavelengths seem to be irregular, there is a clear and consistent seasonal trend. Generally, the vertical wavelengths tend to be shorter at equinoxes and longer at solstices. From May to September, the mean wavelengths decrease from $\sim$37 km to $\sim$25 km and increase from September to December. In December and January, larger vertical wavelengths are often observed. From January to March, the wavelengths decrease again, but not as remarkably as the decrease from May to September.

According to classical tidal theory for an isothermal and motionless atmosphere, the predicted vertical wavelength for the (1,1) Hough mode is around 28 km [*Forbes*, 1995]. For DW1, the Hough modes associated with negative or large positive equivalent depths are trapped in the source region and it is more difficult for them to propagate up to the MLT. Although the vertical wavelengths for (1,2) and (1,3) Hough modes are positive (16 km and 11 km), they are smaller than the vertical wavelength of the (1,1) Hough mode and more vulnerable to wave dissipation due to larger vertical diffusion [*Forbes*, 1995]. So the (1,1) Hough mode is dominant for the tidal component DW1. In addition, the latitudinal

structure of the (1,1) Hough mode is symmetric in the zonal wind and antisymmetric in the meridional wind. In the northern/southern hemisphere, the tidal phase of the meridional wind advances/lags the zonal wind by 6 hrs. The dominance of the (1,1) Hough mode is supported by the meteor radar observation according to the distribution of the vertical wavelength and the phase shift between zonal and meridional winds (Figure 4.6).

It is noticeable that the vertical wavelength in Figure 4.7 indicates a complex distribution. Most of them are within a range of 20-40 km but with considerable variability. This is not surprising because there are many factors controlling the vertical structure of the tides. For instance, the change of the background temperature can alter the scale height and thus change the vertical wavelength [*Forbes*, 1995]. Superposition of nonmigrating tide and mode coupling may also have impacts. *Mayr et al.* [1999] used a nonlinear, 3D, time dependent Numerical Spectral Model (NSM) which incorporated the Doppler Spread Parameterization (DSP) [*Hines*, 1997a,b] for small scale GWs to study the diurnal tide and mean zonal circulation. They reported that between 80 and 120 km, the GW source could amplify the diurnal tide and reduce the vertical wavelength. Based on a mechanical model, *Ortland and Alexander* [2006] found that the vertical wavelength of the diurnal tide was much shorter if GW momentum forcing was included in the simulation. *Ortland* [2005a] also reported that equatorial and midlatitude jets could affect the horizontal structure and vertical wavelength of the tidal modes.

As we discussed in section 4.1, the diurnal tide starts to dissipate above ∼95 km. The diurnal tide propagates upward and reaches maximum amplitude between 92 and 97 km for the zonal wind and between 90 and 94 km for the meridional wind. Above that, severe dissipation occurs and the amplitudes decrease sharply. By comparing the peak altitudes of the maximum amplitudes between observation and models, we can determine whether the dissipation is appropriately parameterized in models. For instance, a sensitivity test on the diurnal tidal response to the GW parameters showed that a proper GW spectrum is a key to drag the peak altitude down from above 100 km to ∼95 km [*Ortland and Alexander*,

2006]. As will be pointed out in section 4.4, the altitudes of maximum amplitudes were not well simulated by either the GSWM or WACCM. The study of growth and dissipation characteristics of the diurnal tide can provide a comparison for the models which may help them to constrain the GW spectrum and other dissipation parameters.

In order to quantify growth and dissipation rates, we defined the amplitude growth rate H_1 and dissipation rate H_2 in equation (4.1). H_1 is positive and describes the amplitude growth rate from the lowest altitude $Z_0 = 80\,\text{km}$ to altitude Z_{max} where the maximum amplitude A_{max} is reached. H_2 is negative and describes the amplitude dissipation rate from altitude Z_{max} to the highest altitude $Z_1 = 100\,\text{km}$. A_0 and A_1 are the wave amplitudes at lowest altitude Z_0 and highest altitude Z_1 respectively.

$$A_{\max} = A_0 e^{\frac{Z_{\max}-Z_0}{2H_1}}, A_1 = A_{\max} e^{\frac{Z_1-Z_{\max}}{2H_2}} \tag{4.1}$$

We define a total amplitude as follows and use it to calculate the growth and dissipation rates of the diurnal tide:

$$A = \sqrt{A_{zonal}^2 + A_{merid}^2} \tag{4.2}$$

where A_{zonal} and A_{merid} are amplitudes for tides in zonal and meridional winds, respectively. Since the DW1 component is dominant, it is still a good approximation to take the growth and dissipation rates based on the total tidal amplitudes.

Figure 4.8 is a histogram showing the distribution of growth rate H_1 (positive side) and dissipation rate H_2 (negative side) for all the seasons. The mean values for are $H_1 \approx 9.4\,\text{km}$ and $H_2 \approx -7.5\,\text{km}$. Figure 4.9 displays the monthly mean growth and dissipation rates and error bars are deviations resulting from the variations within each month. Both figures demonstrate that for some cases, the diurnal tide can freely propagate ($H_1 \approx 7.5\,\text{km}$) before dissipation. The dissipation rate has the same order as the amplitude growth rate. According to Figure 4.9, the mean positive growth rates H_1 are smallest in winter and spring and increase as time goes to summer and fall thus an AO is present for H_1. It is shown in Figure

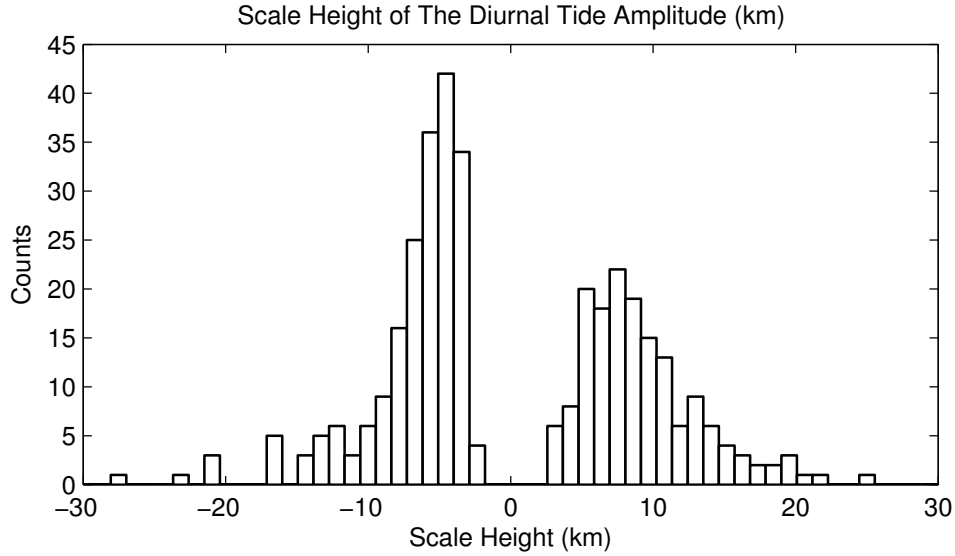

Figure 4.8: Distribution of amplitude growth and dissipation rates calculated on tidal amplitudes.

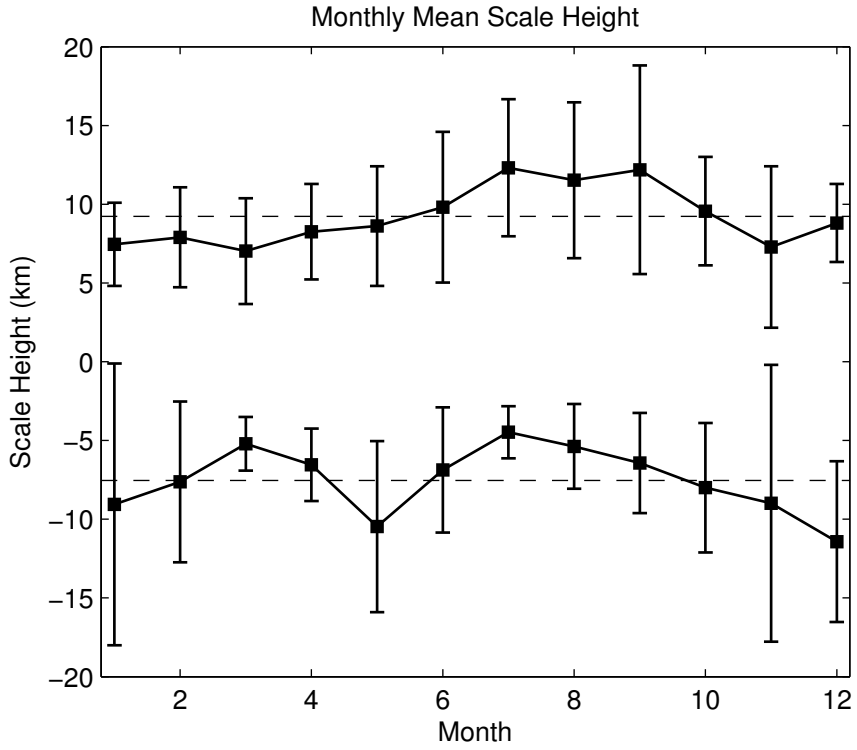

Figure 4.9: Monthly mean growth and dissipation rates averaged for 5 years. Positive values are for H_1 and negative values for H_2. Dashed lines are the mean values.

4.4 that as the AO dominates the amplitude variation, larger amplitudes are found in July and August which correspond to larger H_1 in Figure 4.9. It implies that the growth rate tends to be small when the tidal amplitude is large. The most negative mean dissipation rates H_2 are found in May, December and January, corresponding to slower dissipations. The faster dissipations occur at equinoxes which suggests that the diurnal tide experiences greater dissipation when it is stronger. Therefore, a SAO is found for the dissipation rate.

The dissipation of the diurnal tide has also been reported by *McLandress et al.* [1996] based on Upper Atmosphere Research Satellite (UARS) observations, and it was found that the diurnal propagating tide grew up to 95 km and decayed rapidly above where molecular diffusion greatly reduced the vertical shears. *Chang and Avery* [1997] obtained similar results based on radar observations over Christmas Island. The mechanisms for the dissipation are not conclusively revealed. Molecular diffusion is likely to cause it as it becomes the largest dissipation term above 100 km [*McLandress*, 2002a]. The destructive interference between migrating and nonmigrating tides and interactions of tides with GWs and PWs are also potential candidates. The study on scale heights provides a preliminary result about the propagation and dissipation characteristics of the diurnal tide, while more observation and modeling work are needed to further identify the physical and dynamical dissipation processes.

4.3 Comparisons with the TIMED Wind Tides

According to the studies by *Forbes et al.* [2003] and *Ward et al.* [2010], the superposition of migrating and nonmigrating diurnal tides depends on the longitude because nonmigrating diurnal tides have different wavenumbers compared to the wavenumber 1 of the migrating diurnal tide. The different superposition causes the significant longitudinal variation in the amplitudes and phases of the diurnal tide. The satellite observation provides a global coverage of the tidal fields which can be used to separate each tidal component. The two

instruments TIDI and SABER on board the TIMED satellite enable us to retrieve the migrating and nonmigrating tides and thus reconstruct the superposition of them.

Figure 4.10 shows the monthly mean amplitudes of the migrating and three other nonmigrating diurnal tides at 90 km, based on TIMED satellite observations. DW1 (black line) is the strongest for both zonal and meridional winds. DE3 (blue line) and DW2 (red line) are important for the zonal wind and their maximum monthly mean amplitudes are ∼10

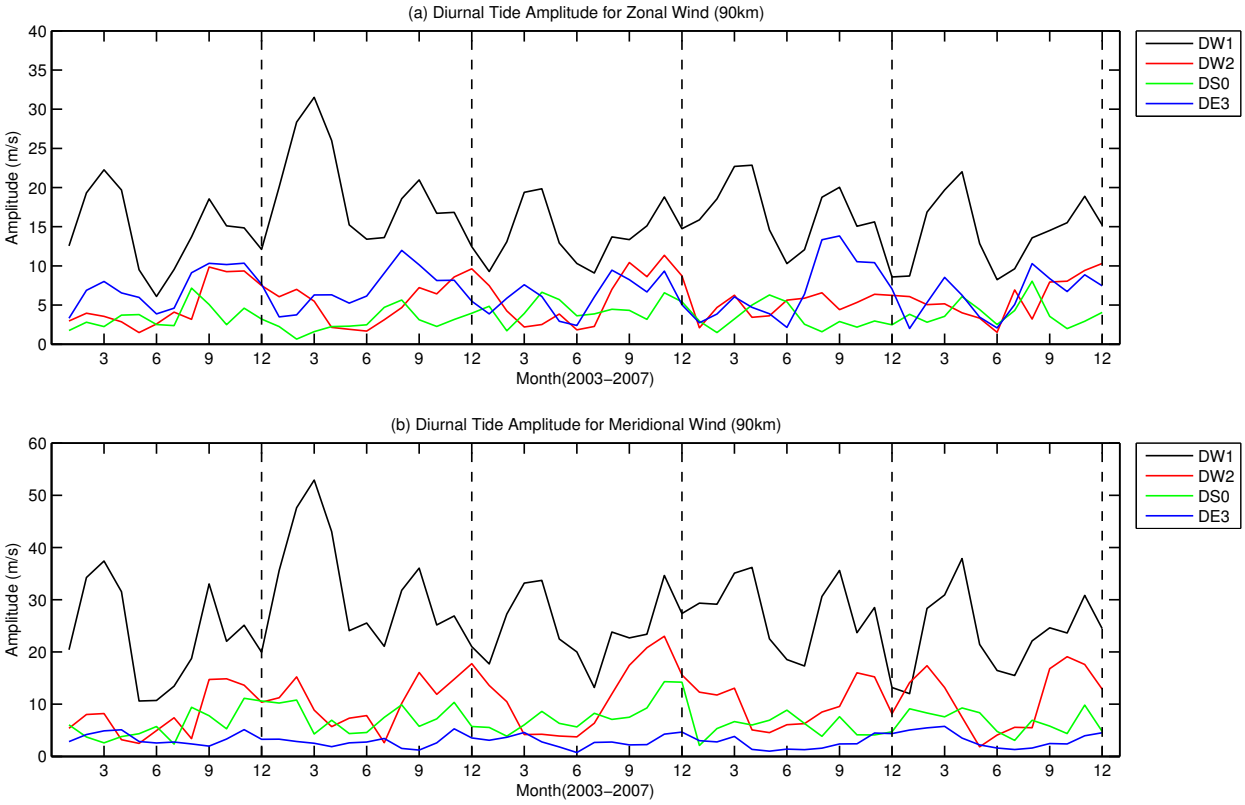

Figure 4.10: Comparisons of the monthly mean tidal amplitudes from TIMED tide measurement. Black, red, green and blue colors represent the wind amplitudes of DW1, DW2, DS0 and DE3, respectively.

$\mathrm{m\,s^{-1}}$. DW2 is larger than DE3 and DS0 for the meridional wind and the largest amplitude can reach ∼20 $\mathrm{m\,s^{-1}}$ in the year 2005. The nonmigrating tides show their own seasonal variations, different from DW1. For instance, DW1 shows the SAO with stronger amplitude at equinox and weaker at solstice while DW2 and DE3 show the AO. DE3 is stronger in August-September in the zonal wind and DW2 is stronger in fall and winter time for both

zonal and meridional winds. The seasonal variation of DS0 though is not as significant as DW2 and DE3.

In order to demonstrate the contribution of nonmigrating tides to the seasonal variation of the diurnal tide, the migrating and nonmigrating diurnal tides are reconstructed by considering both amplitudes and phases in the latitude-longitude grid point corresponding to Maui. All the nonmigrating tides from DW5 to DE3 and the migrating tide DW1 are included and the amplitude of the reconstructed diurnal tide is illustrated by the blue line in Figure 4.11. Meanwhile, DW1 is represented by the dashed black line and the meteor radar

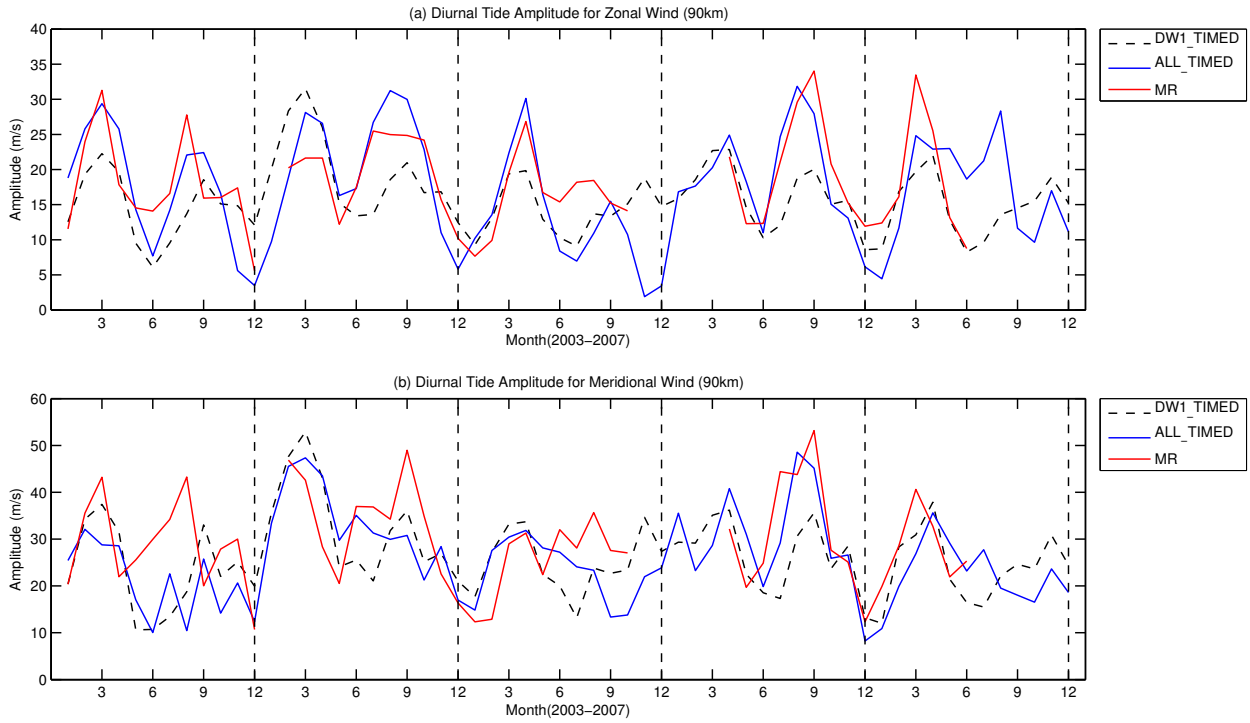

Figure 4.11: Reconstruction of the monthly mean tidal amplitudes based on TIMED tide measurement. Black dashed line is the wind amplitude of DW1. Blue line is the reconstruction of all the tidal components from DW5 to DE3. Red line is the amplitude of the diurnal tide from meteor radar observations.

observation is represented by the red line in Figure 4.11. It is clearly seen that a consistency in the tidal amplitudes is found between the ground-based radar and satellite observations in both zonal and meridional winds. The seasonal variations of the tidal amplitudes from both measurements are also very similar to each other.

The differences between the satellite-reconstructed and radar-observed diurnal tides are possibly due to the errors of calculating the migrating and nonmigrating diurnal tides based on satellite measurements. The amplitude error is about 10% and the phase error is about 1 hr for the migrating tide and the amplitude accuracies for nonmigrating diurnal tide are about 1 $\mathrm{m\,s^{-1}}$ [*Oberheide et al.*, 2006]. If the amplitude of DW1 equals to 40 $\mathrm{m\,s^{-1}}$, the error of the amplitude of the reconstructed tide is around 5 $\mathrm{m\,s^{-1}}$ and if the amplitude of DW1 is 10 $\mathrm{m\,s^{-1}}$, the error is around 3 $\mathrm{m\,s^{-1}}$. So for the most of the time, the reconstructed diurnal tide is within the accuracy range and matches the meteor radar observation very well.

Figure 4.11 also shows that the amplitude of the reconstructed diurnal tide is modulated by the superposition of nonmigrating tides but the seasonal variation is largely determined by the most dominant tidal component DW1. For the zonal wind, some significant changes due to the nonmigrating diurnal tides can be found in the season as both DW2 and DE3 are strong, i.e., August, September and October. Generally, the superposition of nonmigrating tides tends to increase the amplitude during this period.

4.4 Comparisons with the WACCM and GSWM on Seasonal Variabilities

Since direct measurements with sufficient time and altitude coverage on background winds, tidal heating and GW forcing in global scale are not presently available, it is difficult to understand the seasonal variation of the diurnal tide solely based on observations, while models are always useful for facilitating better views on the global tidal dynamics. A single site observation is helpful to verify the model output and provide an opportunity to improve its performance. Here we compare the radar observations with the GSWM and WACCM. It should be noted that the discrepancies between models and observations are not unexpected if the local effects such as stationary PWs and nonmigrating tides are considered. It is challenging for models to realistically simulate the exact local effects in a real time.

The longitudinal variation of the diurnal tide due to the interference of migrating and non-migrating diurnal tides further requires that all the dominant tidal components should be reproduced correctly including amplitudes and phases in order to match the ground-based observation [*Ward et al.*, 2010]. So the heating of tides, temperature and mean winds should be all reasonably captured in the model.

Figure 4.12 shows the comparisons of tidal amplitudes (upper panel) and phases (lower panel) for the zonal wind and Figure 4.13 is for the meridional wind. From left to right are results from the meteor radar, GSWM00, GSWM02 and WACCM, respectively. We also calculated the corresponding amplitudes and phases based on the TIMED satellite

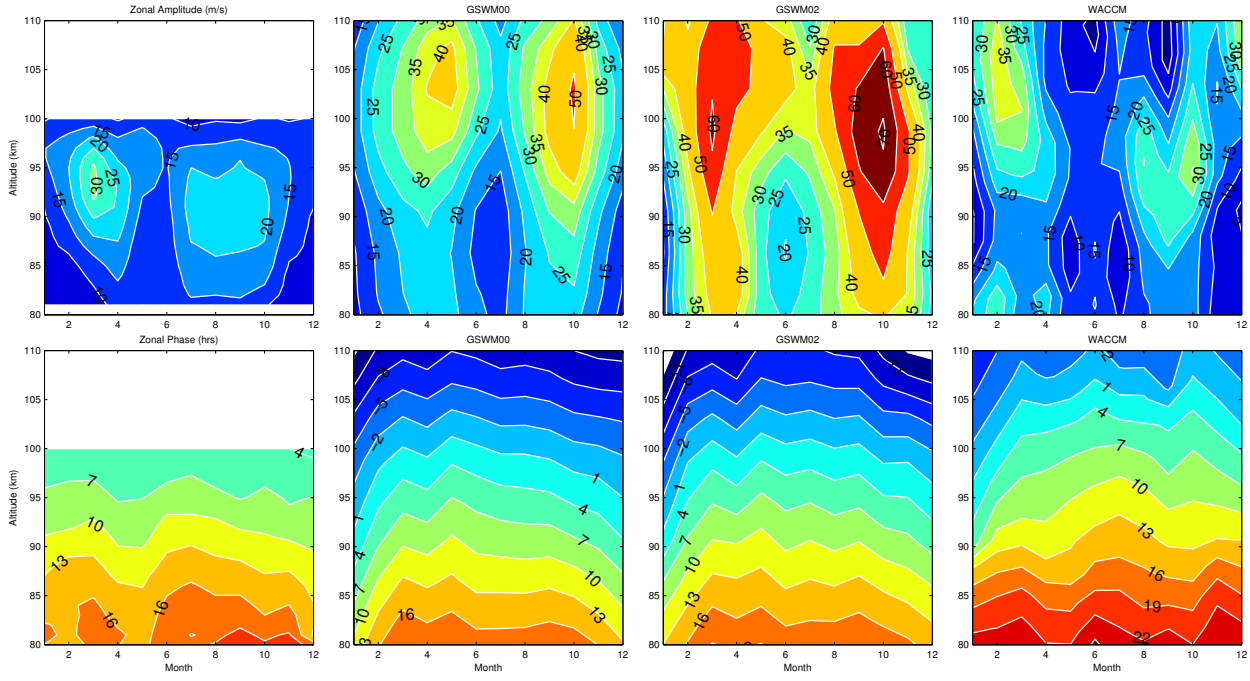

Figure 4.12: Comparisons of tidal amplitudes (upper panel) and phases (lower panel) for zonal winds. Tidal phase is defined as the local time corresponding to the maximum tidal amplitude. From left to right are results from meteor radar, the GSWM00, GSWM02 and WACCM at the location of Maui.

measurement and the results are similar to what we obtained from meteor radar observations (not shown here). The seasonal variation of tidal amplitudes is well reproduced by both models but the magnitude is not quite consistent. Within the altitude range 80-100 km,

the amplitudes reproduced by the WACCM and GSWM00 are comparable to observations while the GSWM02 tends to overestimate the tidal amplitudes. The overestimation of tidal amplitudes by the GSWM02 implies that either wave sources were overestimated or the diurnal tide experienced more dissipation than the model predicted. It is also possible that the phases of the nonmigrating tides relative to the migrating tide are different from observations because the superposition of nonmigrating tides on the migrating tides would change the amplitude for the diurnal tide over the radar station. The WACCM is also capable of reproducing a stronger diurnal tide at spring equinox than fall equinox as observed - a feature not reproduced by the GSWM. The reason for the difference is not clear. Factors such as the radiative tidal heating, latent heating, mean winds and GW forcing are all possible influences on tidal amplitudes, and these terms are all different in the GSWM and WACCM (private communication with Dr. Jia Yue and Dr. Xiaoli Zhang).

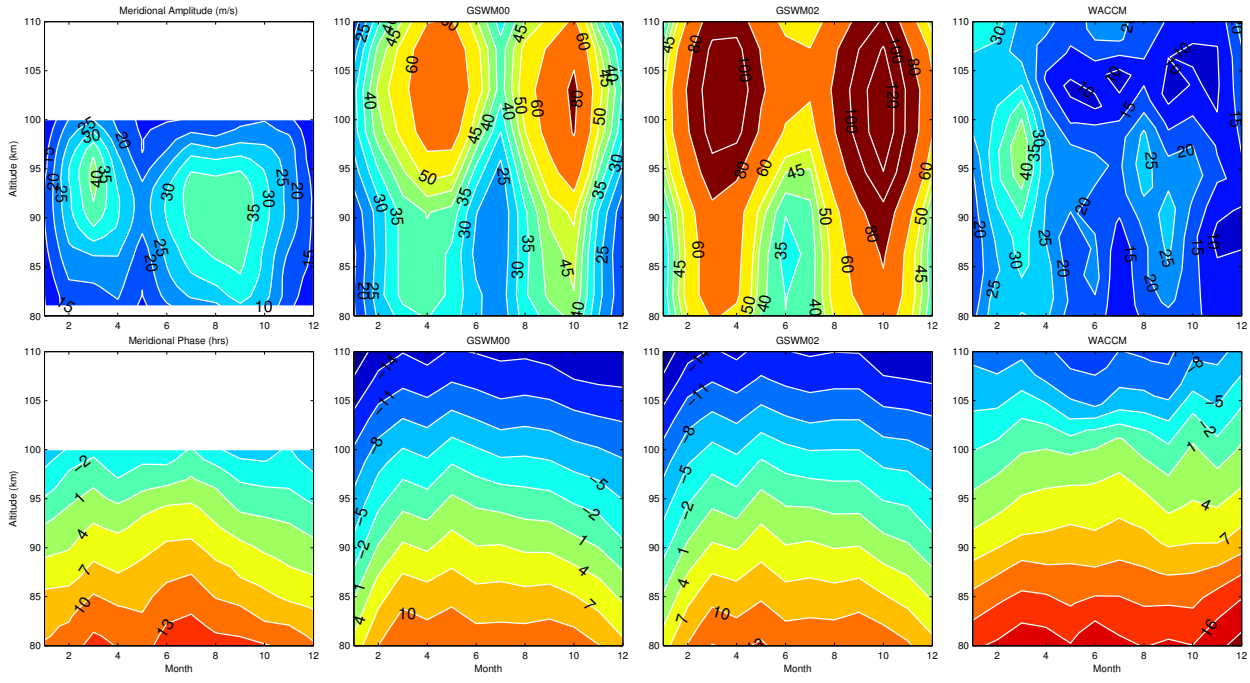

Figure 4.13: Same as Figure 4.12 but for the meridional winds.

In light of the altitudes corresponding to maximum amplitudes, Figure 4.12 and Figure 4.13 show that both models are predicting higher peak altitudes than observations. From

observations, the maximum amplitude is at 90-95 km and it is 5-10 km lower than that in the models. In the GSWM00, the diurnal tide can propagate up to 100-105 km and a great dissipation occurs above it. The WACCM predicts more comparable maximum amplitudes at lower altitudes than the GSWM00/02, but they are still slightly higher than observations. From satellite observations, the diurnal tide at 20°N is also found to decrease its amplitude around 95 km [*McLandress et al.*, 1996; *Wu et al.*, 2008] which is consistent with radar observations and lower than the model results. The altitude with maximum tidal amplitude was dragged down by introducing GWs based on a mechanistic model simulation [*Ortland and Alexander*, 2006]. By including the effect of GW deposition, *Mayr et al.* [1999] also showed the peak altitude became lower than the simulation without GW deposition (Figure 1). So GW forcing is probably one of the important factors to determining the vertical structure of the tidal amplitudes.

The seasonal variation of the phase is also present in models. The GSWM successfully predicts a similar phase advance in winter as the observations but the largest delay occurs in May which is two months earlier than the observation. From the observation, the phase has the largest delay in July and it actually advances for 1-2 hrs in May which is not reproduced by the GSWM. The seasonal variation of tidal phase is also captured by the WACCM and it successfully simulates the largest phase delay in July as observed. A difference between WACCM and observation exists in the phase delay in November and December in WACCM which is not seen in observations. It should be noted that the year-to-year phase variation is not negligible and from Figure 4.2a, the phase from radar observation also shows delays in November and December in year 2003 but advances in the other years. The interannual variations such as the QBO are embedded in the WACCM so a longer term model run is required in future work in order to eliminate interannual effects.

A closer examination reveals the phase differences between radar observation and models. At 90 km, the tidal phase varies within 10-13 LT for the radar observation and the phases in GSWM and WACCM vary within 7-10 LT and 13-16 LT, respectively. So the

GSWM phase leads the radar observed phase while the WACCM phase lags. In a mechanistic model study by *McLandress* [2002b], a strong sensitivity of phase change to the mean wind change indicated that the latitudinal shear of the zonal mean zonal wind was crucial to both absolute value and seasonal variation of the phase. By reducing the zonal mean vorticity to zero above the stratopause, the seasonal variation of phase was greatly changed at 98 km, while by reducing the zonal mean vorticity to zero below the stratopause, the phase was advanced by ∼6 hrs at both 70 and 98 km. When the short-wave radiative heating in the troposphere of WACCM is projected onto the DW1 component, the heating is found to be consistent with that derived from the International Satellite Cloud Climatology Project (ISCCP) radiative heat flux (not shown) [*Zhang et al.*, 2010]. Both heating terms lack a significant seasonal variation. So the phase difference between the observation and the WACCM is likely to be associated with the difference in the mean wind rather than the heating phase.

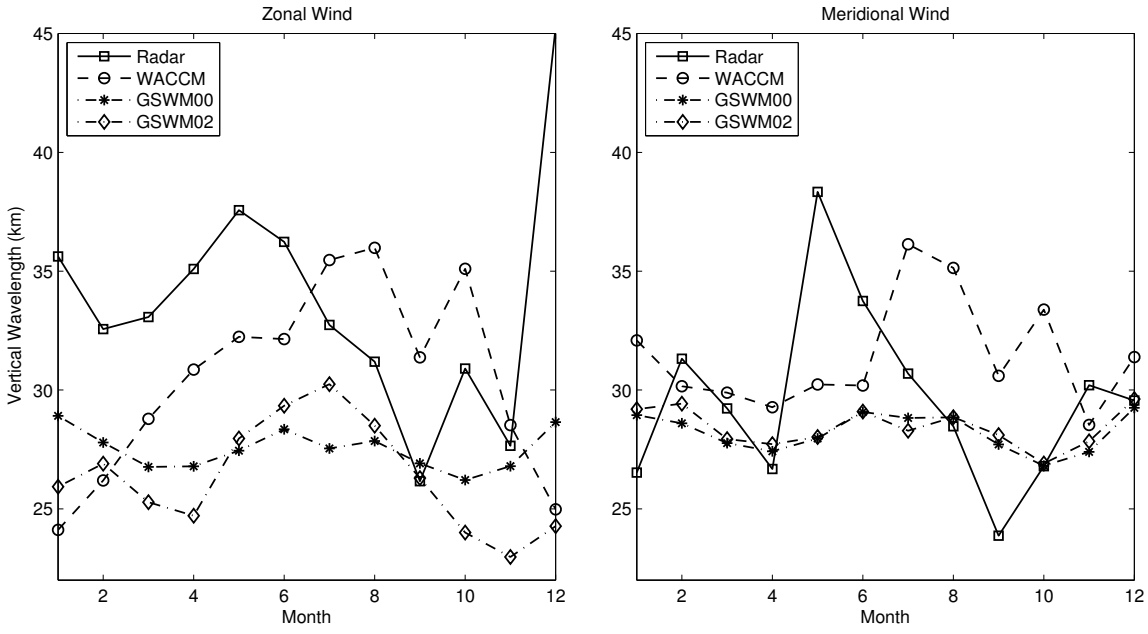

Figure 4.14: Comparisons of the monthly mean vertical wavelengths based on the tidal phases shown in Figure 4.12 and Figure 4.13.

Based on the monthly mean phases in Figure 4.12 and Figure 4.13, we also calculated

and compared the vertical wavelengths reproduced by models, as shown in Figure 4.14. The magnitude of the vertical wavelength is comparable between observation and models but the seasonal variability of the radar observation is stronger than models. The GSWM captures the seasonal variation in terms of the shortening of the vertical wavelength near equinox, especially in the zonal wind of the GSWM00 while the WACCM does not. Instead, an annual cycle in the WACCM shows longer vertical wavelengths for the zonal wind in summer and shorter ones in winter. For the diurnal tide in the zonal wind, both models do not generate long vertical wavelengths in winter as observed.

4.5 Summary

Based on the meteor radar wind measurement during the year 2002-2007 in Maui, HI (20.7°N, 156.3°W), the seasonal variabilities of the diurnal tide including the amplitude, phase, vertical wavelength, growth and dissipation rates are investigated. The SAO is dominant in the amplitude variation above ∼88 km with maximum amplitudes observed at equinoxes and minima at solstices. The tidal amplitude of the meridional wind exceeds the zonal wind by a factor of ∼1.5. The AO and QBO are also observed but with weaker intensities as compared with the SAO. The AO dominates the phase variation such that the phase changes with season annually and advances to an earlier local time in winter. On average, the phase of the diurnal tide advances by ∼3 hrs in winter compared with summer for the zonal wind and ∼6 hrs for the meridional wind. The variability of the vertical wavelength shows a clear seasonal trend characterized by shorter wavelengths at equinoxes. The shortest vertical wavelength is observed at fall equinox with value of ∼25 km. In winter, waves are more likely to be evanescent with longer vertical wavelengths. The diurnal tide can propagate up to ∼95 km but is severely dissipated above that, with many cases in which it propagates freely before dissipation.

The migrating wind diurnal tide is derived from SABER temperature applying the HME

analysis and the nonmigrating wind diurnal tides are derived based on TIDI wind data. The reconstructed diurnal tide is obtained by superposing migrating and nonmigrating diurnal tides, which is found to be very consistent to the ground-based radar observations in terms of amplitude seasonal variations. And the satellite observations suggest that nonmigrating tides can modulate the amplitudes of the total diurnal tide but the SAO of the amplitude is largely contributed by DW1. DW2 is the strongest nonmigrating diurnal tide in the meridional wind, with maximum amplitudes in fall and winter. Both DW2 and DE3 are important nonmigrating tidal components in the zonal wind. The AO of DE3 in the zonal wind is noticeable and it has the largest amplitudes during August-September.

The comparisons between the meteor radar observation and the models (GSWM and WACCM) show both consistency and discrepancy. The seasonal variabilities of tidal amplitudes are well captured by both models. The GSWM00/02 tends to overestimate the maximum amplitude while the WACCM simulation is closer to the observation. The prediction on the peak altitude is higher than observation. The AO of tidal phases are also reproduced by models but with noticeable phase differences between models and observation. The simulated tidal phases in the GSWM00/02 lead those in the observations, while the phases in the WACCM lag the observations. The observed vertical wavelengths are comparable in magnitude with model predictions but the vertical wavelengths observed by the meteor radar vary more significantly than model prediction during the year.

CHAPTER 5

MODEL STUDY OF THE SEASONAL VARIATION OF THE DIURNAL TIDE

As shown in the previous chapter, the WACCM closely captures the SAO of the tidal amplitude and the AO of the phase. In this chapter, we utilize these capabilities of the WACCM to study the seasonal variation of DW1, the dominant component of the diurnal tide observed in Maui, HI. The first part involves momentum budget analysis of DW1. The most important factors that affect the tidal amplitude and phase are identified. The second part aims at investigating the potential mechanisms giving rise to the seasonal variation. Specifically, the effects of the GW forcing, tidal heating and mean winds are evaluated and the responsible mechanisms are proposed.

5.1 Climatology of mean winds, DW1 amplitudes and GW forcing

Before the analysis on DW1 is given, the climatology of the mean winds needs to be examined in order to verify the model performance. Realistic mean winds are also important for the generation and propagation of the atmospheric tides. Figure 5.1 shows the seasonally averaged zonal mean winds obtained from the WACCM. Log pressure altitude is used for the vertical coordinate and it is calculated as: $Z = H \cdot \ln(P_s/P)$, with the surface pressure $P_s = 1000$ hPa and the scale height $H = 7$ km. Compared with the zonal winds based on the Upper Atmosphere Research Satellite (UARS) Reference Atmosphere Project (URAP) [*Swinbank and Ortland*, 2003; *Garcia et al.*, 2007; *Richter et al.*, 2008] shown in Figure 5.2, the WACCM4 captures the salient features of the observed zonal mean wind climatology. For instance, it generates the tropospheric westerly jets in both hemispheres for all sea-

sons. In terms of the NH, the westerly (easterly) stratospheric jets in the winter (summer) hemispheres at solstices are reproduced. The wind reversals at solstices in the mesosphere caused by GW momentum deposition are also simulated in the model. Consistent with the observations, at equinoxes, westerly winds prevail in the stratosphere in both hemispheres except for the equatorial region, where weak easterlies are found.

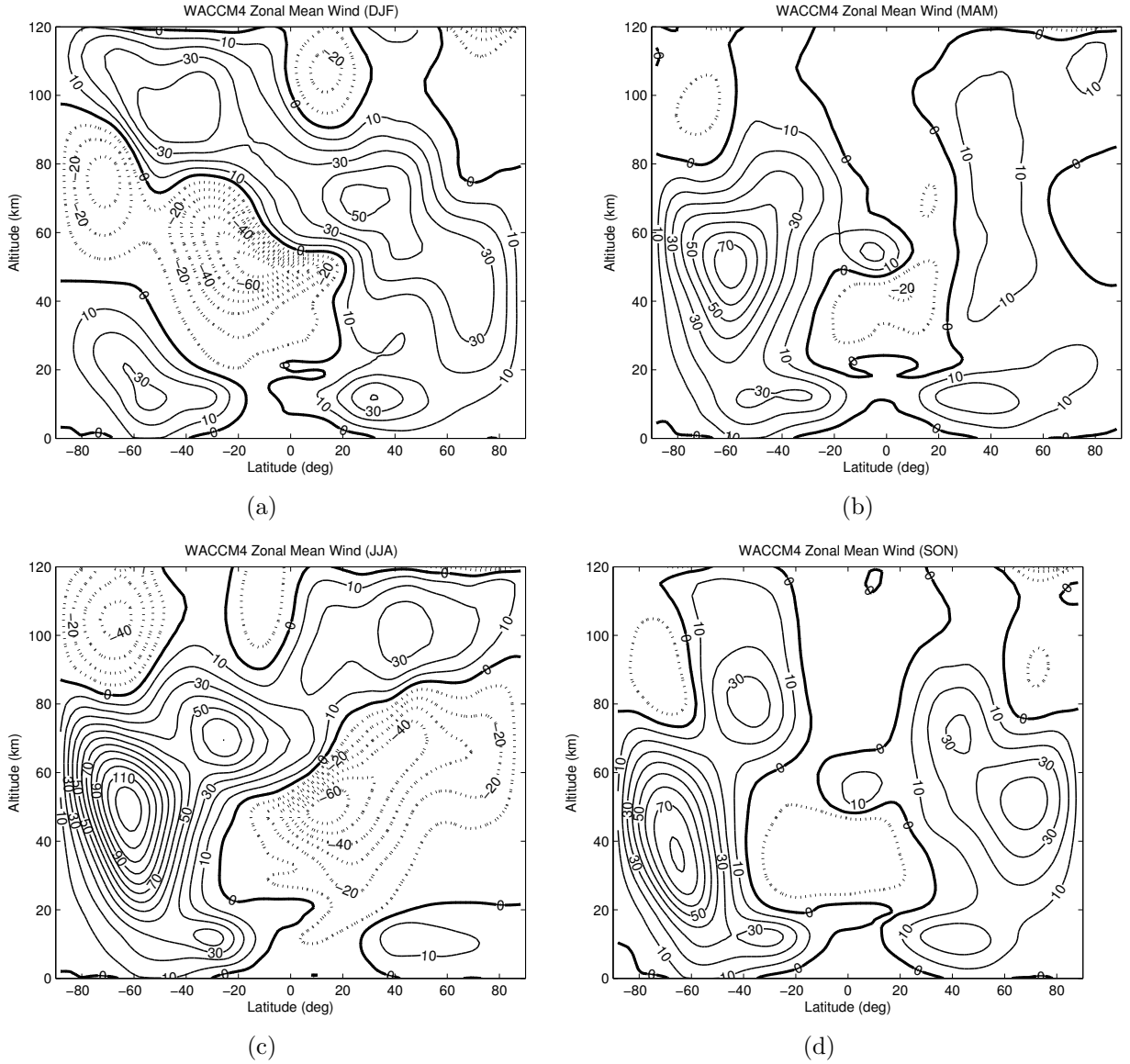

Figure 5.1: Seasonally averaged WACCM zonal mean winds in $\mathrm{m\,s^{-1}}$. Thick solid line is for the zero mean wind. Contour intervals: 10 $\mathrm{m\,s^{-1}}$.

However, the differences between the URAP zonal mean winds and the WACCM simu-

lation are noticeable. The simulated tropospheric westerly jets in the Southern Hemisphere (SH) tend to be stronger than observations by $\sim$10 m s^{-1}. The magnitudes of the tropospheric westerly jets in the NH are relatively closer to observations. A significant difference

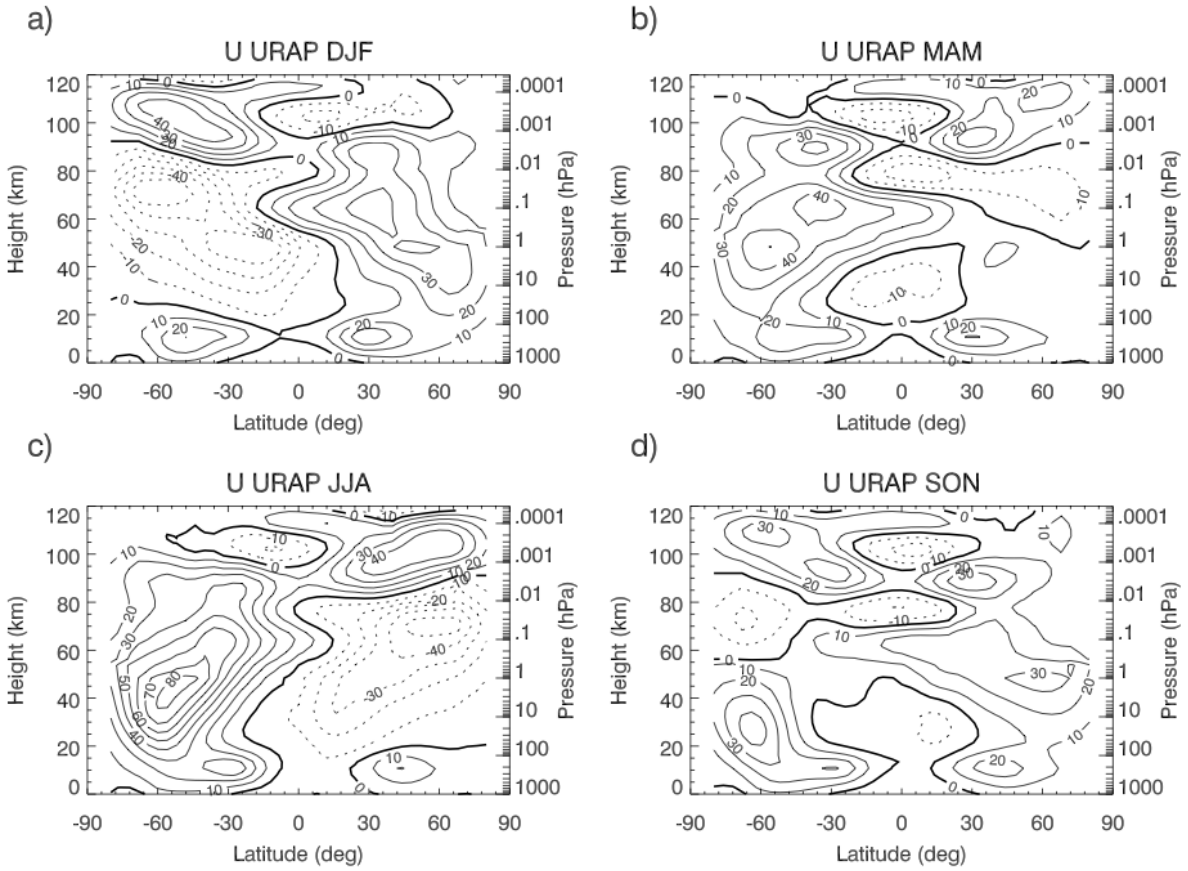

Figure 5.2: Same as Figure 5.1 except for the URAP climatology, *Richter et al.* [2008].

between the WACCM and the URAP zonal mean winds is the altitude that the tropospheric westerly jet can extend into the summer hemisphere at the winter solstice (Figure 5.1a). In the WACCM, this altitude is around 40 km, about 20 km higher than the observation. Another notable difference is the much stronger stratospheric winter jets predicted in the model, especially in the SH (Figure 5.1c). The maximum value reaches 120 m s^{-1} at $\sim$60°S, about 40 m s^{-1} stronger than observation, which is also the case in the WACCM3.5 [*Richter et al.*, 2010]. Overall, the simulation of the mean winds is in good agreement with observations and provides a reasonable background for the DW1 propagation.

As discussed in chapter 4, DW1 has a strong SAO with stronger amplitudes at equinoxes and weaker at solstices [*Wu et al.*, 2008; *Xu et al.*, 2009] and the strongest amplitude of DW1 occurs in March. Figure 5.3 shows the monthly mean amplitudes of DW1 in the zonal wind, meridional wind and temperature in March, based on the WACCM. The zonal and meridional winds reach maximum tidal amplitudes at ∼20° in both hemispheres. The temperature tide is the strongest at the equator and has a secondary peak near ∼30°. The latitudinal structure of DW1 resembles that of the (1,1) Hough mode, except that the zonal wind amplitude peaks 5° equatorward in the model than the prediction by classical tidal theory. Overall, it suggests that the most dominant component of DW1 above 70 km is the (1,1) mode.

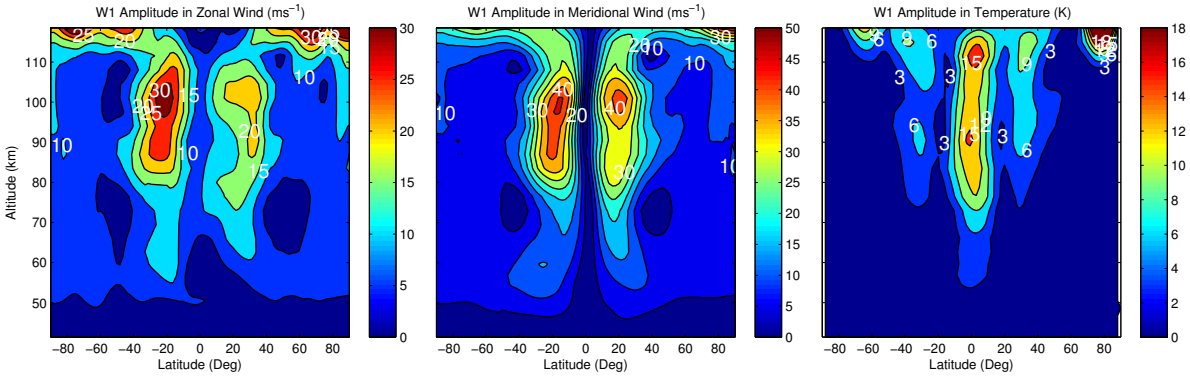

Figure 5.3: Amplitude of DW1 in the zonal wind (left), meridional wind (middle) and temperature (right) in March. The units are m s^{-1} for winds and K for temperature.

The total structure of DW1 is in good agreement with satellite observations while the magnitudes are underestimated in the model, especially for the wind components. From the TIMED/TIDI observations, the maximum amplitudes for zonal and meridional winds are on the order of 50 and 60 m s^{-1} within a 60-day window centered in March [*Wu et al.*, 2008] whereas in the WACCM, the monthly mean amplitudes for zonal and meridional winds are 30 and 50 m s^{-1}, respectively. In the WACCM, the monthly mean amplitude of the tidal temperature has two peaks located at 90 and 110 km with magnitudes of ∼15 K. The TIMED/SABER observation shows the 6-year average amplitude for temperature is 18 K in February-March and reaches double peaks at 85 and 95 km, respectively [*Mukhtarov*

et al., 2009]. As one of the tidal sources, a weak diurnal cycle in the parameterized convective activity is one of the possible causes for the underestimation of DW1 in the WACCM (private communication with Dr. Anne Smith). The other possibility is GW forcing introduces a large damping on DW1.

According to the latitudinal structure of the (1,1) Hough mode, the tidal amplitude is symmetric with respect to the equator. Figure 5.3 shows the tidal amplitudes in the WACCM are not strictly symmetric, which means there are discrepancies caused by the presence of mean winds and dissipation in the real atmosphere. At low and middle latitudes, the strong DW1 is found below 110-120 km. In this region, DW1 is weaker in the NH than in the SH for winds and the opposite for the secondary peak of temperature. As will be seen later, this is partly caused by the asymmetric forcing and dissipation in the different hemispheres. It can be noticed that an enhancement of DW1 persists in the polar lower thermosphere above 110 km, likely due to the auroral heating [*Chang et al.*, 2008]. It is also asymmetric with a stronger amplitude near the Arctic region.

Figure 5.4 shows the projection of GW forcing onto DW1 from the three different GW sources and the total effect. GWs start to play an important role above 70 km as their amplitudes grow large enough to deposit considerable momentum into the mean flow and affect the tide as well. The wave generation from convection is confined to the equatorial region where the strongest convective activities occur most frequently. Frontal systems and orography excite GWs mainly at middle and high latitudes, while the magnitude of orography-generated GW forcing is much smaller than that excited by frontogenesis. The maximum amplitude of the time tendency for the zonal wind ($\partial u/\partial t$) caused by frontogenesis-GWs is $\sim$80 $\mathrm{m\,s^{-1}\,day^{-1}}$, by convection is $\sim$40 $\mathrm{m\,s^{-1}\,day^{-1}}$ and by orography is $\sim$1 $\mathrm{m\,s^{-1}\,day^{-1}}$. These magnitudes are comparable to the GW drag effect on the mean flow [*Richter et al.*, 2010]. It is likely that GW forcing is modulated by DW1, so a large projection of GW forcing onto DW1 implies this modulation is prominent. Compared with the zonal wind, the latitudinal distribution of the GW forcing in the meridional wind is similar while the magnitude is 2

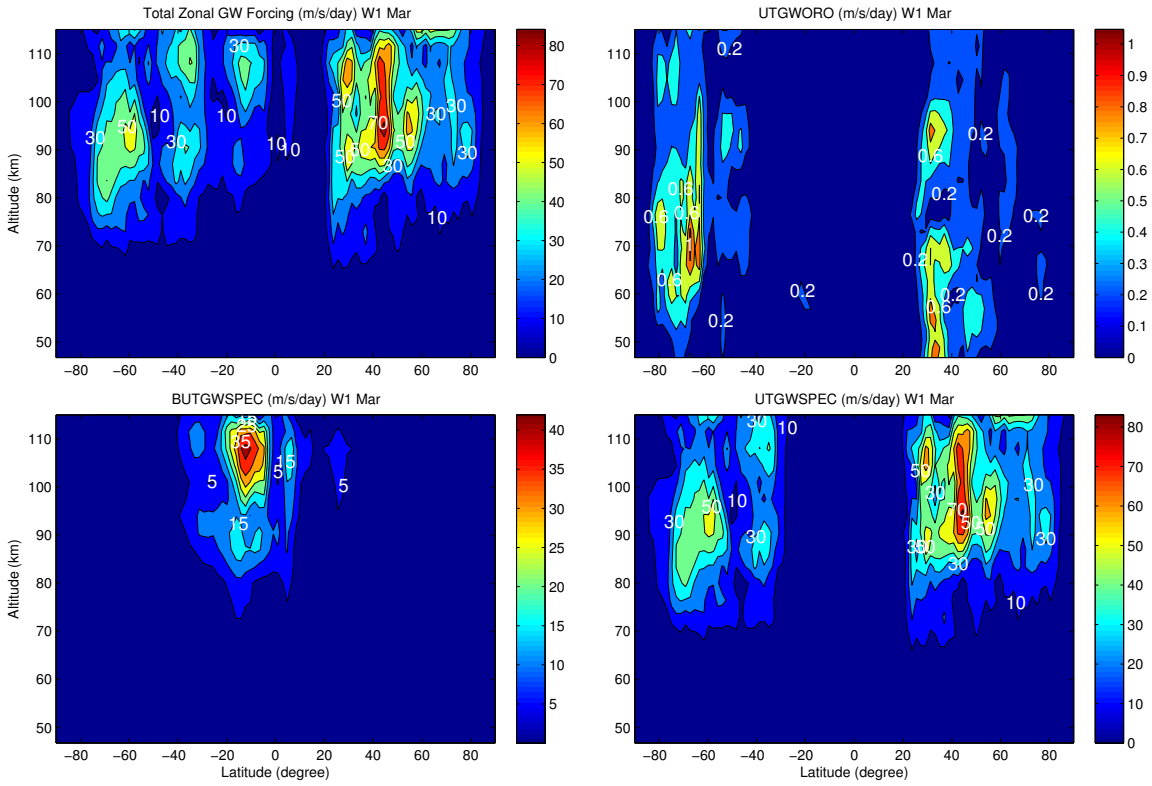

Figure 5.4: Amplitudes of GW forcing originating from orography (UTGWORO), convection (BUTGWSPEC), frontogenesis (UTGWSPEC) and the total forcing (Total) in terms of the time tendency projecting onto DW1.

times smaller (Figure C.1). The total effect on DW1 is basically a combination of the GW forcing by frontogenesis at middle and high latitudes and by convection at low latitudes, while the orography effect is negligible.

The asymmetric structure of GW forcing is notable. For frontal systems, stronger GWs are generated in the NH in most seasons. The distribution of GW forcing generated by deep convection strongly depends on season and tends to move with the Intertropical Convergence Zone (ITCZ). The ITCZ appears as a band of clouds and usually thunderstorms accompanied by strong vertical motion and convective activities. It lies in the equatorial trough and constitutes the ascending branch of the Hadley circulation, where the trade winds, laden with heat and moisture from surface evaporation and sensible heating, converge to form a zone of increased convection, cloudiness and precipitation [*Waliser and Gautier*, 1993]. The deep convection embedded in the ITCZ provides GW sources. The climatology of ITCZ position was described by *Waliser and Gautier* [1993] using the highly reflective cloud dataset. The seasonal variation of location with strong GW forcing is in good agreement with that of the ITCZ position (not shown here). The location of the ITCZ is determined by the solar heating and moves back and forth across the equator following the sun's zenith angle. Thus, during the NH summer, convection generates more GWs in the NH and during the NH winter, it generates more GWs in the SH.

5.2 Comparative Magnitudes of Classical Terms, GW Forcing and Advection

In classical tidal theory, the (1,1) Hough mode is a symmetric mode. The asymmetric latitudinal distribution of the tidal amplitudes shown in Figure 5.3 indicates the discrepancies from classical tidal theory. Based on Figure 5.3, we confine our analysis to latitude region between $\pm 50^{\circ}$, where DW1 attains large amplitudes. Equations (5.1-5.2) are the momentum equations (e.g., *Andrews et al.* [1987]), where u, v and Φ are the zonal wind, meridional wind

and geopotential, respectively. f is the Coriolis parameter. a is the Earth's radius. ϕ and λ are latitude and longitude, respectively. In classical tidal theory, only the first two terms, the Coriolis force (CF) and pressure gradient force (PGF) determine the time tendencies of the horizontal winds ($\partial u/\partial t$ and $\partial v/\partial t$). They are referred to as the classical terms. Other terms as non-classical terms include advection (due to both mean and perturbation winds), curvature, GW forcing and dissipation.

$$\frac{\partial u}{\partial t} = fv - \frac{1}{a\cos\phi}\frac{\partial \Phi}{\partial \lambda} - \vec{V}\cdot\nabla u + \frac{uv}{a}\tan\phi + F_{GW,x} + X \tag{5.1}$$

$$\frac{\partial v}{\partial t} = -fu - \frac{1}{a}\frac{\partial \Phi}{\partial \phi} - \vec{V}\cdot\nabla v + \frac{u^2}{a}\tan\phi + F_{GW,y} + Y \tag{5.2}$$

$F_{GW,x}, F_{GW,y}$ are GW forcings in the zonal and meridional winds. X, Y represent the non-conservative mechanical forcings. In the WACCM4, they mainly include ion drag and eddy and molecular diffusion. In the MLT region, GW drag is more significant than ion drag and the molecular diffusion terms while above 100 km, molecular diffusion becomes dominant [*McLandress*, 2002a].

In order to evaluate the accuracy of classical tidal theory and assess the contribution from the non-classical terms, the amplitude of $\partial u/\partial t$ based on the tidal wind (left hand side of the momentum equation) and the time tendency caused by CF and PGF are calculated. They are shown in Figure 5.5 for the zonal wind and Figure 5.6 for the meridional wind, respectively. By writing the tidal wind as $u' = \hat{u}\cdot e^{i(\omega t - s\lambda)}$, the amplitude of the time tendency can be simply written as $|\partial u'/\partial t| = \omega|\hat{u}|$, where $\hat{u}$ is the complex amplitude in the zonal wind and ω, s are the frequency and zonal wavenumber of DW1. Similarly, for CF in both the zonal and meridional winds and PGF in the zonal wind, the solutions can also be obtained based on the complex amplitudes of horizontal winds ($\hat{u}$, $\hat{v}$) for CF and the geopotential ($\hat{\Phi}$) for PGF. The differences in time tendencies calculated based on classical terms and full primitive equations are also shown in the right panels in Figure 5.5 and Figure

5.6, which represent the contributions from non-classical terms.

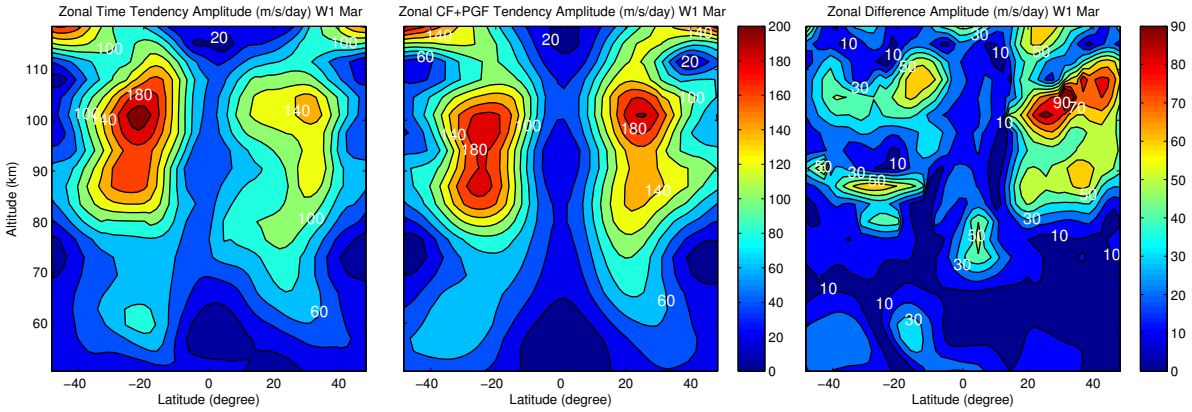

Figure 5.5: Amplitude of the time tendency calculated based on the tidal wind (left), CF+PGF (middle) and the difference between them (right) for the DW1 zonal wind component.

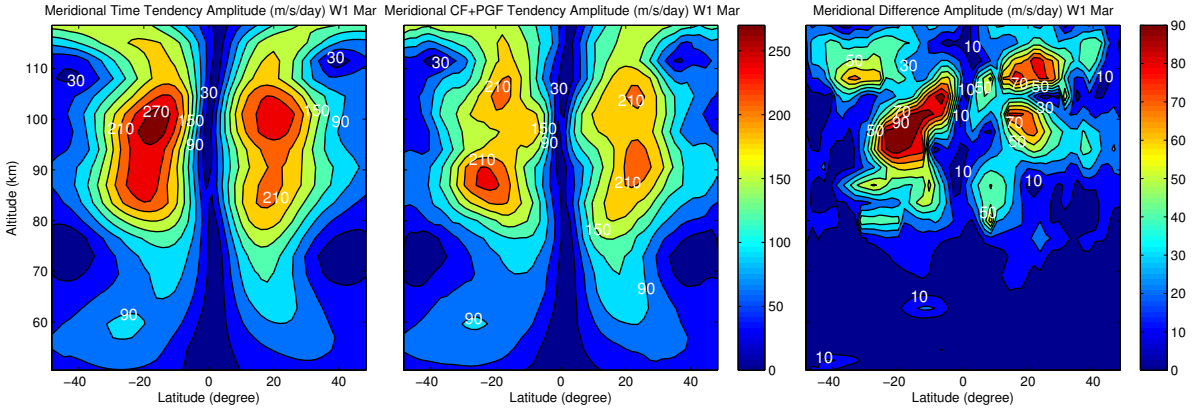

Figure 5.6: Same as Figure 5.5 except for the meridional wind.

Comparison of the left and middle panels in Figures 5.5 and 5.6 illustrates that the calculation based on classical terms provides a reasonable first-order prediction of the structure and magnitude of DW1. The discrepancy is about 2-3 times smaller. In the zonal wind, the amplitude of the time tendency in the presence of only CF and PGF for DW1 is up to 200 $\mathrm{m\,s^{-1}\,day^{-1}}$ and the difference caused by non-classical terms is up to 90 $\mathrm{m\,s^{-1}\,day^{-1}}$. A significant difference between the calculation based on only CF+PGF and the calculation using the full primitive equations (5.1-5.2) is found at latitudes 20-40°N, where the amplitude of DW1 becomes smaller after including the non-classical terms. As will be shown later, the

decrease of the DW1 amplitude is caused by GW drag.

Calculated as $|\partial u'/\partial t| = \omega|\hat{u}|$ and $|\partial v'/\partial t| = \omega|\hat{v}|$, it is seen that the amplitude of the time tendency is proportional to the tidal amplitude. Figure 5.6 shows the amplitude of the time tendency in the meridional tidal wind is larger than the zonal wind component by a factor of $\sim$1.5, consistent with a larger meridional amplitude of DW1 (Figure 5.3). In general, the time tendency $\partial v/\partial t$ due to CF and PGF is smaller than the total tendency, implying that the non-classical terms tend to enhance DW1. Another notable difference is the change of the vertical structure after non-classical forcings are introduced. Based on the prediction due to CF and PGF, the double amplitude peaks are located near 90 and 105 km, which are replaced by a single peak around 100 km when the non-classical terms are included.

As described in equations (5.1) and (5.2), the non-classical terms that may contribute to the discrepancies from the prediction of classical tidal theory are advection, curvature, GW forcing and dissipation. In order to prove that advection and GW forcing are the two most dominant terms in the momentum budget of DW1, we calculate each term and project it onto the DW1 component. GW forcing is obtained from the model output directly. The advection terms are calculated as:

$$F_{advect,x} = -\vec{V} \cdot \nabla u = -(\frac{u}{a\cos\phi}\frac{\partial u}{\partial \lambda} + \frac{v}{a}\frac{\partial u}{\partial \phi} + w\frac{\partial u}{\partial z}) \tag{5.3}$$

$$F_{advect,y} = -\vec{V} \cdot \nabla v = -(\frac{u}{a\cos\phi}\frac{\partial v}{\partial \lambda} + \frac{v}{a}\frac{\partial v}{\partial \phi} + w\frac{\partial v}{\partial z}) \tag{5.4}$$

After writing the mean winds as $u = \bar{u} + u'$ and $v = \bar{v} + v'$, we divide the advection terms into linear and nonlinear advection. Linear advection involves the advection of the mean winds by perturbative winds as well as the advection of perturbative winds by the mean winds. Nonlinear advection involves the advection of perturbative winds themselves.

The linear advection terms are as follows:

$$F_{Linadvect,x} = -\frac{\bar{u}}{a\cos\phi}\frac{\partial u'}{\partial \lambda} - \frac{\bar{v}}{a}\frac{\partial u'}{\partial \phi} - \frac{v'}{a}\frac{\partial \bar{u}}{\partial \phi} - \bar{w}\frac{\partial u'}{\partial z} - w'\frac{\partial \bar{u}}{\partial z} \tag{5.5}$$

$$F_{Linadvect,y} = -\frac{\bar{u}}{a\cos\phi}\frac{\partial v'}{\partial \lambda} - \frac{\bar{v}}{a}\frac{\partial v'}{\partial \phi} - \frac{v'}{a}\frac{\partial \bar{v}}{\partial \phi} - \bar{w}\frac{\partial v'}{\partial z} - w'\frac{\partial \bar{v}}{\partial z} \tag{5.6}$$

where the mean winds $(\bar{u}, \bar{v})$ are computed by averaging the wind fields in time and longitude.

When the time tendency of linear advection is calculated, for the terms having derivatives with respect to time and longitude (e.g., $\partial u'/\partial t$ and $\partial u'/\partial \lambda$), the DW1 component with an explicit form of $u' = \hat{u} \cdot e^{i(\omega t - s\lambda)}$ is taken into account, where $\omega = 2\pi/24$hr and $s = -1$ are the frequency and zonal wavenumber of DW1, respectively. By substituting this form into equations (5.5-5.6), we have:

$$F_{Linadvect,x} = -\frac{is\bar{u}\hat{u}}{a\cos\phi} - \frac{\bar{v}}{a}\frac{\partial \hat{u}}{\partial \phi} - \frac{\hat{v}}{a}\frac{\partial \bar{u}}{\partial \phi} - \bar{w}\frac{\partial \hat{u}}{\partial z} - \hat{w}\frac{\partial \bar{u}}{\partial z} \tag{5.7}$$

$$F_{Linadvect,y} = -\frac{is\bar{u}\hat{v}}{a\cos\phi} - \frac{\bar{v}}{a}\frac{\partial \hat{v}}{\partial \phi} - \frac{\hat{v}}{a}\frac{\partial \bar{v}}{\partial \phi} - \bar{w}\frac{\partial \hat{v}}{\partial z} - \hat{w}\frac{\partial \bar{v}}{\partial z} \tag{5.8}$$

For other terms such as GW forcing, a 2-D Fourier transform with respect to time and longitude is applied at each altitude and latitude grid point to obtain the projection onto the DW1 component. After the linear advection terms for DW1 are derived, the nonlinear advection terms for DW1 are calculated by subtracting these linear advection terms from total advection of DW1. The total advection is calculated based on advection by the total wind fields. Just as for GW forcing, it is projected onto the DW1 component by applying the 2-D Fourier transform. The 2-D Fourier transform method and the method of using the explicit form of DW1 may result in some differences in the derived time tendencies since taking into account the finite-length data may cause some spectrum leakage and lead to smaller amplitudes obtained by the Fourier transform. But the differences are not significant

for the large horizontal scales and it will not change the global structure of time tendencies [*McLandress*, 2002a].

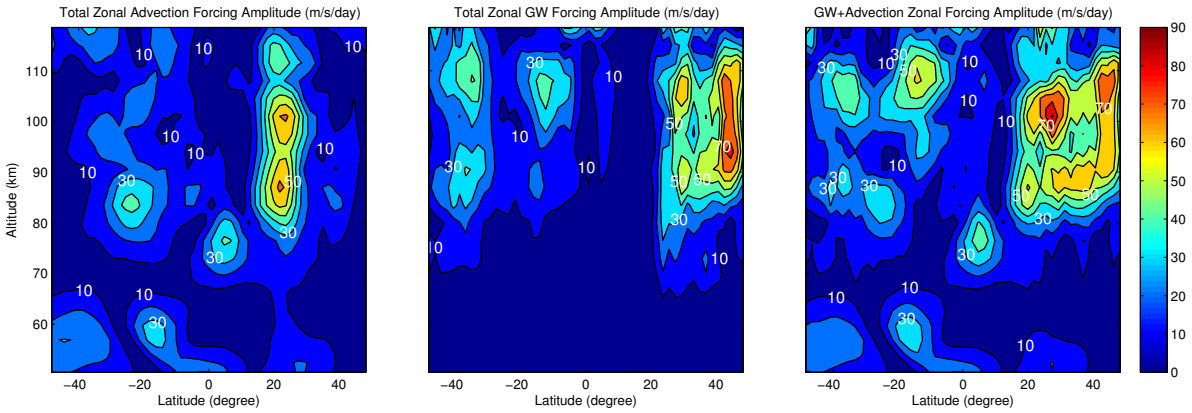

Figure 5.7: Time tendency amplitudes in the DW1 component of total advection forcing (left), total GW forcing (middle) and the sum of them (right) in the zonal wind.

Figure 5.7 shows the time tendencies of DW1 from the total advection (left), GW forcing (middle) and the sum of these two terms (right) in the zonal direction. It is obvious that the effects of the total advection and GW forcing are comparable. GW forcing is more important above 80 km and at latitudes >20°N. Below 80 km, advection terms are dominant at the equator between 70 and 80 km and in the region near 20°S and 60 km. The zonal forcing due to advection terms and GW forcing is stronger in the NH than in the SH. According to Figure 5.4, frontal systems mainly contribute to the GW forcing in the NH while both frontal systems and convection contribute in the SH. As mentioned earlier in section 5.1, the distribution of convection-induced GW forcing is affected by the location of deep convective systems and thus changes with season.

The right panels in Figures 5.5 and 5.7 are similar in both the distribution and magnitude of time tendencies. It indicates that advection terms and GW forcing are two dominant factors to account for the momentum budget of DW1 besides classical terms (i.e. CF and PGF). This is different from the conclusion in *McLandress* [2002a], which states that the direct effect of parameterized GWs is substantially weaker than wave-wave and wave-mean flow interactions. In the CMAM [*McLandress*, 1998, 2002a], the effects of nonorographic

GWs are parameterized based on the Hines' Doppler Spread Parameterization (DSP) [*Hines*, 1997a,b]. Instead, Lindzen's GW scheme is used in the WACCM [*Lindzen*, 1981] and it incorporates a physically based GW source parameterization [*Richter et al.*, 2010]. A GW parameterization is an important factor that leads to different results.

The similar structures in the right panels of Figures 5.6 and 5.8 show the same dominances of advection and GW forcing in the meridional wind. However, in contrast to the zonal wind, GW forcing is less important than the advection terms with the magnitude about 2-3 times smaller. Especially in the equatorial region, the contribution by GW forcing is very weak. Compared to the study by *McLandress* [2002a], the effect of GW forcing is strong and the effect of advection is weak in the WACCM. As discussed by *Richter et al.* [2010], a low frontogenesis threshold is used in order to produce enough GWs to reverse the stratospheric jets and cool the mesopause to the observed temperature. It is likely there is an overestimation of GW generation by fronts, which in turn affects DW1. Since the advection terms involve wave perturbations, the underestimation of the tidal amplitudes is a possible explanation for the underestimation of the advection effect in the WACCM.

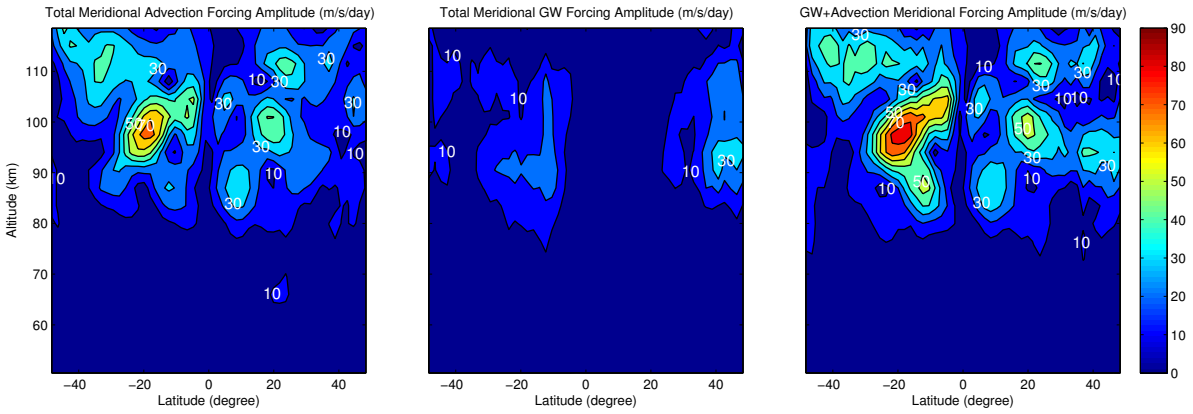

Figure 5.8: Same as Figure 5.7 except for the meridional wind.

In order to further examine which advection term is more important, we show the amplitudes of time tendencies from linear and nonlinear advection separately in Figure 5.9. In the zonal wind, linear advection is about 2-3 times stronger than nonlinear advection and it is the opposite in the meridional wind. If Figure 5.9 is compared with the left panels in

Figures 5.7 and 5.8, it is clearly seen that linear (nonlinear) advection is dominant in the zonal (meridional) wind. Linear advection is essentially a product of mean wind and wave perturbation and nonlinear advection is a product of wave perturbations. Because the zonal mean zonal wind is much stronger than the zonal mean meridional wind, linear advection is stronger in the zonal wind direction. The meridional nonlinear advection is larger because the amplitude of DW1 is stronger in the meridional wind.

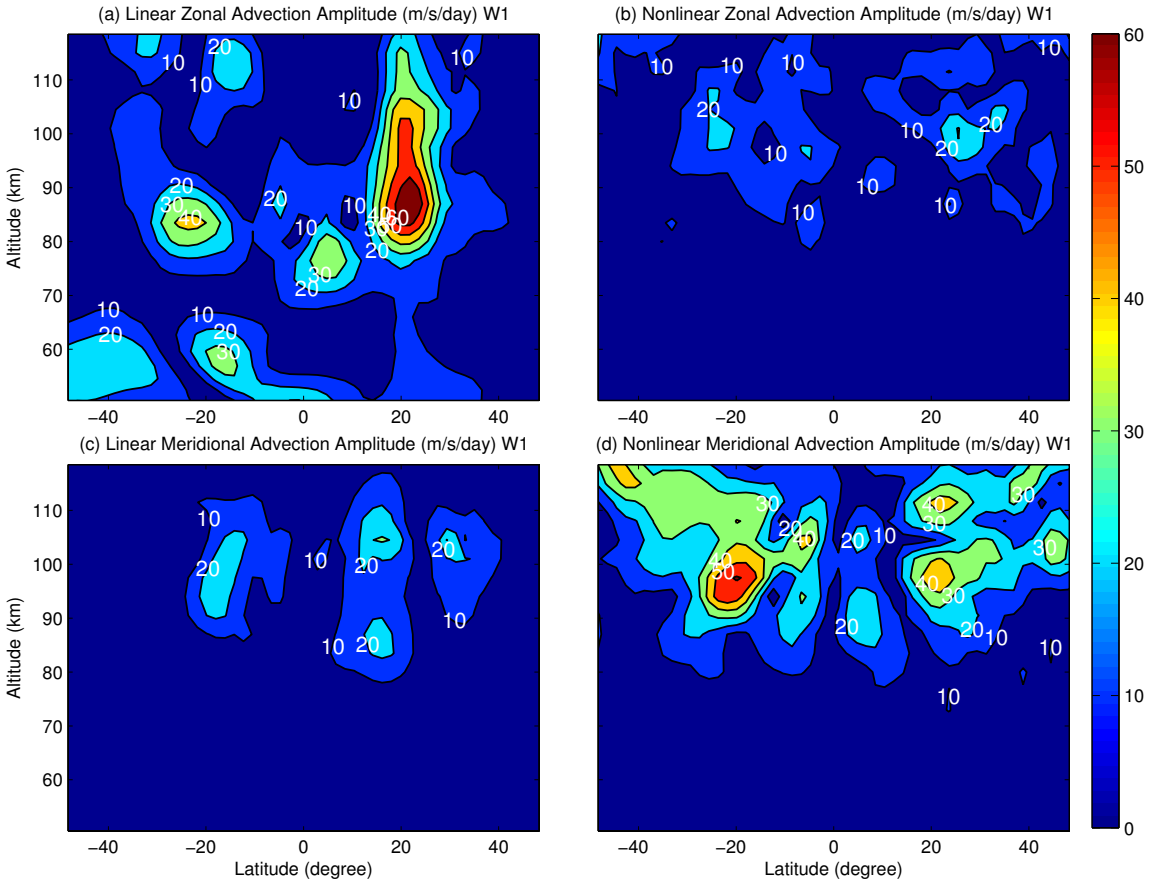

Figure 5.9: Time tendency amplitudes in the DW1 component of linear and nonlinear advection.

5.3 Effects of GW Forcing and Advection

In section 5.2, the relative importance of the GW forcing and the linear and nonlinear advection in the momentum budget of DW1 is investigated. However, it does not provide

the phase relationship between these forcings and DW1. Therefore, it is not clear whether the forcing changes the tidal amplitude or the phase. In order to study the effects on the DW1 amplitude and phase, we introduce a coefficient of the Equivalent Rayleigh Friction (ERF) [*Forbes et al.*, 1991; *McLandress*, 2002a], which is defined as:

$$\gamma_u = -\frac{\hat{F}_u}{\hat{u}} \tag{5.9}$$

where $\hat{F}_u$ and $\hat{u}$ are the complex amplitudes of forcing and DW1. If we write $\hat{u} = a(t)e^{-i\omega\psi(t)}$, where $a(t)$ and $\psi(t)$ represent the amplitude and phase of DW1, $\hat{F}_u$ can be calculated in a form of time tendency as:

$$\hat{F}_u = \frac{\partial \hat{u}}{\partial t} = \frac{\partial a(t)}{\partial t} e^{-i\omega\psi(t)} - i\omega \frac{\partial \psi(t)}{\partial t} \cdot a(t) e^{-i\omega\psi(t)} \tag{5.10}$$

and equation (5.9) becomes:

$$\gamma_u = -\frac{\partial a(t)/\partial t}{a(t)} + i\omega \frac{\partial \psi(t)}{\partial t} \tag{5.11}$$

Thus, the real part of the ERF represents the amplitude change and if $Re(\gamma_u) > 0$ ($Re(\gamma_u) < 0$), it will decrease (increase) the amplitude with time. The imaginary part of the ERF corresponds to the phase change. $Im(\gamma_u) < 0$ corresponds to a phase advance and a local shortening of the vertical wavelength for the tide with upward energy propagation. Conversely, the phase is delayed and the vertical wavelength is increased locally when $Im(\gamma_u) > 0$.

Figure 5.10 shows the real part of the ERF of GW forcing. The regions with tidal amplitudes too small are excluded because the ERF is unreasonably large after dividing by a small complex amplitude of DW1. Above 70 km, $Re(\gamma_u)$ is mostly positive which means that GW drag damps DW1 with few exceptions. The largest value of $\sim 8 \times 10^{-5}$ s^{-1} is found around latitudes 50-60°, where the GW drag is large and the tidal amplitude is small. For the

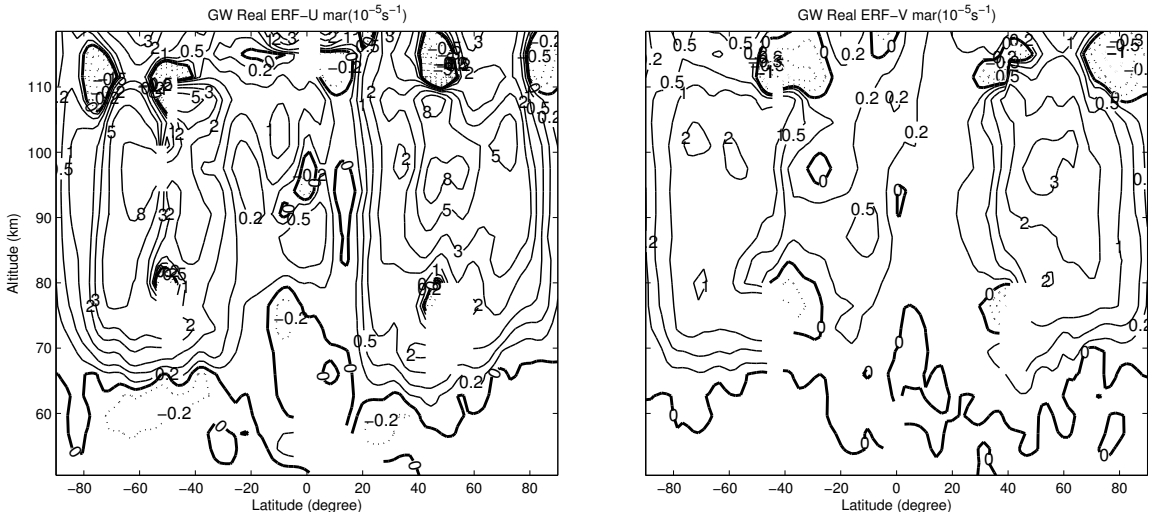

Figure 5.10: Real part of the ERF of GW forcing based on the WACCM. Solid and dotted contours are for positive and negative values, respectively. Zero-value contours are highlighted by the thick solid lines. Contour intervals: ± 0.2, ± 0.5, ± 1, ± 2, ± 3, ± 5, ± 8.

meridional wind, the largest value is $3 \times 10^{-5} s^{-1}$, about ~ 2.5 times smaller than the zonal wind. In the GSWM, the GW drag effect is represented by the effective Rayleigh friction [*Hagan et al.*, 1995, 1999]. It has a seasonal variation with largest values at solstices and smallest at equinoxes (one order of magnitude smaller than solstices). The seasonal variation of the ERF in the WACCM, however, is not as significant as the GSWM (see Figures C.2, C.4, C.6). Figure 5.11 shows the effective Rayleigh friction of the GSWM in January, when it reaches a maximum value through a year. The latitudinal and vertical structure of the effective Rayleigh friction in the GSWM is similar to the ERF in the WACCM while the magnitude is about one order smaller. It is suggested the GW damping effect is larger in the WACCM and may result in the underestimation of the DW1 amplitude.

As shown by Figure 5.12, $Im(\gamma_u)$ and $Im(\gamma_v)$ are negative in the tropical and subtropical regions and become positive towards higher latitudes. Same as the real part, the largest values are found at latitudes where GW forcing is strong and the tide is weak. In these regions, GWs are mainly excited by the frontal systems, indicating that weather systems in the lower atmosphere have a notable impact on DW1 in the MLT region through GW forcing. The effect of GW drag on the phase change of DW1 strongly depends on latitude.

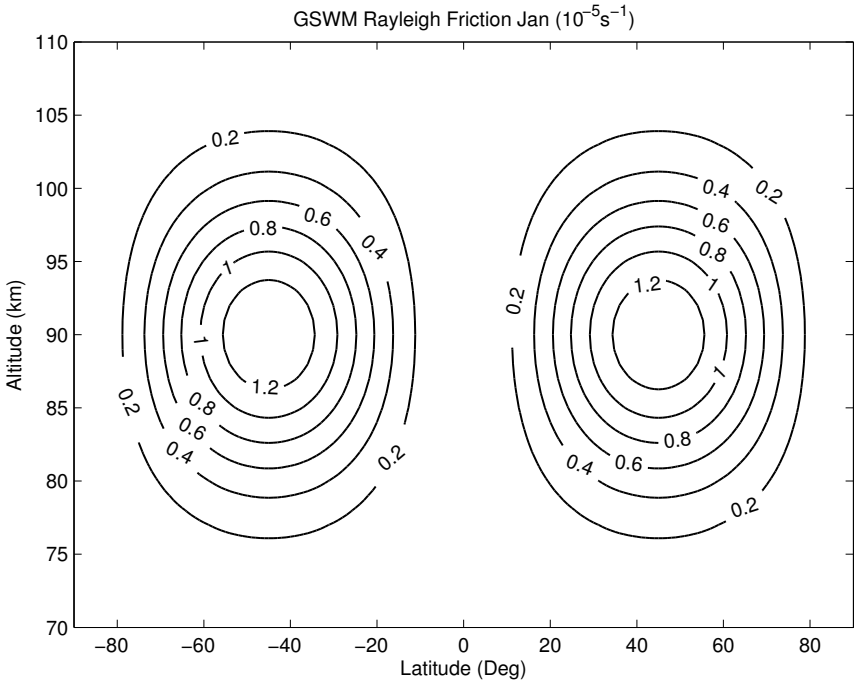

Figure 5.11: Effective Rayleigh friction in the GSWM in January.

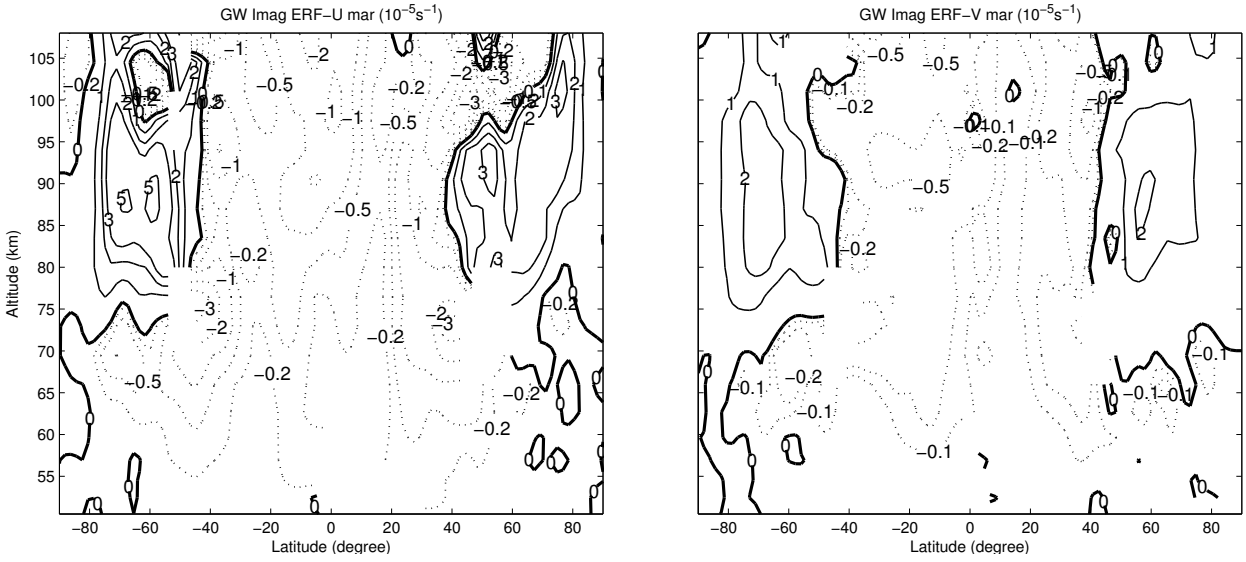

Figure 5.12: Same as Figure 5.10 except for the imaginary part.

It tends to advance it at low latitudes and delay it at middle and high latitudes. In general, the real part of the ERF is larger than the imaginary part, which implies GW drag changes the amplitude more significantly than the phase.

In order to focus on the area where DW1 is relatively stronger, we confine our study within the latitude range of $\pm 50°$. Figures 5.13, 5.14 and 5.15 show both the real and imaginary parts of the ERFs by GW drag and linear and nonlinear advection, respectively. Figure 5.16 displays the total effect by adding them together.

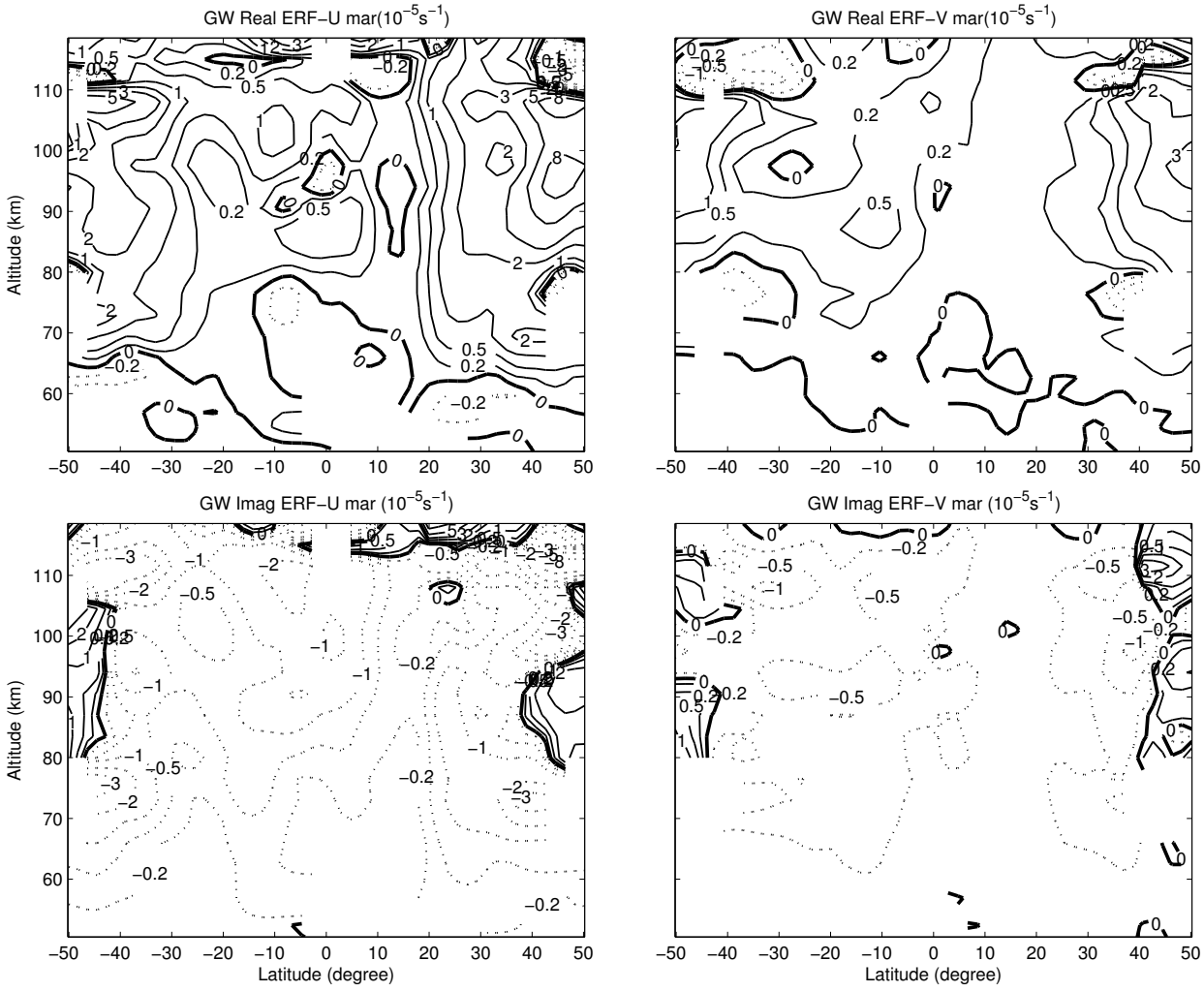

Figure 5.13: Real (upper panels) and imaginary (bottom panels) parts of the ERF for GW forcing in the latitude range between $\pm 50°$. Left and right panels are for the zonal and meridional winds, respectively.

Unlike GW drag which has positive $Re(\gamma_u)$ and negative $Im(\gamma_u)$ in the region of interest,

linear advection and nonlinear advection have finer vertical and latitudinal structures. For instance, $Re(\gamma_u)$ of linear advection resembles a wave structure near the equator. It is positive near 70 km and negative near 90 km. It becomes positive again near 100 km (top left panel in Figure 5.14). Based on equations (5.7) and (5.9), a scale analysis is performed for each term in linear advection. It reveals that the largest term contributing to $Re(\gamma_u)$ is $-\hat{w} \cdot \partial\bar{u}/\partial z$, the vertical advection of zonal mean wind by DW1. The wave-like structure of $Re(\gamma_u)$ is associated with that of the vertical shear of the zonal mean zonal wind ($\partial\bar{u}/\partial z$). It is expected that $Re(\gamma_u)$ has the largest value at the equator, where the amplitude of the vertical wind and the vertical shear of the zonal mean zonal wind are both the strongest.

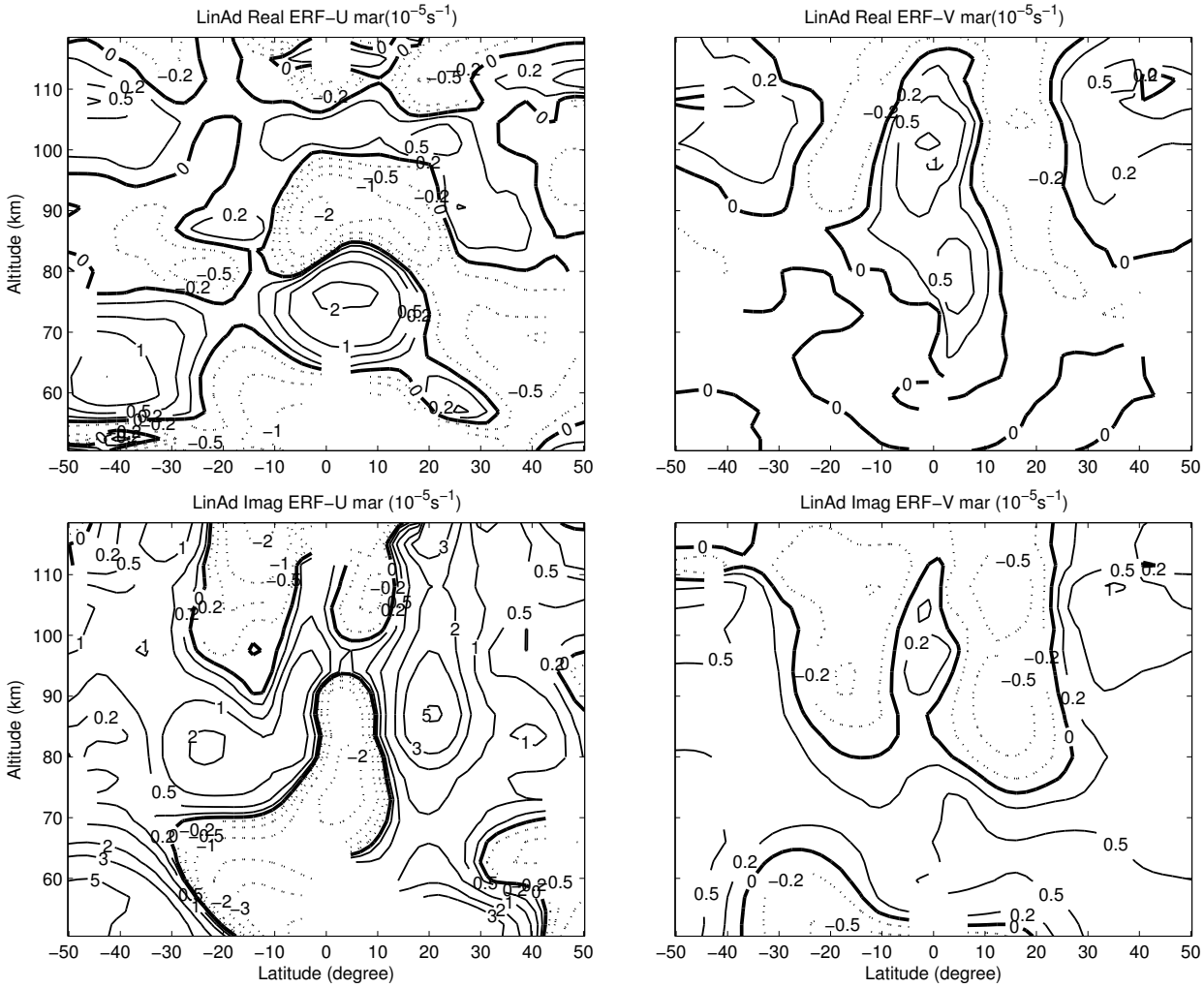

Figure 5.14: Same as Figures 5.13 except for linear advection.

If we compare the bottom left panels in Figures 5.13, 5.14 and 5.15, it can be seen $Im(\gamma_u)$ of linear advection is one order of magnitude larger than that of either GW drag or nonlinear advection. So the linear advection term makes a dominant contribution to the phase change of DW1. For the $Im(\gamma_u)$ of linear advection, a negative area corresponding to an advance of tidal phase is found in the equatorial region below 90 km. It becomes narrower as altitude increases from 50 to 90 km. A maximum value of 5×10^{-5} s^{-1} is located

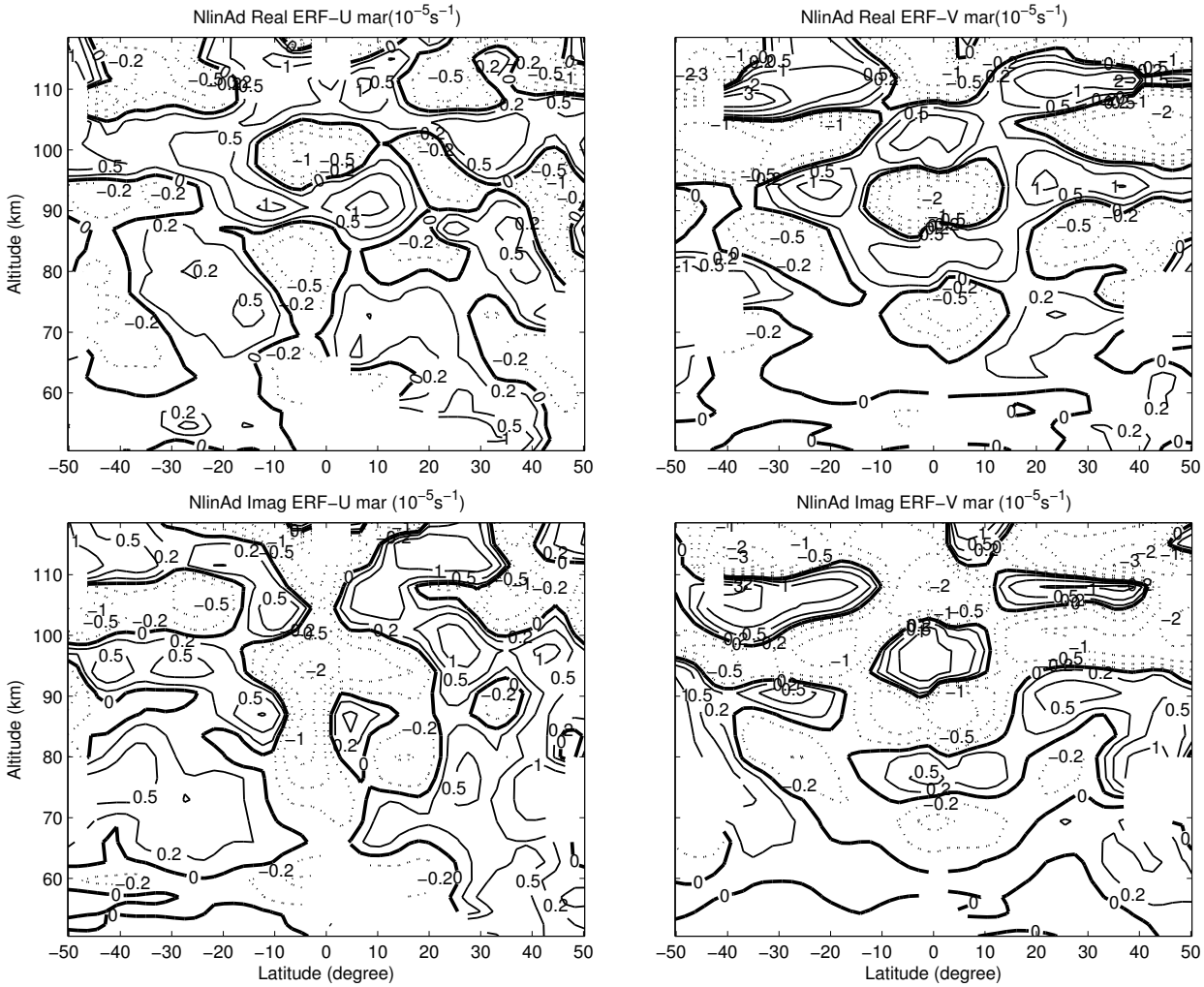

Figure 5.15: Same as Figures 5.13 except for nonlinear advection.

at ∼20°N, corresponding to a delay of the tidal phase by linear advection. As the zonal and meridional tidal winds are roughly 90° out of phase, the term $-(\hat{v}/a) \cdot \partial\bar{u}/\partial\phi$ in equation (5.7) contributes to the imaginary part of the ERF in the zonal wind. This is the largest

factor that determines $Im(\gamma_u)$. Since the latitudinal shear of the zonal mean zonal wind is stronger than that of the mean meridional wind, $Im(\gamma_u)$ is much larger than $Im(\gamma_v)$. Due to the importance of linear advection, the phase change of DW1 is very sensitive to the latitudinal structure of the zonal mean zonal wind, which is similar to the study in *McLandress* [2002b].

By comparing the total $Re(\gamma_u)$ with $Re(\gamma_u)$ of GW forcing and advection, it can be seen that linear advection is important at the equator and GW drag is important at latitudes higher than 20°. Near 20°N, GW forcing is of the order of 10^{-5} s^{-1} in $Re(\gamma_u)$. For a tidal amplitude of 30 $m\,s^{-1}$, the time tendency from GW forcing is about -26 $m\,s^{-1}\,day^{-1}$. It means the amplitude of DW1 would decrease to 4 $m\,s^{-1}$ during one day without heating and other forcing, indicating the GW damping is quite significant. Compared with linear advection and GW drag, nonlinear advection is negligible in modulating the amplitude of DW1 in the zonal wind component.

In terms of the phase modulation, linear advection makes a major contribution since it largely determines the total $Im(\gamma_u)$. GW drag and nonlinear advection also play a role in decreasing or even offsetting the phase delay caused by linear advection. In some regions, phase advances are due to GW drag and nonlinear advection. For example, in the region between latitudes 0° and 10°S and altitudes from 70 to 90 km, $Im(\gamma_u)$ determined by linear advection is positive while the total $Im(\gamma_u)$ after including the effects from GW drag and nonlinear advection is negative. The changing sign of $Im(\gamma_u)$ from positive (delaying the tidal phase by linear advection) to negative (advancing the phase by GW drag and nonlinear advection) can be also found at latitudes 20°-50°S and altitudes 100-110 km.

Opposite to the zonal wind, nonlinear advection is important for the meridional wind. By comparing both $Re(\gamma_v)$ and $Im(\gamma_v)$ in Figure 5.16 with Figures 5.13, 5.14 and 5.15, nonlinear advection largely determines the momentum budget of the meridional wind, besides classical terms. This is due to the fact that the zonal mean meridional wind is weak which means that linear advection is also weak. In addition, the GW drag effect on the meridional

wind is not as strong as that on the zonal wind. Since nonlinear advection involves the products of wave perturbations, after being divided by the tidal wave as in the definition of the ERF, $Re(\gamma_v)$ and $Im(\gamma_v)$ have wave structures with the same vertical scales as DW1. A scale analysis shows that for nonlinear advection, the meridional and vertical advection of the meridional wind perturbations $(-(v'/a) \cdot \partial v'/\partial \phi, -w' \cdot \partial v'/\partial z)$ are the most important terms and as latitude increases to 40°, the zonal advection increases and becomes comparable (not shown).

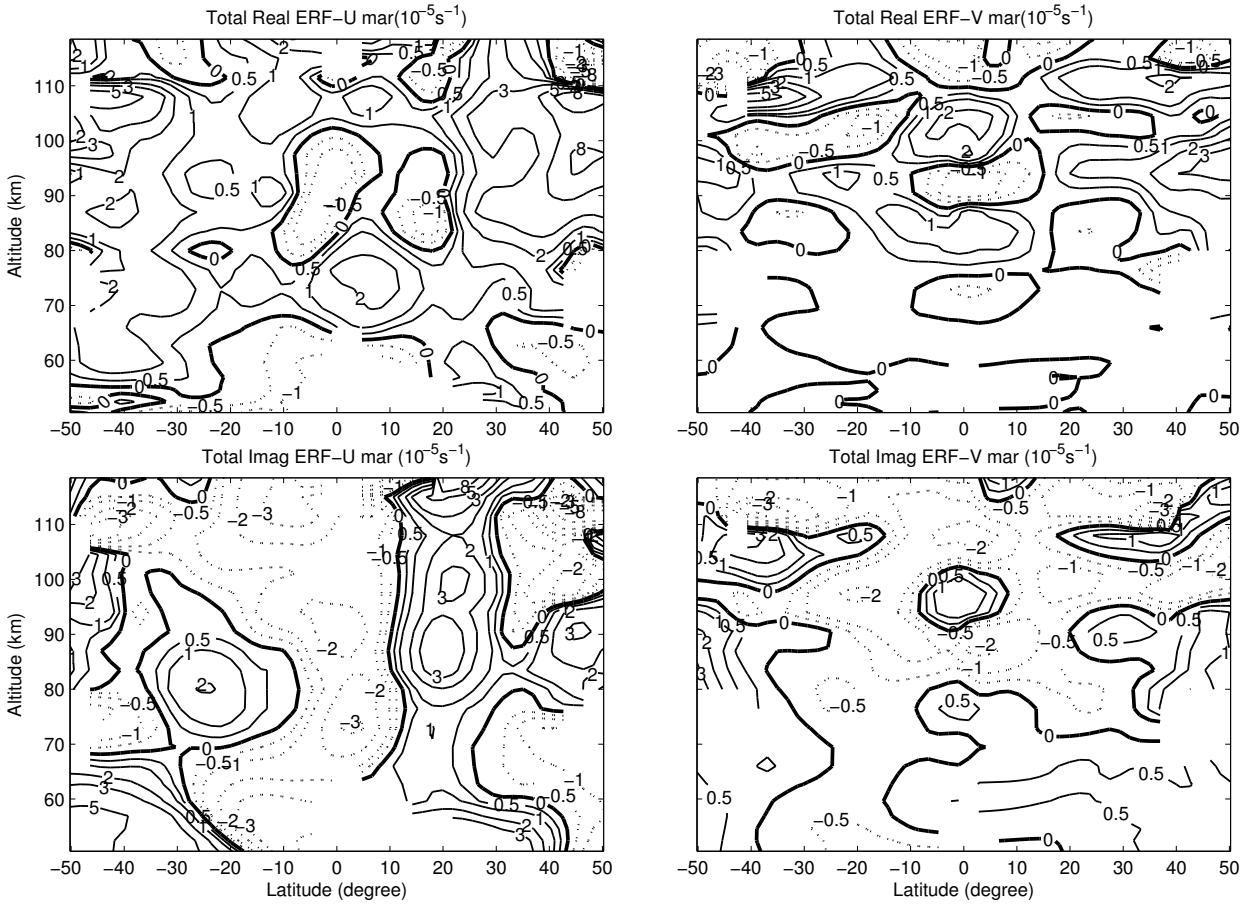

Figure 5.16: Same as Figures 5.13 except for total ERF (GW forcing + linear and nonlinear advection).

5.4 Seasonal Variations of GW Forcing and Tidal Heating

Based on the momentum budget analysis, GW forcing is an important factor contributing to the amplitude change of DW1, especially in the zonal wind. The seasonal variations of the GW forcing onto the zonal mean wind and onto DW1 are shown in Figures 5.17 and 5.18, respectively. The GW source is convection for both figures. Strong GW forcing

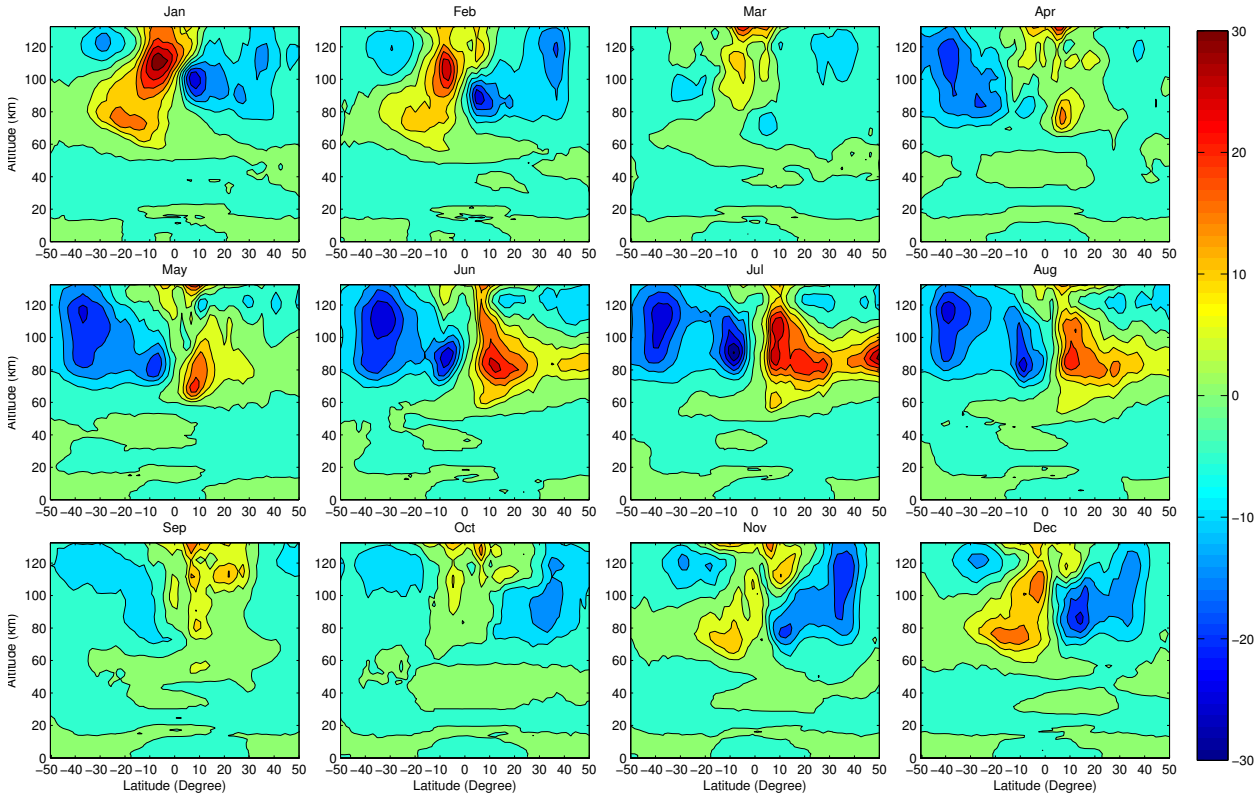

Figure 5.17: Seasonal Variation of the GW forcing onto the zonal mean winds based on the WACCM4. GW forcing is caused by convection.

occurs above 60 km. In the summer (winter) hemisphere, the effect of GW forcing is to drive the mean wind toward the east (west), which is related to the direction that GWs deposit their momentum when they break in the MLT region. At solstices, GWs generated in the lower atmosphere are filtered by the strong stratospheric jets and their propagating directions are preferentially eastward (westward) in the summer (winter) hemisphere. The season-dependent propagating directions of GWs were observed based on the Airglow imager

[*Tang et al.*, 2005].

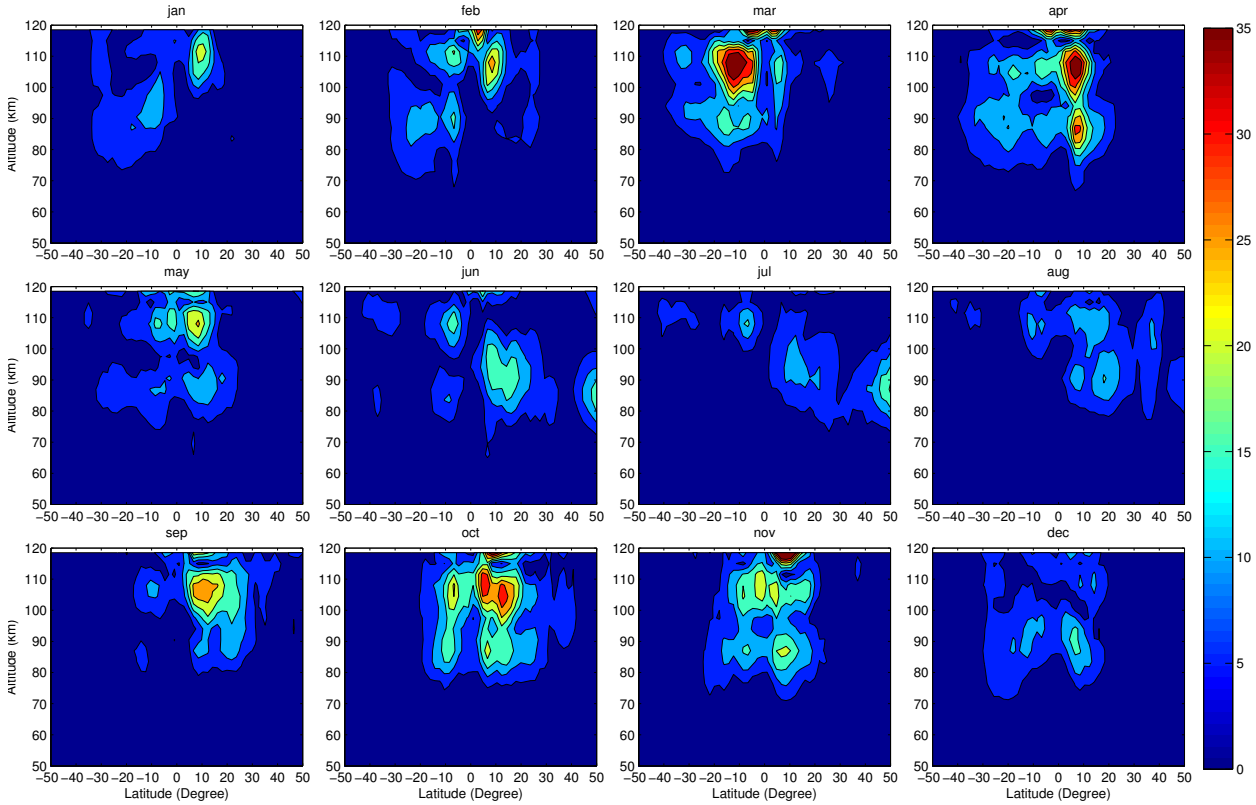

Figure 5.18: Same as Figure 5.17 except for the GW forcing onto DW1.

Figures 5.19 and 5.20 are the same as Figures 5.17 and 5.18 except that the GW source is frontogenesis. A stronger GW forcing onto the zonal mean wind is found at solstice, when the wind filtering effect in the stratosphere is also strong. This strong GW drag to the opposite direction onto the mean wind is responsible to close and reverse the stratospheric jet at solstice. At equinox, GW forcing towards the mean wind is relatively weaker and it is the weakest in March and September.

However, the seasonal variation of GW forcing onto DW1 is very different from the mean wind. For the convection-generated GWs, we observe stronger GW forcings in March, April, September and October while the front-generated GW forcings are stronger in February, March, September and October. Different from the GW forcing onto the mean wind which peaks at solstice, GW forcing onto DW1 peaks at equinox. It suggests that GW forcing

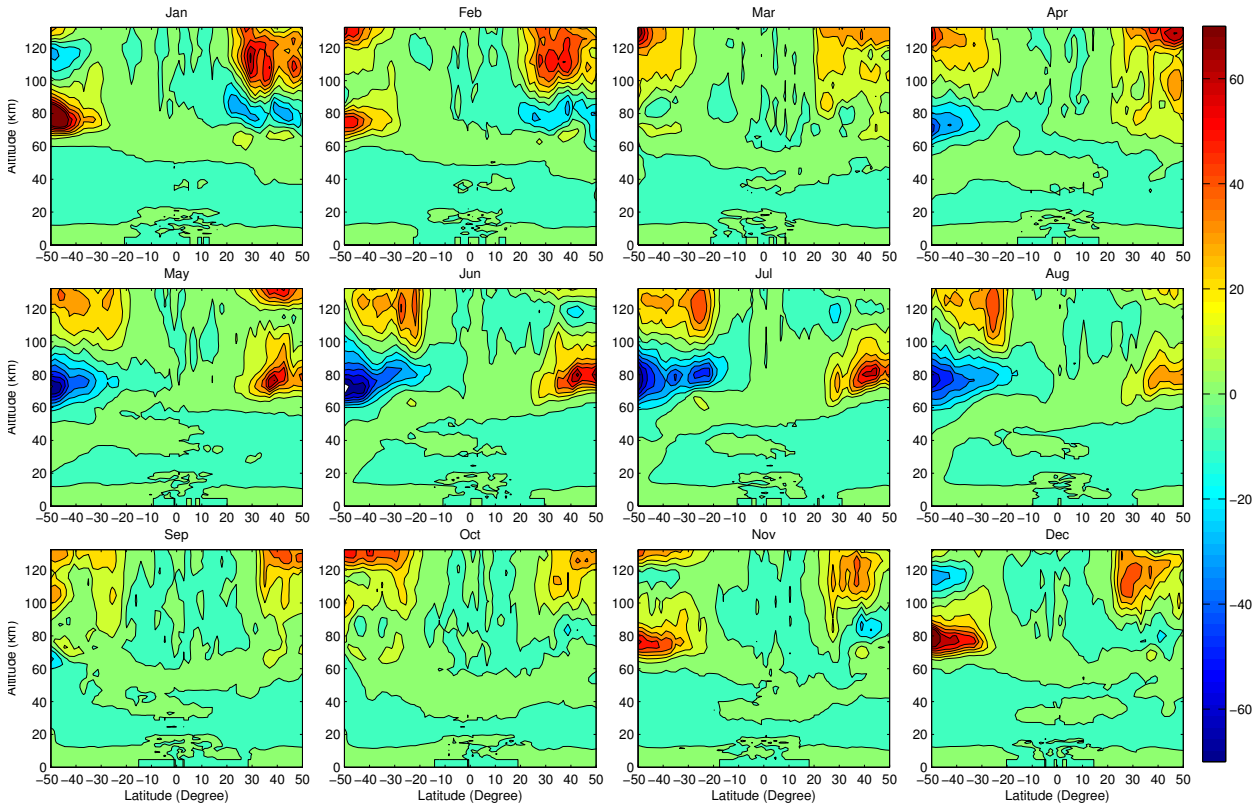

Figure 5.19: Seasonal variation of the GW forcing onto mean wind based on the WACCM4. GW forcing is caused by frontogenesis.

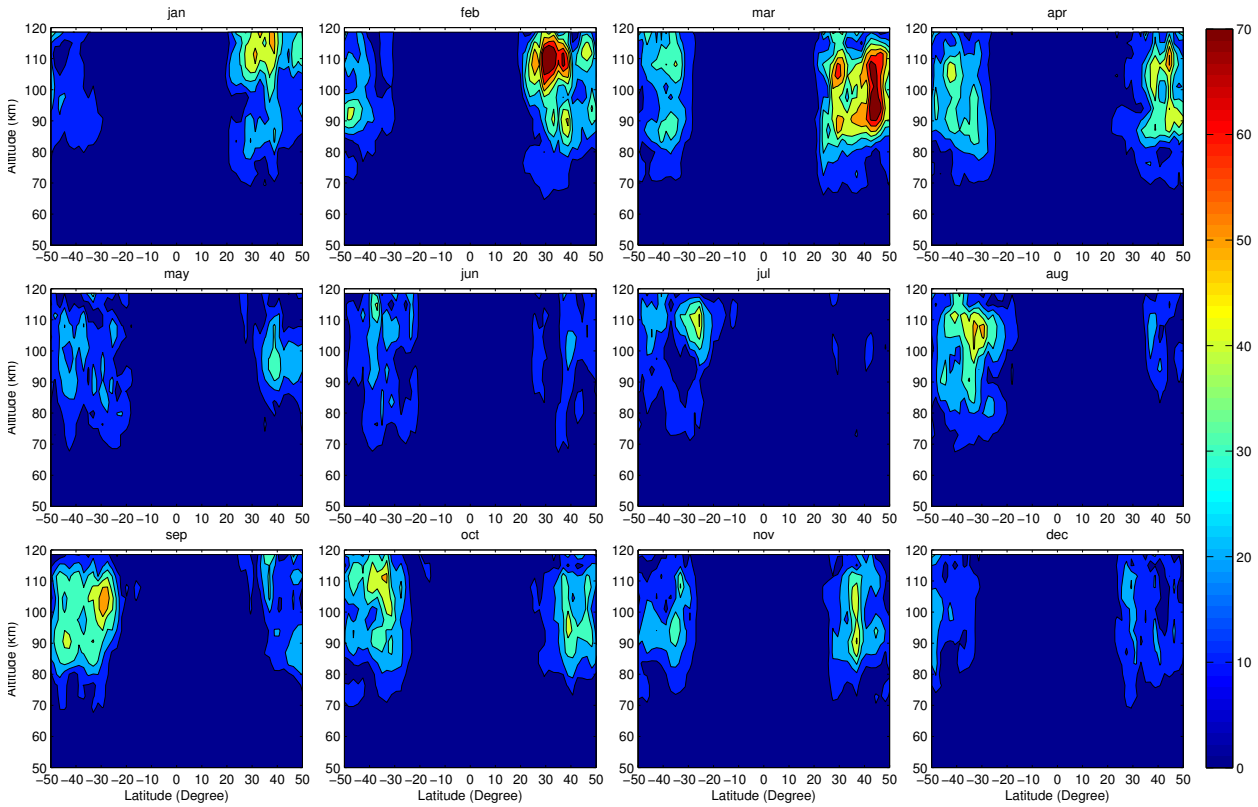

Figure 5.20: Same as Figure 5.19 except for the GW forcing onto DW1.

is not the mechanism causing the seasonal variation of the amplitude because GWs damp DW1. If GW effect is the mechanism, a larger damping at equinox would result in a weaker tide. But as observed by the meteor radar, the diurnal tide is also stronger at equinox.

After ruling out the GW forcing as the potential mechanism, we investigate the seasonal variation of the tidal heating based on the WACCM. Since the most important heating terms are IR heating by water vapor and UV radiative heating by ozone for DW1, we decompose them into two most dominant Hough modes of DW1, (1,1) and (1,2) in the MLT region. Figure 5.21 shows the seasonal variation of the IR solar heating absorbed by water vapor from the surface to 16 km. In the troposphere, the strongest heating rates in the (1,1) mode are found in March and October and peak at 5 km, while the strongest heating rates in the (1,2) mode occur in February and July. As discussed in section 1.2.3, the different seasonal variations of these two modes are due to the different global distribution of solar heating. It is more symmetric and projects more efficiently onto the first symmetric (1,1) Hough mode at equinoxes, while at solstices, the summer hemisphere receives more solar heating and a stronger antisymmetric Hough mode (1,2) is generated.

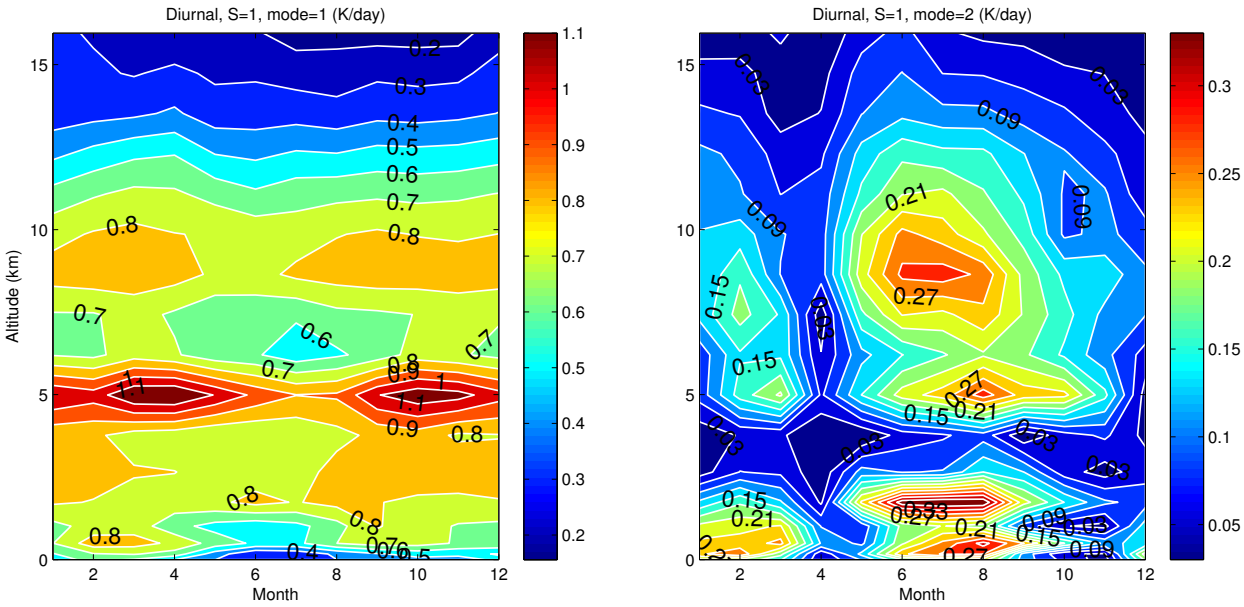

Figure 5.21: Seasonal variation of the tidal heating by water vapor. Left and right panels are projections onto the (1,1) and (1,2) Hough modes, respectively. The unit is K day^{-1}.

.

Figure 5.22 is the same as Figure 5.21 except for the ozone absorption of UV solar radiation. The maximum ozone heating locates around 48 km and the thickness of the heating layer is around 30 km. The altitude of the maximum ozone heating layer is different from the classical ozone layer, which is around 25 km and determined by the ozone concentration. A large amount of UV solar radiation is already absorbed by the ozone in the upper stratosphere before it reaches the ozone layer at 25 km. Different from the water vapor heating in the lower troposphere where the projection on the (1,1) mode is about 3 times as large as that in the (1,2) mode, for the ozone heating, the (1,1) mode is much stronger than the (1,2) mode (about 30 times). For both modes, the strongest heating occurs at solstice. In terms of the month when the maximum heating is reached, the (1,2) mode leads the (1,1) mode for about 1 month.

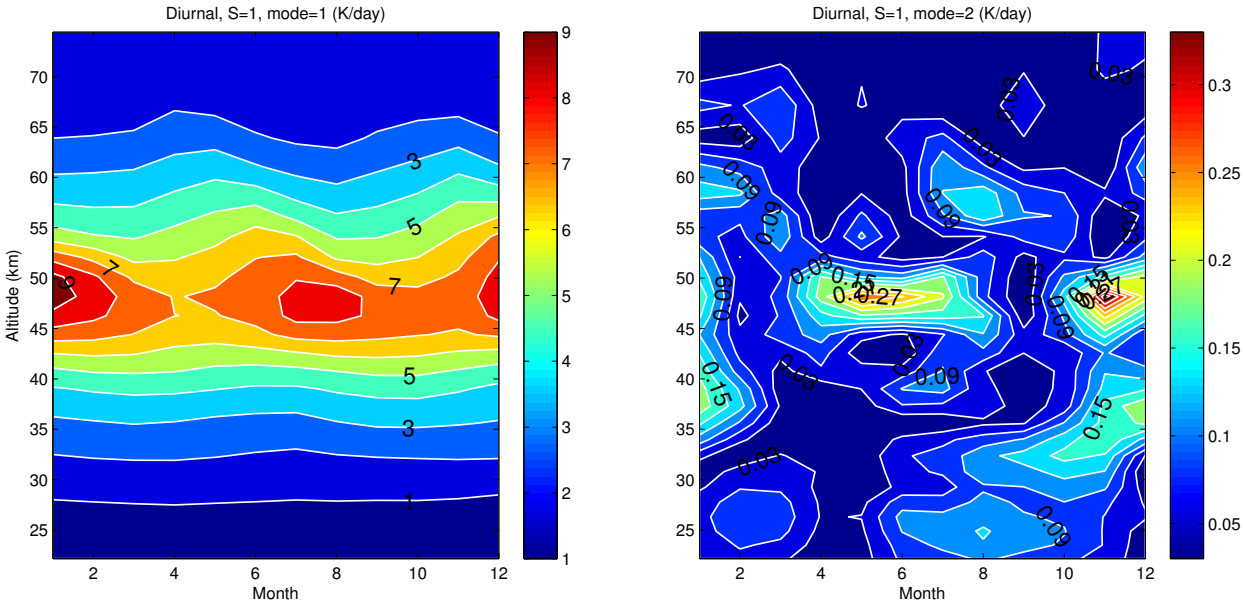

Figure 5.22: Same as Figure 5.21 except for ozone heating.

The seasonal variation of the monthly mean tidal amplitude in temperature is shown in Figure 5.23. Above 60 km, the maximum amplitudes are found in March and September for the (1,1) Hough mode, January and September for the (1,2) mode. The magnitude of the (1,1) mode is about 4 times larger than the (1,2) mode, which again indicates the

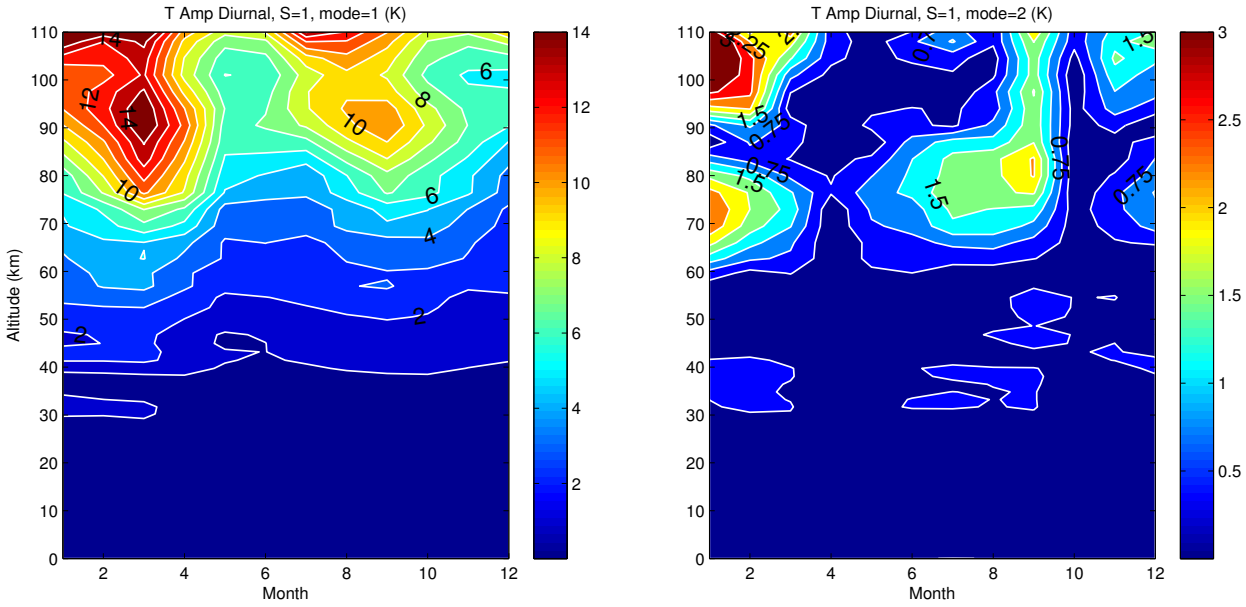

Figure 5.23: Monthly mean temperature for the (1,1) Hough mode (left) and (1,2) Hough mode (right), respectively.

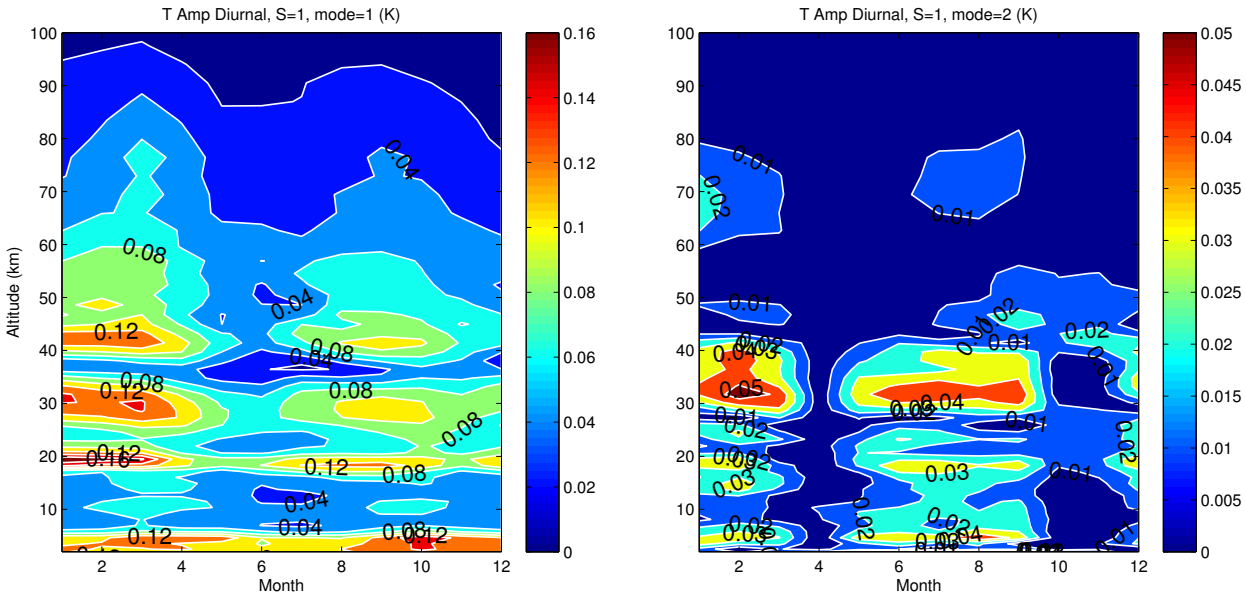

Figure 5.24: Same as Figure 5.23 except the temperature is scaled by a factor of $e^{-z/2H}$.

dominance of the (1,1) mode in the MLT region. In order to consider the effect of the exponential decrease of density, the temperature is scaled by a factor of $e^{-z/2H}$ (H = 7.5 km) and shown in Figure 5.24. In the tropospheric heating region by water vapor ($\sim$5 km), the maximum amplitudes of the (1,1) mode are in March and October, the same as the time when the maximum heating occurs (Figure 5.21). The seasonal variation of the (1,2) mode amplitude is also consistent with the heating in the troposphere, with maxima found in February and July-August. It implies the radiative heating by water vapor is an important factor to cause the seasonal variation of DW1.

However, the heating in the troposphere is not the only factor since the months corresponding to the maximum amplitudes change slightly as altitude increases. For instance, the maximum amplitude of the (1,1) Hough mode occurs in September above 30 km, which is 1 month earlier than that in the lower troposphere. Similarly, the maximum amplitude of the (1,2) Hough mode is found in January above 50 km, 1 month earlier than that in the troposphere and stratosphere. Generally speaking, the seasonal variation of the tidal amplitude follows the radiative heating by water vapor in the lower troposphere, while the 1 month shift of the maximum amplitude may be caused by ozone heating or mean winds.

Since the WACCM is a nonlinear model which can not separate each potential mechanism, linear models were used by previous studies to investigate the seasonal variation. *Forbes et al.* [2001] incorporated the monthly mean tropospheric heating rates from National Centers for Environmental Prediction/National Center for Atmospheric Research (NCEP/NCAR) reanalysis project into the GSWM and the SAO of the amplitude for the diurnal tide is generated (Figure 5.25). In their study, the seasonal variation of radiative heating by ozone is ignored and mean winds are equal to zero. Therefore, the SAO of the amplitude is solely caused by the variation of the tropospheric heating.

McLandress [2002b] also incorporated the heating rates and mean winds from the CMAM into a linear mechanistic model and used it to investigate the seasonal variation of the amplitude and phase of DW1. By considering the seasonal variation of the solar and

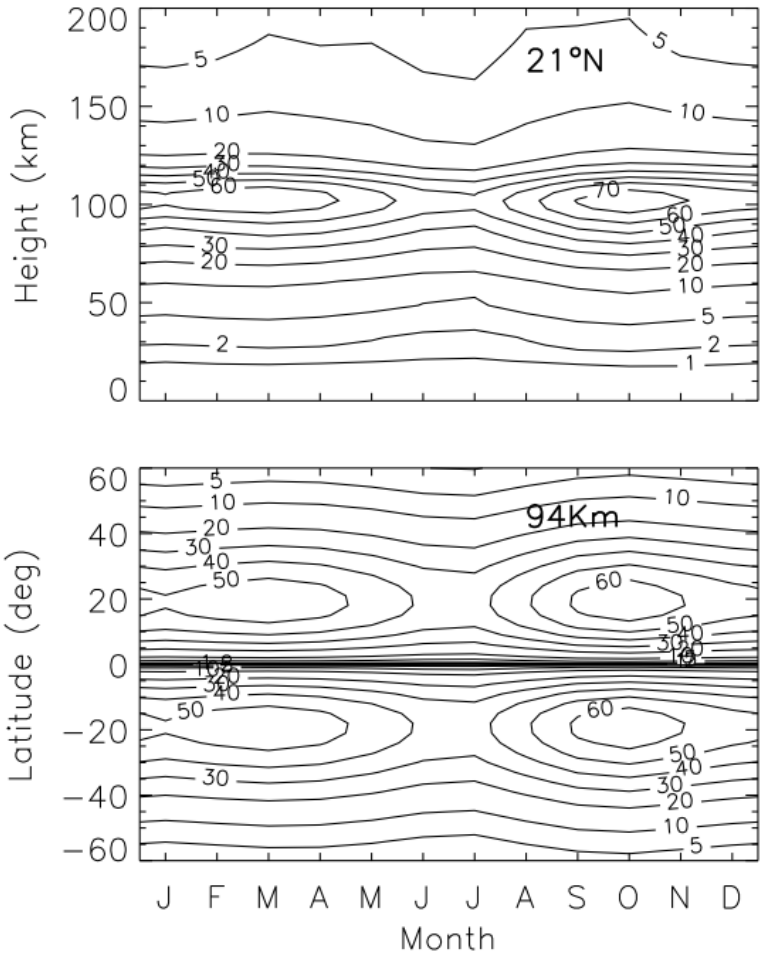

Figure 5.25: Monthly mean migrating diurnal tide in the meridional wind due to variations in heating alone. Top panel shows the amplitude as a function of altitude at latitude 21°N and bottom panel shows the amplitude as a function of latitude at 94 km, [*Forbes et al.*, 2001].

deep convective heating, the SAO of the amplitude for the meridional wind is captured. Figure 5.26 shows the SAO of the meridional wind amplitude at 20°N and 98 km. Note that the variation of the mean winds is not included in this simulation. Thick solid line is the result from the CMAM. Thin solid line is using the solar (SW) and deep convective (DC) heating and dotted line is using the DC heating alone in the mechanistic model. The importance of the solar heating can be identified because the amplitude is much smaller if only the DC heating is considered.

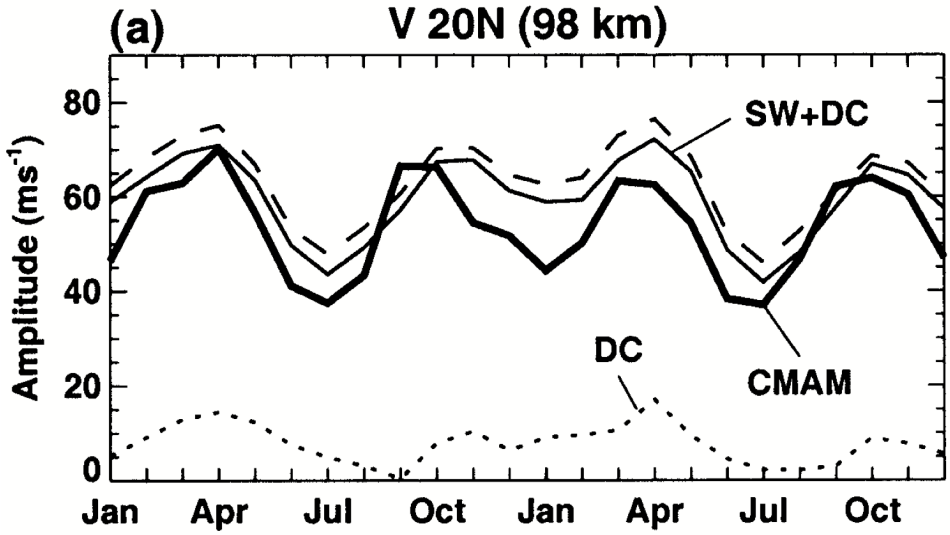

Figure 5.26: Seasonal variation of the meridional wind amplitude of the diurnal tide at 20°N for simulations using the combined solar (SW) and deep convective (DC) heating (thin solid), DC heating (dotted), and the (1,1) Hough mode component of the combined heating (dashed). The CMAM results are given by the thick solid line, [*McLandress*, 2002b].

It is interesting to notice that there is also a 1-month shift between the CMAM and the mechanistic model. The CMAM shows the maximum amplitudes occur in March and September while the prediction of the mechanistic model is 1-month later. It is similar to what we find from the WACCM. After including the effects of the mean winds by using the monthly mean wind climatology, however, the SAO of the amplitude is better simulated as shown in Figure 5.27 [*McLandress*, 2002b]. When the seasonal variations of both heating and mean winds are included in the mechanistic model, the maximum amplitudes occur in

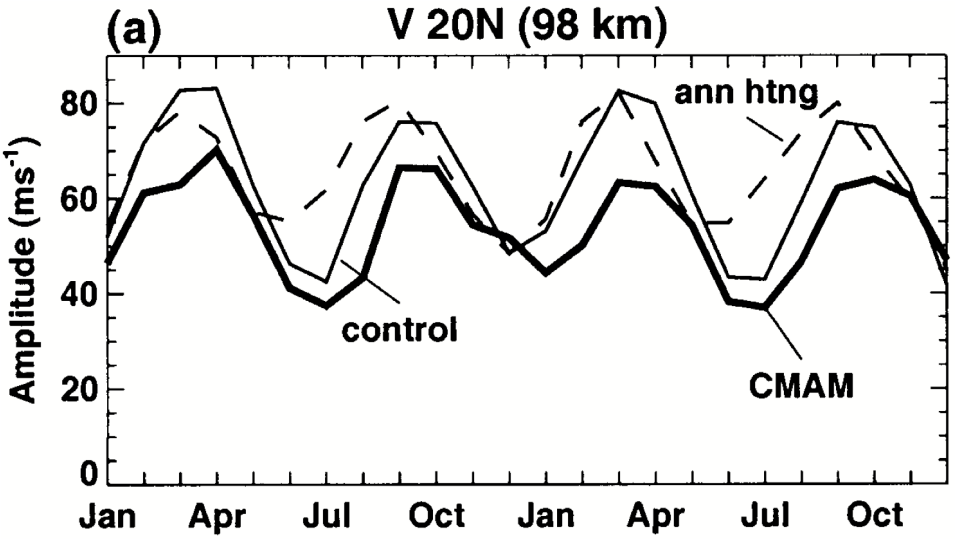

Figure 5.27: Same as Figure 5.26 except the monthly mean winds and temperatures from CMAM are used for simulations. The thin solid and dashed curves denote results using the monthly mean heating and annual-mean heating, respectively, [*McLandress*, 2002b].

March and September, which are consistent with the CMAM prediction and observations. It suggests that the mean winds also play a role in modulating the amplitude of the diurnal tide.

The WACCM tidal heating is utilized in the David Ortland's Primitive Equation (DOPE) model to investigate the seasonal variation of DW1 (private communication with Dr. Dave Ortland). A detailed description about the DOPE model can be found in *Ortland and Alexander* [2006]. The nonlinear interaction of internal GWs and DW1 is investigated by using the DOPE model [*Ortland and Alexander*, 2006]. An advantage of the DOPE model is that various mechanisms can be isolated by including them in the model or not, so their effects can be studied separately. Figure 5.28 shows the amplitudes of DW1 in the meridional wind component by only including the seasonal variation of the H_2O heating. Apparently, the SAO of the amplitude variation is well captured. In Figure 5.29, both H_2O heating and O_3 heating are included. The amplitude of DW1 is slightly decreased, while the seasonal variation is the same.

The third numerical experiment considers the non-zero mean winds retrieved from the

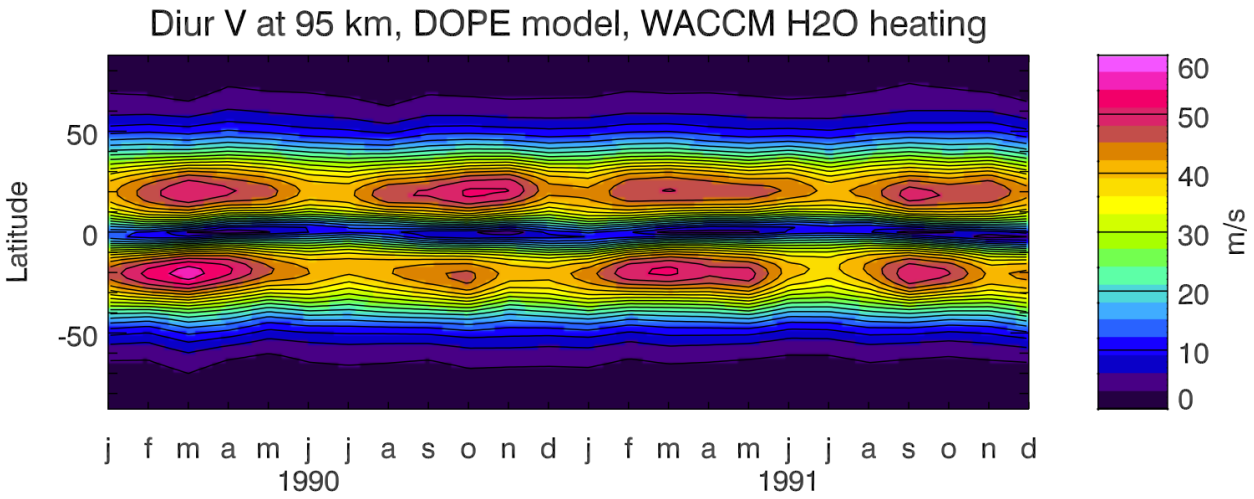

Figure 5.28: Amplitudes of the migrating tide in the meridional wind at 95 km using the DOPE model. The tidal heating is from WACCM H_2O. Courtesy of Dr. Dave Ortland.

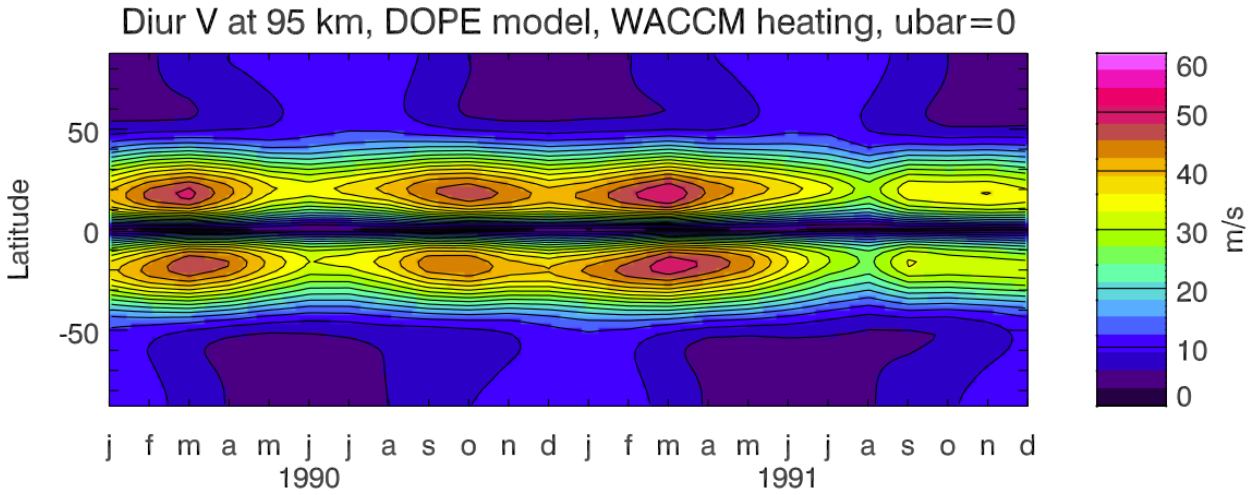

Figure 5.29: Same as Figure 5.28 except both H_2O and O_3 heating from the WACCM are included in the DOPE simulation. Courtesy of Dr. Dave Ortland.

WACCM (Figure 5.30). Significant differences introduced by the mean winds are present in both the magnitude and seasonal variation of the amplitude. For instance, at latitude 20°, the secondary maximum amplitude is found in October in year 1990 if only the tidal heating is considered. It shifts to September after the mean wind effects are included. In year 1991, the mean wind effects also change the seasonal variations of DW1 amplitudes.

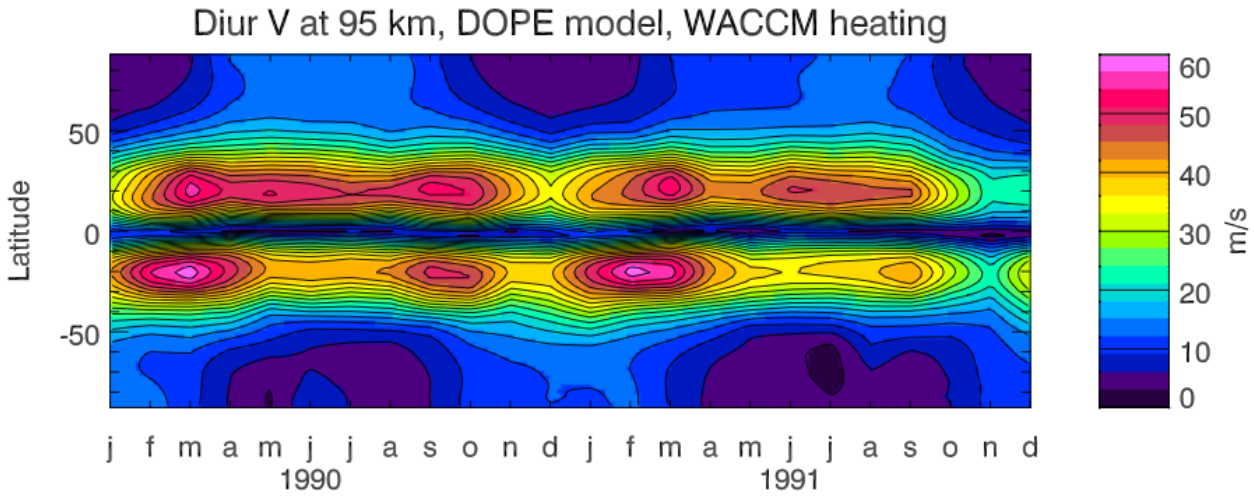

Figure 5.30: Same as Figure 5.29 except the mean winds from the WACCM are included in the DOPE simulation. Courtesy of Dr. Dave Ortland.

In the DOPE model, the maximum amplitude of DW1 is around 60 $\mathrm{m\,s^{-1}}$, which is larger than the WACCM. The GW drag of the WACCM has not been incorporated into the DOPE, and it could the reason why the DOPE model predicts larger DW1 amplitude. In the WACCM, although the GW drag is not the dominant mechanism for the seasonal variation, its damping effect is large and important in modulating the amplitude of DW1. Overall, it demonstrates that in the WACCM, the tidal heating and mean winds are important in the seasonal variation of the DW1 amplitude.

5.5 Seasonal Variation of the Tidal Phase Caused by the Mean Wind Effects

Based on the WACCM simulation, the strongest (1,2) mode is generated in January in the MLT region. In order to illustrate the relative magnitude of each mode and examine the mode superposition effect, DW1 in temperature is decomposed into the Hough modes from (1,-4) to (1,4) and they are shown in the middle and bottom panels of Figure 5.31. It

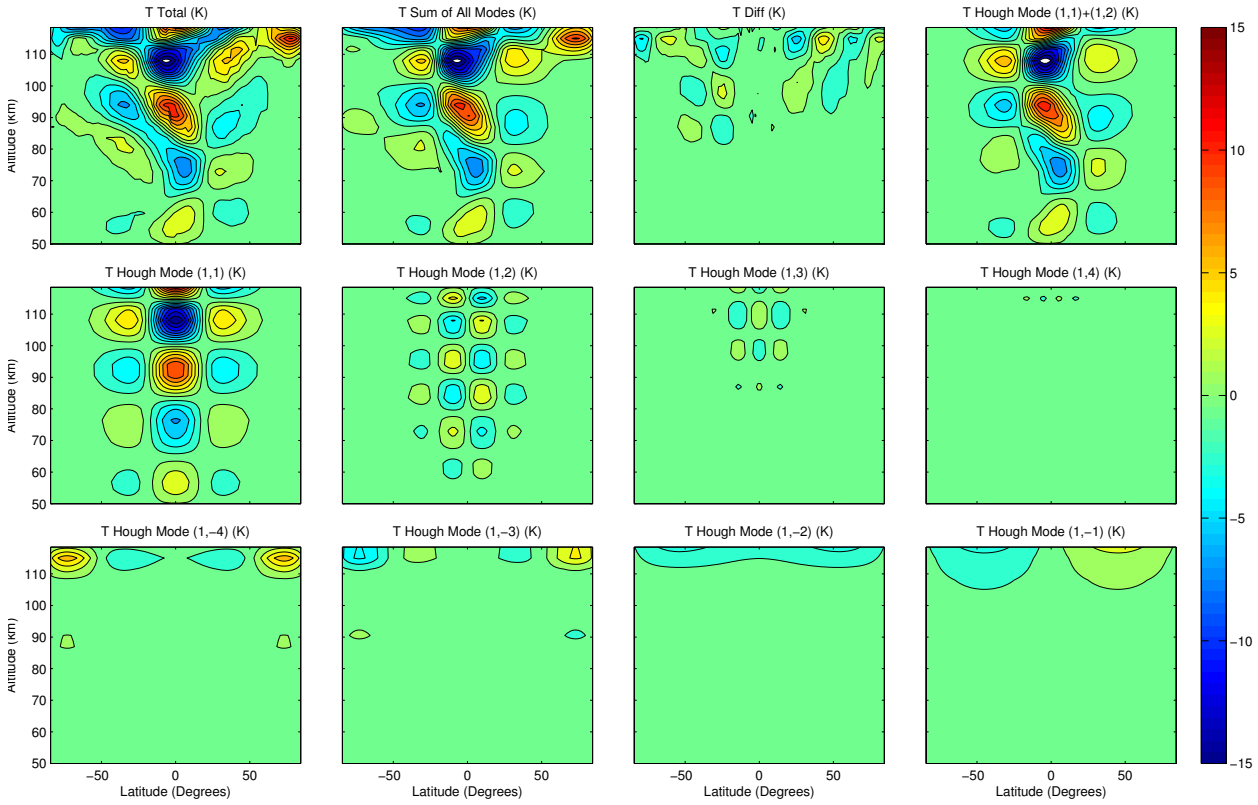

Figure 5.31: Temperature tidal structure for Hough modes from (1,-4) to (1,4) for DW1 in January (second and third rows). In the first row, from left to right, the first figure shows the temperature structure for DW1 derived from WACCM; second figure shows the superposition of the 8 Hough modes and third figure is the difference between the first and second figures; the four figure is the superposition of the (1,1) and (1,2) modes solely.

can be seen that the (1,1) mode is most dominant, stronger than all the other modes. The superposition of the (1,1) and (1,2) modes is largely responsible for the distortion of the tidal structure, which introduces an asymmetry of the tidal amplitude and phase. Between 80 and 100 km where the meteor radar measures the diurnal tide, the superposition of the (1,2)

mode onto the (1,1) mode amplifies (damps) DW1 in the summer (winter) hemisphere. The phase distortion is also significant, which is characterized by a phase advance (delay) in the winter (summer) hemisphere. The vertical wavelengths are also modulated correspondingly.

At equinox, however, the distortion is not prominent since the symmetric (1,1) mode is stronger and the (1,2) mode is weaker. Thus, the superposition effect is not efficient in

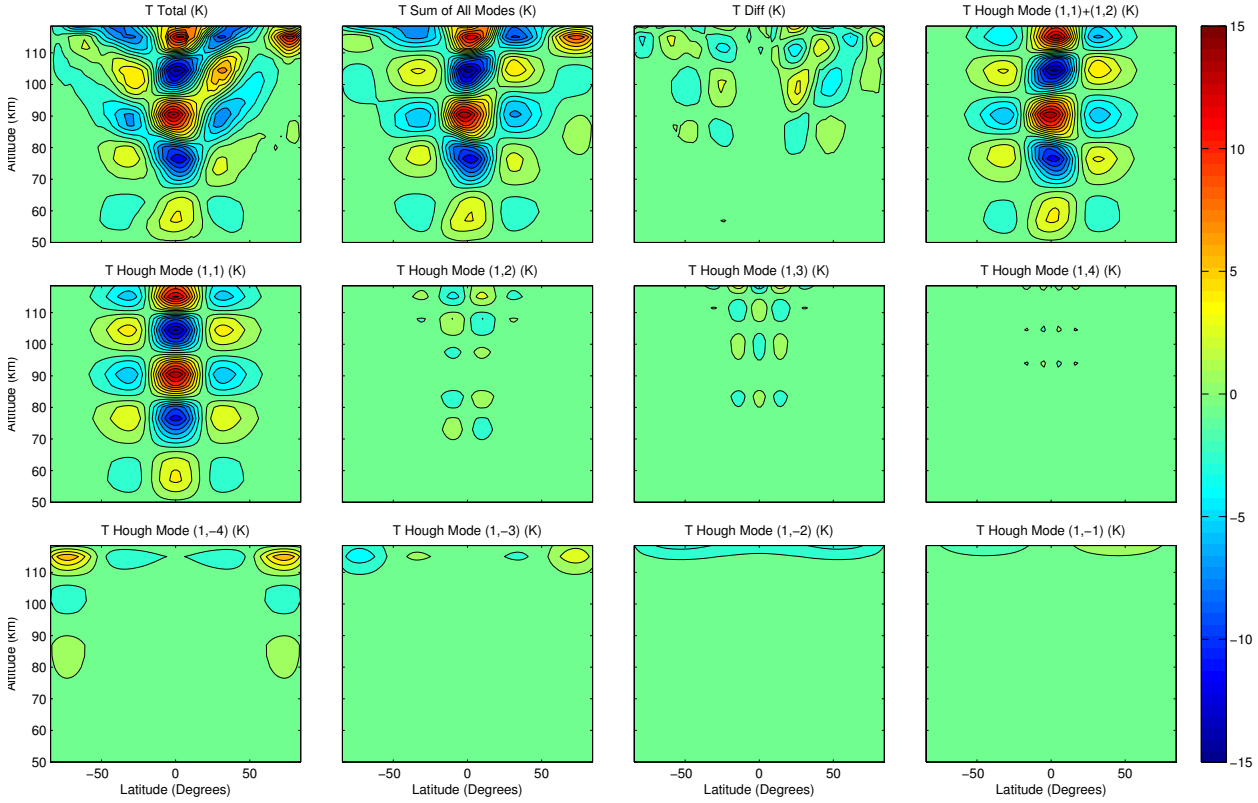

Figure 5.32: Same as Figure 5.31 except for March.

distorting the tidal structure (Figure 5.32). The total tidal structure keeps the symmetry to a larger degree, which is largely determined by the (1,1) mode. A similar season-dependent relative importance of the (1,1) and (1,2) modes and mode superposition also exist for the horizontal winds.

Figures 5.33, 5.34 and 5.35 display the seasonal variations of the structures of the (1,1) mode, (1,2) mode and their superposition, respectively. It is clear that the phase variation of the (1,1) mode is not prominent during the year. Instead, the superposition of the (1,2)

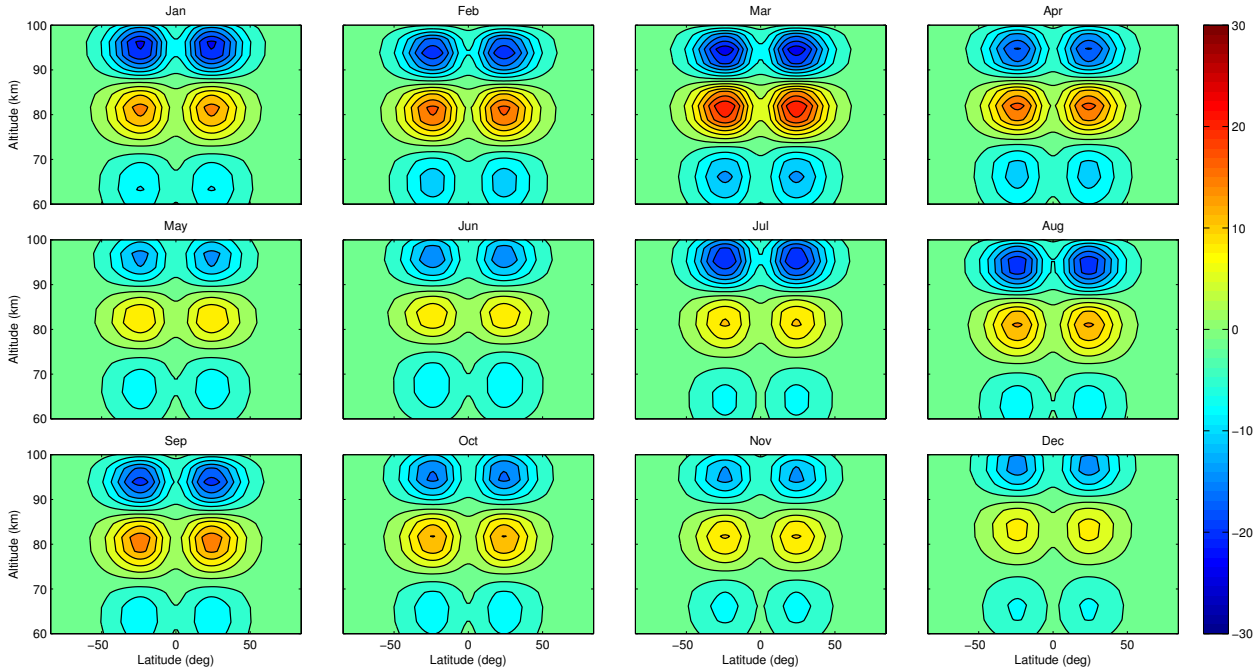

Figure 5.33: Seasonal variation of the (1,1) Hough mode in the zonal wind.

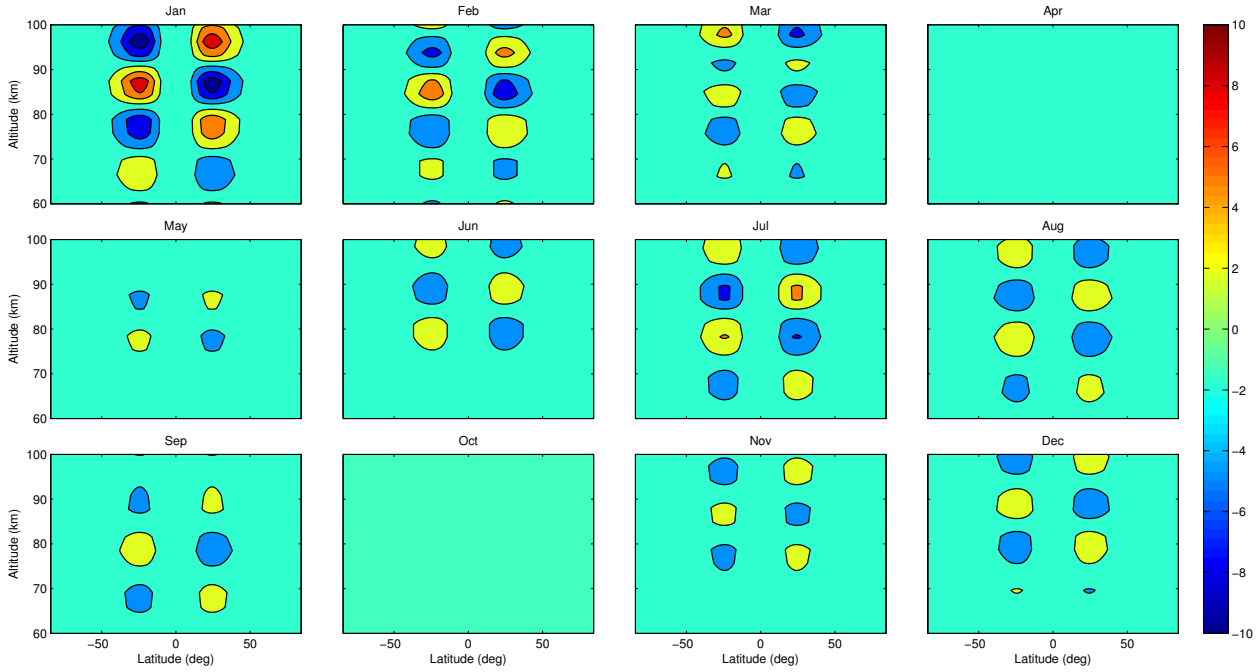

Figure 5.34: Same as Figure 5.33 except for the (1,2) mode.

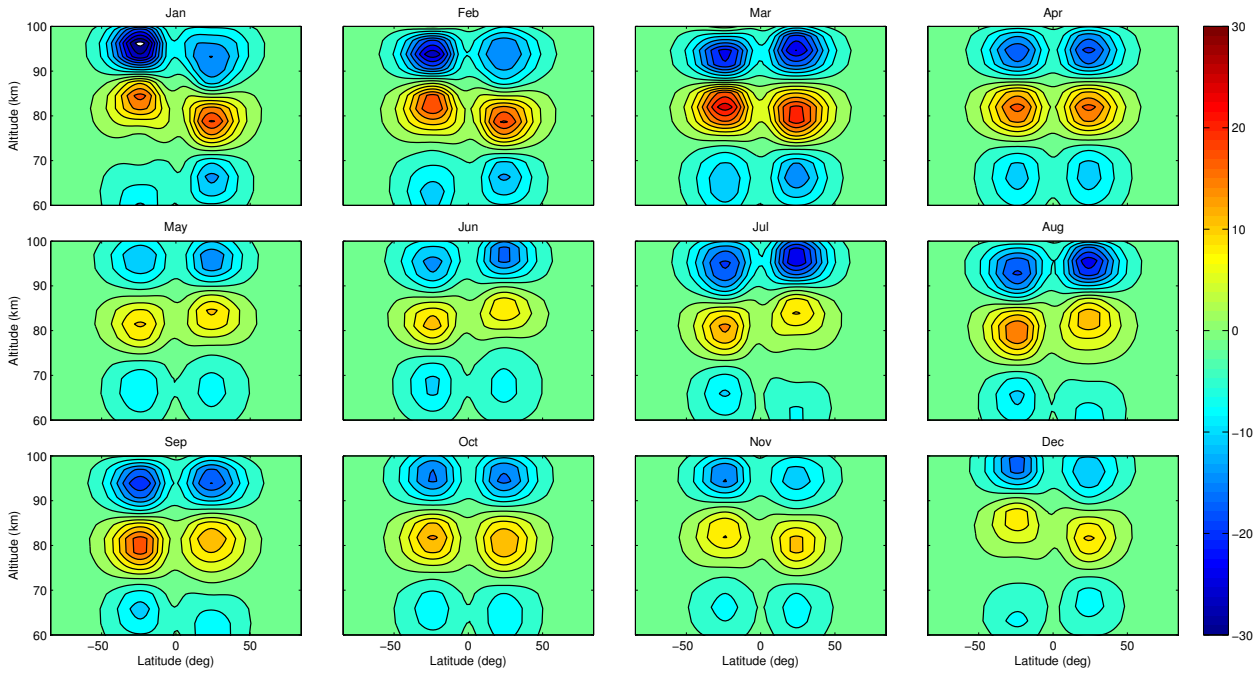

Figure 5.35: Same as Figure 5.33 except for the superposition of (1,1) and (1,2) modes.

mode introduces the inter-hemispheric difference of the tidal structure and also the seasonal variation of the phase. The phase change of the (1,2) mode is 12 hrs from January to July. Thus, its superposition effect is opposite in January and July, which leads to the AO in the phase variation. Near 20°N, the altitude corresponding to the positive maximum amplitude of the (1,1) + (1,2) modes is at ∼79 km in January, increasing with time and reaching a highest altitude around 85 km in June. If we assume the vertical wavelength of the diurnal tide is 30 km, then the introduced phase delay from January to June is equal to 24 hrs$\times$(85 − 79)km/30km = 4.8 hrs, which is quite comparable with the meteor radar observation.

Figure 5.36 shows the seasonal variation of the DW1 phase with zero mean winds based on the prediction of a mechanistic model [*McLandress*, 2002b]. If the mean winds are zero, the phase barely varies with season. So the heating alone can not explain the phase variation. However, the seasonal variation of the phase is well reproduced after the mean wind effects are included (Figure 5.37). *McLandress* [2002b] explained the effects of the mean winds in a

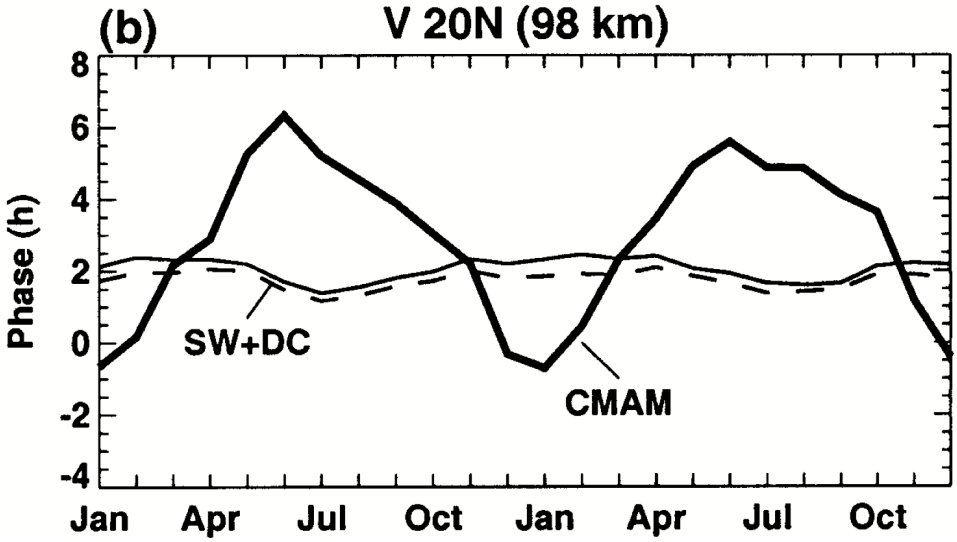

Figure 5.36: Seasonal variation of the meridional wind phase of the diurnal tide at 20°N for simulations using the combined solar (SW) and deep convective (DC) heating (thin solid), DC heating (dotted), and the (1,1) Hough mode component of the combined heating (dashed). The CMAM results are given by the thick solid line, [*McLandress*, 2002b].

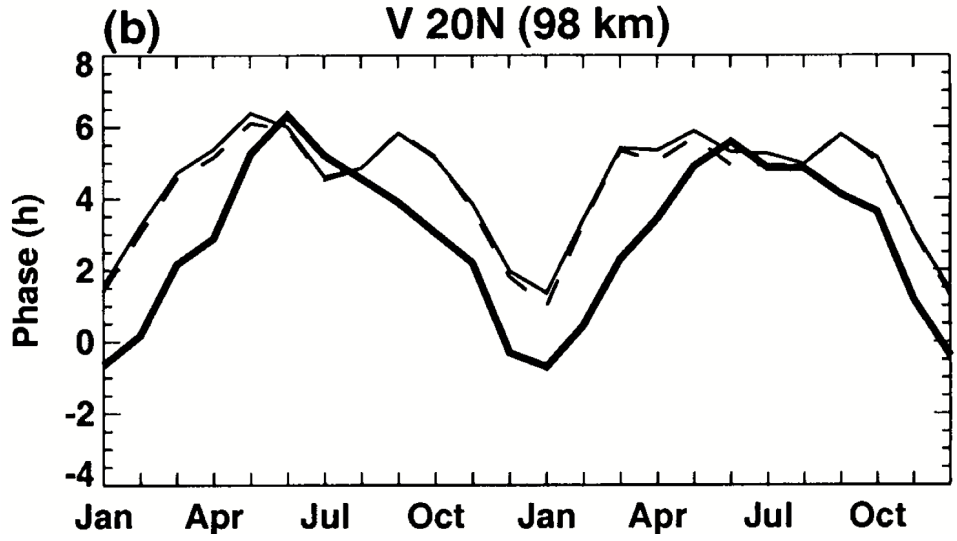

Figure 5.37: Same as Figure 5.36 except mean winds are included in the simulation.

context of mode coupling, which distorts the tidal structure and causes the inter-hemispheric differences in the tidal amplitude and phase.

The mode coupling was also discussed by *Forbes and Hagan* [1988] and shown to be responsible for the asymmetric amplitude and phase structure of DW1. By only including the tidal heating from two symmetric modes (1,1) and (1,-2), the antisymmetric Hough mode (1,2) can be generated due to mode coupling by the mean winds. The (1,2) Hough mode due to the mode coupling is stronger at solstice since the zonal mean wind is more asymmetric with respect to the equator. Because the phase of the (1,2) mode changes 12 hrs every half a year, it advances the tidal phase in winter and delays it in summer at 20°N. *Ortland* [2005a] developed a theory of generalized Hough modes [*Ortland*, 2005b] which takes the mean vorticity into account to explain the hemispheric asymmetries and amplitude broadening. In his studies, the importance of the mean wind effect on the tidal structure was also identified.

5.6 Discussion

Based on the WACCM simulation, the damping effect in the zonal wind caused by GW drag is strong and its corresponding ERF reaches a maximum value of 8×10^{-5} s^{-1}. At the equator, linear advection mainly originates from the advection of the zonal mean zonal wind by the vertical tidal wind, which is also important to change the tidal amplitude. Unlike GW drag, which always damps the tide in the zonal wind direction, the effect of linear advection depends on altitude because the vertical shear of the zonal mean zonal wind switches from negative to positive values as altitude changes. Around 75 km, linear advection damps the tide while near 90 km, the tide is amplified. The contribution from nonlinear advection in the momentum budget of the zonal wind is insignificant when compared to GW drag and linear advection.

In the area where DW1 is strong, GW drag tends to advance the tidal phase and thus

shorten its vertical wavelength locally. But GW drag is not the most important factor in changing the tidal phase. The major contribution for the phase change of DW1 is from linear advection and it is largely determined by the latitudinal shear of the zonal mean zonal wind. Compared to the zonal wind, GW drag and linear advection are less important for the meridional wind. Instead, the changes of amplitude and phase are attributed to nonlinear advection.

Lieberman et al. [2010] studied the momentum budget of DW1 in the MLT region based on TIMED/SABER and TIMED/TIDI observations. Some similarities can be found between the WACCM and observations while differences are non-negligible. In their study, the classical terms and linear advection of the mean winds by tidal perturbations are inferred from measurements and referred to as the momentum budget terms. The residual terms are the sums of linear advection of the tidal perturbations by the mean winds, frictional terms and nonlinear advection. Similar to the WACCM, classical tidal theory provides a good approximation. For the zonal momentum budget, the meridional advection of zonally averaged momentum $-(v'/a)\cdot\partial\bar{u}/\partial\phi$ is found to be the most important nonclassical term, approaching 70-80 $\mathrm{m\,s^{-1}\,day^{-1}}$. In the WACCM, this term also makes a significant contribution to linear advection and it reaches 60 $\mathrm{m\,s^{-1}\,day^{-1}}$, which is slightly smaller than the observations. It is probably due to the underestimation of the tidal amplitude in the meridional wind. From the observations, the net residual zonal force is generally in quadrature with the zonal wind, which means that it advances the tidal phase but has small impact on the tidal amplitude. In the WACCM, we also find that GW drag advances the phase but it also damps DW1. Overall, it suggests that GW drag in the zonal (meridional) direction is overestimated (underestimated) in the WACCM compared to the observations.

It is revealed that the projection of GW drag onto the DW1 component reaches a substantial magnitude, implying that the tide also has a significant modulation on GWs. As pointed out by *Richter et al.* [2010], other extropical GW sources should be included in the model to account for the momentum budget from GWs, instead of applying a relatively low

frontogenesis threshold. A better parameterization for GW source is expected in the future.

5.7 Summary

The momentum budget of DW1 contributed by GW forcing and advection terms is investigated by using the WACCM4, which captures a reasonable seasonal variation of DW1 and realistic mean background winds. Classical tidal theory provides a proper prediction of the magnitude and structure of DW1. The discrepancies mainly result from advection terms and GW dissipation.

The seasonal variation of the amplitude is consistent with the radiative heating by water vapor in the troposphere, while mean winds play a role in modulating the amplitude as well. At equinox, the radiative heating is more symmetric and generates a stronger response of the (1,1) mode, the dominant mode of the diurnal tide in the MLT region. The SAO of the amplitude can be largely attributed to the SAO of the heating.

At solstice, when the mean zonal wind is more antisymmetric, the (1,2) mode is stronger due to mode coupling. The superposition of the (1,1) and (1,2) Hough modes distorts the symmetric structure of the (1,1) mode and results in the inter-hemispheric differences in the amplitude and phase. In terms of the NH, the effect is to advance (delay) the phase in the winter (summer) hemisphere, thus giving rise to the AO of the phase variation. Although the GW damping is large in the WACCM, it can not be used to explain the seasonal variation of DW1.

CHAPTER 6

TIDAL MODULATION OF THE GW VARIANCES

This chapter studies the tidal modulation of the GW variances. A sensitivity test about how the GW variance calculation would be affected by the meteor rate is carried out using the Monte-Carlo simulation. The dominant oscillations of the GW variances are identified and related to the modulations of PWs and tides. The differences in the GW variances between Maui and Urbana are observed and the possible explanations are discussed. The growth rate of the GW variance is also investigated.

6.1 Sensitivity Test On Meteor Counts

A concern of the "MR technique" used to derive the GW variances (section 2.5.4) is whether the derived variances depend on the number of received meteors and how many meteors are needed in order to assure the accuracy. A Monte-Carlo sensitivity test on meteor rate is performed for the Maui meteor radar in order to answer this question. In the first experiment, a single GW with wavelengths ($\lambda_x = 60km, \lambda_y = 60km, \lambda_z = 20km$) is added to the background winds ($u = v = 25$ m s^{-1}). The intrinsic period is derived according to the GW dispersion relation and $\tau = 12.5$ min. The wave amplitude in the meridional wind is equal to 10 m s^{-1} and that in the zonal wind is calculated based on the GW polarization relation. After the background winds and GW perturbations are chosen, they are projected onto each meteor to obtain its horizontal wind. The positions of meteors are randomly selected. Then we go through the procedures of the "MR technique" to calculate the GW variance while for each set of calculation, a certain number of meteors are randomly selected

and the calculation is repeated for 500 times. For each set of calculation, the total amount of meteors is the same but the combination of meteors is different. Basically, it is a Monte-Carlo simulation and the total amount of the meteors received within 4 hrs is increased from 20 to 300 with an increment of 5.

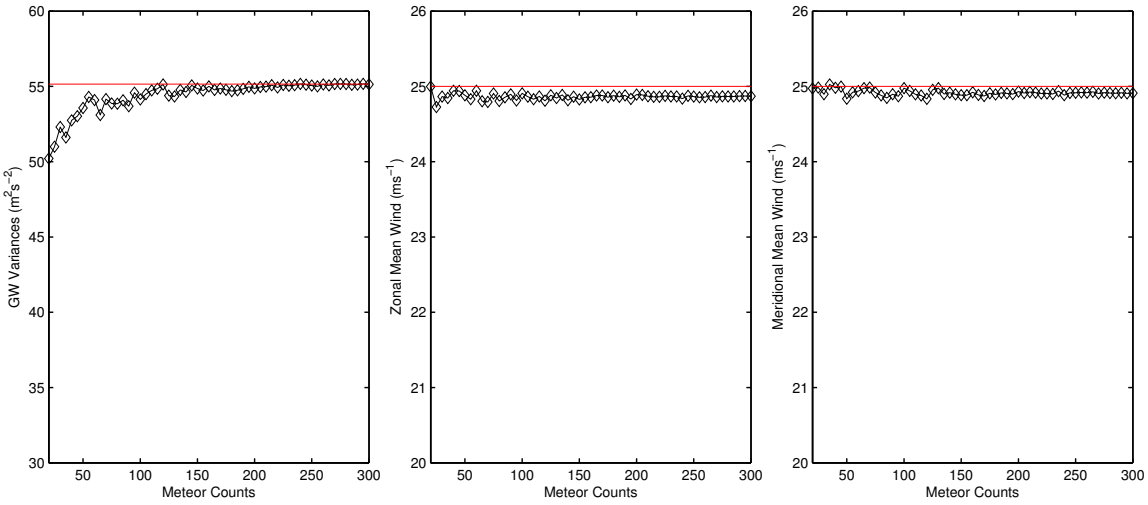

Figure 6.1: Monte-Carlo simulations of GW variances (left panel) and background winds (middle panel for the zonal wind and right panel for the meridional wind) using the MR technique. Red lines show the real GW variances and background winds. A Single GW wave is added to the background winds in this simulation.

For each number of the meteor counts from 20/4hrs to 300/4hrs, we randomly select the combination of the meteors and derive the background winds and GW variances for 500 times. The mean values and standard deviations of the background winds and GW variances can be obtained and they are compared with the "real values", what we already set up for the experiments. Figure 6.1 shows the mean values of GW variances, zonal and meridional background winds as functions of meteor rates. The red lines represent the real input values. The background winds can be well retrieved with a meteor rate as low as 20/4hrs. However, the standard deviation is larger for lower meteor rate, which is about 2 m s^{-1} at a meteor rate of 20/4hrs (Figure 6.2). The GW variances can be derived accurately with meteor counts larger than 50/4hrs, with standard deviations less than ∼15%. When the meteor counts are less than 50/4hrs, the GW variances are slightly underestimated and when the

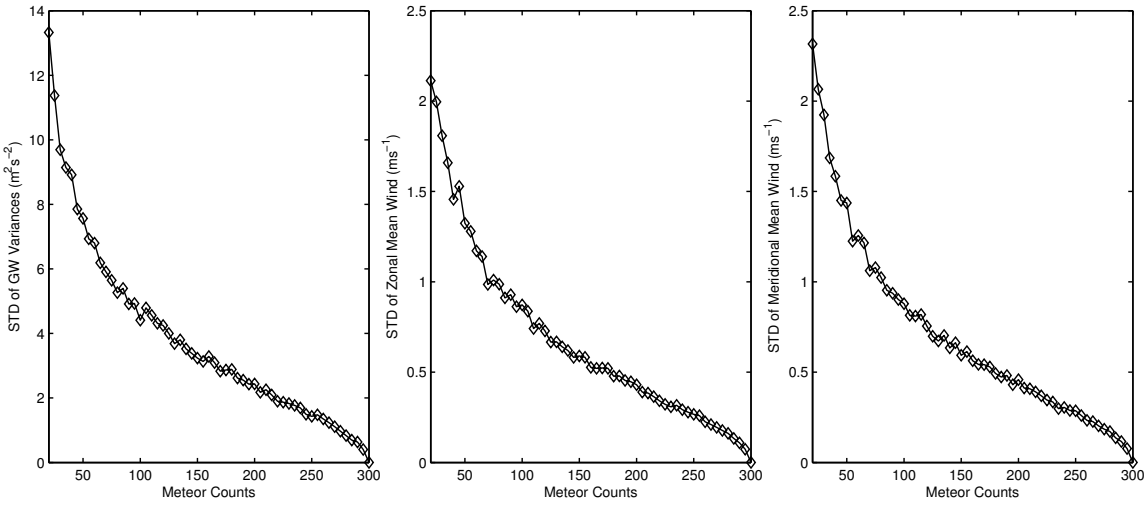

Figure 6.2: Same as Figure 6.1 except for the standard deviations of GW variances and background winds.

meteor count is 20/4hrs, this underestimation is about 9%. Same as the retrievals of the background winds, the standard deviations of GW variances decrease with the increasing meteor counts. When the meteor rate reaches 300/4hrs, both background winds and GW variances can be obtained with high accuracy and small deviation.

For the second experiment, a GW spectrum is added to the background wind fields. The wave phase speed is randomly selected in a range of $20 < c < 40$ m s^{-1} and the ground-based period is randomly chosen between 20 and 200 min. The vertical wavelength is equal to 20 km and the horizontal wavelength is calculated based on the wave phase speed and period, so it is also a random value but in a range of 24-480 km. The wave amplitude is the same as the single wave specified in the first experiment. Totally, 10 waves are included in the GW spectrum. Three simulations are performed by randomly choosing a wave spectrum for each case.

Based on Figure 6.3, it is seen that the real GW variances increase from case 1 to case 3. A different GW variance for each wave spectrum is expected because there are 10 waves added to the background and different wave interference may exist. If the waves interfere destructively, the variances they induce will be smaller and vice versa. For all the three cases,

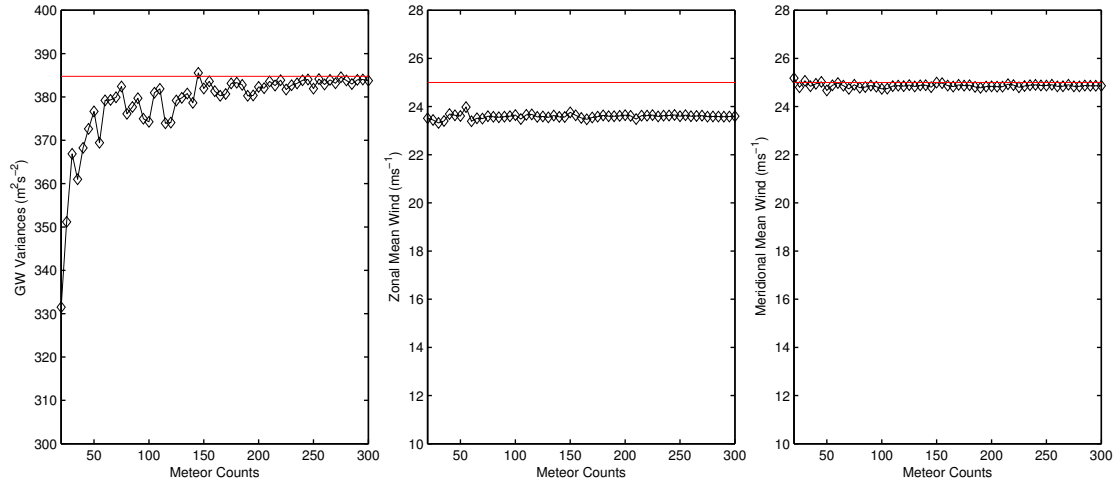

(a) Case 1

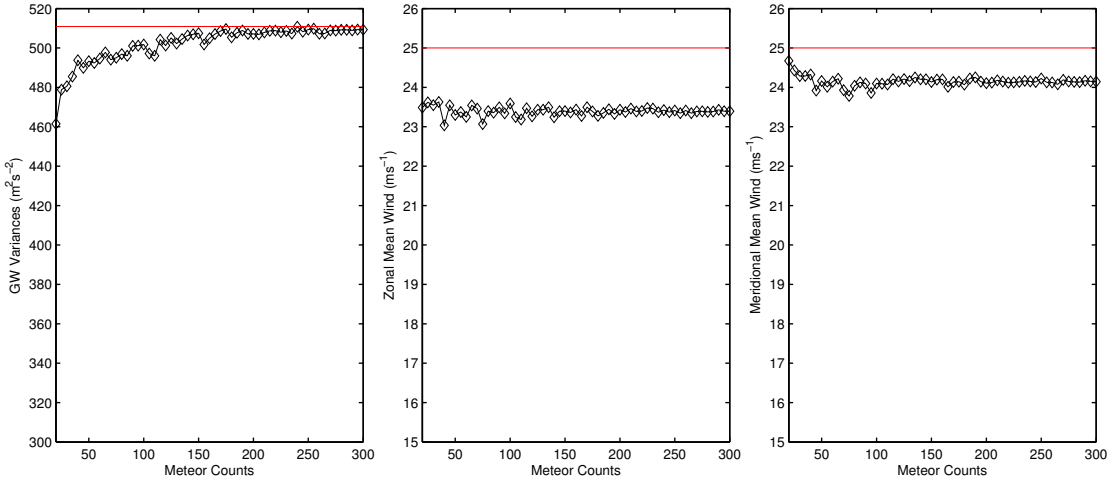

(b) Case 2

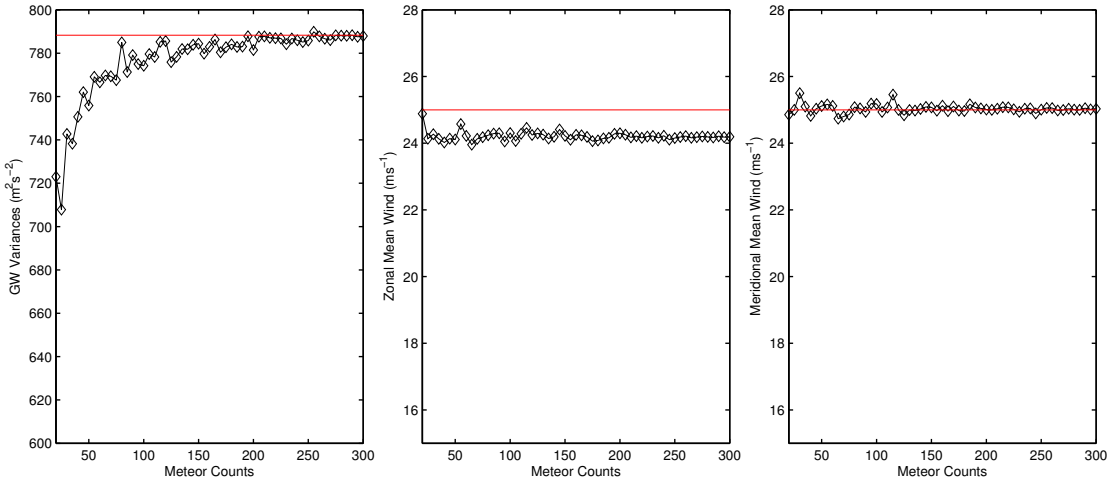

(c) Case 3

Figure 6.3: Same as Figure 6.1 except that a GW spectrum of 10 waves is added to the background. Three cases correspond to different GW spectra.

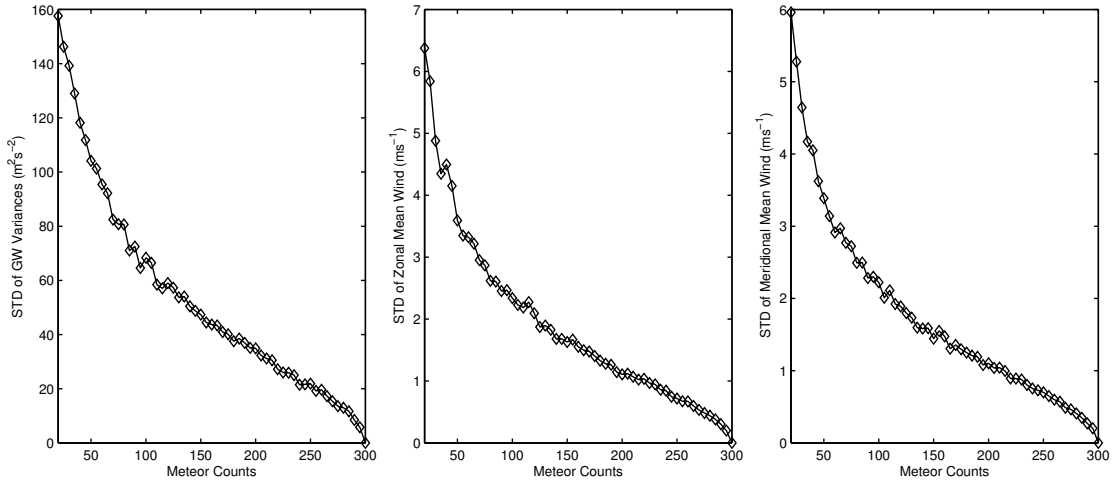

(a) Case 1

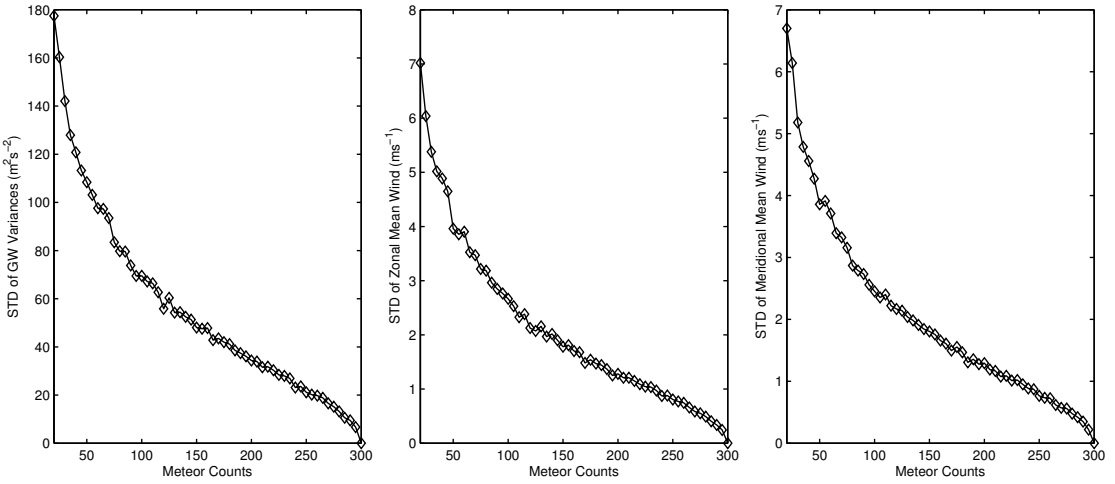

(b) Case 2

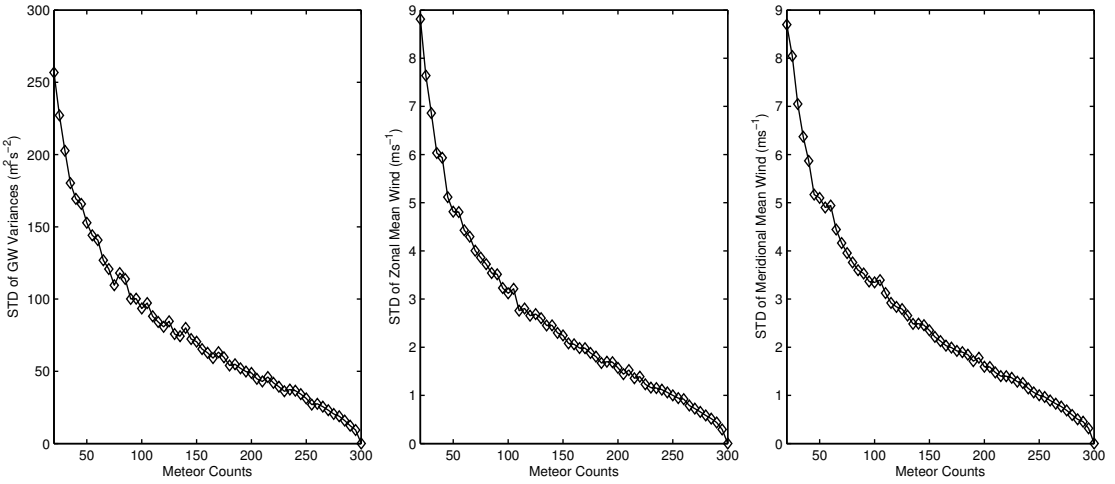

(c) Case 3

Figure 6.4: Same as Figure 6.3 except for the standard deviations.

the background winds can be reasonably retrieved, but not as well as the single wave case. And the retrieval of the background winds depends on which wave spectrum is selected. For case 1 and 3, the meridional winds are very close to the real values but the zonal wind has a discrepancy around 1 $\mathrm{m\,s^{-1}}$ (Figure 6.3a and 6.3c). For case 2, both zonal and meridional winds are different from the real values by ∼1-2 $\mathrm{m\,s^{-1}}$. The standard deviations of the retrieved background winds are demonstrated in Figure 6.4. Same as the single wave case, the simulations with more meteors have smaller deviations. The standard deviations of the background winds also increase slightly as the GW variances increase, which means that the uncertainties of retrieving the background winds are larger if stronger GW perturbations are present.

In terms of the GW variances, the results are similar to the single wave experiment except with larger values due to the presence of more waves. The real values corresponding to the three cases are near 385, 510 and 790 $\mathrm{m^2/s^{-2}}$, which vary significantly depending on the GW spectra. The GW variances can be accurately reproduced with meteor numbers larger than 150/4hrs. When the meteor number equals to 20/4hrs, the underestimations of the GW variances are of the order of 10% for all the three cases. The standard deviations of the GW variances are positively related to the mean values with a percentage of ∼30%. It is expected that a larger mean GW variance has a larger standard deviation.

Vincent et al. [2010] also used a Monte-Carlo simulation to assess the uncertainties in the calculation of mean winds, GW variances and moment fluxes by using the all-sky interferometric meteor radar. They found that mean winds can be recovered at meteor rates as low as 10 $\mathrm{hr^{-1}}$. Horizontal wind variances can be derived with relatively little averaging, while momentum fluxes derived according to the Hocking's method [*Hocking*, 2005] need longer averaging time in order to produce meaningful values.

In their single-wave experiment, the wave amplitude is 10 $\mathrm{m\,s^{-1}}$ with a horizontal wavelength of 50 km and ground-based phase speed 50 $\mathrm{m\,s^{-1}}$. The background wind has a magnitude of 20 $\mathrm{m\,s^{-1}}$ and the direction changes by 15° increment. Figure 6.5 displays

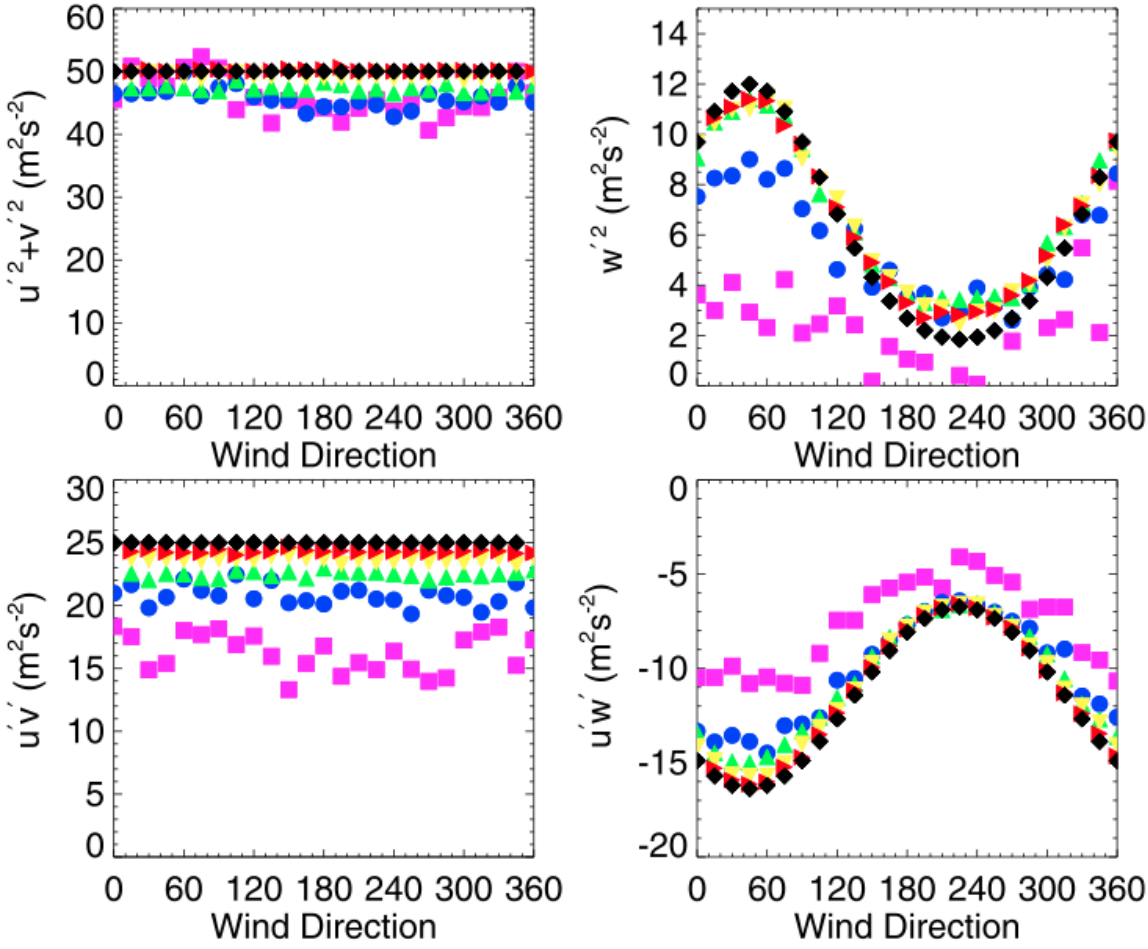

Figure 6.5: Received values of GW fluxes for the case of a single wave of amplitude 10 ms^{-1}. The background wind direction has a magnitude of 20 ms^{-1} and changes by 15° increment. The black diamonds represent the input values and the other symbols represent the mean of 500 retrievals as a function of meteor rate for 10 (magenta squares), 20 (blue circles), 50 (green triangles), 100 (yellow triangles) and 200 (red triangles) hr^{-1}, [*Vincent et al.*, 2010].

the horizontal wind variances, vertical velocity variances, horizontal and vertical momentum fluxes as functions of the background wind direction. The black diamonds denote the input values and the other symbols denote the mean of 500 retrievals with different meteor counts. Similar to our analysis, the horizontal wind variances are underestimated if meteor rates are small and the underestimation of the variances is larger for lower rate. The background wind direction slightly changes the GW variances but the effects are not significant. The derivations of the vertical wind variances and momentum fluxes, however, require more meteors in order to capture the real values. In Figure 6.6, a single GW is replaced by a GW spectrum and the similar results are obtained.

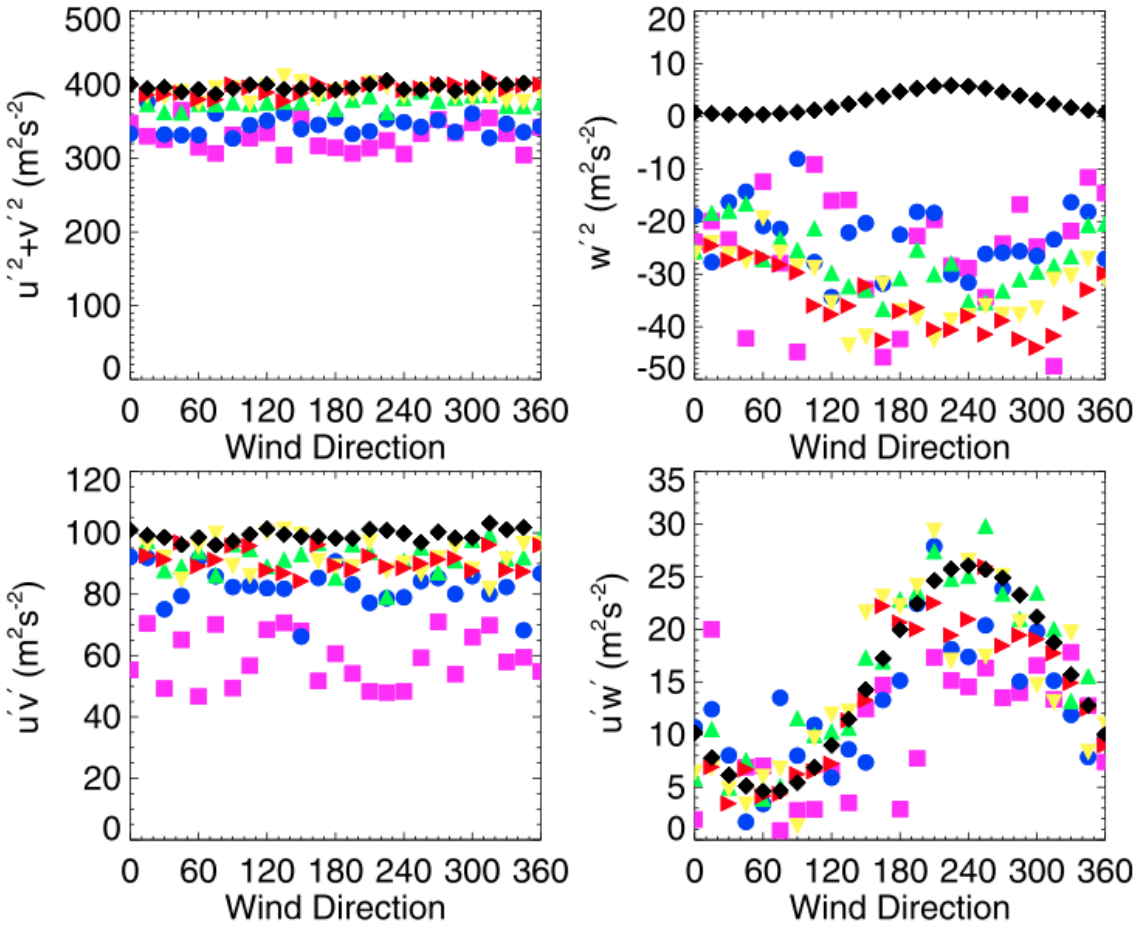

Figure 6.6: Same as Figure 6.5 except for a GW spectrum of 9 waves, [*Vincent et al.*, 2010].

Although the parameters for the single GW and GW spectrum are chosen according to

the observations in this region, the selections are still a little arbitrary. It is not quite clear about the sensitivities of the retrievals of the GW variances on the specified GW parameters, which need more detailed investigations in the future.

6.2 Low-Frequency Wave Modulation on GW Variances

In order to identify the dominant periods of the GW variances, the Lomb-Scargle (LS) periodogram is used to identify the peak frequencies for every month (Figure 6.7). The diurnal cycle of the GW variances is the most prominent feature except for April, when it peaks at a period of 10 days. Besides the diurnal cycle, the semidiurnal cycles are observed in many months as well, such as the months from May to August and October and December. The quasi-2-day periods of the GW variances are present from May to July and in September.

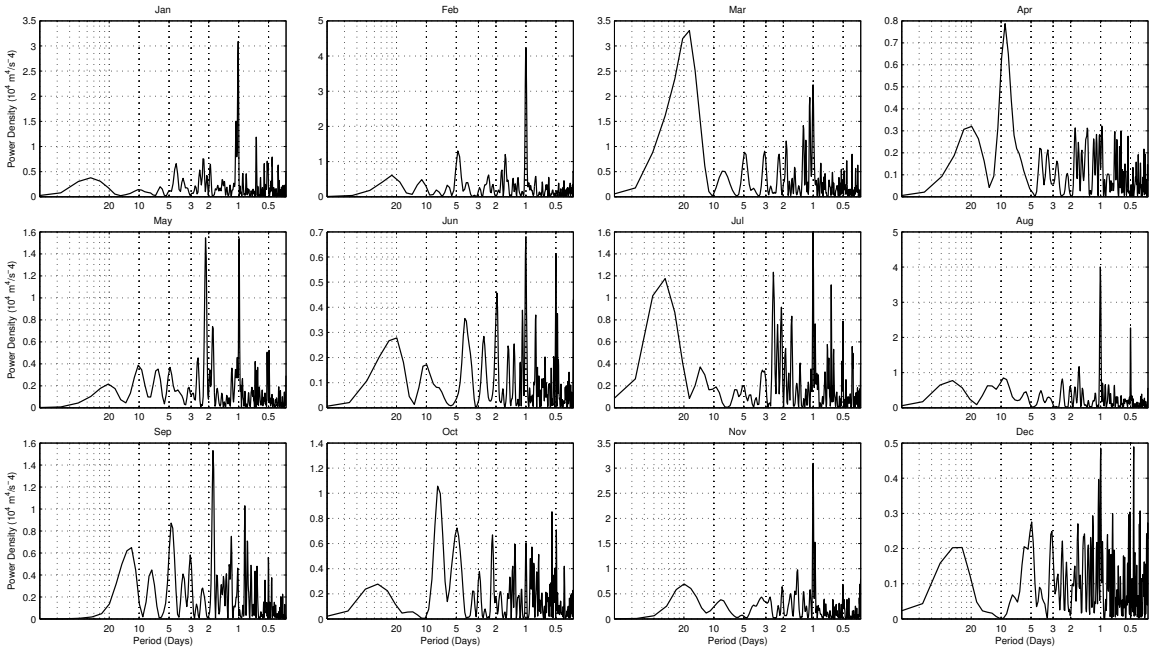

Figure 6.7: Lomb-Scargle periodogram of the GW variance for every month in the year 2003 in Maui, HI. The unit is 10^4 $m^4 s^{-4}$

Some longer-period cycles are also present, such as the oscillations with a quasi-5-day period in Jun, September, October and December, also the quasi-10-day period in April. Although

the diurnal cycle of the meteor rate is observed (section 2.2), these multi-peak and complex spectra of the LS periodograms are not associated with the meteor rates, which uniformly show single peaks at 24 hrs for all the months (not shown). It implies that the low-frequency oscillations of the GW variances are caused by real geophysical mechanisms, probably by the modulations of PWs and tides. The similar results are found in Urbana, IL (Figure D.1).

6.3 Tidal Modulations on GW Variances

We focus on the diurnal and semidiurnal oscillations of the GW variances since they are most dominant according to the LS spectrum analysis. The daily composite GW variances are derived and monthly averaged, as shown in Figures 6.8 for Maui, HI.

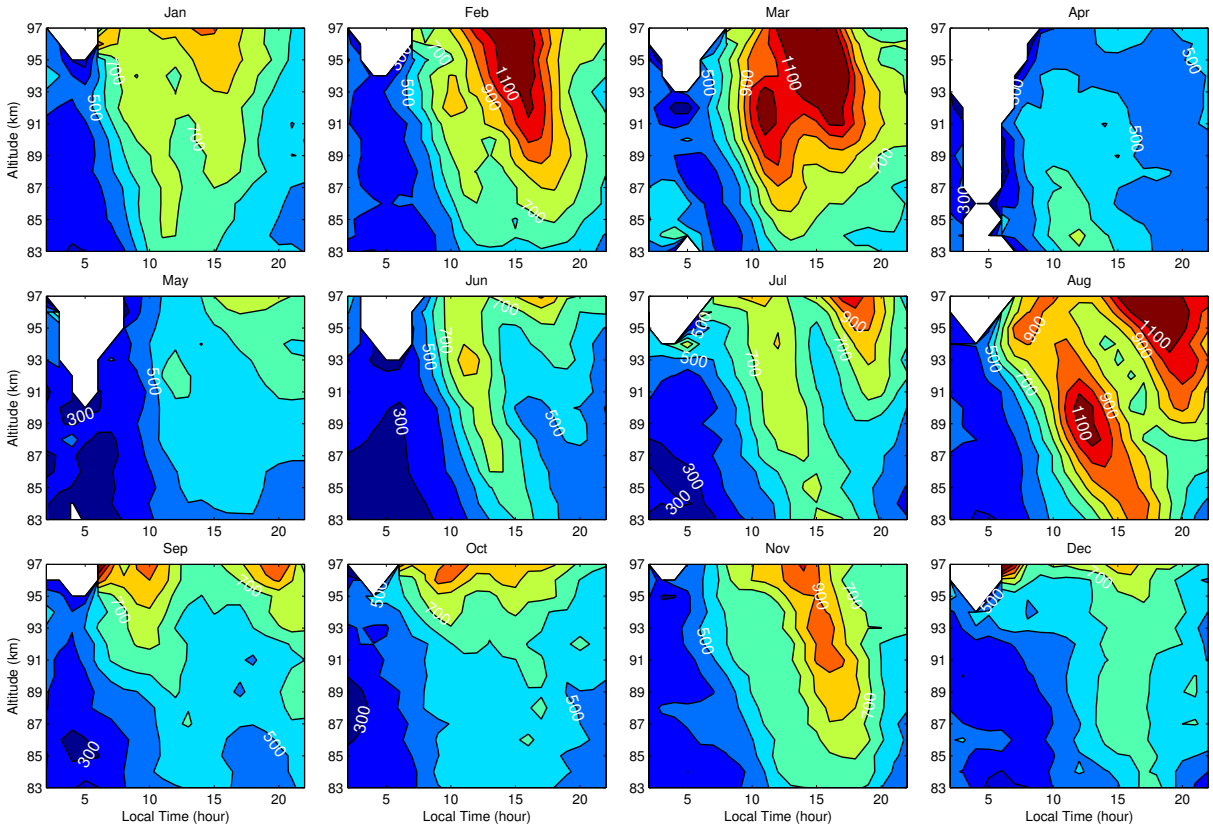

Figure 6.8: Monthly mean daily composite GW variances for each month in the year 2003, Maui, HI. The unit is m^2s^{-2}. Contour intervals are from 200 to 1100 m^2s^{-2}, incremented by 100 m^2s^{-2}.

There are several features that can not be explained by the diurnal variation of the meteor rate. Firstly, the GW variances increase with altitude which are more likely to be caused by the amplitude increases of the GWs rather than the meteor rate, which reaches its maximum at ∼90 km. Secondly, the seasonal variation of GW variances is not consistent with that of the meteor rate. The highest meteor rates occur in January, June and July for Maui, which are not the same as the months with maximum GW variances. The maximum GW variances are found in February, March and August, instead. Thirdly, the downward phase progresses exist for the GW variance profiles but not for the meteor rates. In addition, in some months such as August and September, double peaks of the GW variances are observed, which is not related to the diurnal cycle of the meteor rate. Thus, it indicates that the diurnal variations are real features possibly caused by the tidal modulations, which is also concluded by *Vincent et al.* [2010]. However, it should be recognized that since the GW variances are calculated when the meteor counts are larger than 30/4hrs, the underestimations associated with low meteor rates during 2-8 UT are possible. Even so, the evidences of the probable tidal modulations can be based on other features listed above.

The zonal components of the mean wind, diurnal and semidiurnal tidal winds are obtained by fitting a sinusoidal function to the total zonal wind as:

$$f(t) = a_0 + a_1 \cos\left(\frac{2\pi t}{24} - \phi_1\right) + a_2 \cos\left(\frac{2\pi t}{12} - \phi_2\right) \tag{6.1}$$

where a_0 denotes the mean zonal wind, a_1, a_2 and ϕ_1, ϕ_2 denote the amplitudes and phases of the zonal diurnal and semidiurnal tides, respectively. Figure 6.9 shows the GW variances and the superpositions of the mean and tidal winds. It demonstrates that the vertical tilts of the GW variances are qualitatively in agreement with the slopes of the tidal structure. At the equinoxes, the gradients of the vertical tilts are about 2 km hr^{-1}. The gradients tend to decrease at the solstices, especially in December, when the GW variances and the tidal winds are almost straight up with respect to altitude. At the summer solstice, the gradients

decrease to $\sim$3 km hr^{-1}. This is probably due to the fact that in December, the diurnal tide is weak while the semidiurnal tide is strong and the vertical wavelength of the semidiurnal

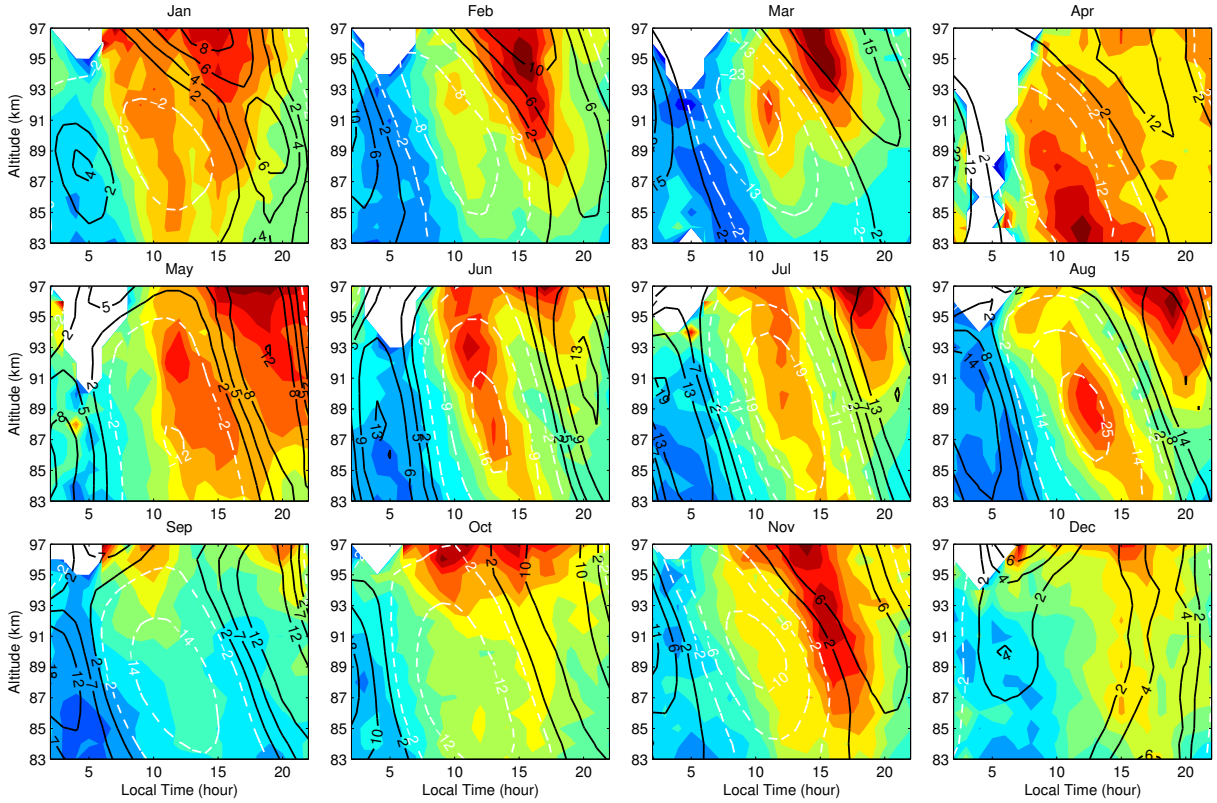

Figure 6.9: The GW variances (colored contours) and the superposition of the mean and tidal winds in Maui (line contours). Black and solid line represents the eastward wind, white and dashed line denotes the westward wind, respectively.

tide ($\sim 70 - 80km$) is much longer than that of the diurnal tide.

In most months, the superpositions of the mean winds and tides are eastward in the beginning of a day (in terms of UT), followed by the westward winds and shifting to the eastward winds again in the end. We refer to the eastward wind as the positive phase and the westward wind as the negative phase. In general, a first peak of the GW variances is found in the negative phase when the westward wind starts to prevail and a following peak is in the secondary positive phase with the prevailing eastward wind. The secondary peak usually occurs and becomes strong at higher altitude such as in March, May, June, July and August. According to the vertical structures of the diurnal and semidiurnal tides, the

maximum diurnal tide is located at ∼95 km and the semidiurnal tide peaks at a higher altitude (∼110 km). So the secondary peak is likely to be associated with the semidiurnal tide. It needs further confirmation and a modeling work would help for identifying the underlying physical mechanisms.

The GW variances observed in Urbana shown in Figure 6.10 are similar to those in Maui in terms of the continuous vertical growths. The structure of the double peaks is also observed in Urbana and the time delay between them are about 8-12 hrs. The double peaks of the GW variances are very significant in January, February, September, November and December, which are in agreement with the months when the semidiurnal tides are strong

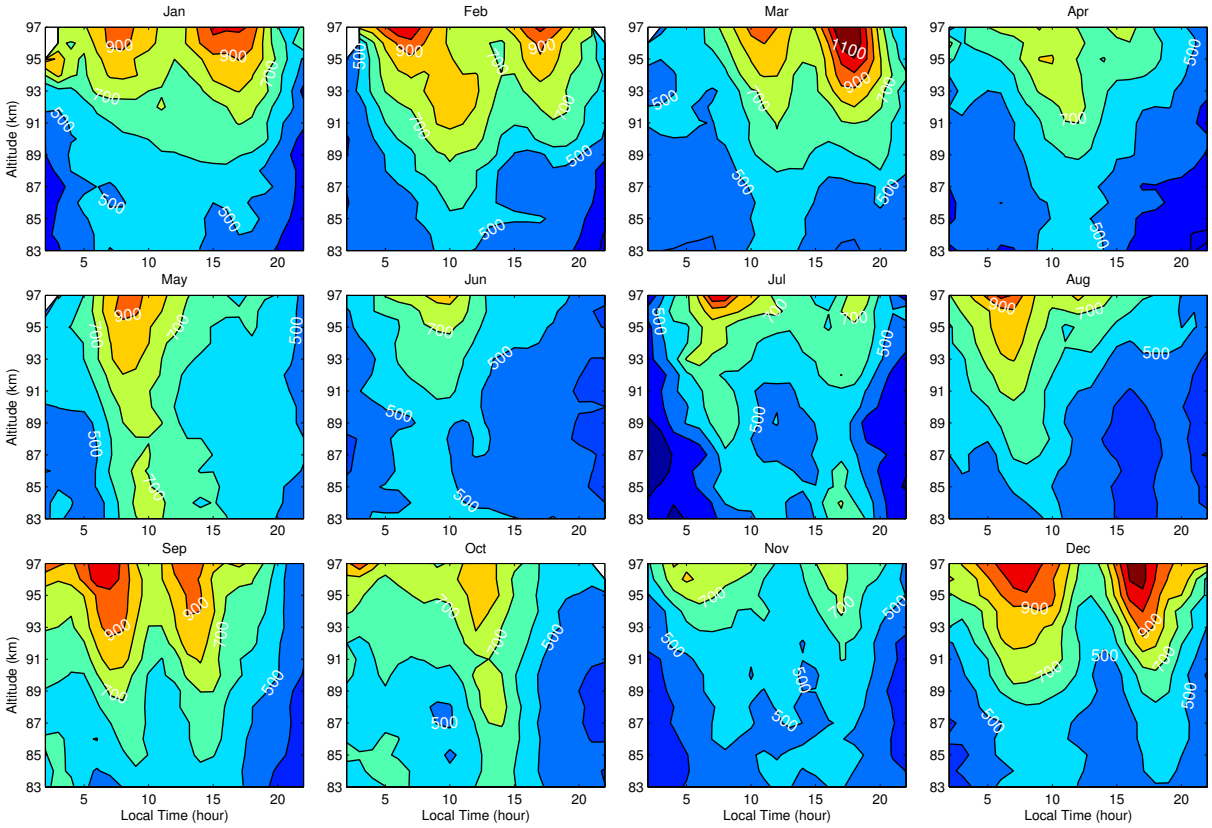

Figure 6.10: Same as Figure 6.8 except for Urbana, IL.

in Urbana (Figure B.5). The modulation of the semidiurnal oscillation is stronger at higher altitude. It suggests that the semidiurnal tides may modulate the GW variances and be responsible for their semidiurnal variations. It is likely that the 8 hrs-oscillation, observed

in September for example, is associated with the terdiurnal tide. But it can also result from the nonlinear interactions between the diurnal and semidiurnal tides since $1/24hr + 1/12hr$ can lead to a period of $1/8hr$.

The differences between Maui and Urbana are observed in light of the vertical phase tilts of the GW variances, which are less significant in Urbana, where the hours corresponding to the peak GW variances usually barely change with altitude. For instance, from April to June, the maximum GW variances occur around 10 UT and vary insignificantly as altitude increases. In September and December when the double peak structures are prominent, the corresponding times change for only ∼2 hrs as altitude increases from 83 to 97 km. In this case, the corresponding vertical wavelength for the semidiurnal variation is around 80 km, which is quite comparable with the vertical wavelength of the semidiurnal tide.

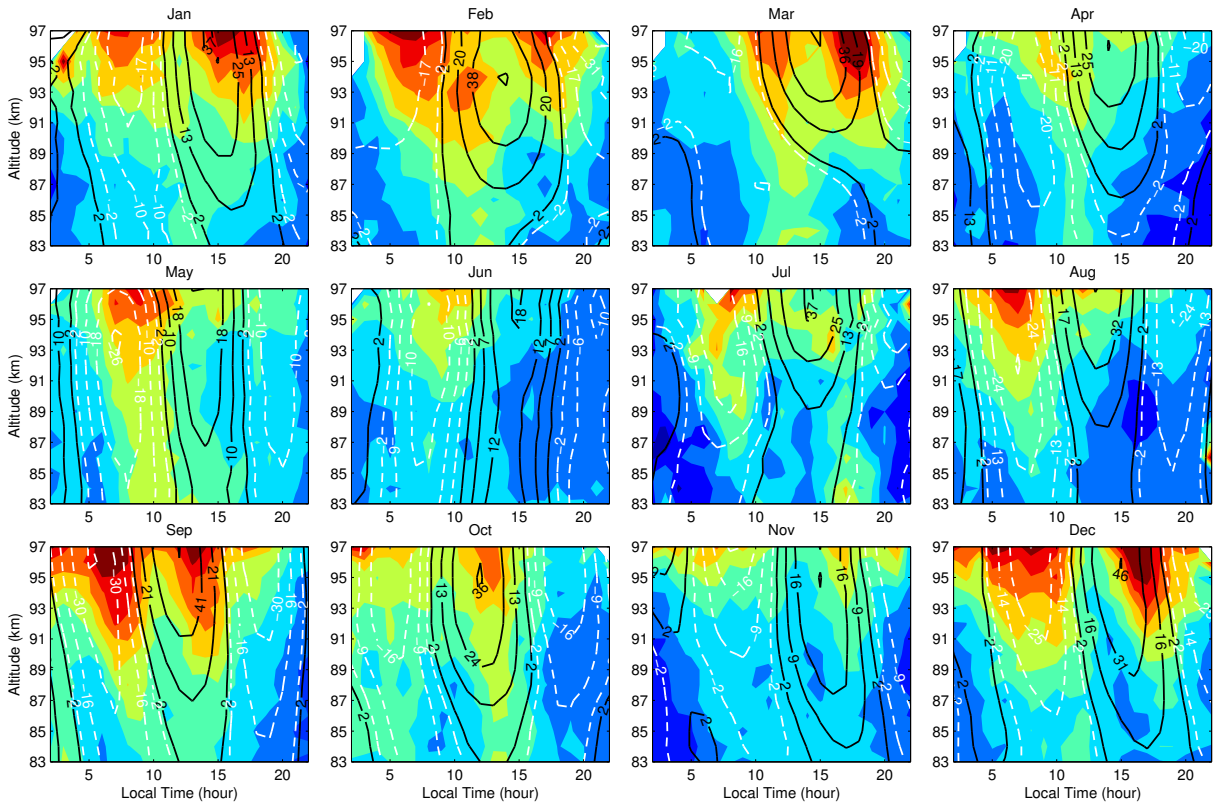

Figure 6.11: Same as Figure 6.9 except for Urbana, IL. The GW variances are linearly detrended at each altitude.

Same as Figure 6.9 for Maui, the superpositions of the mean winds and tidal winds

are over-plotted upon the GW variances for Urbana, as shown in Figure 6.11. The vertical structure of the GW variances follow the vertical shape determined by the mean winds and tides to a large extent except for February. Since in Urbana, the semidiurnal tides are stronger and the diurnal tides are weaker compared to Maui, the vertical tilts of the tidal winds superposed on the mean winds are less significant, so are the GW variances.

6.4 Growth Rates of GW Variances

The GW variances increase in both sites and the grow rates are shown in Figure 6.12 for Maui and Figure 6.13 for Urbana. Note that the vertical profiles of the GW variances are based on the monthly mean daily composite values, so the growth rates are presented in a climatological sense. For Maui, the GW variances grow much slower than the freely propagating case, which means the GWs are partly saturated. In February, March and August, some profiles are close to be freely propagating while in April, GW variances are approximately constant with altitude, which implies waves are saturated. The growth rates of the GW variances are similar in Urbana. Since for Urbana, the GW variances begin to increase significantly above 90 km, such as in March and December. The freely propagating wave variances are also shown for the GWs beginning at 90 km.

The e-fold height of the GW variance H is defined as:

$$A_{z_1} = A_{z_0} e^{\frac{(z-z_0)}{H}} \tag{6.2}$$

where A_{z_0} and A_{z_1} are the GW variances at altitude $z_0 = 83$ km and $z_1 = 97$ km, respectively. They are calculated based on the daily composite vertical profiles of the GW variances. The mean values and standard deviations of H are given in Table 6.1 for each month.

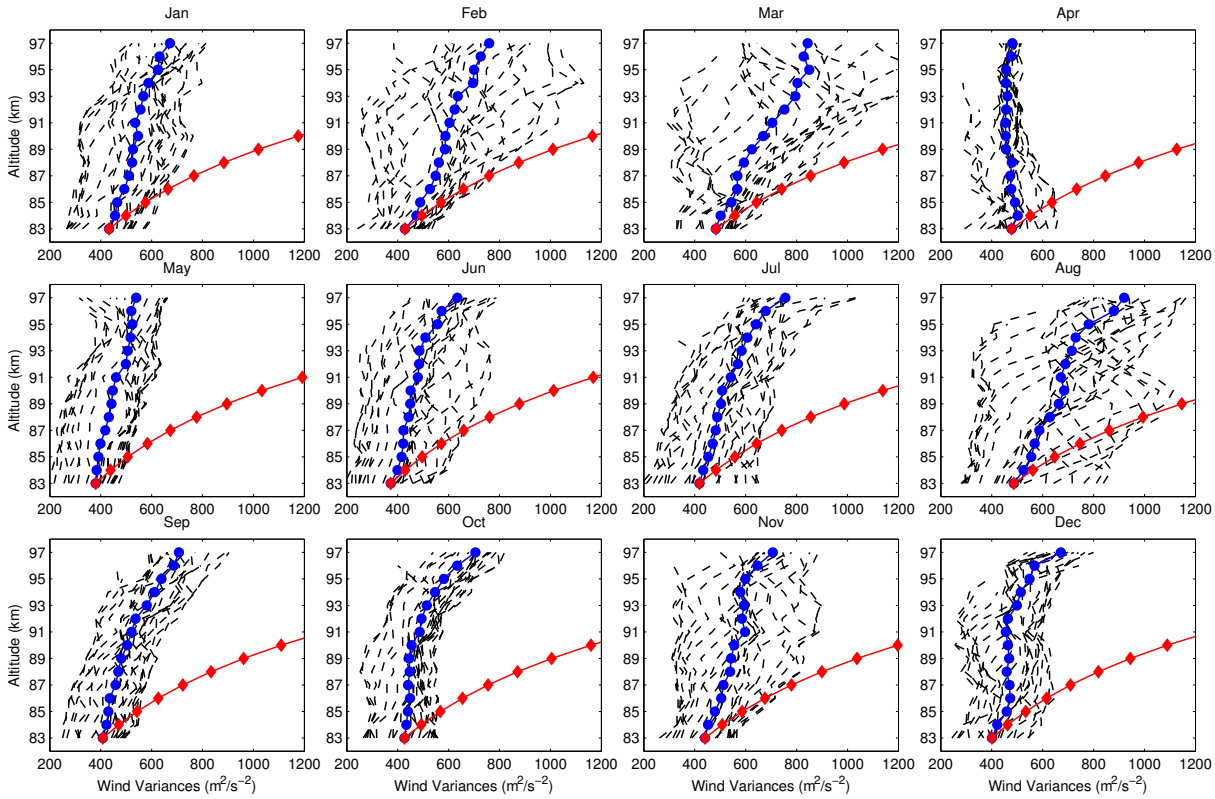

Figure 6.12: The growth rates of the GW variances as compared to the free propagating waves. The black dashed lines are for vertical profiles of the GW variances and the blue circles are the mean variances. The red diamonds correspond to the GW variance increases for freely propagating GWs with same amplitudes at 83 km.

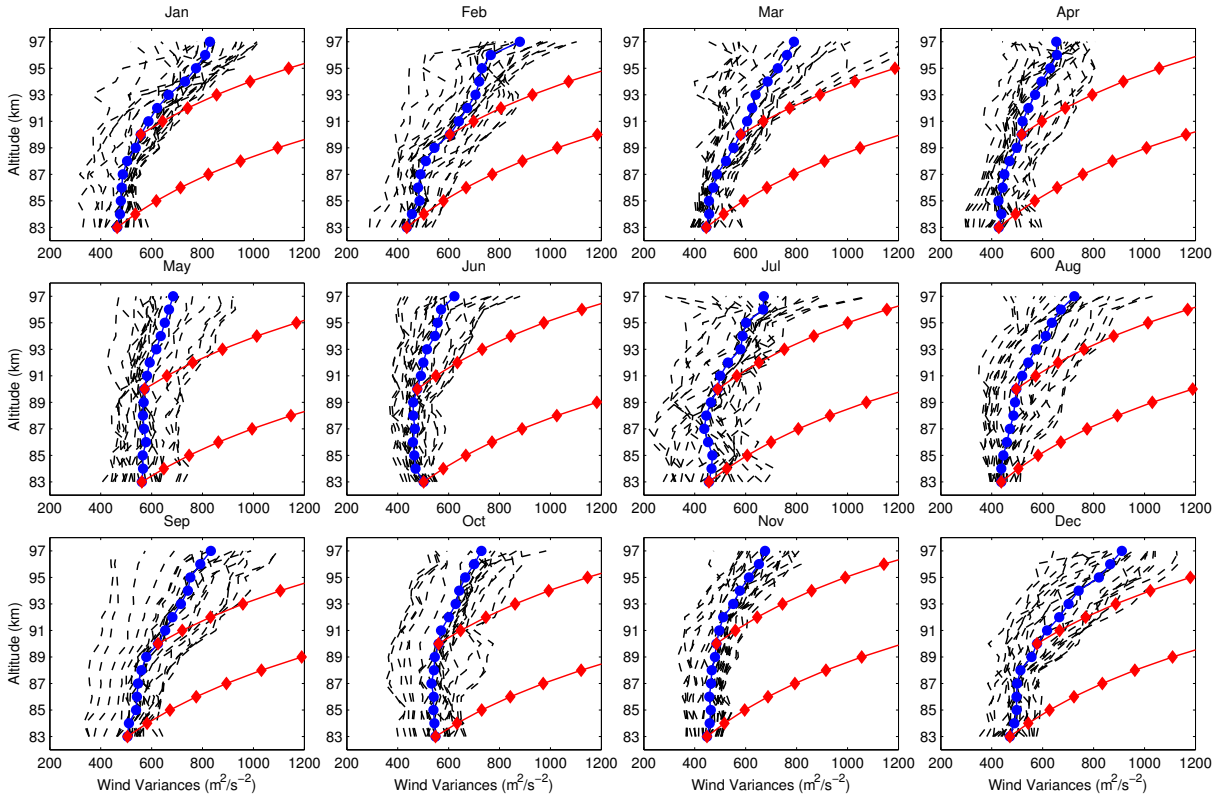

Figure 6.13: Same as Figure 6.12 except for Urbana. The freely propagating GW references are provided at 83 km and 90 km.

Month	Jan	Feb	Mar	Apr	May	Jun	Jul	Aug	Sep	Oct	Nov	Dec
$Mean_1$	37	19	20	40	35	30	23	15	24	33	30	38
STD_1	19.0	6.1	7.3	24.7	13.1	16.6	7.7	4.7	11.1	9.2	12.2	21.8
$Mean_2$	22	19	25	28	44	36	21	26	29	44	33	21
STD_2	6.8	3.4	10.6	7.3	30.0	6.7	7.0	7.0	7.7	19.5	14.4	8.3

Table 6.1: Mean and standard deviation of the growth rate of the GW variance for each month in Maui (subscript 1) and Urbana (subscript 2). The unit is km.

6.5 Summary

By using the meteor radar observations in Maui, HI and Urbana, IL, the GW-induced horizontal wind variances are investigated and the tidal modulations are identified. Two Monte-Carlo simulations are performed in order to evaluate the capability of the MR technique calculating the GW variances. A single-wave and a GW spectrum are added to the background winds for the two simulations, respectively. The background winds and GW variances can be reasonably retrieved by this technique. When the meteor rate is low, the underestimation of the variance exists. The underestimation is about 10% when the meteor rate is as low as 20/4hrs. The standard deviations of the GW variance calculations increase with the decreasing meteor rates.

Two dominant oscillations of the GW variances are diurnal and semidiurnal variations. Other longer period modulations are also observed and their periods are near 2-day, 5-day and 10-day, which are probably associated with the modulations of PWs. Although there is a diurnal cycle of the meteor rate, the possibility that the diurnal variation of the GW variances is solely caused by the meteor rate is ruled out because the GW variances match the tidal structure in many ways. For instance, the vertical tilts of the phases for GW variances and the superposition of the zonal mean and tidal winds are consistent with each other. Also, the variances increase with altitude continuously up to 97 km, while the meteor rate reaches its maximum at 90 km. However, the underestimation with the low meteor rate is still possible, but its effects are not dominant. In addition, the meteor rate only has a diurnal cycle, which can not explain the longer-period and semidiurnal oscillations existing

in the GW variances. Thus, the diurnal and semidiurnal variations of the GW variances probably result from the tidal modulations.

The double peaks of the variances with a time delay of 8-12 hrs between them are frequently observed both in Maui and Urbana based on the monthly mean daily composite GW variances. In Maui, the secondary peaks tend to occur at higher altitudes with stronger strengths in some months. Since the semidiurnal tides are usually reach the maximum amplitudes above 100 km, it is likely that the secondary peaks are associated with the semidiurnal tides. In Urbana, the months with stronger semidiurnal variations of the GW variances are in agreement with the seasonal variations of the semidiurnal tides, again implying the tidal modulations are real. The GW variances in Maui and Urbana are both grow with altitude, but the growth rate is mostly slower than a freely propagating wave. They can freely propagate in limited cases. It suggests that the GWs resolved by this method are partly saturated in a climatological sense.

It is shown that the MR technique can be used to calculate the horizontal wind variances, which are used as a proxy for the GW activities in a certain spectrum. More detailed investigations are needed in order to examine the sensitivity of this method on the GW spectrum chosen for the Monte-Carlo simulation. One possibility for the diurnal and semidiurnal variations of the GW variances that is not considered here is the inherent time variation of the wave source. Also, although the tidal modulations can be identified, they are still complicated and large GW variances can occur in both eastward and westward background winds. The in-depth studies, probably combined with a model simulation, on the possible mechanisms causing these diurnal and smidiurnal variations are required, in order to explain why they occur persistently in the MLT region.

CHAPTER 7

CONCLUSIONS

7.1 Summary

GWs and tides are two most important wave activities in the MLT region, where they affect the mean circulation, thermal balance and composition distribution. They play significant roles in the coupling processes by transporting momentum from the lower to the upper atmosphere and redistributing atmospheric constitutes. This dissertation focuses on the characteristics of an inertial GW observed by Rayleigh and Na lidars, the seasonal variation of the diurnal tide and the possible interactions between GWs and tides.

Based on the simultaneous temperature measurements using the Rayleigh and Na lidars over Hawaii, an inertial GW is found propagating from the stratosphere to the lower thermosphere. The wave parameters, propagation and dissipation characteristics are investigated. The wave intrinsic phase speed is 40 $\mathrm{m\,s^{-1}}$ and intrinsic period is 15 hrs. The horizontal wavelength is about 2140 km. The vertical wavelength changes with altitude from ∼6.4 km in the stratosphere, ∼12.8 km in the lower mesosphere to ∼10.0 km in the upper mesosphere and lower thermosphere. This change of the vertical wavelength is consistent with the change of the buoyancy frequency N, i.e., larger static stability corresponding to a shorter vertical wavelength. The GW propagates northward in the MLT region and is Doppler-shifted by the mean meridional wind. The e-fold height of the wave amplitude in relative temperature perturbation is around 14 km, indicating that the GW is partly dissipated. A prominent damping layer is found right above the stratopause, where the wave amplitude is minimum and wave structure is disturbed. The damping layer corresponds to a low static

stability region, implying a significant impact of the mean background on the vertical wave propagation.

The seasonal variation of the diurnal tide is investigated based on the horizontal wind measurement of the meteor radar in Maui, HI. The SAO is dominant for the amplitude and AO for the phase. Besides the SAO of the amplitude variation, the AO and QBO are also present but with weaker intensities. Tidal amplitudes are stronger at equinoxes and weaker at solstices by a factor of $\sim$1.5. The phase advances in winter and delays in summer, by a difference of $\sim$3 hrs for the zonal wind and $\sim$6 hrs for the meridional wind between winter and summer. The variability of the vertical wavelength shows a clear seasonal trend characterized by shorter vertical wavelengths at equinoxes. The diurnal tide can propagate up to about 95 km and is severely dissipated above that. The ground-based meteor radar observation of the tidal seasonality is consistent with the TIMED wind measurement, based on which DW1 is found to be the dominant tidal component contributing to the seasonal variation of the diurnal tide. The GSWM and WACCM well capture the seasonal variation while discrepancies still exist.

The WACCM is capable of simulating the tidal seasonality, thus it is used to calculate the momentum budget of DW1 and identify the most important terms responsible for changing the amplitude and phase of DW1. Classical tidal theory gives an appropriate first-order depiction of the tidal structure while GW forcing and advection are two most dominant terms resulting in the deviations. In the WACCM, GW forcing tends to damp DW1 and advances its phase in a latitude range of $\pm 50^{\circ}$. Linear advection is important to change the phase of DW1 in the zonal wind. It is largely determined by the latitudinal shear of the zonal mean zonal wind. Unlike the zonal wind, the nonlinear advection is a dominant term contributing to the momentum budget of DW1 in the meridional wind.

Although the GW damping effect on DW1 is large in the WACCM, its seasonal variation can not explain the seasonality of DW1 since both of them are stronger at equinoxes and weaker at solstices. Instead, the radiative solar heating through the absorption by water

vapor in the troposphere has a stronger projection onto the symmetric (1,1) Hough mode since it has more symmetric distribution at equinox. Linear mechanistic models also confirm that incorporating the realistic tidal heating can reproduce the SAO of the amplitude. The mean winds can also modulate the time that the maximum amplitude occurs. More importantly, mean winds are responsible for generating the AO of the phase. At solstice, the antisymmetric (1,2) Hough mode is stronger in the presence of the asymmetric mean wind and distorts the symmetric tidal structure of the (1,1) mode. Since the (1,2) mode switches to the opposite phase from winter to summer, the phase is advanced in the winter hemisphere and delayed in the summer hemisphere, thus resulting in an AO of the phase variation for DW1.

The last part of this dissertation involves the tidal modulations of GW variances based on the meteor radar wind measurements in Maui, HI and Urbana, IL. After removing the contributions from mean winds, PWs and tides to the horizontal winds of meteors, the horizontal wind variances are thought to be caused by high-frequency GWs. The Monte-Carlo simulation indicates that this is a good proxy for calculating the GW-induced variances. Diurnal and semidiurnal oscillations are most dominant for the GW variances, which are likely to be modulated by the diurnal and semidiurnal tides. The evidences of the possible modulations are also shown as the consistent vertical structures of tidal winds and GW variances. Double peaks of the GW variances with a time delay of 8-12 hrs are frequently observed in both Maui and Urbana, which is probably associated with the modulation by the semidiurnal tide. The differences in the GW variances in Maui and Urbana can be related to the different dominant tides. The GW variances increase with altitude in both sites. The growth rate indicates that the resolved GWs are not freely propagating in most cases. It is worth mentioning that a disadvantage of this method is that it can not identify each single wave. Thus, wave interferences can not be resolved if a GW spectrum is considered.

7.2 Future Work

The first part of this dissertation is a case-study on the propagation and dissipation of an inertial GW, and its relation with the static stability of the mean background. Statistical studies are apparently needed in order to make more general and assertive conclusions on wave characteristics, background impacts and wave sources. This requires a collection of simultaneous observations from the lower to the upper atmosphere, which is also valuable in studying coupling processes.

The seasonal variations of DW1 phases in temperature at the equator, zonal and meridional winds at 20°N are shown in Figure 7.1. The seasonal variations become significant and persistent above 50 km. Below 40 km, the seasonal variation of DW1 in temperature is negligible while in zonal and meridional winds, they are different from the counterparts in the MLT region. Based on the DOPE model, *Ortland* also found that the ozone heating ($\sim$45 km) is more sensitive to the mean wind change in terms of the amplitude and phase responses, while the water vapor heating in the troposphere is not (private communication with Dr. David Ortland). The interference of DW1 generated by H_2O and O_3 heating and the mean wind effect for each heating would be interesting to investigate in the future.

It is noted that the conclusions made on the mechanisms causing the seasonal variation of the diurnal tide are mostly based on model simulations up to now, which need to be validated by observations. Observations could provide constraints on the parameterizations, and more realistic parameterizations of heating, convection and GWs are all valuable to obtain a better understanding of this question.

For the last topic of this dissertation, model simulation is needed in order to examine the physical mechanisms causing the tidal modulations of GWs. A wave spectrum can be launched in the lower atmosphere and a GW model can be used to examine the momentum deposition and wave variances as waves propagate through the background determined by mean winds, PWs and tides. The possible relation between the GW variances and back-

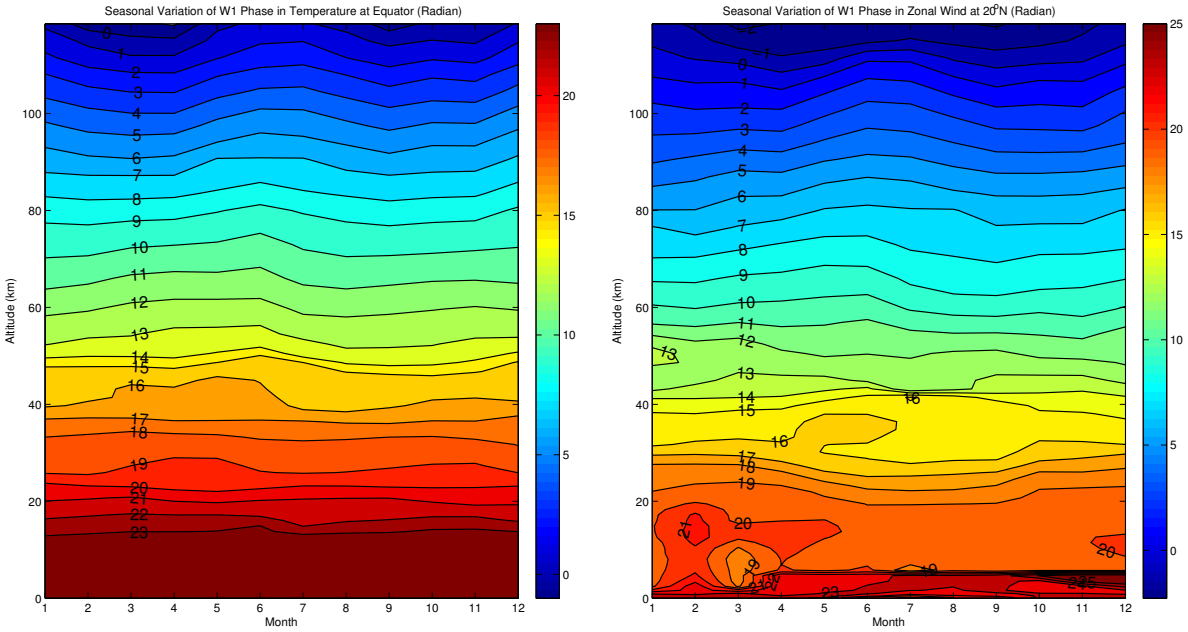

(a) Temperature

(b) Zonal Wind

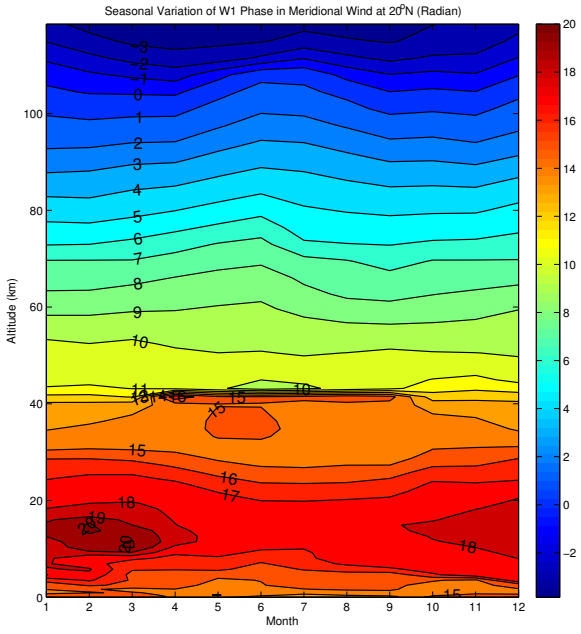

(c) Meridional Wind

Figure 7.1: Seasonal variations of DW1 phases in temperature at the equator (a) and zonal (b) and meridional winds (c) at 20°N.

ground winds can be identified based on the model simulation. As another possibility of the diurnal and semidiurnal variations, wave source needs a thorough evaluation and satellite data capable of showing the convective activities may be used for this study. There are three different sites with the meteor radar wind measurements, Maui, Urbana and Chile. GWs observed in Chile are more likely to be generated by topography, while in Maui and Urbana, convection or frontal systems are probably the primary sources. The different dominant wave sources for them are possible to cause the differences of the GW variances, which will be studied in detail. The differences could due to the different tidal modulations and/or different wave sources, which will be identified.

APPENDIX A

GLOSSARY

u	Zonal wind velocity
v	Meridional wind velocity
w	Vertical wind velocity
P	Pressure
P_s	Pressure at 1000 hPa reference level
Φ	Geopotential
ρ	Density
ρ_0	Basic state density
T	Temperature
θ	Potential temperature
Q	External heating
H	Scale height
R	Ideal gas constant
c_p	Specific heat at constant pressure
κ	Ratio of specific heat
N	Brunt-Väisälä frequency (or buoyancy frequency)
a	Earth radius
g	Gravity acceleration
c_s	Sound speed
ϕ	Latitude
λ	Longitude

Ω Rotation rate of the Earth

f Coriolis parameter $f = 2\Omega \sin \phi$

ω Frequency

s Zonal wavenumber

d/dt Total derivative of time

$\partial/\partial t$ Partial derivative of time

The zonal mean quantities are denoted by barred variables (e.g., $\bar{u}, \bar{v}, \bar{w}$) while the perturbative quantities are denoted by primed variables (e.g., u', v', w'). The complex amplitudes are denoted with a hat (e.g., $\hat{u}, \hat{v}, \hat{w}$).

APPENDIX B

SUPPLEMENTAL FIGURES: CHAPTER 4

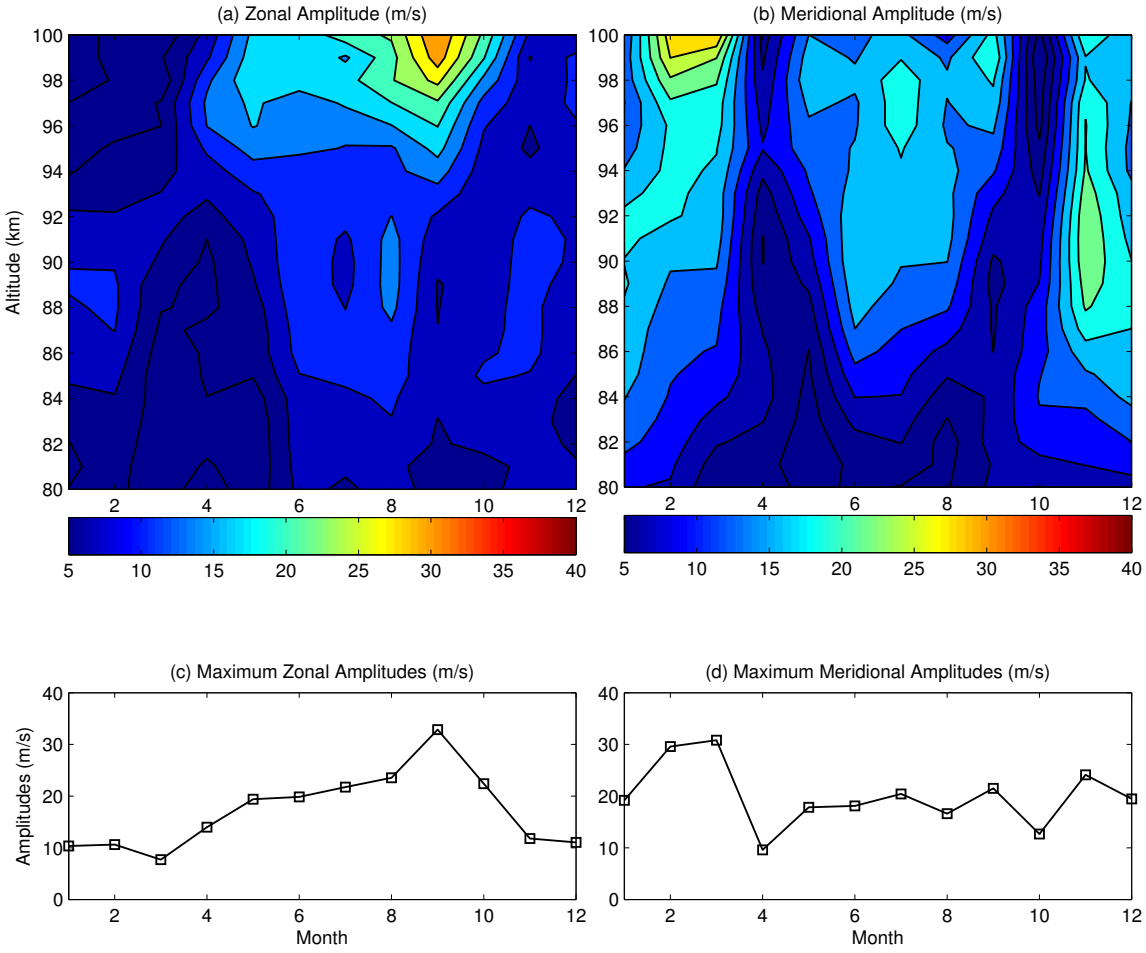

Figure B.1: Seasonal variation of the monthly mean amplitude of the semidiurnal tide in Maui.

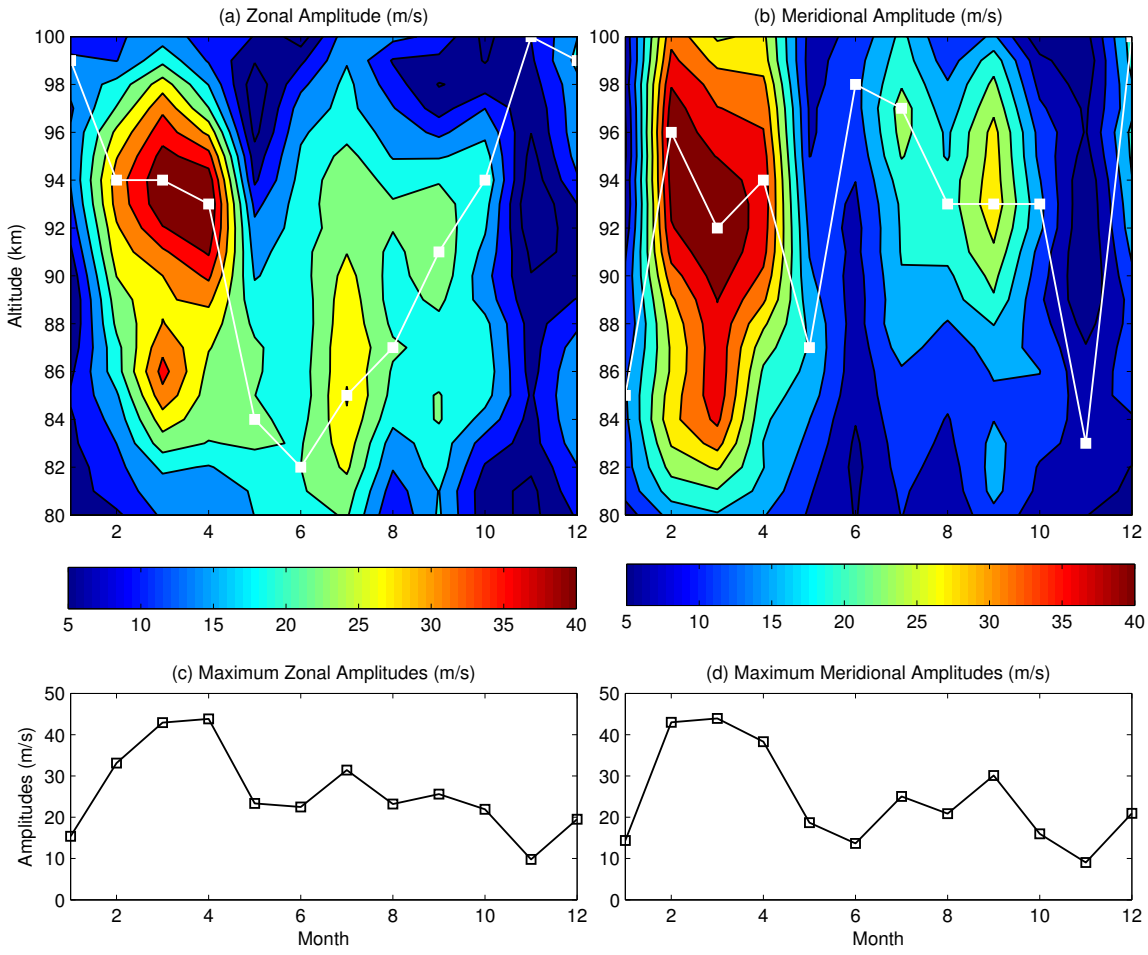

Figure B.2: Seasonal variation of the monthly mean amplitude of the diurnal tide in Chile.

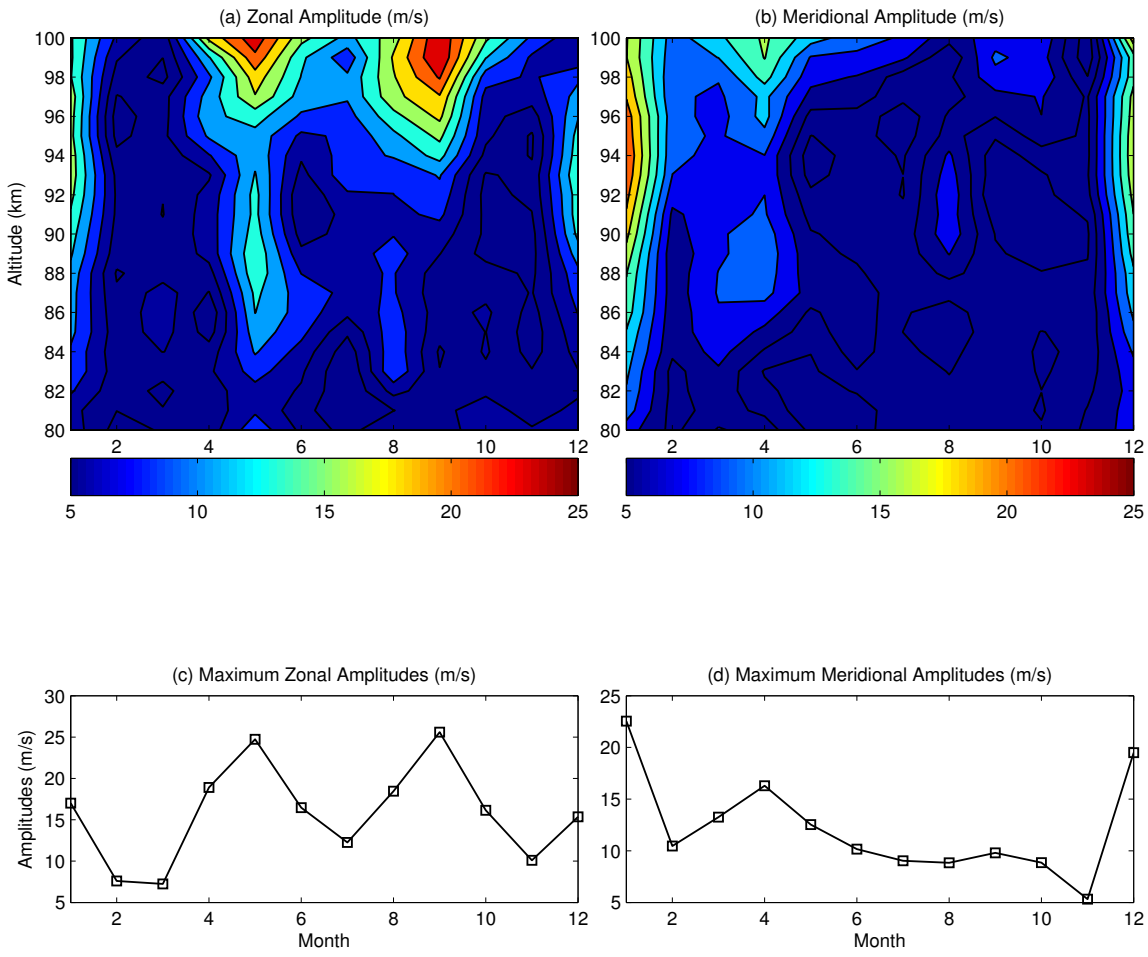

Figure B.3: Same as Figure B.2 but for the denoted semidiurnal tide

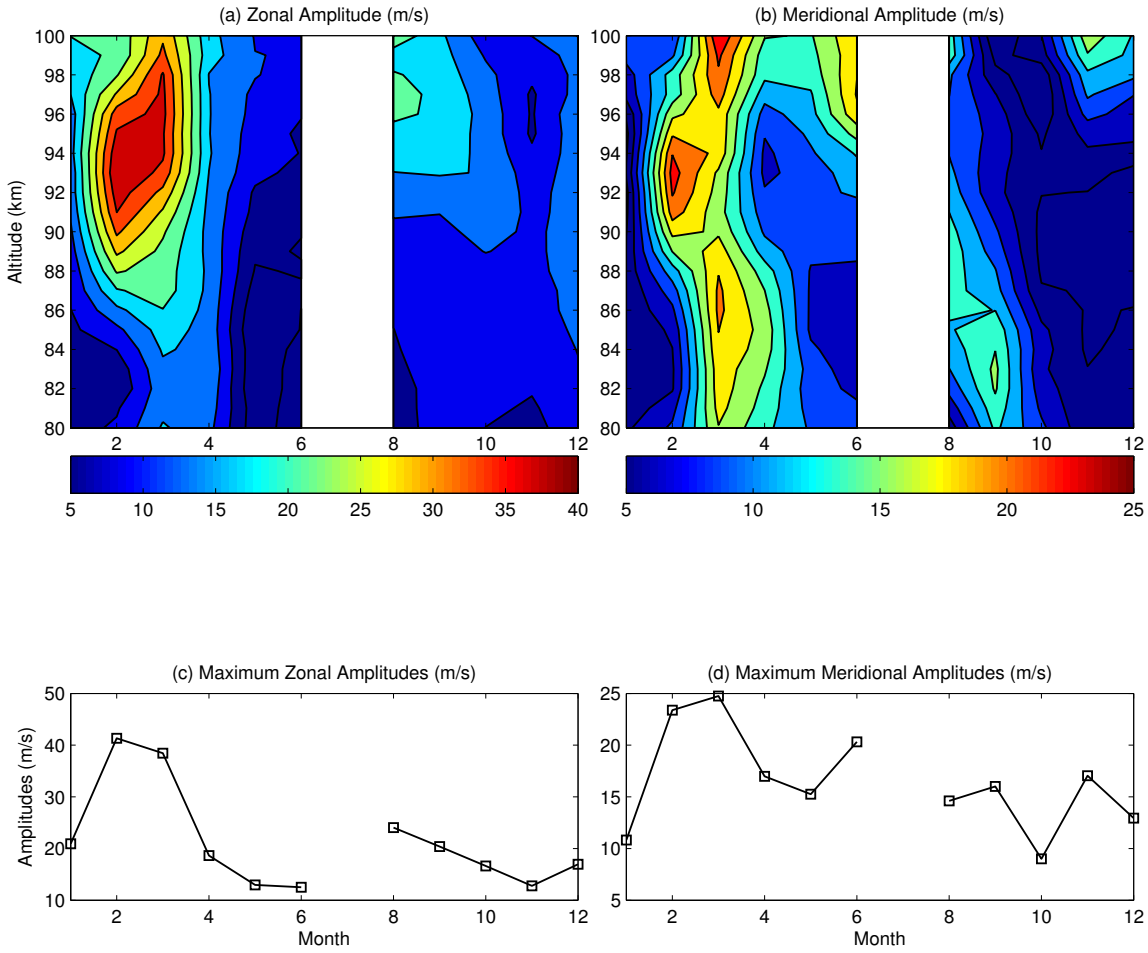

Figure B.4: Seasonal variation of the monthly mean amplitude of the diurnal tide in Urbana.

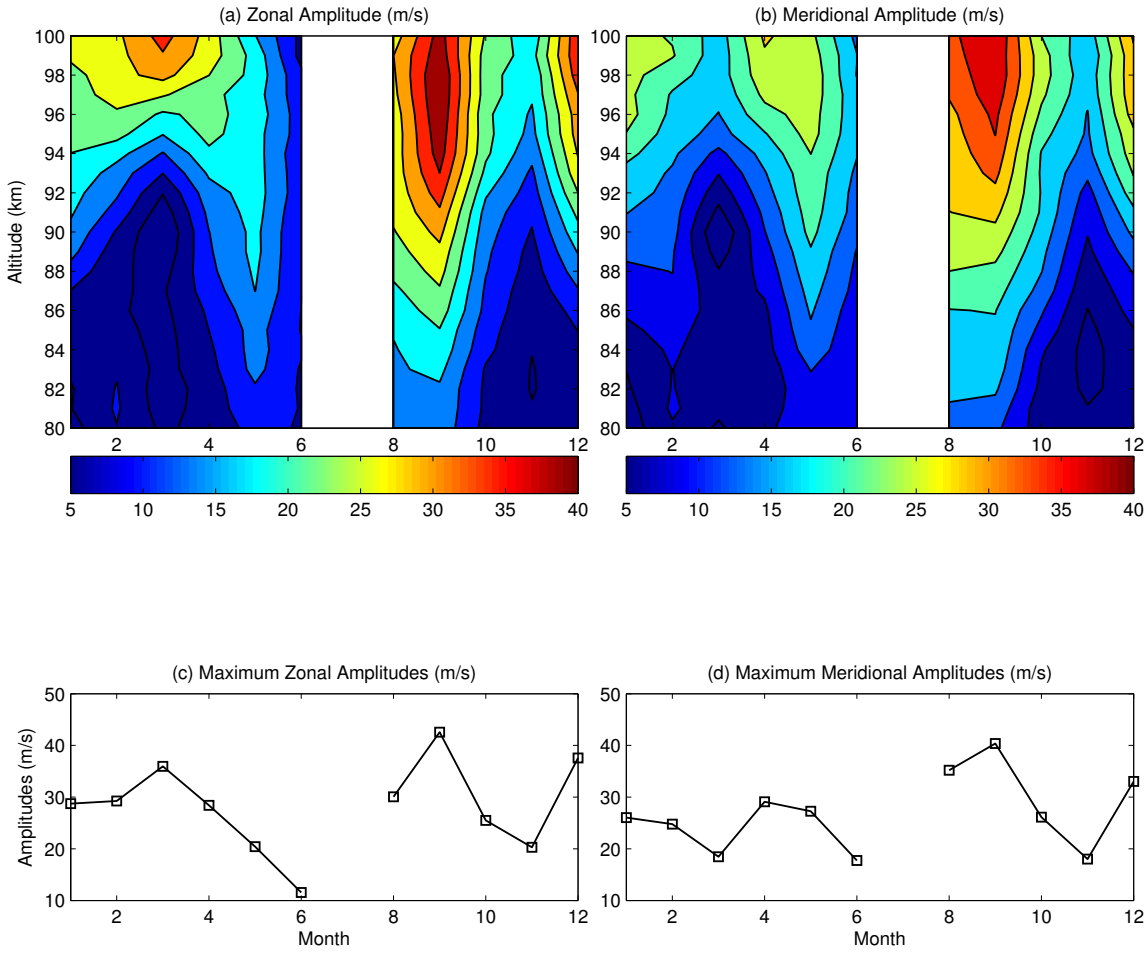

Figure B.5: Same as Figure B.4 but for the semidiurnal tide

APPENDIX C

SUPPLEMENTAL FIGURES: CHAPTER 5

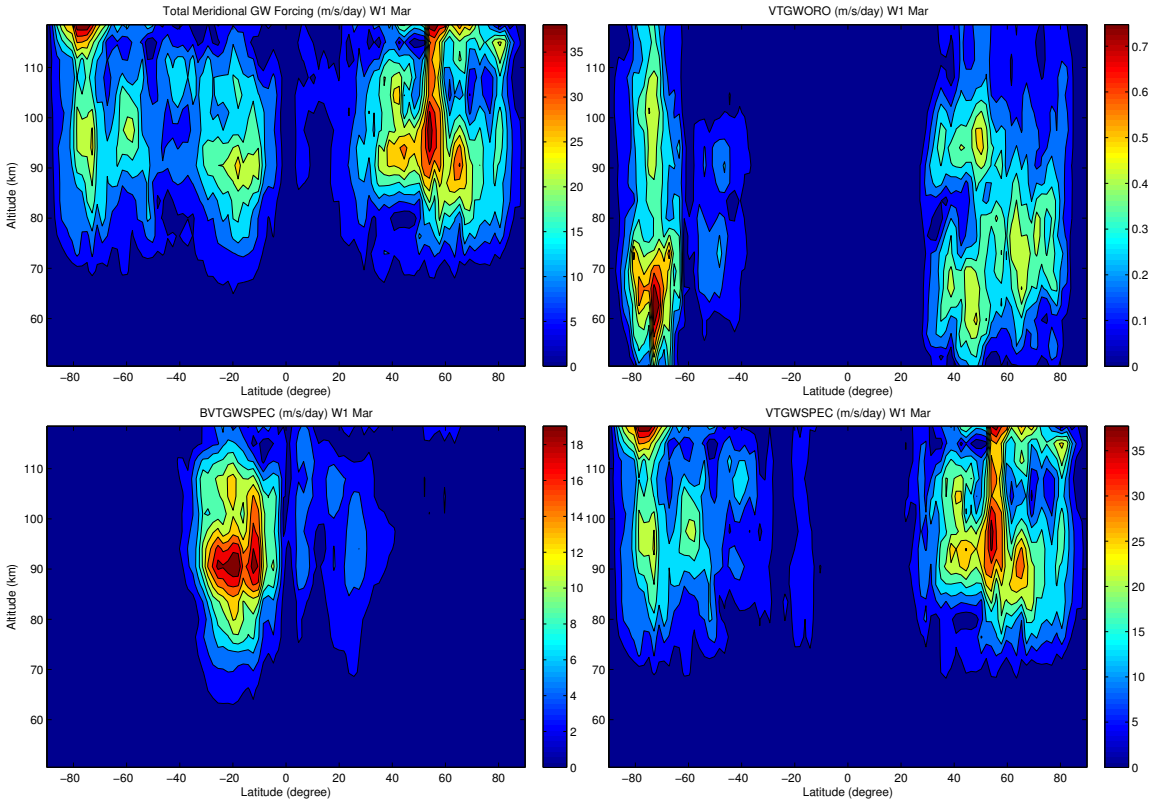

Figure C.1: Amplitudes of GW forcing originating from orography (VTGWORO), convection (BVTGWSPEC), frontogenesis (VTGWSPEC) and the total forcing (Total) in terms of the time tendency projecting onto DW1.

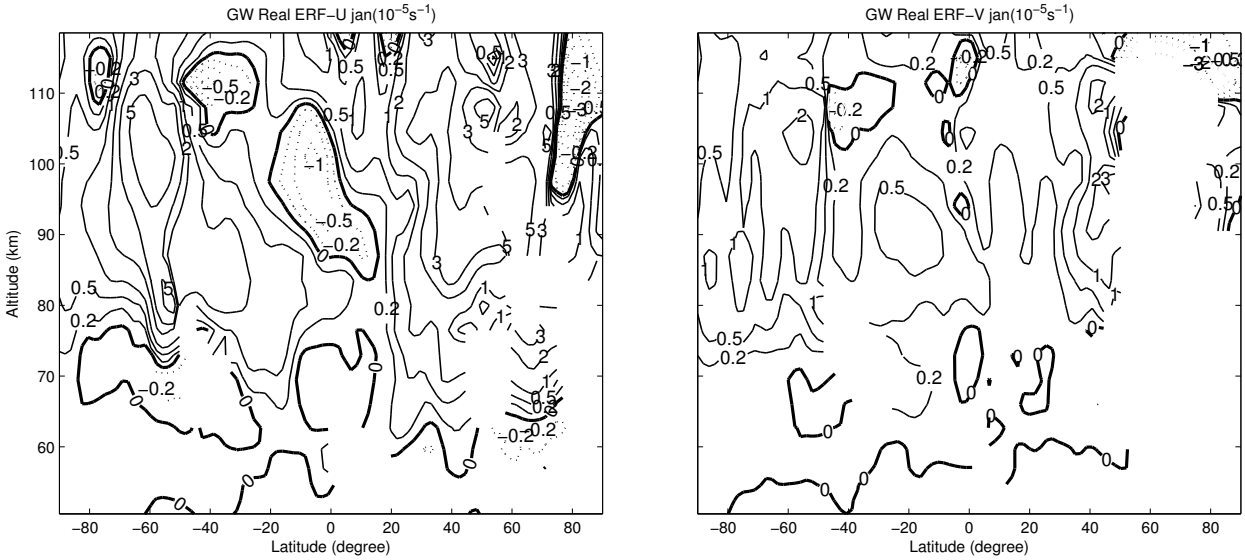

Figure C.2: Real part of the ERF of GW forcing in January. Solid and dotted linear are for positive and negative values, respectively. Zero-value contours are highlighted by the thick solid lines. Contour intervals: ±0.2, ±0.5, ±1, ±2, ±3, ±5, ±8.

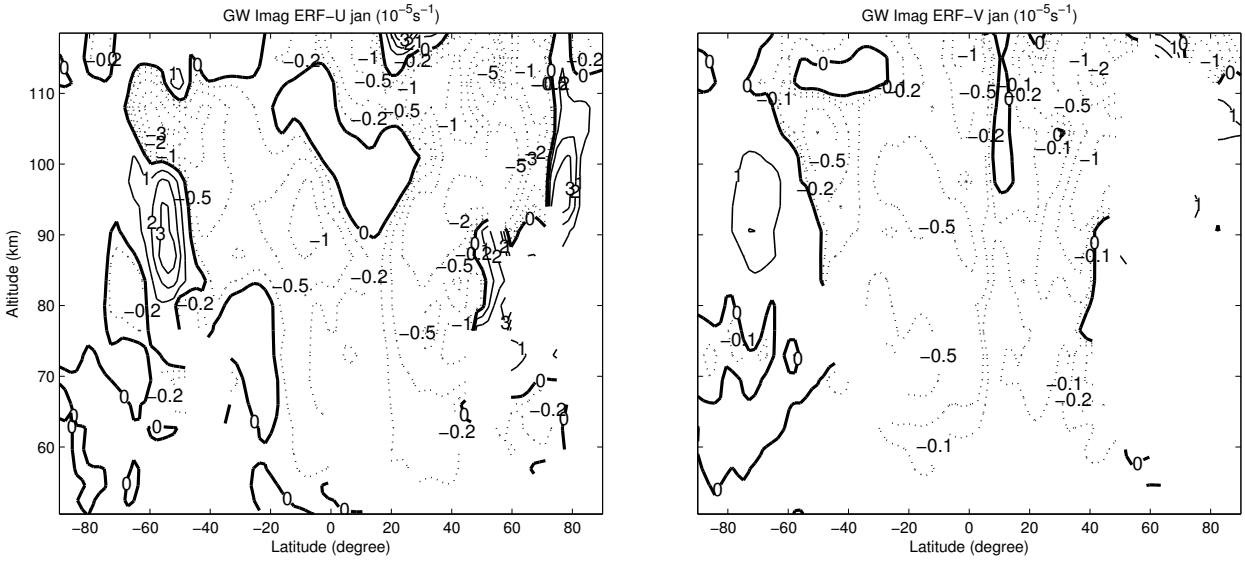

Figure C.3: Same as Figure C.2 except for the imaginary part.

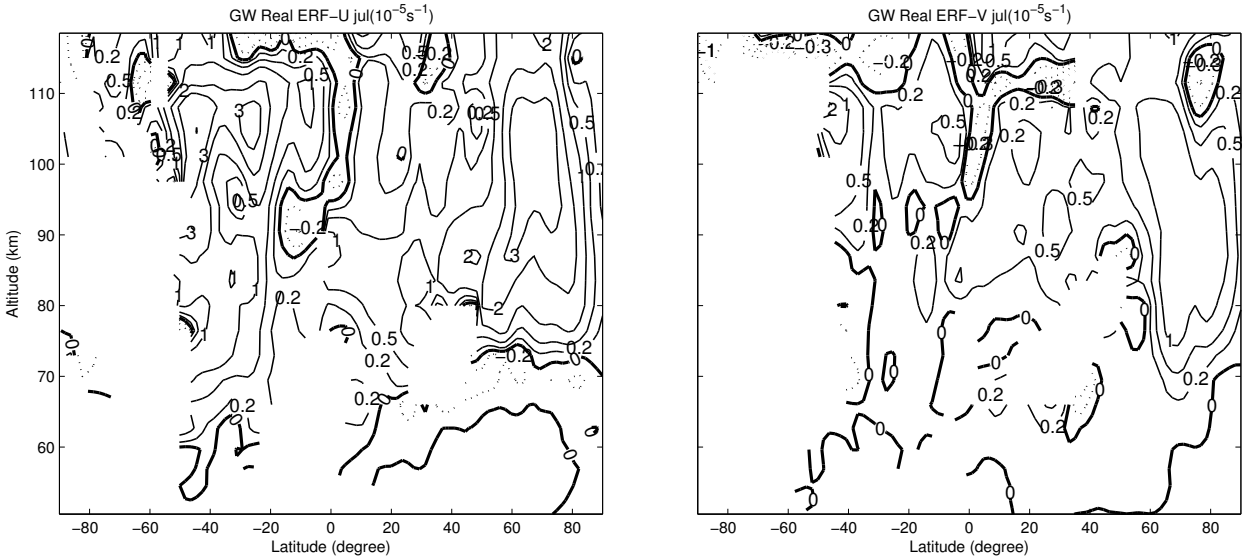

Figure C.4: Same as Figure C.2 except for July.

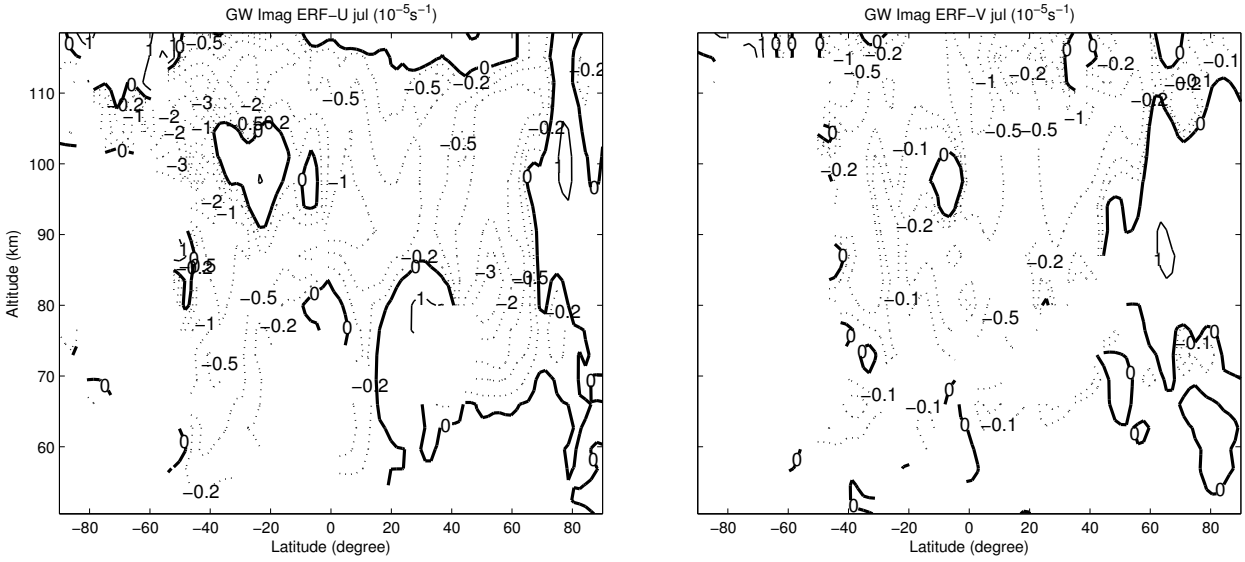

Figure C.5: Same as Figure C.3 except for July.

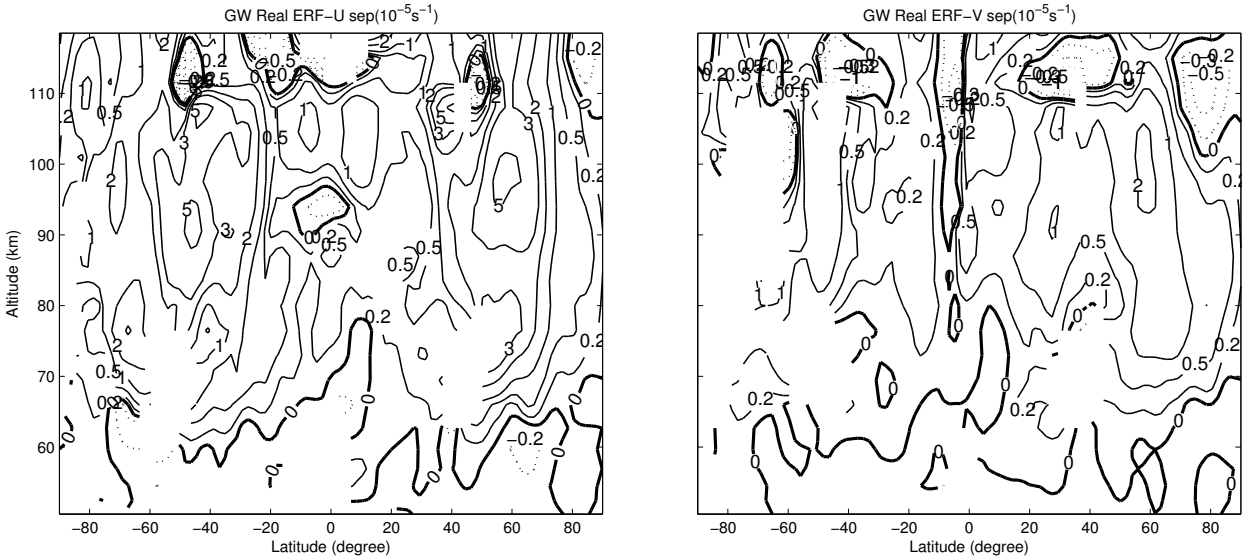

Figure C.6: Same as Figure C.2 except for September.

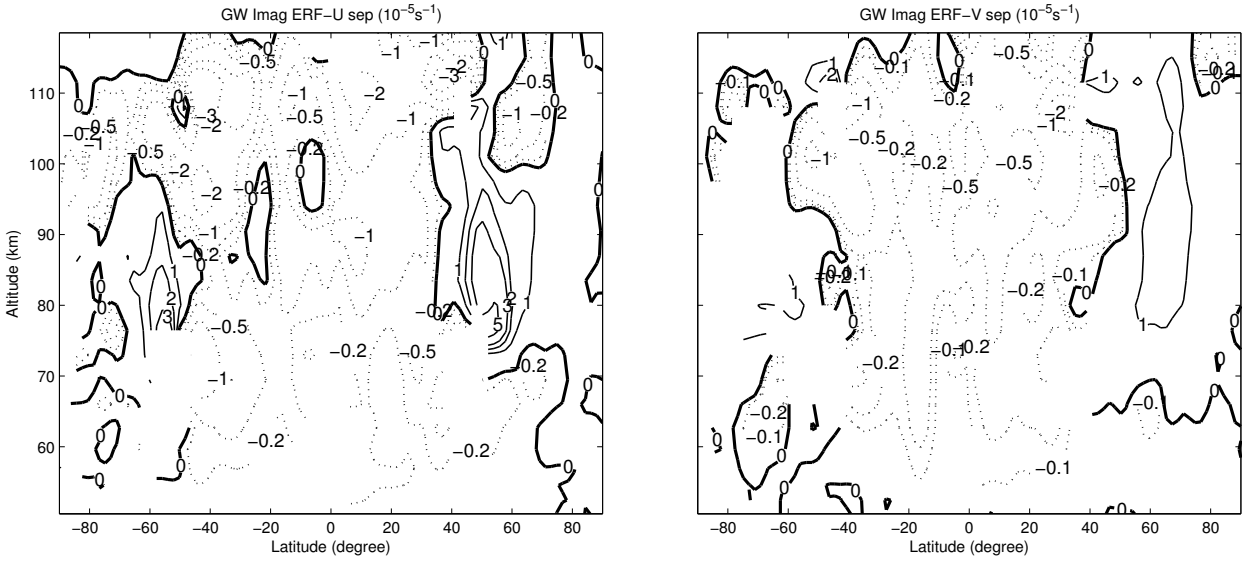

Figure C.7: Same as Figure C.3 except for September.

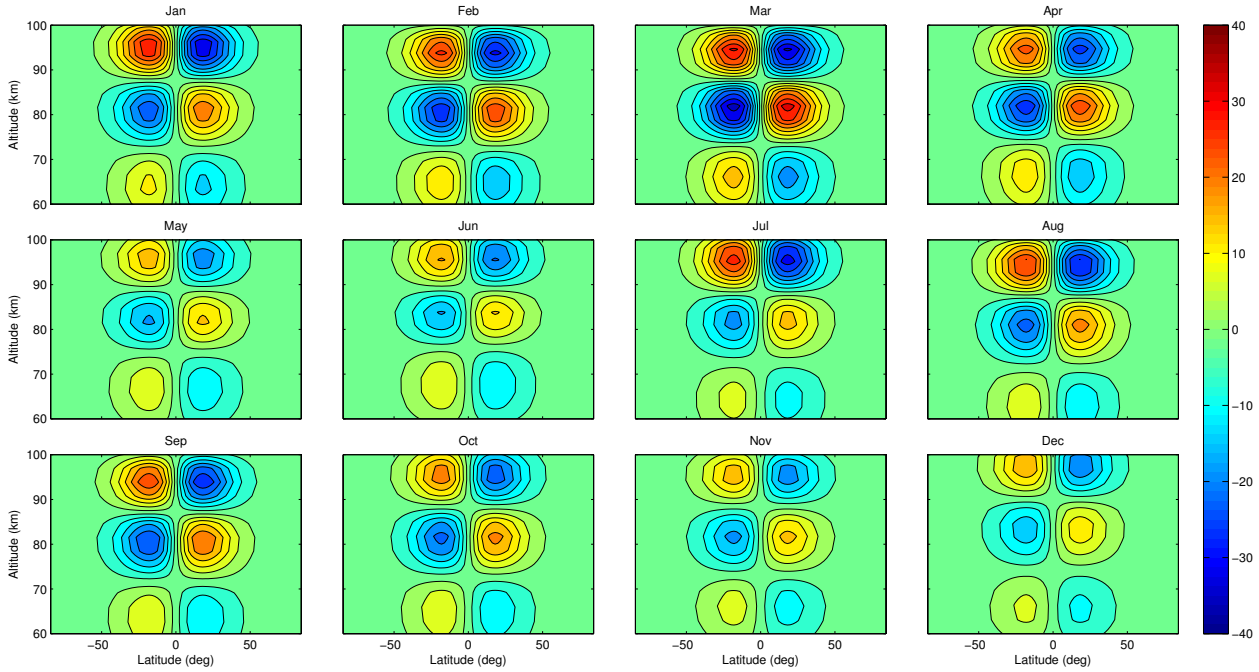

Figure C.8: Seasonal variation of the (1,1) Hough mode in the meridional wind.

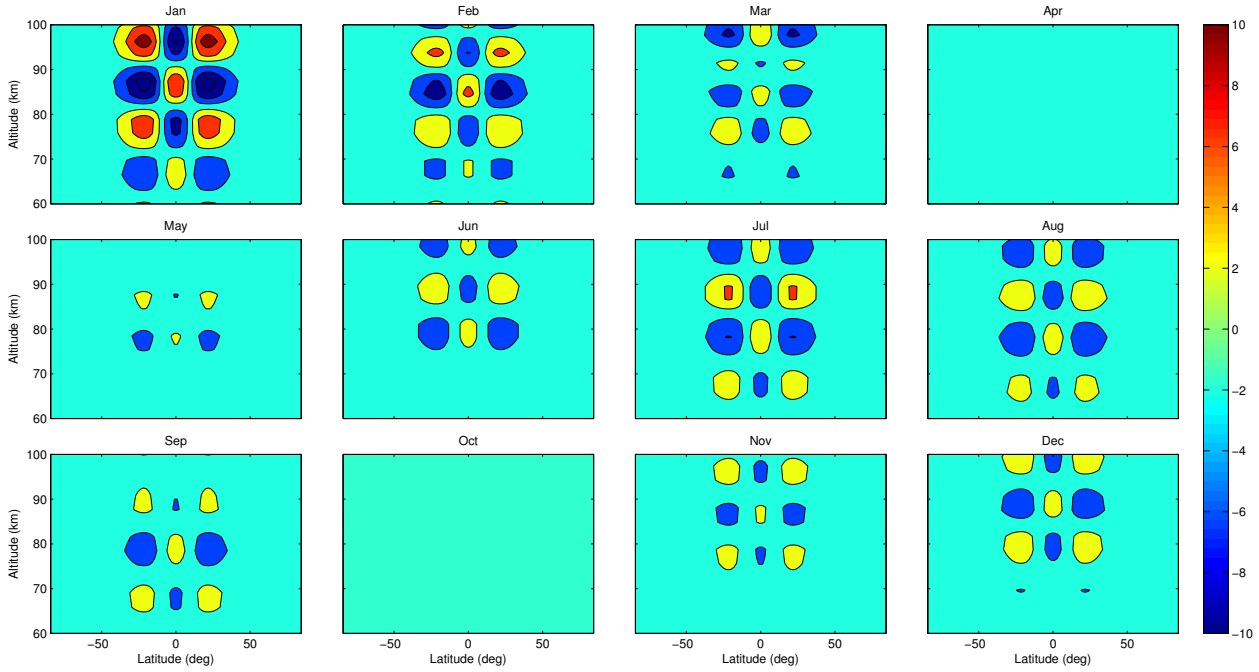

Figure C.9: Same as Figure C.8 except for the (1,2) mode.

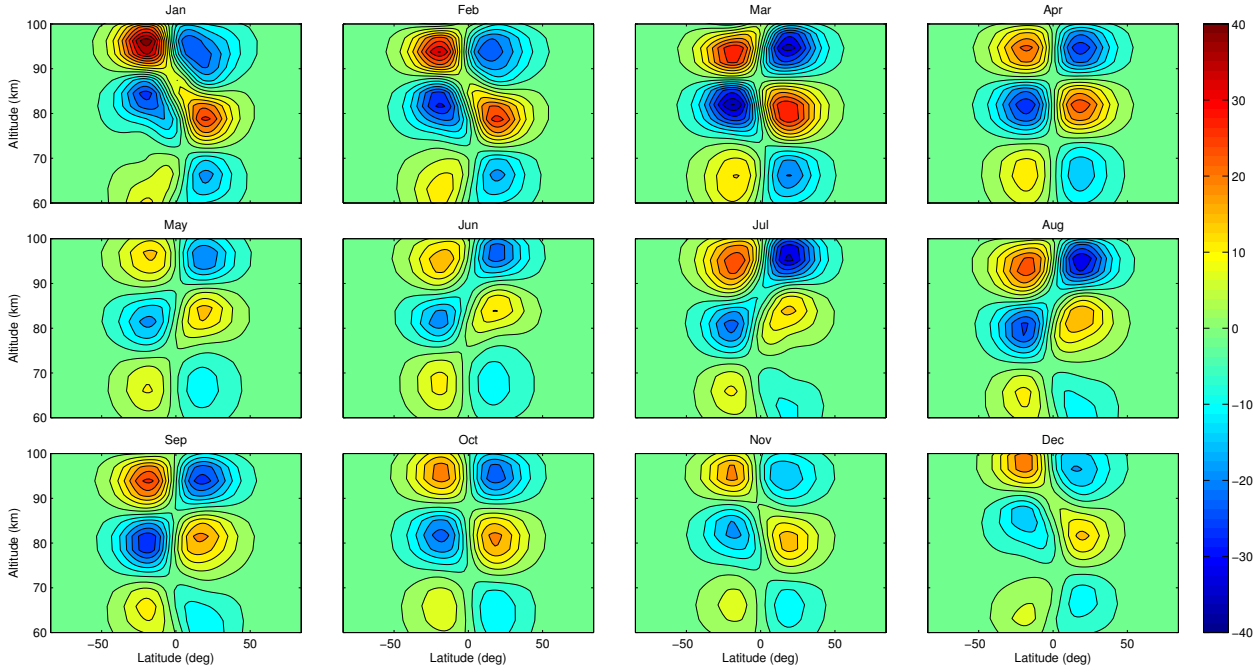

Figure C.10: Same as Figure C.8 except for the superposition of (1,1) and (1,2) modes.

APPENDIX D

SUPPLEMENTAL FIGURES: CHAPTER 6

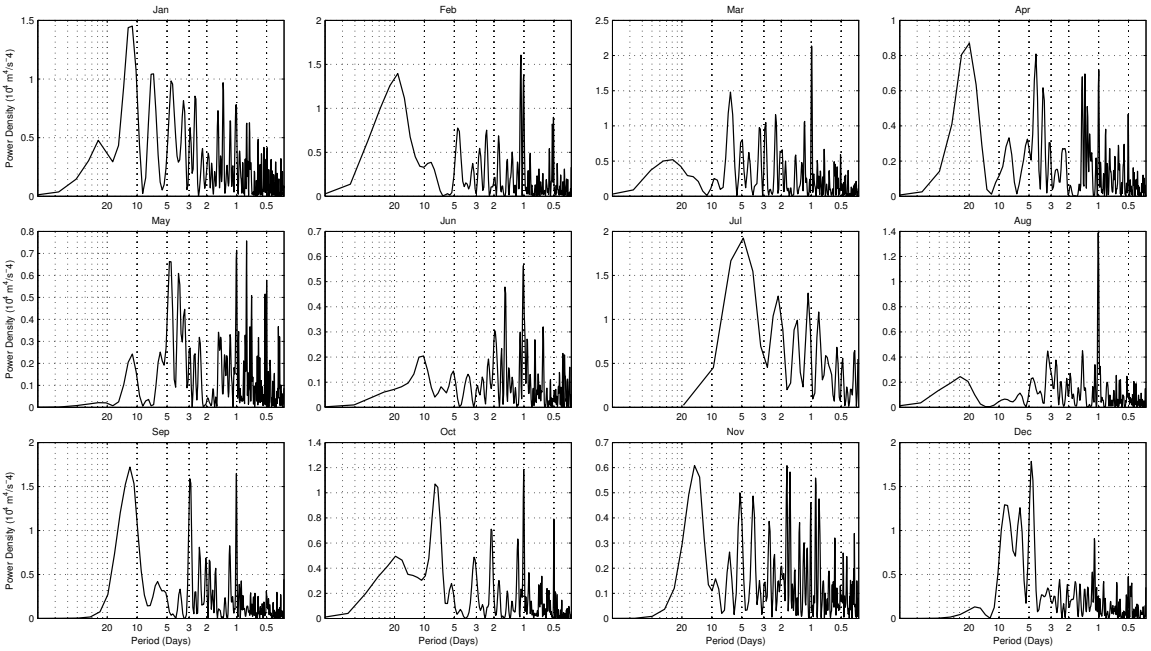

Figure D.1: Same as Figure 6.7 except for Urbana, IL.

REFERENCES

Achatz, U., N. Grieger, and H. Schmidt (2008), Mechanisms controlling the diurnal solar tide: Analysis using a GCM and a linear model, *J. Geophys. Res.*, *113*, 08,303, doi:10.1029/2007JA012967.

Alexander, M. J., and T. J. Dunkerton (1999), A spectral parameterization of mean-flow forcing due to breaking gravity waves., *J. Atmos. Sci.*, *56*, 4167.

Alexander, M. J., et al. (2008), Global estimates of gravity wave momentum flux from high resolution dynamics limb sounder observations, *J. Geophys. Res.*, *113*, D15S18, doi:10.1029/2007JD008807.

Alpers, M., R. Eixmann, C. Fricke-Begemann, M. Gerding, and J. Hffner (2004), Temperature lidar measurements from 1 to 105 km altitude using resonance, rayleigh, and rotational raman scattering, *Atmos. Chem. Phys.*, *4*, 793.

Andrews, D. G., J. R. Holton, and C. B. Leovy (1987), *Middle Atmosphere Dynamics*, *International Geophysical Series*, vol. 40, 489 pp., Academic Press.

Bacmeister, J. T., M. R. Schoeberl, L. R. Lait, P. A. Newman, and B. Gary (1990), ER-2 mountain wave encounter over Antarctica - Evidence for blocking, *Geophys. Res. Lett.*, *17*, 81–84, doi:10.1029/GL017i001p00081.

Beatty, T. J., C. A. Hostetler, and C. S. Gardner (1992), Lidar Observations of Gravity Waves and Their Spectra near the Mesopause and Stratopause at Arecibo, *J. Atmos. Sci.*, *49*, 477.

Beres, J. H., R. R. Garcia, B. A. Boville, and F. Sassi (2005), Implementation of a gravity wave source spectrum parameterization dependent on the properties of convection in the Whole Atmosphere Community Climate Model (WACCM), *J. Geophys. Res.*, *110*, 10,108.

Buhler, O., and M. E. McIntyre (1999), On shear-generated gravity waves that reach the mesosphere. Part II: wave propagation, *J. Atmos. Sci.*, *56*, 3764.

Burrage, M. D., M. E. Hagan, W. R. Skinner, D. L. Wu, and P. B. Hays (1995), Long-term variability in the solar diurnal tide observed by HRDI and simulated by the GSWM, *Geophys. Res. Lett.*, *22*(19), 2641–2644.

Chandra, S., E. L. Fleming, M. R. Schoeberl, and J. J. Barnett (1990), Monthly mean global climatology of temperature, wind, geopotential height and pressure for 0-120 km, *Adv. Space Res.*, *10*, 3, doi:10.1016/0273-1177(90)90230-W.

Chang, J. L., and S. K. Avery (1997), Observations of the diurnal tide in the mesosphere and lower thermosphere over christmas island, *J. Geophys. Res.*, *102*(D2), 1895–1907.

Chang, L., S. Palo, M. Hagan, J. Richter, R. Garcia, D. Riggin, and D. Fritts (2008), Structure of the migrating diurnal tide in the Whole Atmosphere Community Climate Model (WACCM), *Adv. Space Res.*, *41*(9), 1398–1407.

Chanin, M.-L., and A. Hauchecorne (1981), Lidar observation of gravity and tidal waves in the stratosphere and mesosphere, *J. Geophys. Res.*, *86*(C10), 9715–9721.

Chapman, S., and R. S. Lindzen (1970), *Atmospheric Tides*, Gordon and Breach, New York.

Chu, X., C. S. Gardner, and S. J. Franke (2005), Nocturnal thermal structure of the mesosphere and lower thermosphere region at Maui, Hawaii (20.7 °N), and Starfire Optical Range, New Mexico (35 °N), *J. Geophys. Res.*, *110*, D09S03, doi:10.1029/2004JD004891.

Chu, X. Z., and G. C. Papen (2005), Resonance fluorescence lidar for measurement of the Middle and Upper Atmosphere, in *Laser Remote Sensing*, vol. 87, edited by T.Takashi and T.Fukuchi, pp. 179–432, Tayloy & Francis Group.

Deepa, V., G. Ramkumar, M. Antonita, K. K. Kumar, and M. N. Sasi (2006), Vertical propagation characteristics and seasonal variability of tidal wind oscillations in the MLT region over Trivandrum (8.5 °N, 77 °E): first results from SKiYMET Meteor Radar, *Ann. Geophys.*, *24*, 2877–2889.

Deepa, V., G. Ramkumar, T. M. Antonita, and K. K. Kumar (2008), Meteor wind radar observations of tidal amplitudes over a low-latitude station Trivandrum (8.5 °N, 77 °E): Interannual variability and the effect of background wind on diurnal tidal amplitudes, *J. Atmos. Sol. -Terr. Phys.*, *70*, 2005–2013.

England, S. L., A. Dobbin, M. J. Harris, N. F. Arnold, and A. D. Aylward (2006), A study into the effects of gravity wave activity on the diurnal tide and airglow emissions in the equatorial mesosphere and lower thermosphere using the coupled middle atmosphere and thermosphere (cmat) general circulation model, *J. Atmos. Sol. -Terr. Phys.*, *68*, 293.

Espy, P. J., G. O. L. Jones, G. R. Swenson, J. Tang, and M. J. Taylor (2004), Tidal modulation of the gravity-wave momentum flux in the antarctic mesosphere, *Geophys. Res. Lett.*, *31*, 11,111.

Fetzer, E. J., and J. C. Gille (1994), Gravity Wave Variance in LIMS Temperatures. Part I: Variability and Comparison with Background Winds., *J. Atmos. Sci.*, *51*, 2461–2483.

Forbes, J. M. (1995), Tidal and Planetary Waves, in *The upper Mesosphere and Lower Thermosphere: A Review of Experiment and Theory, Geophys. Monogr. Ser*, vol. 87, edited by R.M.Johnson and T.L.Killeen, pp. 67–87, AGU, Washington, D.C.

Forbes, J. M., and M. E. Hagan (1982), Thermospheric extensions of the classical expansion functions for semidiurnal tides, *J. Geophys. Res.*, *87*, 5253, doi:10.1029/JA087iA07p05253.

Forbes, J. M., and M. E. Hagan (1988), Diurnal propagating tide in the presence of mean winds and dissipation - A numerical investigation, *Planet. Space Sci.*, *36*(6), 579–590.

Forbes, J. M., and D. Wu (2006), Solar tides as revealed by measurements of mesosphere temperature by the mls experiment on uars., *J. Atmos. Sci.*, *63*, 1776, doi:10.1175/JAS3724.1.

Forbes, J. M., J. Gu, and S. Miyahara (1991), On the interactions between gravity waves and the diurnal propagating tide, *Planet. Space Sci.*, *39*, 1249.

Forbes, J. M., S. E. Palo, and X. Zhang (2000), Variability of the ionosphere, *J. Atmos. Sol. -Terr. Phys.*, *62*, 685, doi:10.1016/S1364-6826(00)00029-8.

Forbes, J. M., X. Zhang, and M. E. Hagan (2001), Simulations of diurnal tides due to tropospheric heating from the NCEP/NCAR reanalysis project, *Geophys. Res. Lett.*, *28*(20), 3851–3854.

Forbes, J. M., X. Zhang, E. R. Talaat, and W. Ward (2003), Nonmigrating diurnal tides in the thermosphere, *J. Geophys. Res.*, *108*, 1033, doi:10.1029/2002JA009262.

Forbes, J. M., X. Zhang, S. Palo, J. Russell, C. J. Mertens, and M. Mlynczak (2008), Tidal variability in the ionospheric dynamo region, *J. Geophys. Res.*, *113*, 02,310, doi:10.1029/2007JA012737.

Franke, S. J., and D. Thorsen (1993), Mean winds and tides in the upper middle atmosphere at Urbana (40 °N, 88 °W) during 1991-1992, *J. Geophys. Res.*, *98*(D10), 18,607–18,615, doi:10.1029/93JD01840.

Franke, S. J., X. Chu, A. Z. Liu, and W. K. Hocking (2005), Comparison of meteor radar and Na Doppler lidar measurements of winds in the mesopause region above Maui, Hawaii, *J. Geophys. Res.*, *110*, D09S02, doi:10.1029/2003JD004486.

Fricke-Begemann, C., J. Hoffner, and U. von Zahn (2002), The potassium density and temperature structure in the mesopause region (80-105 km) at a low latitude (28 °N), *Geophys. Res. Lett.*, *29*, 24.

Friedman, J. S. (2003), Tropical mesopause climatology over the arecibo observatory, *Geophys. Res. Lett.*, *30*, 44, doi:10.1029/2003GL016966.

Fritts, D. C. (1984), Gravity wave saturation in the middle atmosphere: A review of theory and observations, *Rev. Geophys. Space Phys.*, *22*, 275–308.

Fritts, D. C., and M. J. Alexander (2003), Gravity wave dynamics and effects in the middle atmosphere, *Reviews of Geophysics*, *41*, 1003.

Fritts, D. C., and W. Lu (1993), Spectral estimates of gravity wave energy and momentum fluxes. part ii: Parameterization of wave forcing and variability, *J. Atmos. Sci.*, *50*(22), 3695–3713.

Fritts, D. C., and P. K. Rastogi (1985), Convective and dynamical instabilities due to gravity wave motions in the lower and middle atmosphere: Theory and observations, *Radio Science*, *20*, 1247.

Fritts, D. C., and R. A. Vincent (1987), Mesospheric momentum flux studies at Adelaide, Australia: Observations and a gravity wave-tidal interaction model, *J. Atmos. Sci.*, *44*(3), 605–619.

Fritts, D. C., and L. Yuan (1989), Stability analysis of intertio-gravity wave structure in the middle atmosphere, *J. Atmos. Sci.*, *46*(12), 1738–1745.

Garcia, R. R., and S. Solomon (1985), The effect of breaking gravity waves on the dynamics and chemical composition of the mesosphere and lower thermosphere, *J. Geophys. Res.*, *90*(D2), 3850–3868.

Garcia, R. R., D. R. Marsh, D. E. Kinnison, B. A. Boville, and F. Sassi (2007), Simulation of secular trends in the middle atmosphere, 1950-2003, *J. Geophys. Res.*, *112*, A09,301, doi:10.1029/2006JD007485.

Gardner, C. S., and G. C. Papen (1995), Mesospheric Na wind/temperature lidar, *Laser Review*, *23*(2), 131–134.

Gardner, C. S., and D. G. Voelz (1987), Lidar studies of the nighttime sodium layer over urbana, illinois 2. gravity waves, *J. Geophys. Res.*, *92*(A5), 4673–4694.

Gardner, C. S., M. S. Miller, and C. H. Liu (1989), Rayleigh lidar observations of gravity wave activity in the upper stratosphere at urbana, illinois, *J. Atmos. Sci.*, *46*(12), 1838–1854.

Gardner, C. S., Y. Zhao, and A. Z. Liu (2002), Atmospheric stability and gravity wave dissipation in the mesopause region, *J. Atmos. Sol.-Terr. Phys.*, *64*(8-11), 923–929.

Gavrilov, N. M., S. Fukao, T. Nakamura, T. Tsuda, M. D. Yamanaka, and M. Yamamoto (1996), Statistical analysis of gravity waves observed with the middle and upper atmosphere radar in the middle atmosphere 1. method and general characteristics, *J. Geophys. Res.*, *101*, 29,511.

Gong, J., M. A. Geller, and L. Wang (2008), Source spectra information derived from U.S. high-resolution radiosonde data, *J. Geophys. Res.*, *113*, D10,106, doi:10.1029/2007JD009252.

Griffiths, M., and M. J. Reeder (1996), Stratospheric inertiagravity waves generated in a numerical model of frontogenesis. I: Model solutions., *Q J ROY METEOR SOC*, *122*, 1153–1174.

Guest, F. M., M. J. Reeder, C. J. Marks, and D. J. Karoly (2000), Inertia-Gravity Waves Observed in the Lower Stratosphere over Macquarie Island., *J. Atmos. Sci.*, *57*, 737–752, doi:10.1175/1520-0469(2000)057.

Hagan, M. E., and J. M. Forbes (2002), Migrating and nonmigrating tides in the middle and upper atmosphere excited by tropospheric latent heat release, *J. Geophys. Res.*, *107*(D24), 4754, doi:10.1029/2001JD001236.

Hagan, M. E., and R. G. Roble (2001), Modeling diurnal tidal variability with the National Center for Atmospheric Research thermosphere-ionosphere-mesosphere-electrodynamics general circulation model, *J. Geophys. Res.*, *106*(A11), 24,869–24,882.

Hagan, M. E., J. M. Forbes, and F. Vial (1995), On modeling migrating solar tides, *Geophys. Res. Lett.*, *22*(8), 893–896.

Hagan, M. E., M. D. Burrage, J. M. Forbes, J. Hackney, W. J. Randel, and X. Zhang (1999), GSWM-98: Results for migrating solar tides, *J. Geophys. Res.*, *104*(A4), 6813–6827, doi:10.1029/1998JA900125.

Hagan, M. E., R. G. Roble, and J. Hackney (2001), Migrating thermospheric tides, *J. Geophys. Res.*, *106*, 12,739, doi:10.1029/2000JA000344.

Hecht, J. H., R. L. Walterscheid, D. C. Fritts, J. R. Isler, D. C. Senft, C. S. Gardner, and S. J. Franke (1997), Wave breaking signatures in OH airglow and sodium densities and temperatures 1. Airglow imaging, Na lidar and MF radar observations, *J. Geophys. Res.*, *102*(D6), 6655–6668.

Hedin, A. E., et al. (1996), Empirical wind model for the upper, middle and lower atmosphere., *J. Atmos. Terr. Phys.*, *58*, 1421.

Hines, C. O. (1997a), Doppler-spread parameterization of gravity-wave momentum deposition in the middle atmosphere. Part 1: Basic formulation, *J. Atmos. Terr. Phys.*, *59*(4), 371–386.

Hines, C. O. (1997b), Doppler-spread parameterization of gravity-wave momentum deposition in the middle atmosphere. Part 2: Broad and quasi monochromatic spectra, and implementation, *J. Atmos. Sol.-Terr. Phys.*, *59*(4), 387–400.

Hocking, W. K. (2005), A new approach to momentum flux determinations using SKiYMET meteor radars, *Ann. Geophys.*, *23*, 2433–2439.

Hocking, W. K., T. Thayaparan, and J. Jones (1997), Meteor decay times and their use in determining a diagnostic mesospheric temperature-pressure parameter: Methodology and one year of data, *Geophys. Res. Lett.*, *24*(23), 2977–2980.

Hocking, W. K., B. Fuller, and B. Vandepeer (2001), Real-time determination of meteor-related parameters utilizing modern digital technology, *J. Atmos. Sol. -Terr. Phys.*, *63*, 155–169.

Holton, J. R. (1982), The role of gravity wave induced drag and diffusion in the momentum budget of the mesosphere, *J. Atmos. Sci.*, *39*, 791.

Holton, J. R. (2004), *An Introduction to Dynamic Meteorology, Fourth Edition*, Elsevier Academic Press, London, UK.

Hu, X., A. Z. Liu, C. S. Gardner, and G. R. Swenson (2002), Characteristics of quasi-monochromatic gravity waves observed with lidar in the mesopause region at Starfire Optical Range, NM, *Geophys. Res. Lett.*, *29*(24), 2169, doi:10.1029/2002GL014,975.

Huang, F. T., and C. A. Reber (2003), Seasonal behavior of the semidiurnal and diurnal tides, and mean flows at 95 km, based on measurements from the High Resolution Doppler Imager (HRDI) on the Upper Atmosphere Research Satellite (UARS), *J. Geophys. Res.*, *108*, 4360, doi:10.1029/2002JD003189.

Immel, T. J., E. Sagawa, S. L. England, S. B. Henderson, M. E. Hagan, S. B. Mende, H. U. Frey, C. M. Swenson, and L. J. Paxton (2006), Control of equatorial ionospheric morphology by atmospheric tides, *Geophys. Res. Lett.*, *33*, L15,108, doi:10.1029/2006GL026,161.

Isler, J. R., and D. C. Fritts (1996), Gravity wave variability and interaction with lower-frequency motions in the mesosphere and lower thermosphere over hawaii, *J. Atmos. Sci.*, *55*(1), 37–48.

Karoly, D. J., G. L. Roff, and M. J. Reeder (1996), Gravity wave activity associated with tropical convection detected in toga coare sounding data, *Geophys. Res. Lett.*, *23*, 261, doi:10.1029/96GL00023.

Killeen, T. L., Q. Wu, S. C. Solomon, D. A. Ortland, W. R. Skinner, R. J. Niciejewski, and D. A. Gell (2006), TIMED Doppler Interferometer: Overview and recent results, *J. Geophys. Res.*, *111*, doi:10.1029/2005JA011484.

Kishore, P., S. P. Namboothiri, K. Igarashi, Y. Murayama, and B. J. Watkins (2002), MF radar observations of mean winds and tides over Poker Flat, Alaska (65.1 °N, 147.5 ° W), *Ann. Geophys.*, *20*, 679–690.

Laplace, P. S. (1825), *Mechanique Celeste, 5*, Paris, France.

Leblanc, T., I. S. McDermid, A. Hauchecorne, and P. Keckhut (1998), Evaluation of optimization of lidar temperature analysis algorithms using simulated data, *J. Geophys. Res.*, *103*, 6177.

Leblanc, T., I. S. McDermid, and D. A. Ortland (1999a), Lidar observations of the middle atmospheric thermal tides and comparison with the High Resolution Doppler Imager and Global-Scale Wave Model 1. Methodology and winter observations at Table Mountain (34.4 °N), *J. Geophys. Res.*, *104*(D10), 11,917–11,929.

Leblanc, T., I. S. McDermid, and D. A. Ortland (1999b), Lidar observations of the middle atmospheric thermal tides and comparison with the High Resolution Doppler imager and Global Scale Wave Model 2. October observations at Mauna Loa (19.5 °N), *J. Geophys. Res.*, *104*, 11,931, doi:10.1029/1999JD900008.

Li, F., A. Z. Liu, and G. R. Swenson (2005a), Characteristics of instabilities in the mesopause region over Maui, Hawaii, *J. Geophys. Res.*, *110*, D09S12, doi:10.1029/2004JD005097.

Li, F., A. Z. Liu, G. R. Swenson, J. H. Hecht, and W. A. Robinson (2005b), Observations of gravity wave breakdown into ripples associated with dynamical instabilities, *J. Geophys. Res.*, *110*, D09S11, doi:10.1029/2004JD004849.

Li, T., C. Y. She, H.-L. Liu, and M. T. Montgomery (2007a), Evidence of a gravity wave breaking event and the estimation of the wave characteristics from sodium lidar observation over Fort Collins, CO (41 °N, 105 °W), *Geophys. Res. Lett.*, *34*.

Li, T., C.-Y. She, H.-L. Liu, T. Leblanc, and I. S. Mcdermid (2007b), Sodium lidar-observed strong inertia-gravity wave activities in the mesopause region over Fort Collins, Colorado (41 °N, 105 °W), *J. Geophys. Res.*, *112*, 22,104, doi:10.1029/2007JD008681.

Li, T., T. Leblanc, and I. S. Mcdermid (2008), Interannual variations of middle atmospheric temperature as measured by the JPL lidar at Mauna Loa Observatory, Hawaii (19.5 °N, 155.6 °W), *J. Geophys. Res.*, *113*, 14,109.

Li, T., C. Y. She, H. L. Liu, J. Yue, T. Nakamura, D. A. Krueger, Q. Wu, X. K. Dou, and S. Wang (2009), Observation of local tidal variability and instability, along with dissipation of diurnal tidal harmonics in the mesopause region over Fort Collins, Colorado (41 °N, 105 °W), *J. Geophys. Res.*, *114*, D06,106, doi:10.1029/2008JD011089.

Lieberman, R. S., J. Oberheide, M. E. Hagan, E. E. Remsberg, and L. L. Gordley (2004), Variability of diurnal tides and planetary waves during November 1978-May 1979, *J. Atmos. Sol. -Terr. Phys.*, *66*, 517, doi:10.1016/j.jastp.2004.01.006.

Lieberman, R. S., D. A. Ortland, D. M. Riggin, Q. Wu, and C. Jacobi (2010), Momentum budget of the migrating diurnal tide in the mesosphere and lower thermosphere, *J. Geophys. Res.*, *115*(D20), D20,105, doi:10.1029/2009JD013684.

Lima, L. M., P. P. Batista, H. Takahashi, and B. R. Clemesha (2004), Quasi-two-day wave observed by meteor radar at 22.7 °S, *J. Atmos. Sol. -Terr. Phys.*, *66*, 529, doi:10.1016/j.jastp.2004.01.007.

Lindzen, R. S. (1981), Turbulence and stress owing to gravity wave and tidal breakdown, *J. Geophys. Res.*, *86*, 9707–9714.

Lindzen, R. S., S. S. Hong, and J. Forbes (1977), Semidiurnal Hough mode extensions in the thermosphere and their application, *Tech. rep.*

Lintelman, S. A., and C. S. Gardner (1994), Observation and interpretation of spectra of atmospheric gravity wave perturbations with upward and downward phase progression, *J. Geophys. Res.*, *99*, 16,959.

Liu, A. Z., and C. S. Gardner (2004), Vertical dynamical transport of mesospheric constituents by dissipating gravity waves, *J. Atmos. Sol.-Terr. Phys.*, *66*(3-4), 267–275.

Liu, A. Z., and C. S. Gardner (2005), Vertical heat and constituent transport in the mesopause region by dissipating gravity waves at Maui, Hawaii (20.7 °N), and Starfire Optical Range, New Mexico (35 °N), *J. Geophys. Res.*, *110*, D09S13, doi:10.1029/2004JD004965.

Liu, A. Z., W. K. Hocking, S. J. Franke, and T. Thayaparan (2002), Comparison of Na lidar and meteor radar wind measurements at Starfire Optical Range, NM, USA, *J. Atmos. Sol.-Terr. Phys.*, *64*, 31–40.

Liu, A. Z., R. G. Roble, J. H. Hecht, M. F. Larsen, and C. S. Gardner (2004), Unstable layers in the mesopause region observed with Na lidar during the Turbulent Oxygen Mixing Experiment (TOMEX) campaign, *J. Geophys. Res.*, *109*, D02S02, doi:10.1029/2002JD003056.

Liu, H.-L., et al. (2007), Comparative study of short-term diurnal tidal variability, *J. Geophys. Res.*, *112*, 18,108, doi:10.1029/2007JD008542.

Liu, H.-L., W. Wang, A. D. Richmond, and R. G. Roble (2010a), Ionospheric variability due to planetary waves and tides for solar minimum conditions, *J. Geophys. Res.*, *115*, doi:10.1029/2009JA015188.

Liu, H.-L., et al. (2010b), Thermosphere extension of the Whole Atmosphere Community Climate Model, *J. Geophys. Res.*, *115*(A12), A12,302, doi:10.1029/2010JA015586.

Lombard, P. N., and J. J. Riley (1996), Instability and breakdown of internal gravity waves. i. linear stability analysis, *Phys Fluids*, *8*, 3271, doi:10.1063/1.869117.

Lu, X., A. Z. Liu, G. R. Swenson, T. Li, T. Leblanc, and I. S. Mcdermid (2009), Gravity wave propagation and dissipation from the stratosphere to the lower thermosphere, *J. Geophys. Res.*, *114*, 11,101, doi:10.1029/2008JD010112.

Lu, X., A. Z. Liu, J. Oberheide, Q. Wu, T. Li, Z. Li, G. R. Swenson, and S. J. Franke (2011), Seasonal Variability of the Diurnal Tide in the Mesosphere and Lower Thermosphere over Maui, HI (20.7 °N, 156.3 °W), *J. Geophys. Res.*, doi:10.1029/2011JD015599, in press.

Manson, A. H., and C. E. Meek (1988), Gravity Wave Propagation Characteristics (60-120 km) as Determined by the Saskatoon MF Radar (Gravnet) System: 1983-85 at 52 °N, 107 °W, *J. Atmos. Sci.*, *45*, 932, doi:10.1175/1520-0469(1988)045.

Mayr, H. G., and J. G. Mengel (2005), Interannual variations of the diurnal tide in the mesosphere generated by the quasi-biennial oscillation, *J. Geophys. Res.*, *110*, D10,111, doi:10.1029/2004JD005055.

Mayr, H. G., J. G. Mengel, K. L. Chan, and H. S. Porter (1998), Seasonal variations of the diurnal tide induced by gravity wave filtering, *Geophys. Res. Lett.*, *25*(7), 943–946.

Mayr, H. G., J. G. Mengel, K. L. Chan, and H. S. Porter (1999), Seasonal variations and planetary wave modulation of diurnal tides influenced by gravity waves, *Adv. Space Res.*, *24*(11), 1541–1544.

Mayr, H. G., J. G. Mengel, E. R. Talaat, H. S. Porter, and K. L. Chan (2005), Mesospheric non-migrating tides generated with planetary waves: I. Characteristics, *J. Atmos. Sol. -Terr. Phys.*, *67*(11), 959–980.

Mcdermid, I. S., T. D. Walsh, A. Deslis, and M. L. White (1995), Optical systems design for a stratospheric lidar system, *Applied Optics LP*, *34*, 6201, doi:10.1364/AO.34.006201.

McDonald, A. J., L. Thomas, and D. P. Wareing (1998), Night-to-night changes in the characteristics of gravity waves at stratospheric and lower-mesospheric heights, *Ann. Geophys.*, *16*, 229.

McFarlane, N. A. (1987), The effect of orographically excited gravity wave drag on the general circulation of the lower stratosphere and troposphere., *J. Atmos. Sci.*, *44*, 1775, doi:10.1175/1520-0469(1987)044.

McLandress, C. (1998), On the importance of gravity waves in the middle atmosphere and their parameterization in general circulation models, *J. Atmos. Sol. -Terr. Phys.*, *60*, 1357.

McLandress, C. (2002a), The seasonal variation of the propagating diurnal tide in the mesosphere and lower thermosphere. Part I: The role of gravity waves and planetary waves, *J. Atmos. Sci.*, *59*, 893–906.

McLandress, C. (2002b), The seasonal variation of the propagating diurnal tide in the mesosphere and lower thermosphere. Part II: The role of tidal heating and zonal mean winds, *J. Atmos. Sci.*, *59*, 907–922.

McLandress, C., G. G. Shepherd, and B. H. Solheim (1996), Satellite observations of thermospheric tides: Results from the Wind Imaging Interferometer on UARS, *J. Geophys. Res.*, *101*(D2), 4093–4114.

Mitchell, N., and C. Beldon (2009), Gravity waves in the mesopause region observed by meteor radar: 1. a simple measurement technique, *J. Atmos. Sol.-Terr. Phys.*, *71*(8-9), 866–874.

Miyahara, S., and J. M. Forbes (1991), Interactions between gravity waves and the diurnal tide in the mesosphere and lower thermosphere, *J. Meteor. Soc. Japan*, *69*, 523–531.

Mukhtarov, P., D. Pancheva, and B. Andonov (2009), Global structure and seasonal and interannual variability of the migrating diurnal tide seen in the SABER/TIMED temperatures between 20 and 120 km, *J. Geophys. Res.*, *114*, 02,309, doi:10.1029/2008JA013759.

Murayama, Y., T. Tsuda, R. Wilson, H. Nakane, S. Hayashida, N. Sugimoto, I. Matsui, and Y. Sasano (1994), Gravity-wave activity in the upper-stratosphere and lower mesosphere observed with the Rayleigh lidar at Tsukuba, Japan, *Geophys. Res. Lett.*, *21*(14), 1539–1542.

Norton, W. A., and J. Thuburn (1999), Sensitivity of mesospheric mean flow, planetary waves, and tides to strength of gravity wave drag, *J. Geophys. Res.*, *104*, 30,897, doi:10.1029/1999JD900961.

Oberheide, J., and J. M. Forbes (2008), Tidal propagation of deep tropical cloud signatures into the thermosphere from timed observations, *Geophys. Res. Lett.*, *35*, L04,816, doi:10.1029/2007GL032,397.

Oberheide, J., Q. Wu, T. L. Killeen, M. E. Hagan, and R. G. Roble (2006), Diurnal nonmigrating tides from TIMED Doppler Interferometer wind data: Monthly climatologies and seasonal variations, *J. Geophys. Res.*, *111*, doi:10.1029/2005JA011491.

Ortland, D. A. (2005a), A study of the global structure of the migrating diurnal tide using generalized hough modes, *J. Atmos. Sci.*, *62*, 2684–2702.

Ortland, D. A. (2005b), Generalized hough modes: The structure of damped global-scale waves propagating on a mean flow with horizontal and vertical shear., *J. Atmos. Sci.*, *62*, 2674, doi:10.1175/JAS3500.1.

Ortland, D. A., and M. J. Alexander (2006), Gravity wave influence on the global structure of the diurnal tide in the mesosphere and lower thermosphere, *J. Geophys. Res.*, *111*, A10S10, doi:10.1029/2005JA011467.

O'Sullivan, D., and T. J. Dunkerton (1995), Generation of Inertia-Gravity Waves in a Simulated Life Cycle of Baroclinic Instability., *J. Atmos. Sci.*, *52*, 3695–3716.

Palo, S. E., R. G. Roble, and M. E. Hagan (1999), Middle atmosphere effects of the quasi-two-day wave determined from a General Circulation Model, *Earth Planets Space*, *51*, 629–647.

Pfister, L., S. Scott, M. Loewenstein, S. Bowen, and M. Legg (1993), Mesoscale disturbances in the tropical stratosphere excited by convection: Observations and effects on the stratospheric momentum budget., *J. Atmos. Sci.*, *50*, 1058, doi:10.1175/1520-0469(1993)050.

Picone, J. M., A. E. Hedin, D. P. Drob, and A. C. Aikin (2002), Nrlmsise-00 empirical model of the atmosphere: Statistical comparisons and scientific issues, *J. Geophys. Res.*, *107*, 1468, doi:10.1029/2002JA009430.

Preusse, P., S. D. Eckermann, and D. Offermann (2000), Comparison of global distributions of zonal-mean gravity wave variance inferred from different satellite instruments, *Geophys. Res. Lett.*, *27*, 3877–3880, doi:10.1029/2000GL011916.

Rauthe, M., M. Gerding, J. Hffner, and F.-J. Lbken (2006), Lidar temperature measurements of gravity waves over Khlungsborn (54 °N) from 1 to 105 km: A winter-summer comparison, *J. Geophys. Res.*, *111*, 24,108.

Reeder, M. J., and M. Griffiths (1996), Stratospheric inertiagravity waves generated in a numerical model of frontogenesis. II: Wave sources, generation mechanisms and momentum., *Q J ROY METEOR SOC*, *122*, 1175–1195.

Richter, J. H., F. Sassi, R. R. Garcia, K. Matthes, and C. A. Fischer (2008), Dynamics of the middle atmosphere as simulated by the Whole Atmosphere Community Climate Model, version 3 (WACCM3), *J. Geophys. Res.*, *113*, 08,101, doi:10.1029/2007JD009269.

Richter, J. H., F. Sassi, and R. R. Garcia (2010), Toward a physically based gravity wave source parameterization in a general circulation model, *J. Atmos. Sci.*, *67*, 136, doi:10.1175/2009JAS3112.1.

Rishbeth, H., and M. Mendillo (2001), Patterns of F2-layer variability, *J. Atmos. Sol. -Terr. Phys.*, *63*, 1661, doi:10.1016/S1364-6826(01)00036-0.

Russell, J. M., M. G. Mlynczak, L. L. Gordley, J. J. Tansock, and R. W. Esplin (1999), Overview of the saber experiment and preliminary calibration results, *Proc. SPIE*, *3756*, 277–288.

Sato, K., and M. Yamada (1994), Vertical structure of atmospheric gravity waves revealed by the wavelet analysis, *J. Geophys. Res.*, *99*, 20,623.

Scargle, J. D. (1982), Studies in astronomical time series analysis. II - Statistical aspects of spectral analysis of unevenly spaced data, *Astrophys. J.*, *263*, 835–853.

Serafimovich, A., P. Hoffmann, D. Peters, and V. Lehmann (2005), Investigation of inertia-gravity waves in the upper troposphere/lower stratosphere over Northern Germany observed with collocated VHF/UHF radars, *Atmos. Chem. Phys.*, *5*, 295.

Sharma, S., V. Sivakumar, H. Bencherif, H. Chandra, Y. Acharya, A. Jayaraman, P. Rao, and D. Narayanarao (2006), A comprehensive study on middle atmospheric thermal structure over a tropic and sub-tropic stations, *Adv. Space Res.*, *37*(12), 2278–2283.

She, C. Y., and J. R. Yu (1994), Simultaneous three-frequncy Na lidar measurements of radial wind and temperature in the mesopause region, *Geophys. Res. Lett.*, *21*(17), 1771–1774.

She, C. Y., S. Chen, B. P. Williams, Z. Hu, D. A. Krueger, and M. E. Hagan (2002), Tides in the mesopause region over Fort Collins, Colorado (41 °N, 105 °W) based on lidar temperature observations covering full diurnal cycles, *J. Geophys. Res.*, *107*(D18), 4350, doi:10.1029/2001JD001189.

She, C. Y., et al. (2004), Tidal perturbations and variability in the mesopause region over Fort Collins, CO (41 °N, 105 °W): Continuous multi-day temperature and wind lidar observations, *Geophys. Res. Lett.*, *31*, L24,111, doi:10.1029/2004GL021165.

Shibata, T., T. Fukuda, and M. Maeda (1986), Density fluctuations in the middle atmosphere over Fukuoka observed by an XeF Rayleigh lidar, *Geophys. Res. Lett.*, *13*, 1121–1124, doi:10.1029/GL013i011p01121.

Sica, R. J., and A. T. Russell (1999), How many waves are in the gravity wave spectrum?, *Geophys. Res. Lett.*, *26*, 3617, doi:10.1029/1999GL003683.

Sivakumar, V., P. B. Rao, and H. Bencherif (2006), Lidar observations of middle atmospheric gravity wave activity over a low-latitude site (Gadanki, 13.5 ° N, 79.2 ° E), *Annales Geophysicae*, *24*, 823.

Smith, A. K., D. R. Marsh, and A. C. Szymczak (2003), Interaction of chemical heating and the diurnal tide in the mesosphere, *J. Geophys. Res.*, *108*, 4164, doi:10.1029/2002JD002664.

Smith, S. M., M. Mendillo, J. Baumgardner, and R. R. Clark (2000), Mesospheric gravity wave imaging at a subauroral site: First results from millstone hill, *J. Geophys. Res.*, *105*(A12), 27,119–27,130.

States, R. J., and C. S. Gardner (2000a), Thermal structure of the mesopause region (80-105 km) at 40 °N latitude. Part II: Diurnal variations, *J. Atmos. Sci.*, *57*, 78–92.

States, R. J., and C. S. Gardner (2000b), Thermal Structure of the Mesopause Region (80105 km) at 40N Latitude. Part I: Seasonal Variations, *J. Atmos. Sci.*, *57*(1), 66–77, doi:10.1175/1520-0469(2000)057.

Svoboda, A. A., J. M. Forbes, and S. Miyahara (2005), A space-based climatology of diurnal MLT tidal winds, temperatures and densities from UARS wind measurements, *J. Atmos. Sol. -Terr. Phys.*, *67*, 1533, doi:10.1016/j.jastp.2005.08.018.

Swenson, G. R., A. Z. Liu, F. Li, and J. Tang (2003), High frequency atmospheric gravity wave damping in the mesosphere, *Adv. Space Res.*, *32*(5), 785–793.

Swinbank, R., and D. A. Ortland (2003), Compilation of wind data for the upper atmosphere research satellite (uars) reference atmosphere project, *J. Geophys. Res.*, *108*, 4615, doi:10.1029/2002JD003135.

Tang, J., A. Z. Liu, and G. R. Swenson (2002), High frequency gravity waves observed in oh airglow at starfire optical range, nm: Seasonal variations in momentum flux, *Geophys. Res. Lett.*, *29*, 27.

Tang, J., G. R. Swenson, A. Z. Liu, and F. Kamalabadi (2005), Observational investigations of high frequency gravity wave momentum flux with airglow imaging, *J. Geophys. Res.*, *110*, D09S09, doi:10.1029/2004JD004778.

Taylor, M. J., Y. Y. Gu, X. Tao, and C. S. Gardner (1995), An investigation of intrinsic gravity wave signatures using coordinated lidar and nightglow image measurements, *Geophys. Res. Lett.*, *22*(20), 2853–2856.

Tsuda, T., S. Kato, A. H. Manson, and C. E. Meek (1988), Characteristics of semidiurnal tides observed by the Kyoto Meteor Radar and Saskatoon MediumFrequency Radar, *J. Geophys. Res.*, *93*(D6), 7027–7036.

Tsuda, T., Y. Murayama, T. Nakamura, R. A. Vincent, A. H. Manson, C. E. Meek, and R. L. Wilson (1994), Variations of the gravity wave characteristics with height, season and latitude revealed by comparative observations, *J. Atmos. Sol.-Terr. Phys.*, *56*(5), 555–568.

Tsuda, T., M. Nishida, C. Rocken, and R. H. Ware (2000), A global morphology of gravity wave activity in the stratosphere reveald by the GPS occultationi data (GPS/MET), *J. Geophys. Res.*, *105*(D6), 7257–7273.

Tsuda, T., M. V. Ratnam, P. T. May, M. J. Alexander, R. A. Vincent, and A. MacKinnon (2004), Characteristics of gravity waves with short vertical wavelengths observed with radiosonde and GPS occultation during DAWEX (Darwin Area Wave Experiment), *J. Geophys. Res.*, *109*(D20).

Vincent, R. A., and M. J. Alexander (2000), Gravity waves in the tropical lower stratosphere: An observational study of seasonal and interannual variability, *J. Geophys. Res.*, *105*, 17,971, doi:10.1029/2000JD900196.

Vincent, R. A., S. Kovalam, D. C. Fritts, and J. R. Isler (1998), Long-term MF radar observations of solar tides in the low-latitude mesosphere: Interannual variability and comparisons with the GSWM, *J. Geophys. Res.*, *103*(D8), 8667–8683.

Vincent, R. A., S. Kovalam, I. m Reid, and J. P. Younger (2010), Gravity wave flux retrievals using meteor radars, *Geophys. Res. Lett.*, *37*, 14,802, doi:10.1029/2010GL044086.

Waliser, D. E., and C. Gautier (1993), A Satellite-derived Climatology of the ITCZ, *J. Clim.*, *6*, 2162, doi:10.1175/1520-0442(1993)006.

Walterscheid, R. L. (1981), Intertio-gravity wave induced accelerations of mean flow having an imposed periodic component: Impliciations for tidal observations in the meteor region, *J. Geophys. Res.*, *86*(C10), 9698–9706.

Wang, D.-Y., and D. C. Fritts (1991), Evidence of Gravity Wave-Tidal Interaction Observed near the Summer Mesopause at Poker Flat, Alaska, *J. Atmos. Sci.*, *48*, 572.

Wang, L., and M. A. Geller (2003), Morphology of gravity-wave energy as observed from 4 years (1998-2001) of high vertical resolution U.S. radiosonde data, *J. Geophys. Res.*, *108*(D16), 4489, doi:10.1029/2002JD002,786.

Ward, W. E., et al. (2010), On the consistency of model, ground-based, and satellite observations of tidal signatures: Initial results from the cawses tidal campaigns, *J. Geophys. Res.*, *115*, 07,107, doi:10.1029/2009JD012593.

Warner, C. D., and M. E. McIntyre (2001), An ultrasimple spectral parameterization for nonorographic gravity waves, *J. Atmos. Sci.*, *58*(14), 1837–1857.

Watanabe, S., and S. Miyahara (2009), Quantification of the gravity wave forcing of the migrating diurnal tide in a gravity wave-resolving general circulation model, *J. Geophys. Res.*, *114*, 07,110.

Welch, P. D. (1967), The Use of Fast Fourier Transform for the Estimation of Power Spectra: A Method Based on Time Averaging Over Short, Modified Periodograms, *IEEE Trans. Audio Electroacoust.*, *15*, 70–73.

Whiteway, J. A., and A. I. Carswell (1995), Lidar observations of gravity wave activity in the upper stratosphere over toronto, *J. Geophys. Res.*, *100*, 14,113.

Wilson, R., M. L. Chanin, and A. Hauchecorne (1991), Gravity waves in the middle atmosphere observed by rayleigh lidar 1. case studies, *J. Geophys. Res.*, *96*, 5153, doi:10.1029/90JD02231.

Wu, Q., et al. (2008), Global distribution and interannual variations of mesospheric and lower thermospheric neutral wind diurnal tide: 1. Migrating tide, *J. Geophys. Res.*, *113*(A05308), doi:10.1029/2007JA012542.

Xu, J., A. K. Smith, H.-L. Liu, W. Yuan, Q. Wu, G. Jiang, M. G. Mlynczak, J. M. Russell, and S. J. Franke (2009), Seasonal and quasi-biennial variations in the migrating diurnal tide observed by Thermosphere, Ionosphere, Mesosphere, Energetics and Dynamics (TIMED), *J. Geophys. Res.*, *114*(D13), 16, doi:10.1029/2008JD011298.

Yeh, K. C., and C. H. Liu (1981), The instability of atmospheric gravity waves through wave-wave interactions, *International Symposium on Middle Atmosphere Dynamics and Transport*, *86*, 9722, doi:10.1029/JC086iC10p09722.

Yoshiki, M., and K. Sato (2000), A statistical study of gravity waves in the polar regions based on operational radiosonde data, *J. Geophys. Res.*, *105*(D14), 17,995–18,012.

Yu, J. R., and C. Y. She (1995), Climatology of a midlatitude mesopause region observed by a lidar at Fort Collins, Colorado (40.6 °N, 105 °W), *J. Geophys. Res.*, *100*, 7441, doi:10.1029/94JD03109.

Yuan, T., et al. (2006), Seasonal variation of diurnal perturbations in mesopause region temperature, zonal, and meridional winds above Fort Collins, Colorado (40.6 °N, 105 °W), *J. Geophys. Res.*, *111*(D06103), doi:10.1029/2004JD005486.

Yue, J., C.-Y. She, and H.-L. Liu (2010), Large wind shears and stabilities in the mesopause region observed by Na wind-temperature lidar at midlatitude, *J. Geophys. Res.*, *115*, A10,307, doi:10.1029/2009JA014864.

Zhang, X., J. M. Forbes, M. E. Hagan, J. M. Russell III, S. E. Palo, C. J. Mertens, and M. G. Mlynczak (2006), Monthly tidal temperatures 20-120 km from TIMED/SABER, *J. Geophys. Res.*, *111*, A10S08, doi:10.1029/2005JA011504.

Zhang, X., J. M. Forbes, and M. E. Hagan (2010), Longitudinal variation of tides in the MLT region: 1. Tides driven by tropospheric net radiative heating, *J. Geophys. Res.*, *115*, A06,316, doi:10.1029/2009JA014897.

Zhang, X., J. M. Forbes, and M. E. Hagan (2011), Seasonal-latitudinal Variation of the Eastward-Propagating Diurnal Tide with Zonal Wavenumber 3 in the MLT: Influences of Heating and Background Wind Distribution, *J. Atmos. Sol. -Terr. Phys.*, *In Press, Accepted Manuscript*, doi:DOI: 10.1016/j.jastp.2011.03.005.

Zhao, Y., A. Z. Liu, and C. S. Gardner (2003), Measurements of atmospheric stability in the mesopause region at starfire optical range, NM, *J. Atmos. Sol. -Terr. Phys.*, *65*, 219.